UNIVERSITY OF CALIFORNIA

SANTA CRUZ

THE INFLUENCE OF LIGAND PARAMETERS ON THE PHOTOLABILITY OF NITRIC OXIDE FROM DESIGNED IRON, MANGANESE, AND RUTHENIUM NITROSYLS UNDER VISIBLE LIGHT

A dissertation submitted in partial satisfaction
of the requirements for the degree of

DOCTOR OF PHILOSOPHY

in

CHEMISTRY AND BIOCHEMISTRY

by

Nicole Lynn Fry

June 2012

The Dissertation of Nicole L. Fry
is approved:

_____
Professor Theodore R. Holman, Chair

_____
Professor Pradip K. Mascharak, Advisor

_____
Professor Scott R. J. Oliver

_____
Tyrus Miller
Vice Provost and Dean of Graduate Students

Table of Contents

Appendix A.

List of Figures

Chapter 1.

Chapter 2.

Chapter 3. Part 1.

Chapter 3. Part 2.

Chapter 4.

Appendix A.

List of Tables

Chapter 1.

Chapter 2.

Chapter 4.

Abstract

THE INFLUENCE OF LIGAND PARAMETERS ON THE PHOTOLABILITY OF NITRIC OXIDE FROM DESIGNED IRON, MANGANESE, AND RUTHENIUM NITROSYLS UNDER VISIBLE LIGHT

Nicole Lynn Fry

Photoactive metal nitrosyls (NO complexes of metals) have drawn attention as potential drugs for delivery of nitric oxide (NO) to biological targets under the control of light. Major success in this area has been achieved with designed metal nitrosyls derived from ligands that contain carboxamide group(s). This thesis details the design strategies used to synthesize such carboxamide containing metal nitrosyls. As a first step, DFT and TDDFT calculations were used to elucidate the electronic structures and varying photoactivities of iron, manganese, and ruthenium nitrosyls derived from identical pentadentate ligand frames, as described in Chapter 2.

In Chapter 3, a set of tetradentate dicarboxamide ligand frames with different combinations of phosphine-P, phenolato-O, and/or pyridine-N donors was employed in order to uncover which atom types promote low-energy light absorption in ruthenium nitrosyls. Part one details the reactions of phosphine containing ligands with $RuCl_3$ and subsequent exposure to NO gas. Such reactions lead to the eventual isolation of diamagnetic Ru(II) complexes with oxidized ligand frames and no bound NO.

The second part of Chapter 3 focuses on a set of $\{RuNO\}^6$ nitrosyls with dicarboxamide ligands with a varying numbers of phenolate-O and pyridine-N

donors. The resulting nitrosyls have been characterized by X-ray crystallography. All three complexes are diamagnetic, exhibit νNO in the range 1780-1840 cm^{-1} and rapidly release NO in solution upon exposure to low power UV light. Results of theoretical studies on these $\{RuNO\}^6$ nitrosyls indicate considerable contribution from ligand orbitals in the MOs involved in transitions leading to NO photolability.

In Chapter 4, the attachment of resorufin and fluorescein derived dye chromophores was explored as a way to further sensitize ruthenium nitrosyls to visible light. First, the steric effects of the in-plane ligands in these dye-sensitized $\{RuNO\}^6$ nitrosyls on their NO photolability were examined. Next, the direct conjugation of dye chromophores was compared with dye attachment via a linker to understand the mechanism of photoactivation in these dye-bound ruthenium nitrosyls. In addition the fluorescence properties of these dye-conjugated nitrosyls were characterized and found to provide a potential signal showing when and where NO has been delivered.

Acknowledgments

I would like to thank my research advisor, Prof. Pradip Mascharak for giving me all the necessary tools for becoming a good scientist. His guidance and expertise has taught me not only how to perform scientific experiments but also how to think, talk, and write scientifically.

I must also thank the rest of my thesis committee members, Prof. Ted Holman and Prof. Scott Oliver for their advice and guidance throughout my graduate career. I appreciate their taking time to be at my second year seminar, oral exam, and thesis defense.

Over the years I have worked with several people including Prof. Marilyn Olmstead, Dr. Allen Oliver, Dr. David Rogow, and Honghan Fei during the collection and solving of several crystal structures. I would like to thank each of them for their help and guidance.

I had the pleasure of collaborating with Dr. Anna Merkle and Prof. Nicolai Lehnert (University of Michigan, Ann Arbor) on the Raman and DFT/TDDFT coupled studies of a few manganese nitrosyls. I want to thank them for taking time to answer several of my DFT/TDDFT questions.

My fellow lab mates are the people I interact with most often on a day to day basis. I want to acknowledge all of the help and support I have received from both past graduate lab members (Dr. Michael Rose, Dr. A. Alegra Eroy-Reveles, Dr. Genevieve Halpenny, and Gianna Hoffman-Luca) and present graduate lab members (Margarita Gonzales, Brandon Heilman, Tara deBoer, and Samantha Carrington). I

especially have to thank Dr. Michael Rose for taking me under his wing when I first joined the lab. He was always willing to share his wealth of experience and patient with my many questions. I would also like to thank the undergraduate students who I mentored in the lab (Crystal Nyitray, Tom Zhao, and Julia Wei).

Lastly, I would like to thank my parents, Mike and Anne Fry, and my three sisters, Julie, Jocelyn, and Melanie for all of their love and support which has helped sustain me throughout graduate school. They knew my potential even when I didn't. I also want to acknowledge my grandfather, Robert Wynne and cousin, Virginia Fry for their great love of education and learning. I have always looked up to them and want to thank them for inspiring me to continue my education.

Chapter 1

Introduction

1.1 Nitric Oxide in Biology

In biological systems there is a delicate balance of a myriad of molecules that are highly regulated to insure the proper function of cells. The importance of the larger macromolecules found in cells such as proteins and DNA has been well established for many years. However, more recently several small molecules have been identified that are also important for biological function via cell signaling. Nitric oxide (NO) is a prime example of one of these small signaling molecules. It exhibits a diverse assortment of physiological effects that are greatly dependent on the location and concentration of NO found in the bound.[1-4]

1.1.1 Endogenous Nitric Oxide Generation

NO is produced endogenously by a family of enzymes called nitric oxide synthase (NOS) which have considerable homology with cytochrome P450. These enzymes have a heme containing oxygenase domain [5] as well as a reductase domain [6] with FMN and FAD binding sites. The two domains are linked by a polypeptide interdomain linker which also constitutes a binding site for calmodulin (Figure 1.1).[7,8] The proper function of these enzymes requires complex cosubstrate and cofactor requirements that include heme, O_2, NADPH, FAD, FMN, tetrahydrobiopterin and calmodulin. When all are present, NO is produced from L-arginine within the oxygenase domain via two consecutive monooxygenation reactions. First the L-arginine substrate binds directly above the heme plane and two electrons are delivered

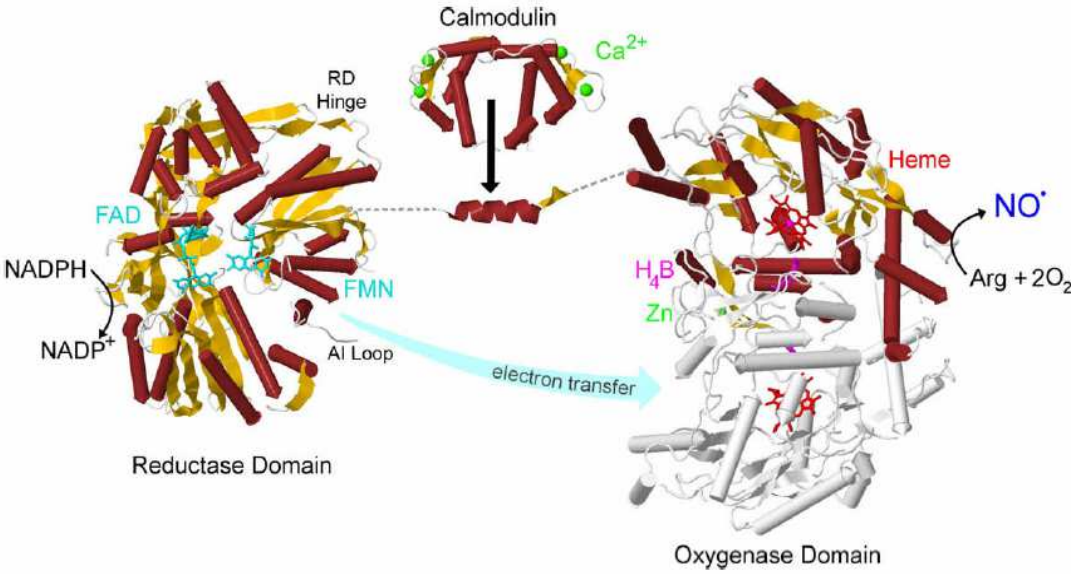

Figure 1.1 Structures of the different fragments of NO synthase aligned in order of amino-acid sequence. The dimeric oxygenase domain of nNOS (1ZVL) [5], CaM-binding linker of eNOS with bound CaM (1NIW) [7] and the reductase domain of nNOS (1TLL). [6] (Adapted from Ref. 8)

from the reductase domain (via NADPH dehydrogenation) to the heme. This allows the activation of dioxygen and the addition of a single oxygen

atom into the L-arginine substrate forming N-hydroxy-L-arginine. The second monooxygenation reaction only requires one electron for oxygen activation leading to the formation of NO and citrulline.[9]

There are three different isoforms of NOS which are encoded by separate gene sequences and found in various region of the body. The two constitutive isoforms of enzyme are neuronal NOS (nNOS) [10] and endothelial NOS (eNOS).[11] The neuronal isoform is expressed in nerve cells, skeletal muscle, and heart muscle while the endothelial isoform is produced in cells lining blood vessels. The third isoform is

called the inducible NOS (iNOS) [12] expression for this isoform is induced in several different cell types (such as macrophages) as part of the body's immune response. While all three isoforms produce NO from L-arginine as describe above, there are some physical characteristics of each that distinguish them from each other. The iNOS has the shortest amino acid sequence and a bound Ca^{2+} (which is necessary for NO production).[13] Although both eNOS and nNOS activity also require bound Ca^{2+}, they have a lower affinity for Ca^{2+} than iNOS. Thus changes in the concentration of Ca^{2+} can greatly affect the production of NO in these isoforms.[14] The eNOS isoform has an additional autoinhibitory loop (AI, Figure 1.1) within the FMN domain as well as another 42 amino acid extension in its C-terminal reductase domain which are not present in iNOS and are modified in nNOS. In addition, nNOS has a 200 amino acid extension in the N-terminal oxygenase domain called a PDZ domain which is used to localize the enzyme within cells.[15]

The predominant stimulus for the continuous formation of NO in endothelial cells is thought to be the shear stress generated by the flow of blood over the endothelial layer. This shear stress regulates the enzyme's activity by activation of the serine/threonine protein kinase Akt/PKB which phosphorylates eNOS, leading to an increase in NO production.[16] In the case of nNOS, NO is produced almost exclusively after activation of NMDA receptors. The postsynaptic density protein PSD95 connects nNOS (via the PDZ domain) to the NMDA receptors. Activation of the NMDA receptor directly exposes nNOS to a flux of Ca^{2+}. This results in Ca^{2+} binding which allows nNOS to further bind calmodulin and results in the production

of NO.[17] While both eNOS and nNOS are constantly expressed, the inducible isoform iNOS is only expressed in response to cytokines and microbial products. For example, the bacterial lipopolysaccharide (LPS) induces iNOS expression via the NF-kappa B promoter site
on the gene encoding iNOS.[18]

1.1.2 Nitric Oxide Reactivity and Biological Function

As a gaseous small molecule with rich redox chemistry, NO is capable of interacting either directly or indirectly with several different cellular targets.[19] At low NO concentrations (less than 1 μM) NO can interact directly with transition metals found in various metalloproteins such as hemoglobin,[20] guanylate cyclase,[21] cytochrome P450,[22] and cytochrome c oxidase.[23] However, when concentrations of NO become higher (above 1 μM), NO can indirectly interact with biological targets via reactive nitrogen oxide species (RNOS) generated from the reaction of NO with either oxygen or superoxide (Figure 1.2).[19, 24] The indirect pathway can be divided into nitrosation, oxidation, and nitration chemistry. Nitrosation occurs when intermediates generated from the reaction between NO/O_2 are added to amine, thiol, or hydroxy aromatic groups generating nitrosamines or S-nitrosothiols.[25, 26] RNOS can also participate in oxidation chemistry via removal of electrons or hydroxylation reactions of substrates such as DNA [27] or lipids.[28] Lastly, nitration of aromatic groups such as tyrosine residues in proteins can also occur via RNOS generating nitrotyrosine.[29]

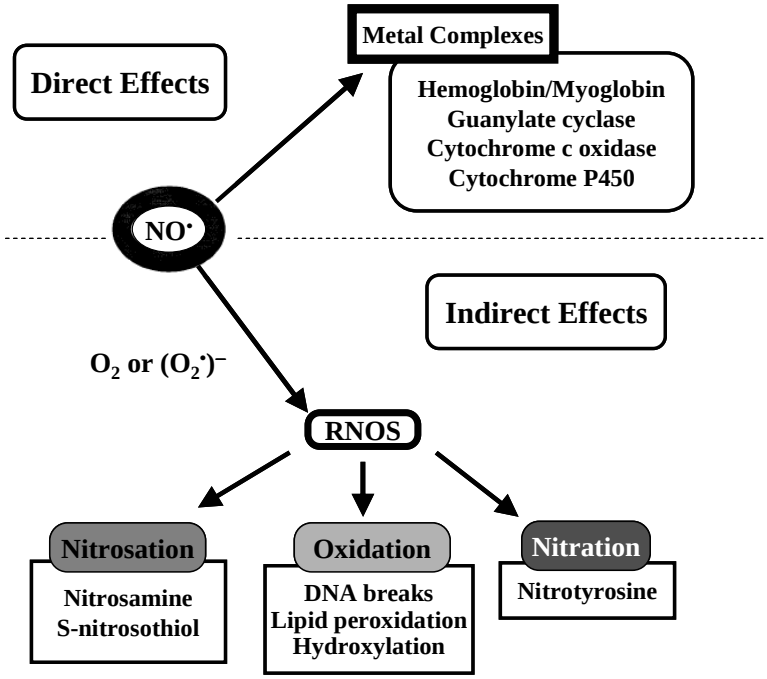

Figure 1.2 The chemical biology of nitric oxide (Adapted from Ref. 19)

At low μM to nM concentrations, NO promotes normal function of cells. The constitutive isoforms nNOS and eNOS both produce NO concentrations within this range. Such NO production by eNOS activates smooth muscle cell relaxation through direct NO binding to the iron center of the heme moiety of guanylate cyclase.[30] This disrupts the planar conformation of the iron which activates the enzyme toward cGMP production.[31] The resulting cGMP modulates the function of cGMP-dependent protein kinase which phosphorylates and consequently activates a calcium-sensitive potassium channel leading to vascular smooth muscle relaxation and vasodilation of blood vessels. Thus NO production is responsible for regulating vascular blood pressure.[32] In this manner, NO has also been shown to inhibit blood

platelet adhesion and aggregation (via cGMP production) reducing the formation of blood clots.[33] In addition, adhesion of leukocytes can also be modulated by NO resulting in anti-inflammatory properties.[34] Similar low concentrations of NO, produced in neuronal cells by nNOS act as a neurotransmitter via the glutamate receptor, NMDA which mediates most of the fast excitory synaptic transmissions in the central nervous system. Many studies have suggested that there is a link between the activation of the NMDA receptor and the production of NO which leads to induction of downstream signaling cascades in neurons.[35]

When the concentration of NO is increased into the μM to mM range, the deleterious role of NO (by means of RNOS) becomes apparent. This is clearly seen during the activation of body's immune system which causes the production of high concentrations of NO in different phagocytes (such as macrophages) in order to help kill invading pathogens. For example, certain cytokines and bacterial lipopolysaccharides can activate macrophages to express iNOS which then produces large concentration of NO.[13, 36] In this context, the release of NO usually coincides with the production of ROS. For example, enzymes such as NADPH oxidases (NADPHox) and xanthine oxidase, become activated in many cellular systems to actively produce large amounts of superoxide.[37] Such ROS can react with NO to form RNOS such as peroxynitrite, nitrogen dioxide, and dinitrogen trioxide (Figure 1.3). These RNOS are much stronger oxidants than NO alone and thus can degrade

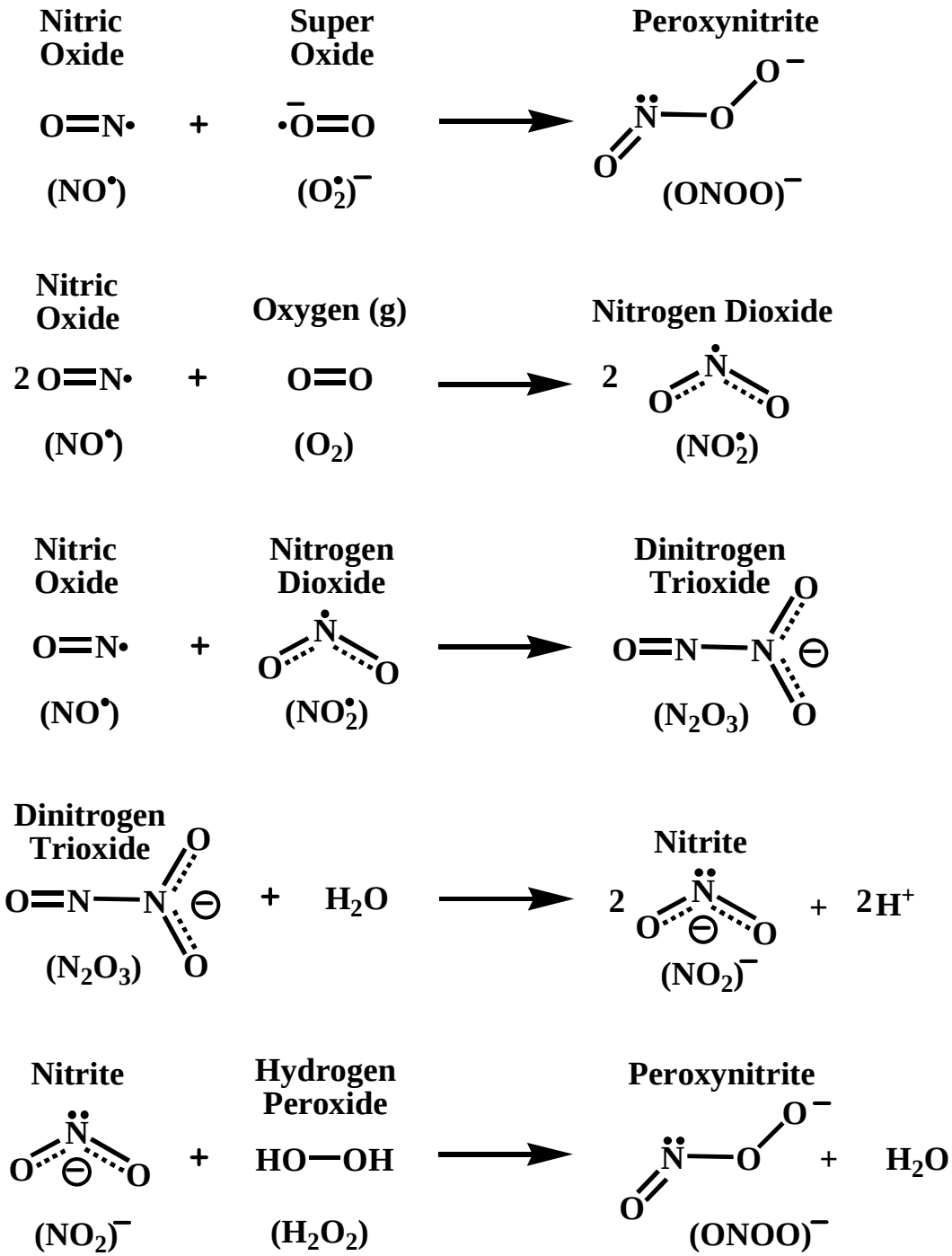

Figure 1.3. Reaction pathways leading to the formation of reactive nitrogen oxygen specie (RNOS)

microbial cell walls via the oxidation of lipids, interference with cellular respiration, and damage to the DNA of the invading pathogens.[3]

It has also been found that such high concentrations of NO can induce apoptosis in certain cancer cells which can lead to tumor regression and/or inhibition of metastasis. Apoptosis or programmed cell death is initiated by specific signals that activate the elimination/death of unnecessary or harmful cells in a controlled fashion (Figure 1.4). Under these conditions, the cellular contents are systematically

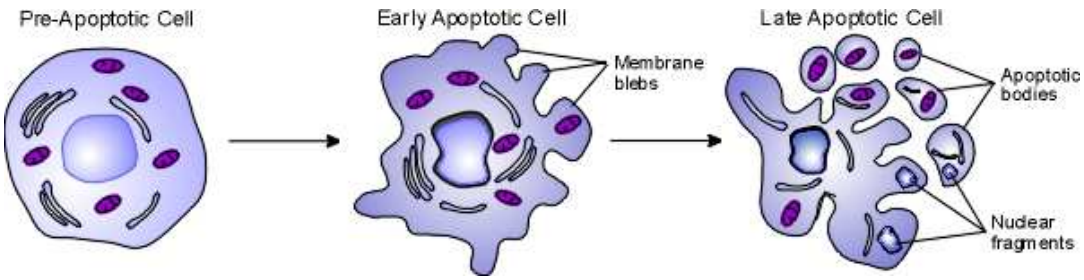

Figure 1.4. Stages of cellular apoptosis

dispersed and up taken by surrounding cells. This is in direct contrast to cell death via necrosis (or uncontrolled cell death) which causes cells to swell and burst releasing cellular content. This leads to inflammation and damage to neighboring healthy tissues. Studies have revealed that apoptosis in response to NO donors or endogenous NO generation is accompanied by an early accumulation of the tumor suppressor protein p53, caspase activation, and DNA fragmentation.[39] NO has been shown to directly interact with DNA causing damage and inhibition of mitochondrial respiration via destruction of Fe–S clusters, both of which can elicit a rapid stress

response leading to apoptosis.[40] Further, high concentration of NO can cause nitrite accumulation in the cell supernatant and results in p53 accumulation which is a known regulator of cell death.[41] Lastly, the disruption of the mitochondrial transmembrane potential by NO can also lead to apoptosis via inhibition of several mitochondrial enzymes including aconitase and cytochrome c oxidase.[42]

It has been suggested several research groups that peroxynitrite formation from the reaction of NO with superoxide is one of the primary pathway of NO metabolism.[43] The reaction between superoxide and NO is very fast occurring at rates near diffusion control.[44] Once generated, peroxynitrite can interact with several different molecules. The nitration of tyrosine residues is one such reaction. The presence of the resulting nitrotyrosine residues in biological systems is used by many researches as a marker of peroxynitrite formation. Nitrotyrosine is formed from peroxynitrite through two different pathways depending on the pH or presence of carbon dioxide in the environment (Figure 1.5).[45] For example, protonation of peroxynitrite (peroxynitrous acid) can result in the formation of hydroxyl radicals and nitrite radicals. The hydroxyl radical can then generate tyrosyl radicals which will react with the nitrite radical to form nitrotyrosine. Alternatively, nitrosoperoxy-carbonate can breakdown into a carbonate radical and nitrite radical. Again throsyl radicals are generated that further react with nitrite radical to form nitrotyrosine.

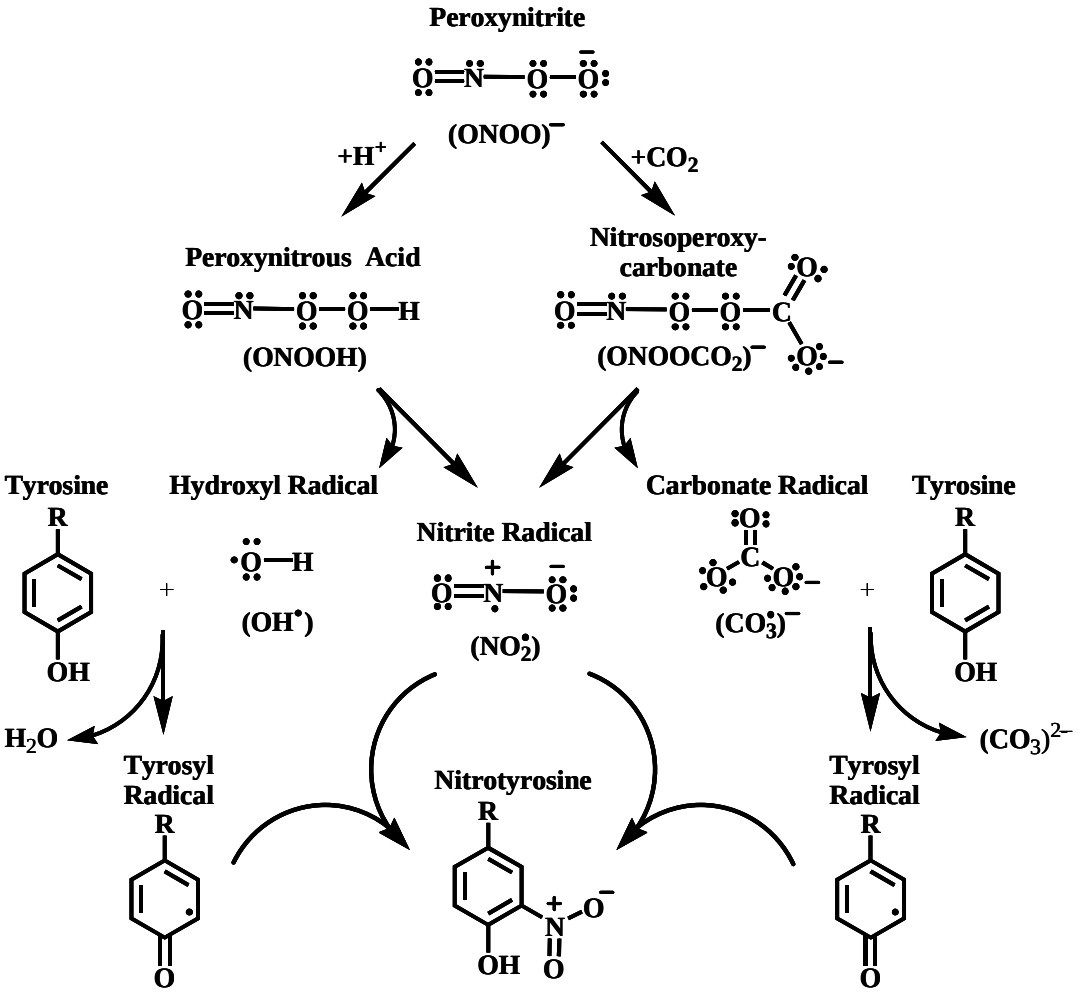

Figure 1.5. Reaction scheme of tyrosine nitration by peroxynitrite

1.2 Metal Nitrosyls

1.2.1 Electronic Description

The discovery that nitric oxide (NO) acts as a key signaling molecule in many important biological processes has stimulated interest in the chemistry and biochemistry of various NO bound metal complexes (nitrosyls). NO forms such metal

nitrosyls with many different metal centers (such as Fe, Ru, Mn, Re, Mo, W, Cr, and Os to name a few).[46-53] In most cases, the metal and ligands type can dramatically affect the electronic configuration of metal nitrosyls due to the non-innocent nature of NO (with the possibility of existing as NO^+, $NO^\bullet$ or NO^- in metal-nitrosyl complexes). The Feltham and Enemark notation $\{M–NO\}^n$ (where n represents the sum of metal d and π^* NO electrons) provides a general formalism that deals with the ambiguous electronic structure of the metal nitrosyls.[54] However, many research groups have strived to elucidate the exact electronic descriptions of various nitrosyls.

For ruthenium nitrosyls, the $\{Ru\text{-}NO\}^6$ configuration is the primary form of almost all reported ruthenium nitrosyls (Table 1.1). This is mainly due to the large crystal-field stabilization energy of ruthenium which leads to a diamagnetic low spin Ru(II)-NO^+ species. The NO^+ electronic description is generally accepted due to the high NO stretching frequencies (ν_{NO} = 1820–1960 cm^{-1}) of $\{RuNO\}^6$ nitrosyls compared to free NO (1750 cm^{-1}).[55] Additionally, $\{Ru\text{-}NO\}^6$ nitrosyls exhibit spectroscopic properties (sharp ^{1}H-NMR spectra and EPR silent) similar to those of true low-spin diamagnetic Ru(II) species.

In the case of nitrosyls derived from the first row transition metals such as iron and manganese, the electronic structures are not as straightforward due to the accessibility of both high spin and low spin electronic configuration (Table 1.1). This has made the formal assignment of such nitrosyls quite difficult. For example, Mn nitrosyls with a $\{Mn–NO\}^6$ electronic description have three possible electronic descriptions: Mn(I)–NO^+, Mn(II)–$NO^\bullet$, or Mn(III)-NO^-. In earlier work, researchers

Table 1.1. Possible electronic structures of iron, ruthenium and manganese nitrosyls

Iron		Ruthenium	Manganese	
Fe(II)	Fe(III)	Ru(II) Ru(III)	Mn(I) Mn(II)	Mn(III)
{Fe-NO}^{6}	{Fe-NO}^{7}	{Ru-NO}^{6}	{MnNO}^{5}	{MnNO}^{6}
Fe(II)–NO$^+$	Fe(II)–NO$^\bullet$	Ru(II)–NO$^+$	Mn(II)–NO$^+$	Mn(I)–NO$^+$
Fe(III)–NO$^\bullet$	Fe(III)–NO$^-$	Ru(III)–NO$^\bullet$	Mn(III)–NO$^\bullet$	Mn(II)–NO$^\bullet$
				Mn(III)–NO$^-$

have suggested formal oxidation states based on the metric parameters of the Mn–N–O unit. Using this method, a low-spin Mn(I)–NO$^+$ formulation has been suggested for the diamagnetic {Mn-NO}^{6} complexes [Mn(TPP)(NO)] (TPP^{2-} = tetraphenylporphinato dianion) [56] and [Mn-(5-CH_3SALDPT)(NO)] (SALDPT = dianionic pentadentate Schiff base ligand).[57] These complexes have similar NO stretching frequencies (ν(N-O) = 1735 and 1715 cm^{-1}, respectively) indicating similar electronic descriptions. However, more recently Lippard and Ghosh have used density functional theory (DFT) calculations[58] in addition to magnetic and spectroscopic data to assign the paramagnetic tropocoronand complex, [Mn(NO)(TC-5,5)], as a Mn(III)–NO$^-$ species.[59] Interestingly, the Mn–N–O angle and Mn–N/N–O bond distances of [Mn(NO)(TC-5,5)] (174.1(3)^o, 1.699(3) and 1.179(3) Å, respectively) are very similar to those of [Mn(TPP)(NO)] (174.9(6)^o, 1.644(5) and

1.176(7) Å, respectively). Clearly, the use of metric data alone is not enough to correctly assign the oxidation states of the metal centers in such nitrosyls.

Recently, more researchers have started to use DFT and time-dependent DFT (TDDFT) calculations to help establish the distinctive geometric and electronic structures of various metal nitrosyls.[60-64] Due to the interesting and varied reactivity of metal nitrosyls, such studies can provide deeper understanding of the structure–function relationships in these NO complexes. For example, the existence of photoinduced long-lived metastable states MSI (η1-ON, O-end-on bonding) and MSII (η2-NO, side-on bonding, Figure 1.6) has been confirmed experimentally with low

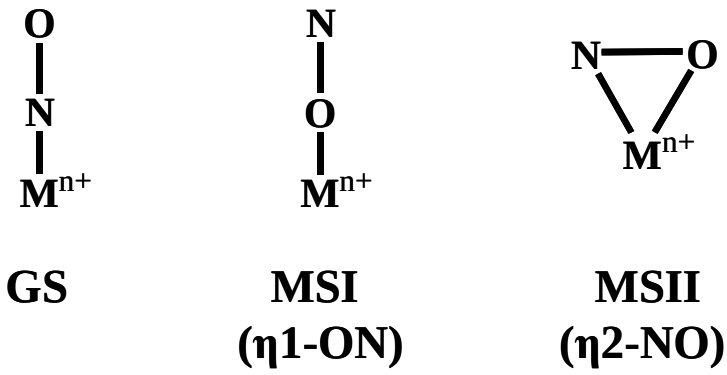

Figure 1.6. The different metal binding modes of nitric oxide (NO)

temperature spectroscopy for many metal nitrosyls and TDDFT studies have provided additional structural and mechanistic details about these metastable states.[64,65] Similar calculations have also been used to better explain the rich redox chemistry observed for many nitrosyls, i.e., the specific location of the oxidizing or reducing equivalents in metal nitrosyls derived from various ancillary ligands.[66]

It has also been observed that certain metal nitrosyls are photoactive and release nitric oxide upon exposure to light. Historically, the bulk of research on photolabile metal-nitrosyls involved iron- and ruthenium-nitrosyls.[64, 67] As discussed earlier, there are many heme containing proteins (such as hemoglobin, guanylate cyclase, and cytochrome C oxidase) that can interact with NO. In order to better understand the structure-function relationship at the heme active sites of such enzymes, many small molecule iron-porphyrin model complexes were synthesized.[60] In addition, since ruthenium and iron belong to the same group in the periodic table and thus behave similarly, the corresponding ruthenium-porphyrin complexes were also synthesized and studied.[68] Interestingly it was found that many of these iron and ruthenium nitrosyls derived from porphyrin-based ligands are sensitive to light and release NO upon illumination.[69] In addition, there are also many non-heme iron and ruthenium nitrosyls that are photoactive as well.[70, 67] More recently several manganese nitrosyls have also been shown to release NO upon exposure to light.[71]

TDDFT have been used to better understand the mechanism of photoactivation of several different complexes including a few metal nitrosyls.[62,63,72,73] These studies have mainly been used to calculate the electronic absorption spectra of the complexes and assign the specific transitions involved in the absorption of light necessary for photoactivity. In many of these studies, such transitions excite electrons into orbitals with substantial antibonding character between the metal center and the photodissociative ligand. However, when no such allowed transitions are noted, a few studies have used TDDFT to show that

intersystem crossing (ISC) into nearby excited cited states with antibonding metal-ligand character which could account for the observed photolability in these complexes. For a set of photoactive ruthenium polypyridyl complexes (that release pyridine ligand derivatives), TDDFT studies have shown that initial excitation into a ^{1}MLCT singlet excited state is followed by intersystem crossing into corresponding ^{3}MLCT triplet excited state.[72] Further, TDDFT calculations were used to show that lengthening of the metal-pyridine bound (as would be observed during ligand dissociation) causes a mixing of the ^{3}MLCT with a ^{3}MC (metal centered triplet excited state) with a substantial amount of antibonding metal-pyridine character. Thus this state is most possibly responsible for the photodissociation of the pyridine ligands in these complexes. Similar TDDFT studies have also been performed to understand the photodissociation of Co-C bond in methyl- and ethylcobalamin.[73] In this thesis, we have used DFT and TDDFT calculation to better understand the electronic structures of several metal nitrosyls in order to uncover the origin of their NO photolability.

1.2.2 Exogenous NO Donors

In recent years, several groups have been active in the development of NO complexes of transition metals as exogenous sources of NO (NO donors) that are capable of NO release upon exposure to light.[74-76] This distinctive property of metal nitrosyls could be exploited in site-specific delivery of NO to cellular targets under the control of light. Since several metal-nitrosyls readily release large quantities of NO upon light

exposure, they would be ideal for site specific delivery of NO to malignant locations as a new form of Photodynamic Therapy (PDT).[77,78] The high concentrations of NO are capable of inducing apoptosis in cancerous cells which could lead to tumor regression and/or inhibition of metastasis. Such large bursts of NO produced by metal nitrosyls could also mimic the activity of inducible NOS which produces micromolar concentration of NO that acts as an antibiotic against invading pathogens such as bacteria, parasites, and fungi.[79,80]

To date, many organic molecules have been developed as exogenous NO donors such as organic nitrites (RONO), nitrates ($RONO_2$), S-nitrosothiols (RSNO), and diazeniumdiolates (NONOates) which have all been shown to deliver NO to cellular targets (Figure 1.7).[81,82] In addition, glyceryl trinitrate (GTN) and S-nitroso-N-acetyl-penicillamine (SNAP) have been used clinically as vasodilators.[74] These compounds are systemic donors that release NO in response to stimuli such as heat,

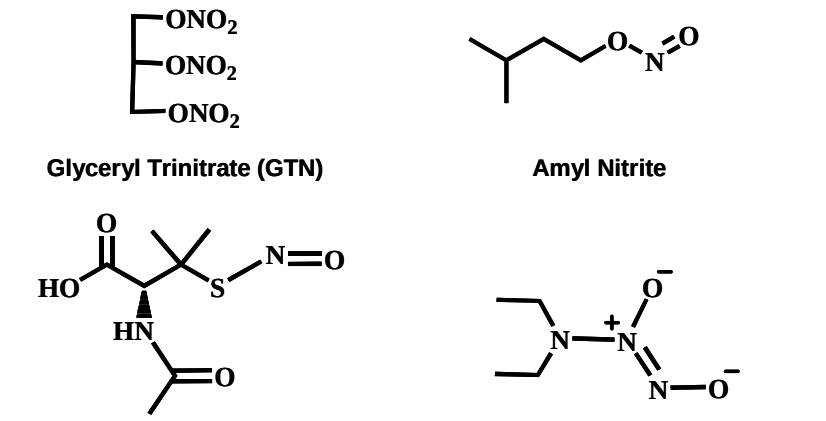

Figure 1.7. Systemic exogenous nitric oxide donors

pH change, or enzymatic activity. As a consequence, they cannot be used in site-specific controlled delivery of NO. Therefore there is a clear need for compounds such as metal nitrosyls that can provide high doses of NO at selected targets under controlled conditions to avoid harming surrounding healthy tissue.

Early on several groups have utilized sodium nitroprusside ($Na_2[Fe(CN)_5(NO)]$) [83] and Roussin's salts ($(NH_4)[Fe_4S_3(NO)_7]$ and $Na_2[Fe_2S_2(NO)_4]$) [84] in their light-driven NO release studies (Figure 1.8). Studies in this area have indicated that iron-nitrosyls tend to be more sensitive to low-energy visible light releasing large amounts of NO. However, the toxicity of these nitrosyls limit there use as NO donors. In the case of nitroprusside, the auxiliary CN ligands do not stay

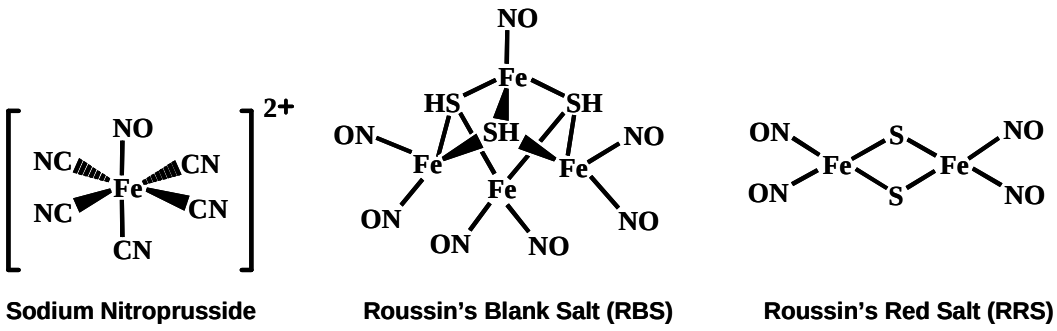

Figure 1.8. Photoactive iron nitrosyls

bound to the iron-center upon NO loss and exhibit unwanted toxicity. In addition, the Roussin's salts were found to be toxic even without exposure to light and NO release. Thus these complexes could also harm healthy tissues that haven't been exposed to light. A major requirement for successful use of metal nitrosyls as exogenous NO-donors in biology is their structural integrity in aqueous environments. Unfortunately,

many iron nitrosyls exhibit unpredictable stability under biological conditions leading to hydrolytic decomposition, NO_x disproportionation reactions, or ferric hydroxide (or oxide) precipitation.[85]

1.2.3 Ruthenium Nitrosyls

Among metal nitrosyls, ruthenium nitrosyls are a promising class of NO donor because of their increased thermal stability in biological media compared to other metal (Mn and Fe) nitrosyls.[86,87] Complexes such as [Ru(salen)(Cl)] (salen = N,NO-ethylenebis-(salicylideneiminato) dianion), [(bpb)Ru(NO)(Cl)] (bpb = 1,2-bis(pyridine-2-carboxamido)benzene dianion), $K_2[Ru(NO)(Cl)_5]$ all release NO when exposed to UV light.[88,89] Since UV light is inherently detrimental to cellular targets, there is still a need to increase the efficiency (quantum yield) of NO release from ruthenium nitrosyls when exposed to lower energy light for delivery of NO to biological targets. Progress in this area requires understanding of the structural and electronic parameters that lead to the absorption of lower energy light in ruthenium nitrosyls.

Research in our lab on NO donating ruthenium nitrosyls began with the synthesis of a nitrosyl derived from the designed polypyridine pentadentate ligand $PaPy_3H$ (N,N-bis(2-pyridylmethyl)amine-N-ethyl-2-pyridine-2-carboxamide, H denotes the dissociable amide H) with a single carboxamido donor, namely $[(PaPy_3)Ru(NO)](BF_4)_2$ (Figure 1.9).[90] However, the lowest energy absorption band of this complex is found at 410 nm, well within the UV-region. Thus the principal

limitation of this NO donor has been its lack of NO photolability under visible light. Clearly, further alteration of the ligand frame was required to overcome this deficiency.

With $[(PaPy_3)Ru(NO)](BF_4)_2$ in hand, we wanted to uncover the specific features of the polydentate ligand frame that contribute to the overall photolability of the $\{RuNO\}^6$ nitrosyl. Most noticeably, the deprotonated carboxamido nitrogen (a strong σ-donating negatively charged donor) is trans to NO. This feature prompted us to first investigate the role of the carboxamide functionality in the overall NO photolability of the nitrosyls. We therefore synthesized two other $\{RuNO\}^6$ nitrosyls with similar poly-pyridine pentadentate ligands with zero or two carboxamido-N donor atoms, namely $[(SBPy_3)Ru(NO)](BF_4)_3$ ($SBPy_3$ = N,N-bis(2-pyridylmethyl)amine-N-ethyl-2-pyridine-2-aldimine) and $[(Py_3P)Ru(NO)]BF_4$ (Py_3PH_2 = N,N-bis(2-(2-pyridyl)ethyl)pyridine-2,6-dicarboxamide) respectively.[91] The ligand frame of $[(SBPy_3)Ru(NO)](BF_4)_3$ is similar to that of $[(PaPy_3)Ru(NO)](BF_4)_2$ except for the replacement of the charged carboxamido-N with a neutral imine-N donor atom (Figure 1.9). Both carboxamido-N and imine-N donors are bound trans to NO in $[(PaPy_3)Ru(NO)](BF_4)_2$ and $[(SBPy_3)Ru(NO)](BF_4)_3$ respectively. Conversely, $[(Py_3P)Ru(NO)]BF_4$ contains two carboxamido-N donors in the equatorial plane with a neutral pyridine-N bound trans to NO. Interestingly, as one increases the number of carboxamido-N donors, the absorption bands of the resulting nitrosyls are red shifted. For example, $[(SBPy_3)Ru(NO)](BF_4)_3$ with Schiff base functionality absorbs at 310 nm while $[(PaPy_3)Ru(NO)](BF_4)_2$ and $[(Py_3P)Ru$-

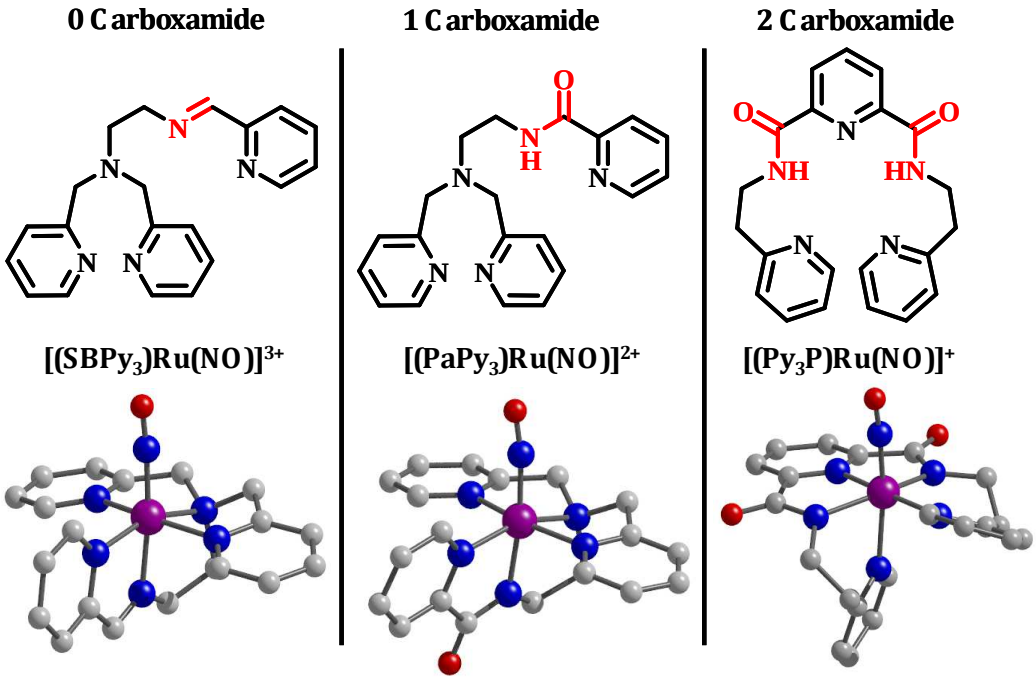

Figure 1.9. Pentadentate ligands with zero ($SBPy_3$), one ($PaPy_3H$), two (Py_3PH_3) carboxamide donors and the corresponding $\{RuNO\}^6$ nitrosyls

$(NO)]BF_4$ (with one and two carboxamido-N donor) absorb at 410 and 530 nm respectively (all measurements in MeCN). All three nitrosyls show photolability upon exposure to low-power (2-5 mW) UV light. However, only $[(Py_3P)Ru(NO)]BF_4$ shows appreciable photoactivity when exposed to visible light with a quantum yield at 532 nm (ϕ_{532}) of 0.050 in MeCN. In addition, the presence of carboxamide group in such $\{RuNO\}^6$ nitrosyls imparts more stability in aqueous medium. For example, unlike $[(PaPy_3)Ru(NO)](BF_4)_2$ and $[(Py_3P)Ru(NO)]BF_4$, $[(SBPy_3)Ru(NO)](BF_4)_3$ shows partial degradation (with concomitant $NO \rightarrow NO_2$ conversion) [67] in aqueous buffer (pH 7). Thus ligands with carboxamide groups

afford $\{RuNO\}^6$ nitrosyls that are more suitable for photoinduced NO delivery to biological targets.

1.3 Direction of Research

The main goal of this thesis is to uncover new design strategies for the syntheses of visible-light activated metal nitrosyls for use as NO donors in biological systems. As a first step, chapter 2 looks at the inherent photolability of certain metal nitrosyls. In this chapter, DFT and TDDFT calculations are used to describe the electronic structures and photoactivities of a set of iron, manganese, and ruthenium nitrosyls all derived from the same $PaPy_3$ ligand frame. The following chapters are further focused on the design of ruthenium nitrosyls. Chapter 3 describes a set of tetradentate dicarboxamide ligand frames with systematic changes in donor atom type. Different combinations of phosphine-P, phenolato-O, and/or pyridine-N donors are used in order to uncover which atom types promote the most low-energy light absorption in ruthenium nitrosyls. Again DFT and TDDFT calculations were employed to understand the different light absorption properties of the resulting ruthenium nitrosyls. In the final chapter (Ch. 4), the attachment of various dye chromophores is explored as a way to further sensitize ruthenium nitrosyls to visible light. The direct conjugation of dye chromophores is compared with dye attachment via a linker in order to understand the mechanism of photoactivation in these dye-bound ruthenium nitrosyls.

1.4 References

1. *Nitric Oxide: Biology and Pathobiology*; Ignarro, L. J., Ed; Academic Press: San Diego, 2000.

2. Kalsner S. *Nitric Oxide and Free Radicals in Peripheral Neurotransmission*; Birkhäuser: Boston, 2000.

3. *Nitric oxide and Infection*; Fang, F. C., Ed; Kluwer Academic/Plenum Publishers: New York, 1999.

4. *Nitric Oxide and Cell: Proliferation, Differtiation and Death*. Moncada S., Higgs, E. A., Bagetta, G., Eds; Portland Press: London, 1998.

5. H. Matter, H. S. A. Kumar, R. Fedorov, A. Frey, P. Kotsonis, E. Hartmann, L. G. Frohlich, A. Reif, W. Pfleiderer, P. Scheurer, D. K. Ghosh, M. Schlichting, H. Schmidt, *J. Med. Chem.* **2005**, *48*, 4783.

6. E. D. Garcin, C. M. Bruns, S. J. Lloyd, D. J. Hosfield, M. Tiso, R. Gachhui, D. J. Stuehr, J. A. Tainer, E. D. Getzoff, *J. Biol. Chem.* **2004**, *279*, 37918.

7. M. Aoyagi, A.S. Arvai, J.A. Tainer, E.D. Getzoff, *EMBO J.* **2003**, *22*, 766.

8. Daff, S. *Nitric Oxide*, **2010**, *23*, 1.

9. (a) Stuehr, D. J.; Kwon, N. S.; Nathan, C. F.; Griffith, O. W.; Feldman, P. L.; Wiseman, J. *J. Biol. Chem.* **1991**, *266*, 6259; (b) Stuehr, D. J. *Biochim. Biophys. Acta Bioenerg.* **1999**, *1411*, 217.

10. Li, H. Y.; Shimizu, H.; Flinspach, M.; Jamal, J.; Yang, W. P.; Xian, M.; Cai, T. W.; Wen, E. Z.; Jia, Q. A.; Wang, P.G.; Poulos, T. L. *Biochemistry*, **2002**, *41*, 13868.

11. (a) Fischmann, T. O.; Hruza, A.; Niu, X. D.; Fossetta, J. D.; Lunn, C. A.; Dolphin, E.; Prongay, A. J.; Reichert, P.; Lundell, D. J.; Narula, S. K.; Weber, P. C. *Nat. Struct. Biol.* **1999**, *6*, 233; (b) Raman, C. S.; Li, H.Y.; Martasek, P.; Kral, V.; Masters, B. S. S.; Poulos, T.L. *Cell*, **1998**, 95, 939.

12. Crane, B. R.; Arvai, A. S.; Ghosh, D. K.; Wu, C. Q.; Getzoff, E. D.; Stuehr, D.J.; Tainer, J.A. *Science*, **1998**, *279*, 2121.

13. Alderton, W. K.; Cooper, C. E.; Knowles, R. G. *Biochem. J.* **2001**, *357*, 593.

14. Cho, H. J.; Xie, Q. W.; Calaycay, J.; Mumford, R.A.; Swiderek, K. M.; Lee, T. D.; Nathan, C. *J. Exp. Med.* **1992**, *176*, 599.

15. Brenman, J. E.; Chao, D. S.; Gee, S. H.; McGee, A.W.; Craven, S. E.; Santillano, D. R.; Wu, Z. Q.; Huang, F.; Xia, H. H.; Peters, M. F.; Froehner, S. C.; Bredt, D. S. *Cell*, **1996**, *84*, 757.

16. Dimmeler, S; Fleming, I; Fisslthaler, B; Hermann, C; Busse, R; Zeiher, A. M. *Nature*, **1999**, *399*, 601.

17. Kiss, J. P.; Vizi, E. S. *Trends Neurosci*. **2001**, *4*, 211.

18. MacMicking, J.; Xie, Q.; Nathan, C. *Annu. Rev. Immunol*. **1997**, *15*, 323.

19. Wink, D. A.; Mitchell, J. B. *Free Radical Biol. Med.* **1998,** *25*, 434.

20. Jia L; Bonaventura C; Bonaventura J; Stamler, J. S. *Nature*, **1996**, *380*, 221.

21. Garthwaite, J. *Trends Neurosci.* **1991**, *14*, 60.

22. Kim, Y. M.; Begonia, H. A.; Muller, C.; Pitt, B. R.; Watkins, W. D.; Lancaster, J. R. *J. Biol. Chem.***1995**, *270*, 5710.

23. Harris, C. C. *Toxicol. Lett.* **1995**, *82*, 1.

24. Stamler, J. S.; Singel, D. J.; Loscalzo, J. *Science*, **1992**, *258*, 1989.

25. Williams, D. L. H. *Nitrosation.* Oxford, UK:Cambridge Press;1988.

26. (a) Lander, H. M.; Milbank, A. J.; Tauras, J. M.; Hajjar, D. P.; Hempstead, B. L.; Schwartz, G. D.; Kraemer, R. T.; Mirza, U. A.; Chait, B. T.; Burk, S. C.; Quillia, C. *Nature*, **1996**, *381*, 380; (b) Lander, H. M.; Ogiste, J. S.; Pearce, S. F.; Levi, R.; Novogrodsky, A. *J. Biol. Chem.* **1995**, *270*, 7017.

27. Nguyen, T.; Brunson, D.; Crespi, C. L.; Penman, B. W.; Wishnok, J. S.; Tannenbaum, S. R. *Proc. Natl. Acad. Sci. USA*, **1992**, *89*, 3030.

28. Hogg, N.; Darley-Usmar, V. M.; Wilson, M. T.; Moncada, S. *FEBS Lett.* **1993**, *326*, 199.

29. Pacher, P.; Beckman, J.; Liaudet, L. *Physiol. Rev.* **2007**, *87*, 315.

30. Murad, F. *Recent Progr. Horm. Res.* **1994**, *49*,239.

31. (a) Yu, A. E.; Hu, S.; Spiro, T. G.; Burstyn, J. N. *J. Am. Chem. Soc.* **1994**, *116*, 4117; (b) Stone, J. R.; Marletta, M. A. *Biochemistry*, **1994**, *33*, 5636.

32. Degoute, C. S. *Drugs*, **2007**, *67*, 1053.

33. (a) Hetrick, E. M.; Schoenfisch, M. H. *Chem. Soc. Rev.* **2006**, *35*, 780; (b) Frost, M. C.; Reynolds, M. M.; Meyerhoff, M. E. *Biomaterials*, **2005**, *26*, 1685.

34. (a) Fang, F. C. *Nature Rev. Microbiol.* **2004**, *2*, 820; (b) Fang, F. C. *J. Clin. Invest*. **1997**, *99*, 2818.

35. Florio, S. K.; Loh, C.; Huang, S. M.; Iwamaye, A. E.;Kitto, K. F.; Fowler, K. W.; Treiberg, J. A.; Hayflick, J. S.; Walker, J. M.; Fairbanks, C. A.; Lai, Y. *British J. Pharma.* **(2009), 158,** 494–506

36. Moncada, S.; Palmer, R. M. J., Higgs, E. A. *Pharmacol. Rev.* **1991,** *43*, 109.

37. Lundberg, J. O.; Weitzberg, E.; Gladwin, M. T. *Nature*, **2008**, *7*, 156.

38. a) Simeone, A. M.; Collela, S.; Krahe, R.; Johnson, M. M.; Mora, E.; Tari, A. M. *Carcinogenesis*, **2006**, *27*, 568; (b) Crowell, J. A.; Steele, V. E.; Sigman, C. C.; Fay, J. R. *Mol. Cancer Ther.* **2003**, *2*, 815; (c) Hobbs, A. J.; Higgs, A.; Moncada, S. *Ann. Re*V. *Pharmacol. Toxicol.* **1999**, *39*, 1910;

39. Brüne, B.; von Knethen, A.; Sandau, K. *Eur. J. Pharmacol.* **1998**, *351*, 261.

40. Henry, Y.; Lepoivre, M.; Drapier, J.C.; Ducrocq, C.; Boucher, J.L.; Guissani, A. *FASEB J.*, **1993**, *7*, 1124.

41. Wang, X.W., Harris, C.C. *J. Cell. Physiol.* 1997, *173*, 247.

42. (a) Szabo, C.; Day, B.J.; Salzman, A.L. *FEBS Lett.* **1996**, *381*, 82; (b) Balakirev, M.Y.; Khramtsov, V.V.; Zimmer, G. *Eur. J. Biochem.* **1997**, *246*, 710.

43. Beckman, J.; Koppenol, W. H. *Am. Physiolo. Soc.* **1996**, C1424.

44. Huie, R. E.; Padmaja, S. *Free Radic. Res. Commun.* **1993**, *18*, 195.

45. Hurst, J. K. *J. Clin. Invest.* **2002**, *109*, 1287.

46. Rose, M. J.; Betterley, N. M.; Oliver, A. G.; Mascharak, P. K. *Inorg. Chem.* **2010**, *49*, 1854.

47. Patra, A. K.; Rose, M. J.; Murphy, K. A.; Olmstead, M. M. and Mascharak P. K. *Inorg. Chem.* **2004**, *43*, 4487.

48. Eroy-Reveles, A. A.; Leung, Y.; Beavers, C. M.; Olmstead, M. M.; Mascharak, P. K. *J. Am. Chem. Soc.* **2008**, *130*, 4447.

49. Boone, B. J.; Klein, D. P.; Seyler, J. W.; Méndez, N. Q.; Arif, A. M.; Gladysz, J. A. *J. Am. Chem. Soc.*, **1996**, *118*, 2411.

50. Agapie, T.; Odom, A. L.; Cummins, C. C. *Inorg. Chem.*, **2000**, *39*, 174.

51. Chisholm, M. H.; Cotton, F. A.; Extine, M. W.; Kelly, R. L. *Inorg. Chem.*, **1979**, *18*, 116.

52. Malito, J. T.; Shakir R.; Atwood, J. L. *J. Chem. Soc., Dalton Trans.*, **1980**, 1253

53. Wilson, R. D.; Ibers, J. A. *Inorg. Chem.*, **1979**, *18*, 336.

54. Enemark, J. H.; Feltham, R. D. *Coord. Chem. Rev.* 1974, **13**, 339.

55. (a) Roncaroli, F.; Videla, M.; Slep, L. D.; Olabe, J. A. *Coord. Chem. Rev.* **2007,** *252*, 1903. (b) Videla, M.; Jacinto, J. S.; Baggio, R.; Garland, M. T.; Singh, P.; Kaim, W.; Slep, L. D.; Olabe, J. A. *Inorg. Chem.* **2006**, *45*, 8608. (c) Roncaroli, F.; Ruggiero, M. E.; Franco, D. W.; Esti'u, G. L.; Olabe, J. A. *Inorg. Chem.* **2002,** *41*, 5760.

56. Scheidt, W. R.; Hatano, K.; Rupprecht, G. A.; Piciulo, P. L. *Inorg. Chem.* **1979**, *18*, 292.

57. Coleman, W. M.; Taylor, L. T. *J. Am. Chem. Soc.* **1978**, *100*, 1705-1710.

58. Tangen, E.; Conradie, J.; Franz, K.; Friedle, S.; Telser, J.; Lippard, S. J.; Ghosh, A. *Inorg. Chem.* **2010**, *49*, 2701-2705.

59. Franz, K. J.; Lippard, S. J. *J. Am. Chem. Soc.* **1998**, *120*, 9034-9040.

60. (a) L. E. Goodrich, F. Paulat, V. K. K. Praneeth, N. Lehnert, *Inorg. Chem.*, 2010, **49,** 6293; b) V. K. K. Praneeth, F. Paulat, T. C. Berto, S. D. George, C. Näther, C. D. Sulok, N. Lehnert, *J. Am. Chem. Soc.*, 2008, **130**, 15288; (c) I.

V. Novozhilova, P. Coppens, J. Lee, G. B. Richter-Addo, K. A. Bagley, *J. Am. Chem. Soc.*, 2006, **128**, 2093; (d) A. Ghosh, *Acc. Chem. Res.*, 2005, **38**, 943; (e) B. M. Leu, M. Z. Zgierski, G. R. A. Wyllie, W. R. Scheidt, W. Sturhahn, E. E. Alp, S. M. Durbin, J. T. Sage, *J. Am. Chem. Soc.*, 2004, **126**, 4211;

61. (a) J. Conradie, K. H. Hopmann, A. Ghosh, *J. Phys. Chem. B*, 2010, **114**, 8517; (b) G. Schenk, M. Y. M. Pau, E. I. Solomon, *J. Am. Chem. Soc.*, 2004, **126**, 505; (c) T.A. Jackson, E. Yikilmaz, A. Miller, T. C. Brunold, *J. Am. Chem. Soc.*, 2003, **125**, 8348.

62. (a) M. Jaworska, *Inorg. Chem. Comm.*, 2006, **9**, 284; (b) M. Jaworska, Z. Stasicka, *J. Mol. Struct.* 2006, **785**, 68; (c) S. N. Greene, N. G. J. Richards, *Inorg. Chem.*, 2004, **43**, 7030.

63. (a) J. G. Małecki, M. Jaworska, R. Kruszynski, *Polyhedron*, 2005, **24**, 359; (b) O. V. Sizova, N. V. Ivanova, V. V. Sizov, A. B. Nikol'skii, *Russ. J. Gen. Chem.*, 2004, **74**, 481; (c) S. I. Groelsky, S. C. da Silva, A. B. P. Lever, D. W. Franco, *Inorg. Chim. Acta*, 2000, **30**, 689.

64. (a) V. I. Baranovskii, O. V. Sizova, *Journal of Structural Chemistry.*, 2008, **49**, 803; (b) G. F. Caramori, G. Frenking, *Organometallics*, 2007, **26**, 5815; (c) K. Karidi, A. Garoufis, A. Tsipis, N. Hadjiliadis, H. den Dulk, J. Reedijk, *Dalton Trans.*, 2005, 1176; (d) P. Boulet, M. Buchs, H. Chermette, C. Daul, E. Furet, F. Gilardoni, F. Rogemond, C.W. Schla1pfer, J. Weber, *J. Phys. Chem. A*,

2001, **105**, 8999; (e) S.I. Groelsky, A.B.P. Lever, *Int. J. Quant. Chem.*, 2000, **80**, 636.

65. (a) P. Coppens, I. Novozhilova and A. Kovalevsky, *Chem. Rev.*, 2002, **102**, 861; (b) S. C. Da Silva and D. W. Franco, *Spectrochim. Acta, Part A.*, 1999, **55**, 1515; (c) M. D. Carducci, M. R. Pressprich, P. Coppens, *J. Am. Chem. Soc.*, 1997, **119**, 2669.

66. (a) P. Surawatanawong, S. Sproules, F. Neese, K. Wieghardt, *Inorg. Chem.* 2011, **50**, 12064; (b) M. Jaworska, G. Stopa, Z. Stasicka, *Nitric Oxide*, 2010, **23**, 227; (c) P. Singh, A. Kumar Das, B. Sarkar, M. Niemeyer, F. Roncaroli, J. A. Olabe, J. Fiedler, S. Záliš, W. Kaim, *Inorg. Chem.*, 2008, **47**, 1706; (d) M. Videla, J. S. Jacinto, R. Baggio, M. T. Garland, P. Singh, W. Kaim, L. D. Slep, J. A. Olabe, *Inorg. Chem.*, 2006, **45**, 8608.

67. Rose, M. J.; Mascharak, P. K. *Coord. Chem. Rev*. **2008**, *252*, 2093.

68. Kurtikyan, T. S.; Martirosyan,G. G.; Lorkovic, I. M.; Ford, P. C. *J. Am. Chem. Soc.* **2002**, 124, 10124.

69. (a) Hoshino, M.; Laverman, L. E.; Ford, P. C. *Coord. Chem. Rev.* **1999**,*187*, 75; (b) Cooper, C. E.; *Biochim. Biophys. Acta*, **1999**, *1411*, 290.

70. (a) Harrop, T. C.; Mascharak, P. K. *Acc. Chem. Res.* **2004**, *37*, 253; (b) Patra, A. K.; Afshar, R. K.; Olmstead, M. M.; Mascharak, P. K. *Angew. Che. Intl. Ed*. **2002**, *41*, 2512.

71. (a) Ghosh, K.; Eroy-Reveles, A. A.; Holman, T. R.; Olmstead, M. M.; Mascharak, P. K. *Inorg. Chem*. **2004**, *43*, 2988; (b) Hoffman-Luca, C. G.; Eroy-Reveles, A. A.; Alvarenga, J.; Mascharak, P. K. *Inorg. Chem*. **2009**, *48*, 9104.

72. Salassa, L.; Garino, C.; Salassa, G.; Gobetto, R.; Nervi, C. *J. Am. Chem. Soc.* **2008**, *130*, 9590.

73. Lodowski, P.; Jaworska, M.; Andruniow, T.; Kumar, M.; Kozlowski, P. M. *J. Phys. Chem. B*, **2009**, *113*, 6898.

74. Wang, P. G.; Cai, T. B.; Taniguchi, N. *Nitric Oxide Donors for Pharmaceutical and Biological Applications.* Wiley-VCH: Weinheim, Germany, 2005.

75. Eroy-Reveles, A. A.; Mascharak, P. K. *Future Med. Chem*. **2009**, *8*, 1497.

76. (a) Al-Sa´doni, H. H.; Ferro, A. *Re*v. *Med. Chem.* **2005**, *5*, 247; (b) Napoli, C.; Ignarro, L. J. *Annu. Re*v. *Pharmacol. Toxicol.* **2003**, *43*, 97; (c) Wang, P. G.; Xian, M.; Tang, X.; Wu, X.; Wen, X.; Cai, T.; Janczuk, A. J. *Chem. Re*v. **2002**, *102*, 1091; (d) Butler, A. R.; Megson, I. L. *Chem. Rev*. **2002**, *102*, 1155.

77. Castano, A. P.; Mroz, P.; Hamblin, M. R. *Nat. Rev. Cancer* **2006**, *6*, 535.

78. Detty, M. R.; Gibson, S. L.; Wagner, S. J. *J. Med. Chem.* **2004**, *47*, 3897.

79. Halpenny, G. M.; Steinhardt, R. C.; Okialda, K. A.; Mascharak, P. K. *J. Mater. Sci. Mater. Med.* **2009**, *20*, 2353.

80. Heilman, B. J.; Halpenny, G. M.; Mascharak, P. K. *J. Biomed. Mater. Res. B Appli. Biomater.* **2011**, *99B*, 328.

81. (a) Keefer, L. K. *Curr. Top. Med. Chem.* **2005**, *5*, 625. (b) Hrabie, J. A.; Keefer, L. K. *Chem. Re*v. **2002**, *102*, 1135.

82. Wang, K.; Zhang, W.; Xian, M.; Hou, Y. C.; Chen, X. C.; Cheng, J.P.; Wang, P. G. *Curr. Med. Chem.* **2000**, *7*, 821.

83. a) Singh, R. J.; Hogg, N.; Neese, F.; Joseph, J.; Kalyanaraman, B. *Photochem. Photobiol.* **1995**, *61*, 325 ; b) Kudo, S.; Bourassa, J. L.; Boggs, S. E.; Sato, Y.; Ford, P. C.; *Anal. Biochem.* **1997**, *247*, 193.

84. a) Bourassa, J.; DeGraff, W.; Kudo, S.; Wink, D. A.; Mitchell, J. B.; Ford, P. C. *J. Am. Chem. Soc.* **1997**, *119*, 2853; b) Bourassa, J. L.; Ford, P. C. *Coord. Chem. Rev.* **2000**, *200*, 887.

85. (a) Ford, P. C.; Lorkovic, I. M. *Chem. Rev.*, 2002, **102**, 993; (b) Lin, R.; Farmer, P. J. *J. Am. Chem. Soc.*, 2001, **123**, 1143.

86. Rose, M. J.; Fry, N. L.; Marlow, R.; Hink, L.; Mascharak, P. K. *J. Am. Chem. Soc.* **2008**, *130*, 8834.

87. Szundi, I.; Rose, M. J.; Sen, I.; Eroy-Reveles, A. A.; Mascharak, P. K.; Einarsdóttir, Ó. *Photochem. Photobiol.* **2006**, *82*, 1377.

88. Rose, M. J.; Mascharak, P. K. *Curr. Opin. Chem. Biol*. **2008**, *12*, 238.

89. Ford, P. C.; Bourassa, J.; Miranda, K.; Lee, B.; Lorkovic, I.; Boggs, S.; Kudo, S.; Laverman, L. *Coord. Chem. Rev.* **1998**, *171*, 185.

90. Patra, A. K.; Mascharak, P. K. *Inorg. Chem*. **2003**, *42*, 7363.

91. Rose, M. J.; Patra, A. K.; Alcid, E. A.; Olmstead, M. M.; Mascharak, P. K. *Inorg. Chem.* **2007**, *46*, 2328.

Chapter 2

Density Functional Theory Studies to Uncover the Origin of Photolability in Iron, Ruthenium, and Manganese Nitrosyls Derived from $PaPy_3H$

2.1 Background

Our lab became interested in metal nitrosyls while studying the non-heme Fe center found at the active site of *nitrile hydratase* (Fe-NHase).[1] NO binds the Fe(III) center of the enzyme in the absence of light (dark inactive form). Upon exposure to light, NO is released with concomitant binding of water, a step that renders the active site ready for nitrile hydrolysis. The X-ray structure of Fe-NHase has revealed an octahedral geometry of the low spin Fe(III) center coordinated to two deprotonated carboxamido-N donors from the peptide backbone.[2] The equatorial coordination is completed by two cysteinato-S donors that are post-translationally oxygenated to a sulfinate ($-SO_2$) and a sulfenate (-SO) moieties (in the active form) while the axial site contains a third cysteine-S donor (unmodified). The sixth site is exposed to the solvent allowing H_2O (catalytically active) or NO (inactive dark form) to bind. Over the past two decades, our lab as well as others have developed several model complexes of this active site to elucidate the mechanism of photoactivation of Fe-NHase via NO release.[3,4] For example, we have recently reported a $\{FeNO\}^6$ nitrosyl containing a ligand with both carboxamido-N and sulfinato ($\underline{S}O_2$) donor atoms (Figure 2.1) namely, $(NEt_4)[(Cl_2PhPep\{SO_2\}_2)Fe(NO)(DMAP)]$.[5] Due to the close resemblance of this model complex to that of the active site of Fe-NHase it was not surprising that it also exhibited similar NO photolability.

Density functional theory (DFT) and time dependant DFT (TDDFT) studies on $(NEt_4)[(Cl_2PhPep\{SO_2\}_2)Fe(NO)(DMAP)]$ have revealed the importance of both the carboxamido-N and sulfinato-SO_2 donors in the photolability of this nitrosyl.[6]

We had also previously synthesized another photoactive $\{FeNO\}^6$ nitrosyl derived from a pentadentate polypyridine ligand with a single carboxamide group and no sulfinato-SO_2 donors (Figure 2.1), namely $[(PaPy_3)Fe(NO)]^{2+}$ which rapidly releases NO upon illumination with visible light.[7] Thus we became interested in origin of photoactivity of this nitrosyl since it did not contain the sulfinato-SO_2 donors necessary for photoactivity in Fe-NHase and the model complex $(NEt_4)[(Cl_2PhPep\{SO_2\}_2)Fe(NO)(DMAP)]$. In addition, we intended to understand why the corresponding $\{FeNO\}^7$ species, $[(PaPy_3)Fe(NO)](ClO_4)$ exhibits no sensitivity to light.[8] Therefore we set out to investigate the underlying principles behind the difference in photochemical behavior of the two closely-related $\{FeNO\}^6$ and $\{FeNO\}^7$ nitrosyl species (derived from $[PaPy_3]^-$) with density functional theory (DFT) and time-dependent DFT (TDDFT) studies.[9] The objective of this work was to gain insight into the electronic structures of these two nitrosyls and the transitions that lead to their different NO photolabilities.

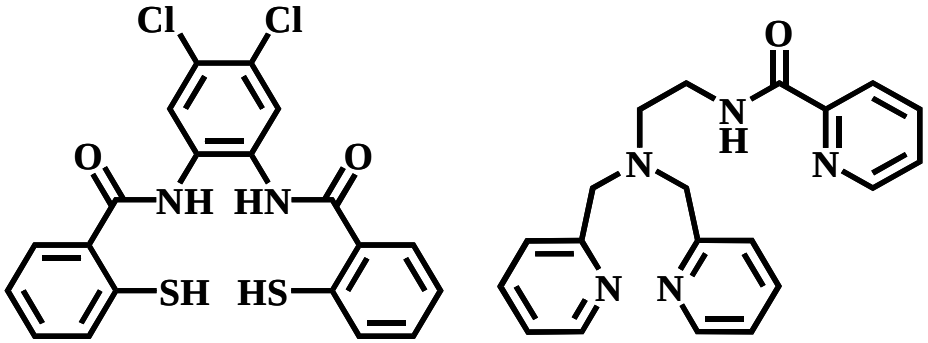

$Cl_2PhPepSH_4$ **$PaPy_3H$**

Figure 2.1. Ligands used for model complexes mimicking Fe-NHase

The high NO photolability of $[(PaPy_3)Fe(NO)]^{2+}$ under visible light prompted the syntheses of the corresponding manganese and ruthenium nitrosyls, $[(PaPy_3)Mn(NO)]^{+}$ [10] and $[(PaPy_3)Ru(NO)]^{2+}$.[11] In all three of the resulting $PaPy_3$-based nitrosyls, NO is bound trans to the carboxamido-N donor (a strong σ-donating center) as seen in Figure 2.2. Despite the similar binding mode of the $PaPy_3$ ligand frame in these nitrosyls, the manganese and ruthenium complexes exhibit greater stability in aqueous media compared to $[(PaPy_3)Fe(NO)]^{2+}$. This stability has led to the successful use of both $[(PaPy_3)Mn(NO)]^{+}$ and $[(PaPy_3)Ru(NO)]^{2+}$ as NO donors to biological targets with the use of light.[12] For example, the kinetics of binding of the photogenerated NO (from $[(PaPy_3)Mn(NO)]^{+}$ and $[(PaPy_3)Ru(NO)]^{2+}$) to reduced cytochrome c oxidase (CcO) and myoglobin (Mb) were investigated using time-resolved optical absorption spectroscopy.[13] However, these studies were done using

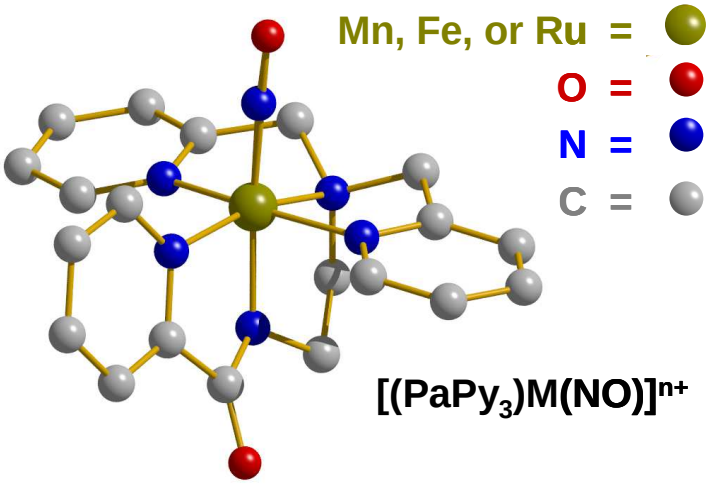

Figure 2.2. The similar binding mode of the $[PaPy_3]^{-}$ ligand frame in $[(PaPy_3)Mn(NO)]^{+}$, $[(PaPy_3)Fe(NO)]^{2+}$ and $[(PaPy_3)Ru(NO)]^{2+}$

355 nm laser light and for use in living cells, visible or near-IR light is necessary to assure cell viability. Similar to other ruthenium nitrosyls, $[(PaPy_3)Ru(NO)]^{2+}$ releases NO only upon illumination with UV light (quantum yield value of NO release of 0.05 at 410 nm).[11a] On the other hand, $[(PaPy_3)Mn(NO)]^{+}$ shows a wide range of NO photoactivity throughout the 450-600 nm visible region. Quantum yield values of 0.41 and 0.58 have been measured at 500 and 550 nm respectively for the NO release from $[(PaPy_3)Mn(NO)]^{+}$.[15]

As alluded to above, the color of the three nitrosyls is strikingly different in solution as $[(PaPy_3)Fe(NO)]^{2+}$ is red, $[(PaPy_3)Mn(NO)]^{+}$ is green, and $[(PaPy_3)Ru(NO)]^{2+}$ is orange. Similar to other ruthenium nitrosyls, the absorption bands of $[(PaPy_3)Ru(NO)]^{2+}$ are in the UV region. Its lowest energy absorption band barely extends into the visible region with a λ_{max} of 410 nm and moderate intensity (ε = 1550 $M^{-1}cm^{-1}$, Figure 2.3, bottom panel). Switching to iron in the case of $[(PaPy_3)Fe(NO)]^{2+}$, this band becomes slightly less intense and shifts to 500 nm (ε=1050 $M^{-1}cm^{-1}$, Figure 2.3, middle panel). The lowest energy absorption maximum of $[(PaPy_3)Mn(NO)]^{+}$ is further red-shifted to 635 nm with an even greater decrease in intensity (ε = 220 $M^{-1}cm^{-1}$, Figure 2.3, top panel). The origin of this shift of absorption maximum to lower energy with different metal centers in this series of structurally similar nitrosyls has been investigated to gain insight into their NO photolability. Insights in this regard can provide help in future design of metal nitrosyls as NO donors since their use requires sensitivity to visible or near-IR light.[14]

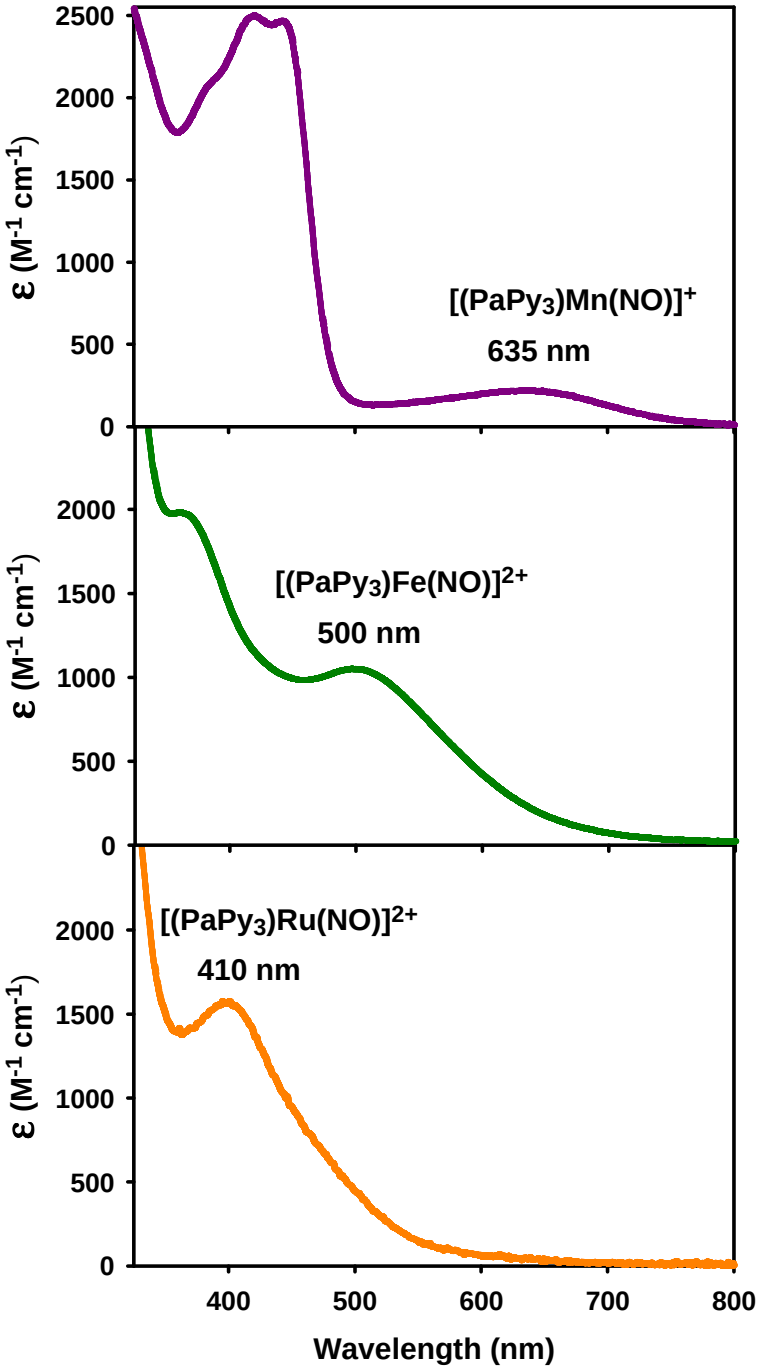

Figure 2.3. Electronic absorption spectra of $[(PaPy_3)Mn(NO)]^+$ (top), $[(PaPy_3)Fe(NO)]^{2+}$ (middle), $[(PaPy_3)Ru(NO)]^{2+}$ (bottom) in MeCN

2.2 Electronic Structures

2.2.1 $\{FeNO\}^6$ and $\{FeNO\}^7$ Nitrosyls Derived from $PaPy_3H$

Examination of the X-ray crystal structures of $[(PaPy_3)Fe(NO)]^{2+}$ and $[(PaPy_3)Fe(NO)]^{+}$ (as seen in Figure 2.4) reveals a striking difference in the Fe-N-O bond angles of the two complexes that is characteristic of $\{FeNO\}^6$ vs $\{FeNO\}^7$ nitrosyls. The more linear Fe-N-O angle (173.1°) of $[(PaPy_3)Fe(NO)]^{2+}$ is expected for $\{FeNO\}^6$ nitrosyls, while the bent Fe-N-O angle (141.29°) of $[(PaPy_3)Fe(NO)]^{+}$ is more consistent with an $\{FeNO\}^7$ electronic configuration. However, these descriptions do not reveal specific electronic distributions within the FeNO units. Thus we have employed DFT calculations to uncover the exact electronic description of these two nitroysls. We first optimized the geometry of the nitrosyls to obtain the lowest energy ground state structures of both $[(PaPy_3)Fe(NO)]^{2+}$ and $[(PaPy_3)Fe(NO)]^{+}$. As expected, there were only slight differences between the DFT optimized ground state structures and the crystallographically determined structures (Table 2.1). The linear vs bent Fe-N-O angles of the nitrosyls are also supported by

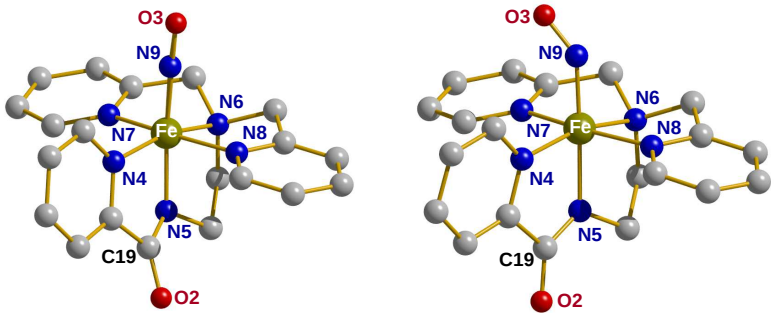

Figure 2.4. X-ray crystal structure of $[(PaPy_3)Fe(NO)]^{2+}$ ($\{FeNO\}^6$, left) and $[(PaPy_3)Fe(NO)]^{+}$ ($\{FeNO\}^7$, right). H-atoms have been removed for clarity.

the DFT results. However one minor difference arises in the dihedral angle of the carboxamido group of $[(PaPy_3)Fe(NO)]^{2+}$ (Table 2.1). In the optimized structure of $[(PaPy_3)Fe(NO)]^{2+}$ the carboxamido group (dihedral angle = -172.3°) shifts into a more planar configuration compared to that of the crystal structure (dihedral angle = 155.4°). This difference most possibly arises from crystal packing forces in the solid state of $[(PaPy_3)Fe(NO)]^{2+}$. In the case of $[(PaPy_3)Fe(NO)]^{+}$, the carboxamido moiety is planar in both the optimized and X-ray crystal structures. Richards and coworkers have investigated $[(PaPy_3)Fe(NO)]^{2+}$ and also noted this difference in the dihedral angle in their theoretical study and attributed this difference to crystal packing forces.[16]

Comparison of the geometry of rest of the structures of the $\{FeNO\}^6$ and $\{FeNO\}^7$ species very similar metric parameters in the equatorial plane of each nitrosyl. However, there are striking differences along the N_{amido}–Fe–N–O axial vector. For example, the additional electron in the $\{FeNO\}^7$ unit increases the Fe–N_{amido}, Fe–N(O), and N–O bond lengths in both the crystal and DFT optimized structures. The lengthening of the N–O bond supports the hypothesis that the additional electron is more localized in a π^*(NO) orbital rather than a d(Fe) orbital in $[(PaPy_3)Fe(NO)]^{+}$. Thus as the π-accepting ability of the NO ligand is decreased ($NO^+ > NO^{\bullet}$), it becomes more difficult for the negatively charged carboxamido nitrogen to approach the Fe metal center causing a lengthening of the Fe–N_{amido} bond in $[(PaPy_3)Fe(NO)]^{+}$. This is clearly observed when the calculated Mayer bond orders (MBO) [17] of the two nitrosyls are compared (Table 2.2). For example, the

Table 2.1. Selected bond distances (Å**)** and angles (deg) of $\{FeNO\}^6$ and $\{FeNO\}^7$ complexes $[(PaPy_3)Fe(NO)]^{2+}$ and $[(PaPy_3)Fe(NO)]^{+}$ along with the optimized DFT bond distances and bond angles for comparison

	$\{FeNO\}^6$		**$\{FeNO\}^7$**	
	X-ray	**DFT**	**X-ray**	**DFT**
Fe-N4(py)	1.978(2)	2.007	1.9801(15)	1.982
Fe-N5(amido)	1.901(2)	1.895	1.9577(15)	1.960
Fe-N6(N^o)	1.972(2)	2.020	1.9946(16)	2.030
Fe-N7(py)	1.982(2)	2.020	1.9837(15)	1.989
Fe-N8(py)	1.983(2)	2.016	1.9989(15)	2.003
Fe-N9(NO)	1.677(2)	1.673	1.7515(16)	1.758
N9-O3(NO)	1.139(3)	1.153	1.190(2)	1.190
N5-C19(amido)	1.341(3)	1.368	1.322(2)	1.345
C19-O2(amido)	1.233(3)	1.223	1.247(2)	1.236
Fe-N9-O3	173.1(2)	171.8	141.29(15)	142.7
Fe-N5-C19-O2	155.4	-172.3	-175.5	-171.3

calculated Fe–$N_{(amido)}$ bond order of $[(PaPy_3)Fe(NO)]^{2+}$ (0.8162) is significantly higher than that of $[(PaPy_3)Fe(NO)]^{+}$ (0.6923). This trend in consistent with a Fe(II)–NO^+ and Fe(II)–$NO^{\bullet}$ assignment of $[(PaPy_3)Fe(NO)]^{2+}$ and $[(PaPy_3)Fe(NO)]^{+}$ respectively based on Mössbauer and EPR data.[8] Also, it is important to note that addition of the electron to the π^*(NO) orbital in the $\{FeNO\}^7$ species lowers the bond order of the NO unit. And finally, examination of the calculated Löwdin population analysis of both nitrosyls was carried out to further investigate the differences in metal–ligand interactions. The calculated spin density of the $\{FeNO\}^7$ nitrosyl is somewhat spread over the FeNO unit with +0.326, +0.381, and +0.240 spin density on the Fe, N, and O atoms respectively. This spin distribution attests that the spin

Table 2.2. Selected Mayer bond orders (MBO) of the $\{FeNO\}^6$ and $\{FeNO\}^7$ nitrosyls at their PW91-optimized geometries

	$\{FeNO\}^6$	$\{FeNO\}^7$
Bond	**MBO**	**MBO**
Fe-N4(py)	0.7157	0.6923
Fe-N5(amido)	0.8162	0.6923
Fe-N6(N^o)	0.6739	0.5973
Fe-N7(py)	0.6414	0.6318
Fe-N8(py)	0.6510	0.5951
Fe-N9(NO)	1.3797	1.3086
N9-O3(NO)	1.7726	1.6809
N5-C19 (amido)	1.2487	1.3446
C19-O2(amido)	2.0501	2.0325

density of the extra electron in the $\{FeNO\}^7$ nitrosyl is located more on the NO moiety and in turn supports its Fe(II)–$NO^{\bullet}$ description.

2.2.2 $\{RuNO\}^6$ and $\{MnNO\}^6$ Nitrosyls Derived from $PaPy_3H$

Ruthenium is a second row transition metal and thus has a large d-orbital splitting. As a consequence, all diamagnetic $\{RuNO\}^6$ ruthenium nitrosyls are described as having a low spin Ru(II)-NO^+ electron configuration. A clean ^{1}H-NMR spectrum of $[(PaPy_3)Ru(NO)]^{2+}$ confirms that it is a diamagnetic S = 0 species and therefore has a Ru(II)-NO^+ configuration.[11] Manganese being in the first row transition series is however not as straightforward since it can access several different oxidation states. In the case of $\{MnNO\}^6$ nitrosyls, several electron configurations are possible. Four of the most likely are low spin Mn(I)–NO^+ (S = 0), strongly

coupled Mn(II)–NO$^{\bullet}$ (S = 0), uncoupled Mn(II)–NO$^{\bullet}$ (S = 1), and low spin Mn(III)–NO^{-} (S = 1). Therefore IR and Raman spectroscopy studies coupled with DFT calculations were preformed in order to decide the correct electronic description of $[(PaPy_3)Mn(NO)]^+$.[18]

The IR spectrum of $[(PaPy_3)Mn(NO)]^+$ contains a strong signal at 1733 cm^{-1}. Upon $^{15}N^{18}O$ isotope labeling, this peak shifts to 1664 cm^{-1}, which confirms its assignment as the N-O stretching mode, ν(N-O) . In order to determine the energies of the Mn-NO stretching and Mn-N-O (linear) bending modes, ν(Mn-NO) and δ(Mn-N-O) respectively, Raman spectroscopy was applied. Figure 2.5 shows the non-

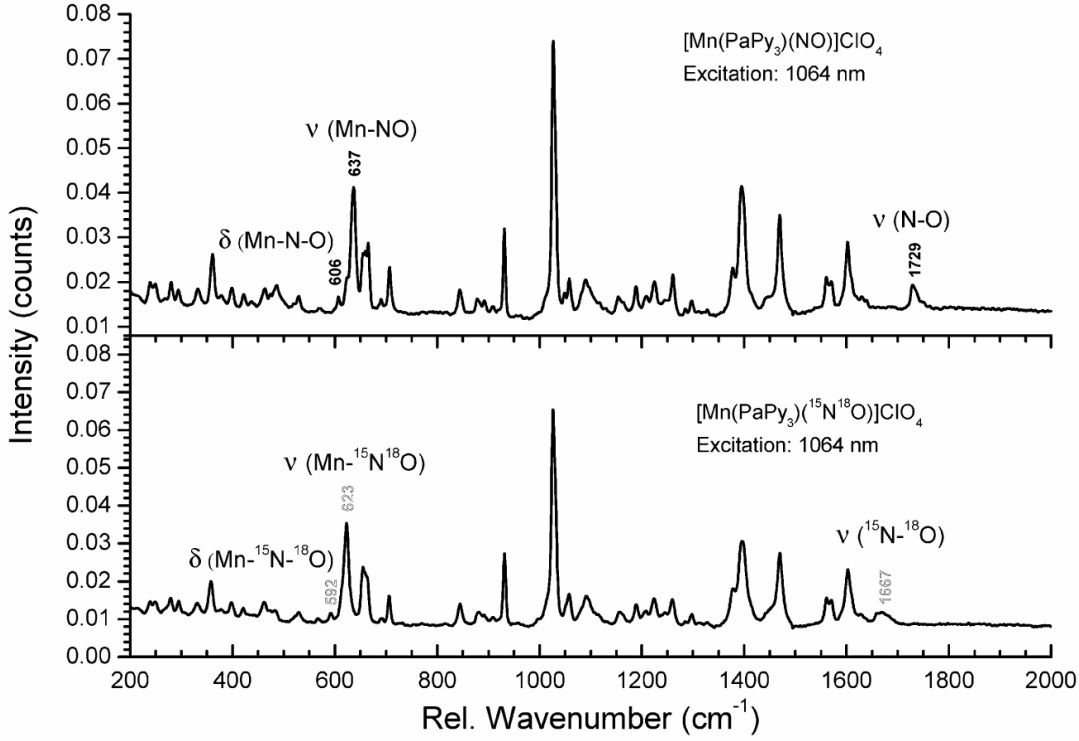

Figure 2.5. FT-Raman spectra of $[Mn(PaPy_3)(NO)]^+$ (top) and $[Mn(PaPy_3)(^{15}N^{18}O)]^+$ (bottom), excited at 1064 nm

resonance FT-Raman spectrum of $[(PaPy_3)Mn(NO)]^+$ and that of the corresponding $^{15}N^{18}O$ isotope labeled complex. From these data, two isotope-sensitive features are readily identified at 637 cm^{-1} and 606 cm^{-1}, which shift to 623 cm^{-1} and 592 cm^{-1}, respectively, in the $^{15}N^{18}O$ compound. We assign the higher energy feature to the Mn-NO stretch based on the fact that this feature shows resonance enhancement upon laser excitation in the visible region as shown in Figure 2.6 (observed at 639 cm^{-1} in frozen solution), whereas the 606 cm^{-1} feature is not observed under these conditions. Resonance Raman enhancement of metal-ligand vibrations is in most cases related to charge-transfer transitions between the metal and the ligand that lead to a change in

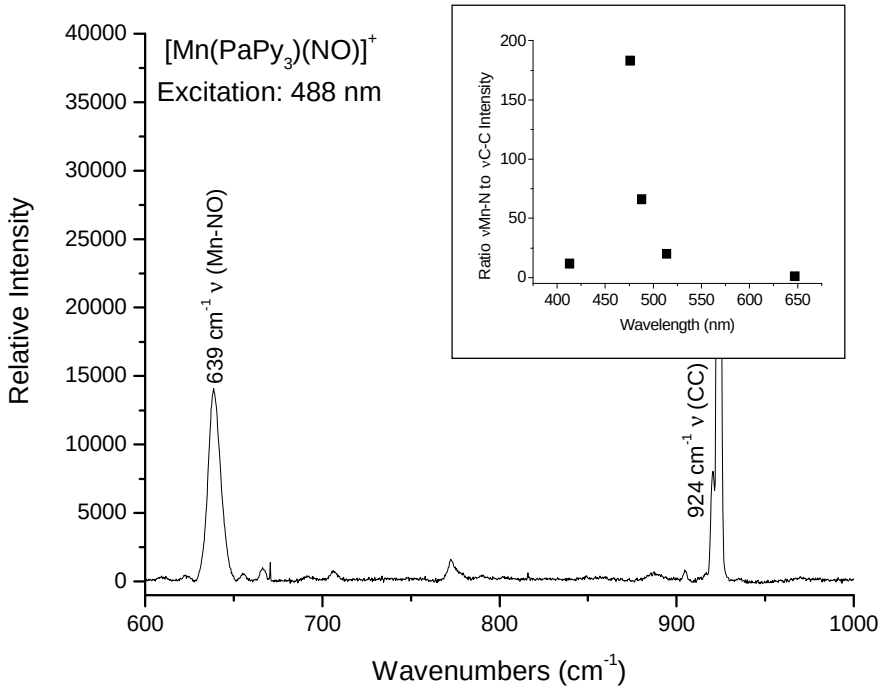

Figure 2.6. Resonance Raman spectrum of $[Mn(PaPy_3)(NO)]^+$ obtained at an excitation wavelength of 488 nm. Insert: resonance Raman excitation profile of the 639 cm^{-1} feature, showing resonance enhancement of this vibration towards the UV region. The ratio of ν(Mn-NO) to ν(C-C) (MeCN) Raman intensity is normalized to the value observed at the excitation wavelength of 647 nm (intensity ratio set to 1).

the metal-ligand bond in the excited state resulting in an excited state displacement, ΔQ.[19] These excited state displacements are generally much more pronounced for metal-ligand bond distances compared to angles, and hence, the metal-ligand stretching modes are in most cases resonance enhanced while the bending modes are not.[20]

With these experimental IR and Raman results in hand, DFT calculations were then performed to define the ground state including the formal oxidation states of Mn and NO in $[Mn(PaPy_3)(NO)]^+$. Its structure was optimized for both S = 0 and S = 1 as potential ground states. These calculations were able to reproduce the geometric and spectroscopic parameters well in the diamagnetic (S = 0) state of the complex, whereas in the alternative triplet ground state, a distinct weakening of the Mn-NO bond was observed. In addition, the predicted vibrational data for the S = 0 and S = 1 states (Table 2.3) provide further support for the idea that $[Mn(PaPy_3)(NO)]^+$ has a diamagnetic (S = 0) ground state. For example, the Mn-NO stretch and the Mn-N-O bend appear to be very sensitive to the difference in spin state, with a 70–80 cm^{-1} difference in frequency between the singlet and triplet states as shown in Table x.

Table 2.3. Comparison of key calculated vibrational data (BP86/TZVP) between the potential S = 0 and S = 1 ground states of $[Mn(PaPy_3)(NO)]^+$ and $[Mn(PaPy_2Q)(NO)]^+$

Complex	Vibrations	Singlet: S = 0	Triplet: S = 1	Experimental
$[Mn(PaPy_3)(NO)]^+$	ν(N-O)	1758 cm^{-1}	1761 cm^{-1}	1733 cm^{-1}
	ν(Mn-NO)	653 cm^{-1}	582 cm^{-1}	637 cm^{-1}
	δ(Mn-N-O)	613 / 631 cm^{-1}	520 / 550 cm^{-1}	606 cm^{-1}
$[Mn(PaPy_2Q)(NO)]^+$	ν(N-O)	1737 cm^{-1}	1746 cm^{-1}	1725 cm^{-1}
	ν(Mn-NO)	669 cm^{-1}	590 cm^{-1}	
	δ(Mn-N-O)	612 / 630 cm^{-1}	525 / 551 cm^{-1}	

Based on this comparison of these values with the corresponding experimental data, it can be concluded that $[Mn(PaPy_3)(NO)]^+$ has a diamagnetic (S = 0) ground states. Room temperature magnetic susceptibility data and sharp resonances in the ^{1}H-NMR spectrum of the complex also comfirm that it is diamagnetic (S = 0) in both the solid state and in solution.[10]

Once the diamagnetic (S = 0) ground state of $[Mn(PaPy_3)(NO)]^+$ was confirmed, the DFT optimized structure was used to further distinguish between a low spin Mn(I)–NO^+ and a strongly coupled Mn(II)–$NO^{\bullet}$ electronic description (both S = 0) of $[Mn(PaPy_3)(NO)]^+$. Examination of the DFT calculated molecular orbitals with significant Mn and NO character reveal that the complex is best described as Mn(I)-NO^+, where Mn(I) is in the diamagnetic $[t_{2g}]^6$ low-spin state, and the NO^+ ligand forms two very strong π backbonds with the d_{xz} and d_{yz} orbitals of the metal (where the Mn-N(O) bond corresponds to the z axis). This explains the strong Mn-NO bonds observed for this complex as reflected by its high Mn-NO stretching frequency discussed above. The strength of the Mn(I)-NO^+ π backbond was estimated from the occupied HOMO-3 which has 54% Mn and 36% NO^+ character, whereas the corresponding antibonding LUMO+2 has 54% NO^+ and 37% Mn contributions. The fact that the occupied MO has more metal character is again in agreement with the idea that these electrons should formally be assigned to manganese, in accordance with the Mn(I)-NO^+ description. These charge contributions correspond to an extraordinarily strong π backbond, due to the soft nature of the formally Mn(I) center.

2.3 Molecular Orbitals and UV-Visible Spectra

Once the spin states of the different mental nitrosyls were determined, time dependent DFT (TDDFT) calculations were performed to reveal which molecular orbitals are involved in the absorption of light resulting in the photolabilization of NO. Specifically, we were interested in assigning the lowest energy absorption bands of each compound in order to gain insights into their different sensitivities to visible light Comparison of the $\{FeNO\}^6$ and $\{FeNO\}^7$ nitrosyls revealed that only the $\{FeNO\}^6$ nitrosyls exhibits NO photoactivity while the $\{FeNO\}^7$ species appears to be insensitive to light. The first part of this section will compare the differences in the molecular orbital (MO) shape/location and absorption spectra of $[(PaPy_3)Fe(NO)]^{2+}$ and $[(PaPy_3)Fe(NO)]^{+}$ to gain insight into the origin of NO photolability. The second part of this section will compare the MO's and absorption spectra of the three $\{MNO\}^6$ nitrosyls with either Fe, Mn, or Ru centers to better understand the drastic differences in their ability to absorb low energy visible light leading to NO labilization.

2.3.1 Comparison of $\{FeNO\}^6$ and $\{FeNO\}^7$ Nitrosyls

The frontier MO's (HOMO–4 through LUMO+4) of $[(PaPy_3)Fe(NO)]^{2+}$ and $[(PaPy_3)Fe(NO)]^{+}$are shown in Figure 2.7. These are the main orbitals involved in the lower energy electronic transitions of these nitrosyls as indicated by their TDDFT calculations. The singly occupied molecular orbital (SOMO) of $[(PaPy_3)Fe(NO)]^{+}$ is

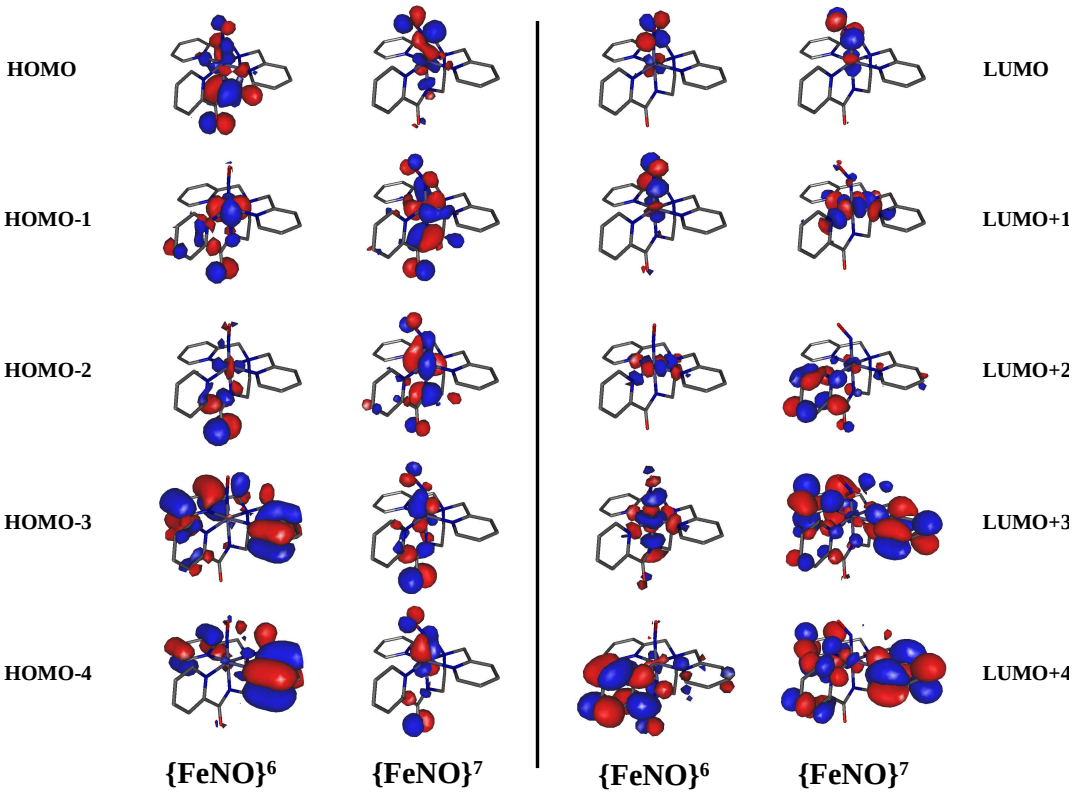

Figure 2.7. DFT-calculated HOMO through HOMO–4 orbitals (left) and LUMO through LUMO–4 orbitals (right) of $[(PaPy_3)Fe(NO)]^{2+}$and $[(PaPy_3)Fe(NO)]^{+}$

its highest occupied molecular orbital (HOMO). Both nitrosyls have partial d(Fe)–π*(NO) bonding character in their HOMO's. However, there is more of a Fe–NO π–bonding (π(FeNO)) interaction in the HOMO of $[(PaPy_3)Fe(NO)]^{2+}$ and more σ–bonding (σ(FeNO)) in $[(PaPy_3)Fe(NO)]^{+}$. In addition, both HOMO's contain non-bonding amido (nb(amido)) character. In the case of $[(PaPy_3)Fe(NO)]^{2+}$, the nb(amido) orbitals are the dominant feature in HOMO while the partial Fe–NO bonding orbital is more prominent in the HOMO of $[(PaPy_3)Fe(NO)]^{+}$. The HOMO–1 through HOMO–4 of $[(PaPy_3)Fe(NO)]^{+}$ has more nb(amido) and π(FeNO)

bonding character similar to the HOMO of $[(PaPy_3)Fe(NO)]^{2+}$. However, the HOMO–1 and HOMO–2 of complex $[(PaPy_3)Fe(NO)]^{2+}$ contain d(Fe) and nb(amido) orbitals with very little NO character. There is more pyridine character to the HOMO–3 and HOMO–4 of $[(PaPy_3)Fe(NO)]^{2+}$. The LUMO and LUMO+1 of $[(PaPy_3)Fe(NO)]^{2+}$ are perpendicular orbitals predominately $d_{\pi}(Fe)–\pi*(NO)$ anti-bonding orbitals ($\pi*(FeNO)$). Interestingly in the case of $[(PaPy_3)Fe(NO)]^{+}$, only the LUMO has some $\pi*(FeNO)$ anti-bonding character. The LUMO+1 is dominated by a $d_{x^2-y^2}(Fe)–\sigma*(N_{py})$ anti-bonding interaction. A similar orbital is observed in the LUMO+2 of $[(PaPy_3)Fe(NO)]^{2+}$. The LUMO+3 of $[(PaPy_3)Fe(NO)]^{2+}$ contains an anti σ–bonding interaction along the N_{amido}–Fe–NO axis. In the case of $[(PaPy_3)Fe(NO)]^{+}$, the LUMO+3 and LUMO+4 are dominated by π–orbitals extending over the polypyridine ligand frame (π_{py}).

Interestingly, examination of Figure 2.7 reveals a difference in the number of unoccupied orbitals containing Fe-NO antibonding character. Transitions into these antibonding orbitals would be expected to lead to significant weakening of the Fe–NO bond and thus could provide a *direct pathway* to NO labialization through the initial electronic excitation. In the case of $[(PaPy_3)Fe(NO)]^{+}$, its LUMO is the only orbital in the series with some Fe-NO antibonding character while the LUMO, LUMO+1, and LUMO+3 all contain Fe-NO antibonding character in $[(PaPy_3)Fe(NO)]^{2+}$. We suggest that this key difference in the antibonding Fe-NO

characters in the LUMO through LUMO+4 of the two nitrosyls plays a major role in their different NO photoactivities.

In Figures 2.8 and 2.9, the TDDFT calculated absorption spectra of $[(PaPy_3)Fe(NO)]^{2+}$ and $[(PaPy_3)Fe(NO)]^{+}$ (respectively) are simulated using Lorentzian broadening of the calculated electronic transitions (dashed lines) and the experimental electronic absorption spectrum of each complex (solid lines) is shown for comparison. The TDDFT calculated transitions are shown as a bar graph with the height of each bar corresponding to the relative oscillator strength of each transition. The transitions responsible for the lowest energy absorption bands are highlighted in red and the orbitals involved in those transitions are shown below the graph. The experimental absorption spectra of both $\{FeNO\}^6$ and $\{FeNO\}^7$ species consist of two low energy bands that are reasonably well reproduced by TDDFT calculations (Figure 2.8 and 2.9). The lowest energy band of appreciable oscillator strength in the calculated electronic spectrum of $[(PaPy_3)Fe(NO)]^{2+}$ arises from a nb(amido)-π(FeNO) to π^*(FeNO) transition (480 nm, HOMO $\rightarrow$ LUMO+1). The next lowest energy peak contains another high intensity calculated electron transition (337 nm) also ending in the π^*(FeNO) orbital (LUMO+1) from a d_{xy}-nb(amido) orbital (HOMO−1). These transitions all originate from MOs with some carboxamido character and end in Fe–NO antibonding MOs. It is evident that these transitions will significantly weaken the Fe–NO bond, thereby increasing the likelihood of photodissociation through this initial electronic excitation as a direct pathway. In their theoretical study, Richards and coworkers have also identified similar ligand-to-

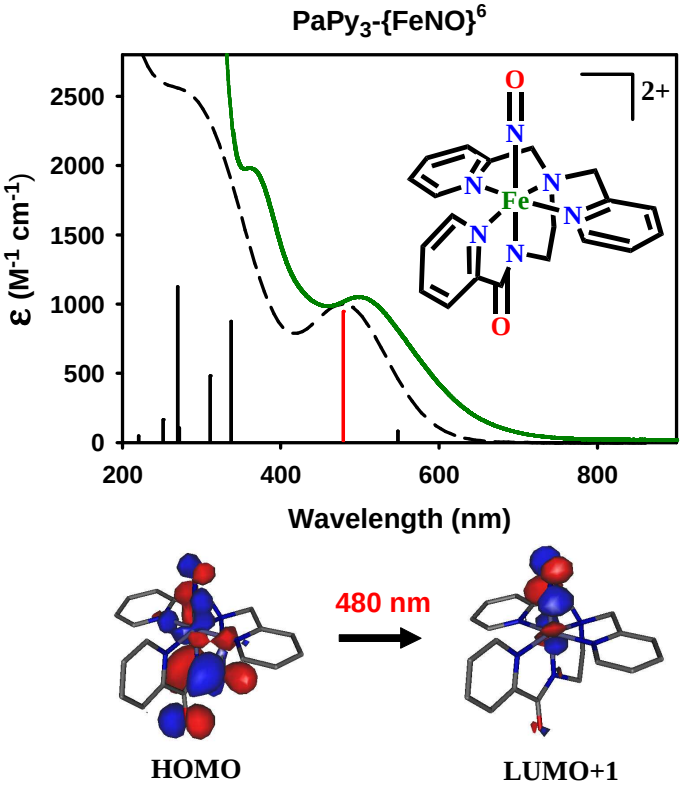

Figure 2.8. TDDFT calculated energy transitions and oscillator strengths (shown as vertical lines, red = major low energy transition) with the Lorentzian broadened spectra (dashed line) and the experimental electronic absorption spectra (solid lines) of $[(PaPy_3)Fe(NO)]^{2+}$. The most prominent MOs involved in the lowest energy transitions (labeled in red) and their diagrams are shown below.

metal transitions (LMCT) as the possible origin of NO photolability observed with $[(PaPy_3)Fe(NO)]^{2+}$.[16] Furthermore, TDDFT calculations on the photoactive nitrosyl $(NEt_4)[(Cl_2PhPep\{SO_2\}_2)Fe(NO)(DMAP)]$ also predict transition from the carboxamido-N into Fe-NO antibonding orbitals.[6] The theoretical results point to the importance of carboxamido-N donor in the visible light absorption leading to NO photodissociation in this complex. The strong σ-donating ability of the carboxamido moiety appears to facilitate low energy electronic transition into the Fe–NO

antibonding orbital, thus promoting photodissociation in $[(PaPy_3)Fe(NO)]^{2+}$. Interestingly, there is an absence of TDDFT predicted electronic transitions into the Fe–NO antibonding orbitals of two other Fe-NHase model complexes without carboxamido-N donors or NO photolability, namely $[Fe(III)S_2{}^{Me2}N_3(Pr,Pr)(NO)]^+$ and $[(bmmp\text{-}TASN)FeNO]^+$.[16] While carboxamido-N donors are not a necessity for NO photolability, their presences does appear to promote NO photolability when combined with the proper mix of other donor types in $\{MNO\}^6$ nitrosyls.

In the case of $[(PaPy_3)Fe(NO)]^+$, the two low energy absorption bands in the calculated spectrum do not contain transitions into Fe–NO antibonding MOs. Instead the lowest energy band in the calculated spectrum arises from a transition starting in a σ(FeNO)-nb(N_{amido}) orbital and ending in a π_{py} orbital (525 nm, HOMO → LUMO+3). The next lowest energy band also arises from a transition originating from the same σ(FeNO)-nb(N_{amido}) orbital and ending in a higher energy π_{py} orbital (395 nm, HOMO → LUMO+4). There are also two lower intensity transitions in the calculated spectrum that contribute to this second band (see Figure 2.9). These transitions (455 and 430 nm) both end in the SOMO of $[(PaPy_3)Fe(NO)]^+$. The lack of photolability observed in $[(PaPy_3)Fe(NO)]^+$ can therefore be explained by the absence of any calculated low energy transitions into MO's with Fe–NO antibonding character. In addition, the main low energy transitions calculated for $[(PaPy_3)Fe(NO)]^+$ are mostly metal-to-ligand transitions (MLCT) whereas in $[(PaPy_3)Fe(NO)]^{2+}$ they are more LMCT in character. It thus appears that the additional electron in the FeNO unit of the $\{FeNO\}^7$ nitrosyl allows for transitions

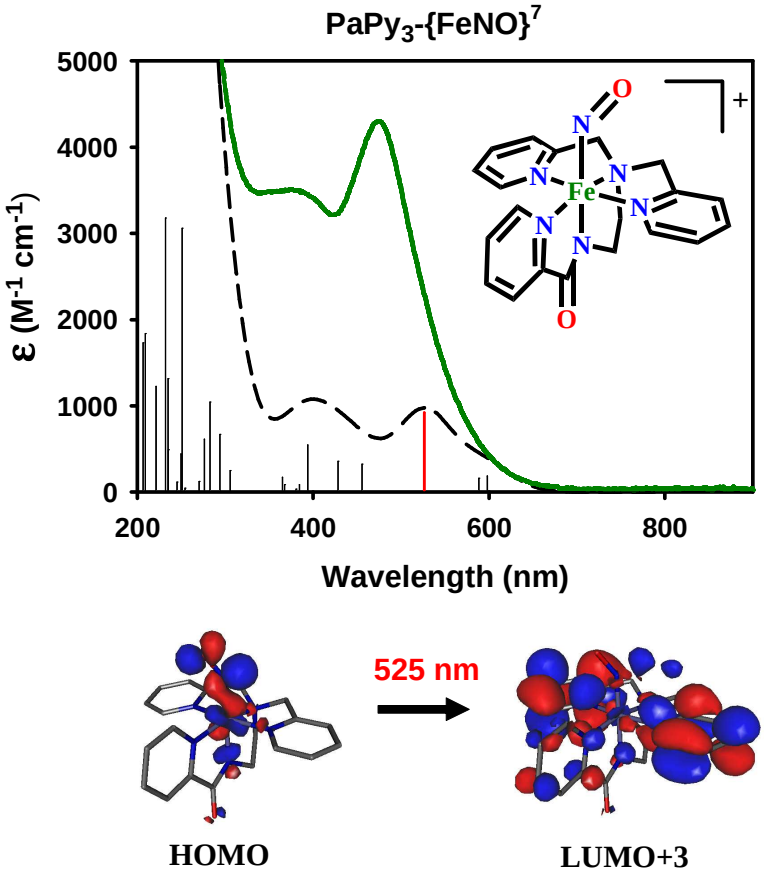

Figure 2.9. TDDFT calculated energy transitions and oscillator strengths (shown as vertical lines, red = major low energy transition) with the Lorentzian broadened spectra (dashed line) and the experimental electronic absorption spectra (solid lines) of $[(PaPy_3)Fe(NO)]^+$. The most prominent MOs involved in the lowest energy transitions (labeled in red) and their diagrams are shown below.

from MO's centered at the FeNO unit to the π–system of the polypyridine ligand frame. In contrast, the FeNO unit in the $\{FeNO\}^6$ nitrosyl has less electron density thus allowing for more electron donation from the trans carboxamido moiety into the π*(FeNO) anti-bonding orbital promoting photolability.

2.3.2 Comparison of $\{MNO\}^6$ Nitrosyls (M = Fe, Mn, or Ru)

DFT and TDDFT calculations on $[(PaPy_3)Fe(NO)]^{2+}$, $[(PaPy_3)Mn(NO)]^{+}$, and $[(PaPy_3)Ru(NO)]^{2+}$ have been used to assign the electronic transitions responsible for the different absorption bands observed for these nitrosyls. One of the main differences observed when comparing the frontier molecular orbitals of the$\{FeNO\}^6$, $\{MnNO\}^6$, and $\{RuNO\}^6$ nitrosyls (Figure 2.10) is that the LUMO and LUMO+1 of both $[(PaPy_3)Fe(NO)]^{2+}$ and $[(PaPy_3)Ru(NO)]^{2+}$ are perpendicular $d_\pi(M)$–$\pi^*(NO)$

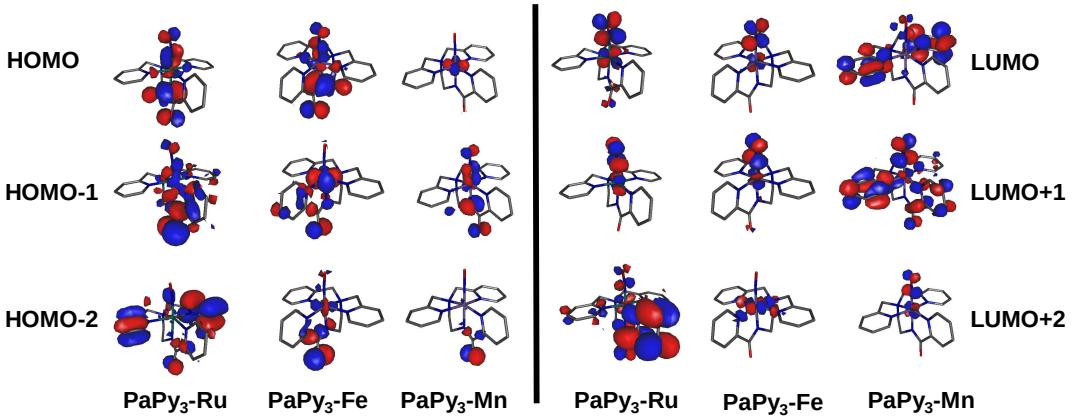

Figure 2.10. DFT-calculated HOMO through HOMO-2 orbitals (left) and LUMO through LUMO+2 orbitals (right) for $[(PaPy_3)Ru(NO)]^{2+}$, $[(PaPy_3)Fe(NO)]^{2+}$, and $[(PaPy_3)Mn(NO)]^{+}$

antibonding orbitals. However, the LUMO and LUMO+1 of $[(PaPy_3)Mn(NO)]^{+}$ are predominantly pyridine-based orbitals. The LUMO+1 also has some $\pi^*(NO)$ character, but no metal character at all. Only the LUMO+2 and LUMO+4 orbitals of $[(PaPy_3)Mn(NO)]^{+}$ contain any significant $d_\pi(Mn)$–$\pi^*(NO)$ antibonding character. Another key difference is also observed between the HOMOs of the ruthenium and iron nitrosyls compared to that of the manganese nitrosyl. The HOMO's of both

$[(PaPy_3)Fe(NO)]^{2+}$ and $[(PaPy_3)Ru(NO)]^{2+}$ have $d_\pi(M)–\pi^*(NO)$ bonding character in addition to carboxamide character while the HOMO of $[(PaPy_3)Mn(NO)]^{+}$ is primarily a $d_{xy}(Mn)$ orbital.

TDDFT calculations reveal that the lowest energy absorption band of the $\{RuNO\}^6$ species arises due to a transition (at 418 nm) from a $d_\pi(M)–\pi^*(NO)$ bonding/carboxamido orbital to a $d_\pi(M)–\pi^*(NO)$ antibonding orbital (HOMO → LUMO, Figure 2.11). These orbitals are almost exactly the same as those involved in the low energy transition of $[(PaPy_3)Fe(NO)]^{2+}$ (at 514 nm) described above (Figure 2.8). In the case of $[(PaPy_3)Mn(NO)]^{+}$, similar calculated transitions into orbitals with dominant $d_\pi(Mn)–\pi^*(NO)$ antibonding character (LUMO+2 and LUMO+4) are found at 404 and 455 nm (Figure 2.12). The assignment of these transitions is supported by a strong resonance Raman enhancement of the Mn–NO stretch observed experimentally for $[(PaPy_3)Mn(NO)]^{+}$ upon laser excitation in the 400-500 nm region.[18] Such strong resonance enhancements suggest an excited state that has a substantial displacement along the Mn–NO bond which agrees with the predicted electron excitation into a Mn–NO antibonding orbital. Thus the observed photolability of $[(PaPy_3)Mn(NO)]^{+}$ and $[(PaPy_3)Ru(NO)]^{2+}$ using near-UV light could also be explained by a similar *direct pathway* as that describe above for $[(PaPy_3)Fe(NO)]^{2+}$, through a metal–NO antibonding excited state that would cause significant weakening of the metal–NO bond. It is important to note that the energy required for the transition from $d_\pi(M)–\pi^*(NO)$ bonding/carboxamido orbital to a

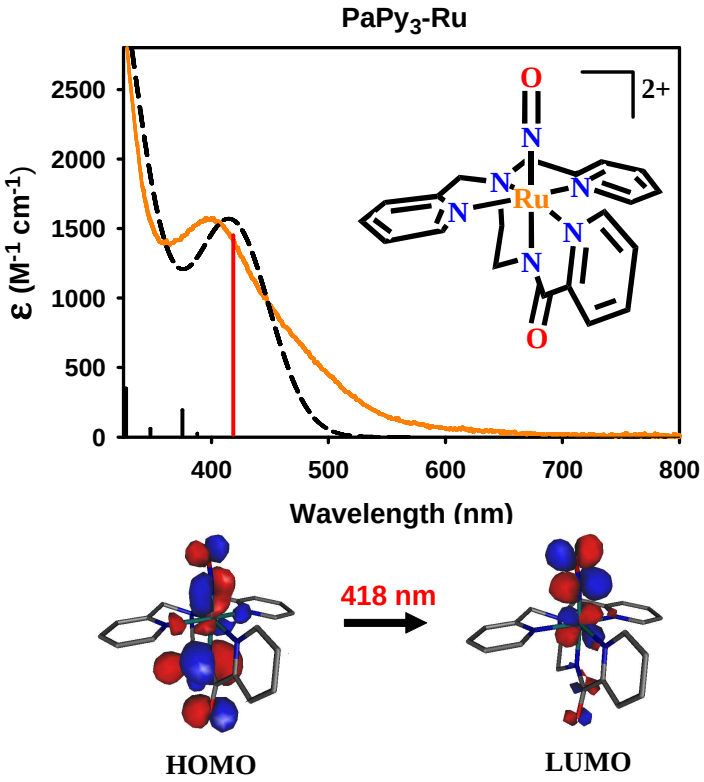

Figure 2.11. TDDFT calculated energy transitions and oscillator strengths (shown as vertical lines, red = major low energy transition) with the Lorentzian broadened spectra (dashed line) and the experimental electronic absorption spectra (solid lines) of $[(PaPy_3)Ru(NO)]^{2+}$. The most prominent MOs involved in the lowest energy transitions (labeled in red) and their diagrams are shown below.

d_π(M)–π*(NO) antibonding orbital (the one responsible for NO photolability) in these $\{FeNO\}^6$, $\{MnNO\}^6$ and $\{RuNO\}^6$ nitrosyls follows the order of the stability of the reduced state of the metal center. For example, the most stable Ru(II) center allows such transition in the ~400 nm range while the least resistant Fe(II) center permits such transfer of electron at 500 nm. The Mn(I) center lies in the middle and hence the transfer of an electron to the d_π(M)–π*(NO) antibonding orbital occurs at ~450 nm in case of $[(PaPy_3)Mn(NO)]^+$.

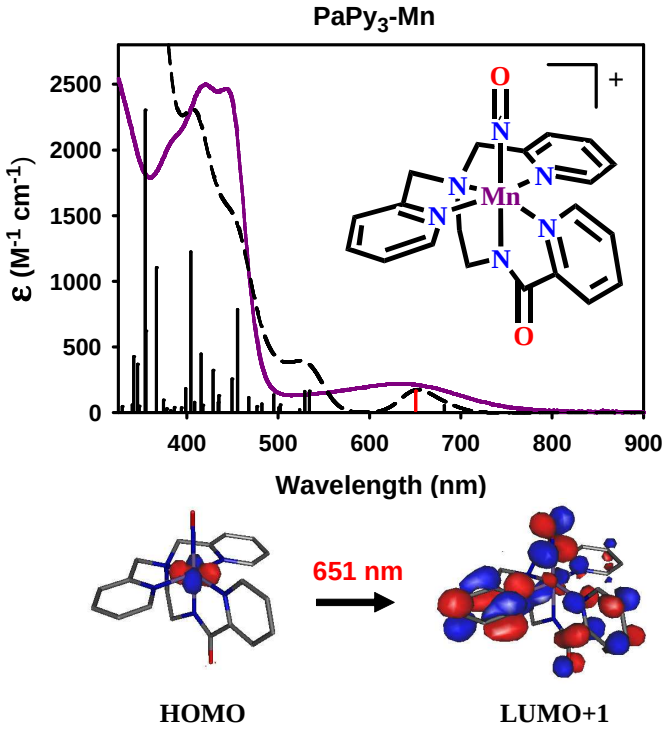

Figure 2.12. TDDFT calculated energy transitions and oscillator strengths (shown as vertical lines, red = major low energy transition) with the Lorentzian broadened spectra (dashed line) and the experimental electronic absorption spectra (solid lines) of $[(PaPy_3)Mn(NO)]^+$. The most prominent MOs involved in the lowest energy transitions (labeled in red) and their diagrams are shown below.

The direct mechanism however does not explain the NO photolability of $[(PaPy_3)Mn(NO)]^+$ observed upon illumination with 500-600 nm light since no excited states with significant Mn-NO antibonding character are predicted in this region. Instead, the calculated transitions are predominantly metal-to-pyridine transitions. Specifically, the lowest energy absorption band of $[(PaPy_3)Mn(NO)]^+$ arises due to a transition (at 651 nm) from a d_{xy}(Mn) orbital into a π-pyridine based orbital with some NO (but no metal d) character (HOMO → LUMO+1, Figure 2.12). Therefore it is proposed that NO photorelease of $[(PaPy_3)Mn(NO)]^+$ in the visible

region is due to an *indirect mechanism*. In this mechanism, photoexcitation initially leads to occupation of the d_{xy}(Mn) → π-pyridine excited state. This initial excited state then interconverts to a lower singlet excited state that is ideally set up to undergo intersystem crossing into the corresponding Mn-NO antibonding triplet state (T1) due to strong spin-orbit coupling promoted by the strong admixture of d_π character into the unoccupied π* orbitals of NO^+. Such intersystem crossing into the corresponding triplet state would be advantageous for NO photorelease due to the extended life times of triplet excited states along with the Mn(II)-$NO^\bullet$ type electronic structure of M-NO triplet states. Once the molecule has entered the T1 excited state, the Mn-NO antibonding nature of this state promotes NO dissociation. Similar indirect mechanisms have also been demonstrated by rigorous TDDFT calculations for the photodissociation of ligands in $[Ru(bpy)_2L_2]^{2+}$ (L = 4-aminopyridine, pyridine, and butylamine) complexes [21] and methylcobalamine.[22]

2.4 Conclusions

Theoretical studies of the designed metal nitrosyls derived from the $PaPy_3$ ligand have provided some important clues related to their NO photolability. Specifically the presence of carboxamido-N donors appears to plays a key role in the photolability of the three photoactive metal nitrosyls $[(PaPy_3)Fe(NO)]^{2+}$, $[(PaPy_3)Mn(NO)]^+$ and $[(PaPy_3)Ru(NO)]^{2+}$). For example, the TDDFT results reveal that the calculated electronic transitions of these nitrosyls in the region of 350-500 nm all originate from molecular orbitals with significant carboxamido character. It was

also found that these photoactive nitrosyls all have a low spin d^6 metal configuration with NO in the NO^+ oxidation state (d^6(M)–NO^+). This NO^+ character helps to facilitate the observed transitions into Fe-NO antibonding excited states. Such states cause significant weakening of the metal-NO bond and thus allow NO release directly through an initially excited singlet state.

In case of $[(PaPy_3)Mn(NO)]^+$, an additional low energy transition at 650 nm (a d_{xy}(Mn) → π-pyridine transition) is observed that does not contribute to NO-photolability through this direct pathway. Instead, intersystem crossing from the initial excited state into a π(Mn)-π*(NO) antibonding triplet state finally allows NO release in this nitrosyl. It is important to note that since manganese resides left to both iron and ruthenium in the periodic table, it is in a 1+ oxidation state while iron and ruthenium are in a 2+ oxidation state in these d^6(M)–NO^+ type nitrosyls. Thus unlike the Fe and Ru containing nitrosyls, the softer nature of the Mn-center in $[(PaPy_3)Mn(NO)]^+$ allows a low energy transition that transfers the excess metal electron density into the π-system of pyridine donors of the ligand frame. Thus the Mn(I)–NO^+ combination allows for both direct photorelease of NO due to carboxamide → Mn-NO antibonding electronic transitions (in the 350-500 nm region) as well as d_{xy}(Mn) → π-pyridine transitions (500-650 nm) that lead to NO photorelease via low lying Mn-NO antibonding triplet excited states.

In the case of $[(PaPy_3)Fe(NO)]^{2+}$, this d^6(M)–NO^+ electronic distribution is altered resulting in the loss of NO photoactivity. The addition electron in the $\{FeNO\}^7$ unit goes to the NO^+ moiety while the Fe center remains predominantly in

the 2+ oxidation state resulting in a Fe(II)–$NO^{\bullet}$ species The decreased π-accepting ability of the $NO^{\bullet}$ moiety in $[(PaPy_3)Fe(NO)]^{+}$ does not favor transitions similar to those observed in the photoactive $PaPy_3$ $\{MNO\}^6$ nitrosyls. Instead, transitions from MOs centered on the $\{FeNO\}^7$ unit to MOs with π_{py} character become more favorable thus cutting off the direct pathway for NO photolability through the initial Fe-NO antiboding excited state.

A similarly trend is also observed in the case of two other related iron nitrosyls designed (in our lab) from ligands containing carboxamido-N and thiolato-S donors, namely $[(Cl_2PhPepS)Fe(NO)(DMAP)]^{-}$ and $[(Cl_2PhPep\{SO_2\}_2)$-$Fe(NO)(DMAP)]^{-}$.[5,6] The thiolato-S containing nitroysl $[(Cl_2PhPepS)Fe(NO)$-$(DMAP)]^{-}$ does not show any NO photoactivity. However NO photoactivity is turned on when the thiolato-S centers are converted into sulfinato-SO_2 moieties (via oxygenation) in $[(Cl_2PhPep\{SO_2\}_2)Fe(NO)(DMAP)]^{-}$. Results of DFT and TDDFT calculations suggest that the S-oxygenation of the ligand frame in $[(Cl_2PhPepS)Fe(NO)(DMAP)]^{-}$ stabilizes a S = 0 spin state in the resulting $[(Cl_2PhPep\{SO_2\}_2)Fe(NO)(DMAP)]^{-}$. For example, at low temperature (-40 ºC), the absorption spectrum of $[(Cl_2PhPepS)Fe(NO)(DMAP)]^{-}$ is more similar to that of the S = 0 TDDFT spectrum which supports a Fe(II)-NO^{+} configuration. With rise in temperature, the experimental absorption spectrum of $[(Cl_2PhPepS)Fe(NO)(DMAP)]^{-}$ changes and at room temperature matches more closely with the TDDFT spectrum calculated for a S = 1 spin state. It thus appears that the strong σ-donating thiolato-S

donors provide stability to the Fe(III)–$NO^{\bullet}$ configuration in $[(Cl_2PhPepS)Fe(NO)(DMAP)]^{-}$ at room temperature leading to some S = 1 spin crossover. Conversely, the oxygen atoms in the sulfinato-SO_2 donors of $[(Cl_2PhPep\{SO_2\}_2)Fe(NO)(DMAP)]^{-}$ reduce the amount of negative charge donated into the metal center thus allowing for an exclusive Fe(II)–NO^{+} configuration (S = 0). Together, these results support our conclusion that the difference in π-accepting ability of the NO ligand (NO^{+} > $NO^{\bullet}$) in these nitrosyls affects their NO photoactivity.

2.5 Computational Methods

The first set of DFT calculations preformed in our lab were carried out with the aid of the program PC-GAMESS.[23] This program worked well for DFT energy and geometry optimization of both iron and ruthenium nitrosyls of various spin states. In addition, we were able to successfully predict the electronic absorption spectra of compounds with a singlet (S = 0) ground state via TDDFT calculations also preformed using PC-GAMESS. However when we became interested in predicting and assigning the electronic absorption spectra of complexes with more complicated spin states (such as $[(PaPy_3)Fe(NO)]^{+}$), we had to switch to a new program, namely ORCA.[24] ORCA was developed by an inorganic chemist (Frank Neese) and specifically designed to address some of the unique features of metal complexes, such as their complex and varied spin states. With ORCA we were then able to perform TDDFT calculations to gain information about triplet excited states for complexes with either singlet or triplet ground states.

In the studies discussed above, PC-GAMESS was used for both the DFT and TDDFT calculations for $[(PaPy_3)Ru(NO)]^{2+}$ (with a singlet ground state) while ORCA was employed for all the calculations done for the $\{FeNO\}^6$ and $\{FeNO\}^7$ nitrosyls. The geometry of $[(PaPy_3)Fe(NO)]^{2+}$ was optimized in its low spin (S = 0) state. Unrestricted Kohn-Sham formalism (UKS) was applied during the geometry optimization of the $\{FeNO\}^7$ species in its low spin (S = 1/2) and high spin (S = 3/2) electronic states. The S = 1/2 state was found to be 12.18 kcal/mol lower in energy than the S = 3/2 state thus correctly predicting the S = 1/2 state proposed by experimental data. In the case of $[(PaPy_3)Mn(NO)]^+$, the DFT optimization was preformed by our collaborators using a third DFT program, Gaussian 03.[25] The structure of $[(PaPy_3)Mn(NO)]^+$ was fully optimized for both the singlet (S = 0) and triplet (S = 1) states using Gaussian 03. ORCA was then used for the TDDFT calculations. In addition to calculations performed to assign the electronic absorption spectrum of $[(PaPy_3)Mn(NO)]^+$, IR and non-resonance Raman intensities were also calculated to assist in spectral assignments. All of these calculations were performed using Gaussian 03 as well.

Crystal structure coordinates of the previously synthesized nitrosyls were used as a starting point for the DFT gas-phase energy and geometry optimizations of the ground states. Different DFT functionals were chosen for these calculations depending on the metal center of the nitrosyl. In the case of the nitrosyls containing first row transition metel centers (Fe and Mn), pure DFT functionals were employed while hybrid functionals were chosen for second row transition metal centers (Ru).

The specific functionals within either the pure or hybrid classification were chosen based on how well the energy, overall shape, and relative height of the peaks of the calculated TDDFT data matched with the experimental data. For the iron nitroysls, the results obtained using the PW91 functional made the most sense in terms of the observed differences in the photolabilities of the $\{FeNO\}^6$ and $\{FeNO\}^7$ nitrosyls. In addition, the use of ORCA COSMO solvation model of acetonitrile in the $[(PaPy_3)Fe(NO)]^{2+}$ and $[(PaPy_3)Fe(NO)]^{+}$ TDDFT calculations provided calculated electronic absorption spectra that matched more closely with the overall shape of the experimental spectra. The BP86 functional was found to work best for the manganese nitroysl calculations while the PBE0 functional was used for the ruthenium nitrosyl calculations. It was previously found that for ruthenium nitrosyls the addition of solvent (EtOH) effects using PC-GAMESS Polarized Continuum Model (PCM) [26] is necessary to obtain calculated electronic absorption bands with similar energies to those observed experimentally.

Slightly different basis sets were also used for the various atom types (C, N, O, H, Ru, Mn, Fe) present in these nitrosyls during the DFT and TDDFT calculations. Either Ahlrichs or Pople style basis sets were chosen for the first row transition metals as well as for the C, N, O, and H atoms. Both types are split-valence (SV) type basis sets which use more contractions to describe the valence orbitals than the core orbitals in order to speed up calculation times. In the case of $[(PaPy_3)Mn(NO)]^{+}$, Ahlrichs's triple-zeta valence basis set with one set of first polarization functions (TZVP) was used for all of the atoms.[27] For the iron centered $PaPy_3$ nitrosyls

Ahlrichs's triple-zeta valence basis set with three sets of first polarization functions (TZVPP) was employed.[28] The extra polarization provides more flexibility and thus increased the accuracy but also increased the time of these calculations. However, the additional time was not detrimental to the overall progress of the project. Because ruthenium has many more electrons compared to iron and manganese, a smaller basis set is necessary in order to perform calculations that can be completed in a reasonable amount of time. We have therefore used Pople style double zeta basis set (instead of the triple zeta basis sets described above) with polarization (6-31G*) [29] for all of the heavy atoms except Ru for which the quasi-relativistic Stuttgart-Dresden effective core potential (ECP) was implemented. Since the core orbitals are not generally affected significantly by changes in chemical bonding, ECP treats the inner shell electrons as an averaged potential rather than individual particles. This modification generates a much more efficient computation that is a good deal faster. Unfortunately, ECP is not yet available for ORCA and thus the $[(PaPy_3)Ru(NO)]^{2+}$ calculations were completed using PC-GAMESS.

The optimized structure geometries as well as the molecular orbital energies and electron densities were visualized with either MacMolPlt [30] for the PC-GAMESS data or with Gabedit [31] for the ORCA data. All calculated absorption energies and oscillator strengths were fit to normalized Lorentzian functions using Gabedit to generated the predicted electron absorption spectra. From these data, it was established that a constant empirical shift of 4.5 eV was required for the calculated spectra of both $\{FeNO\}^6$ and $\{FeNO\}^7$ nitrosyls in order to compare them with their

experimental spectra. The calculated electron absorption spectra for both $[(PaPy_3)Mn(NO)]^+$ and $[(PaPy_3)Ru(NO)]^{2+}$did not require any adjustments.

2.6 References

1. (a) I. Endo, M. Nojiri, M. Tsujimura, M. Nakasako, S. Nagashima, M. Yohda, M. Odaka, *J. Inorg. Biochem.* 2001, **83**, 247; (b) M. Kobayashi, S. Shimizu, *Curr. Opin. Chem. Biol.* 2000, **4**, 95; (c) I. Endo, M. Odaka, M. Yohda, *Trends Biotechnol.* 1999, **17**, 244.

2. (a) S. Nagashima, M. Nakasako, N. Dohmae, M. Tsujimora, K. Takio, M. Odaka, M. Yohda, N. Kamiya, I. Endo, *Nat. Struct. Biol.* 1998, **5**, 347; (b) W.J. Huang, J. Jia, J. Cummings, M. Nelson, G. Schneider, Y. Lindqvist, *Structure*,1997, **5**, 691.

3. (a) T. C. Harrop, P. K. Mascharak, *Acc. Chem. Res.* 2004, **37**, 253; (b) P. K. Mascharak, *Coord. Chem. Rev.* 2002, **225**, 201.

4. J. Kovacs, *Chem. Rev.* 2004, **104**, 825.

5. M. J. Rose, N. M. Betterley, P. K. Mascharak, *J. Am. Chem. Soc.* 2009, **131**, 8340.

6. M. J. Rose, N. M. Betterley, A. G. Oliver, P. K. Mascharak, *Inorg. Chem.* 2010, **49**, 1854.

7. A. K. Patra, R. K. Afshar, M. M. Olmstead, P. K. Mascharak, *Angew. Chem. Int. Ed.* 2002, **41**, 2512.

8. A. K. Patra, J. M. Rowland, D. S. Marlin, E. Bill, M.M. Olmstead, P.K. Mascharak, *Inorg. Chem.* 2003, **42**, 6812.

9. N. L. Fry, X. P. Zhao, P. K. Mascharak, *Inorg. Chim. Acta*, 2011, **367**, 194.

10. K. Ghosh, A. A. Eroy-Reveles, T. R. Holman, M. M. Olmstead, P. K. Mascharak, *Inorg. Chem.* 2004, **43**, 2988.

11. (a) M. J. Rose, A. K. Patra, E. A. Alcid, M. M. Olmstead, P. K. Mascharak, *Inorg. Chem.* 2007, **46**, 2328; (b) A.K. Patra, P.K. Mascharak, *Inorg. Chem.* 2003, **42**, 7363.

12. (a) A. A. Eroy-Reveles, P. K. Mascharak, *Future Med. Chem.* 2009, **1**, 1497; (b) M. Madhani, A. K. Patra, T. W. Miller, A. A. Eroy-Reveles, A. J. Hobbs, J. N. Fukuto, P. K. Mascharak, *J. Med. Chem*. 2006, **49**, 7325.

13. I. Szundi, M. J. Rose, I. Sen, A. A.Eroy-Reveles, P. K. Mascharak, O. A. Einarsdottir, *Photochem. Photobiol.* 2006, **82**, 1377.

14. N. L. Fry, P. K. Mascharak, *Acc. Chem. Rev.* 2011, **44**, 289

15. C. G. Hoffman-Luca, A. A. Eroy-Reveles, J. Alvarenga, P. K. Mascharak, *Inorg. Chem.* 2009, **48**, 9104; (b) A. A. Eroy-Reveles, Y. Leung, C. M. Beavers, M. M. Olmstead, P. K. Mascharak, *J. Am. Chem. Soc.* 2008, **130**, 4447.

16. S. N. Greene, N. G. J. Richards, *Inorg. Chem.* 2004, **43**, 7030.

17. I. Mayer, Int. J. Quant. Chem. 1984, **26**, 151.

18. A. C. Merkle, N. L. Fry, P.K. Mascharak, N. Lehnert, *Inorg. Chem.* 2011**, 50**, 12192.

19.(a) A. C. Albrecht, *J. Chem. Phys.* 1961, **34**, 1476; (b) T. G. Spiro, *Iron Porphyrins*; A. B. P. Lever, H. B.Gray, Eds.; Addison-Wesley: Reading, Mass. 1983; Part 2, Pg. 91–159; (b) L. Krushinskii, P. P.Shorygin, *Opt. Spectry.* 1961, **11**, 12.

20. N. Lehnert, R. Y. N. Ho, L. Que, E. I. Solomon, *J. Am. Chem. Soc.* 2001, **123**, 8271.

21. L. Salassa, C. Garino, G. Salassa, R. Gobetto, C. Nervi, *J. Am. Chem. Soc.* 2008, **130**, 9590.

22. P. Lodowski, M. Jaworska, T. Andruniow, M. Kumar, P. M. Kozlowski, *J. Phys. Chem. B*, 2009, **113**, 6898.

23. Nemukhin, A. V.; Grigorenko, B. L.; Granovsky, A. A. *Moscow Univ. Chem. Bull*, 2004, **45**, 75.

24. F. Neese; Version 2.2 ed. Max-Planck Institut für Bioanorganische Chemie, Mülheim/Ruhr, Germany, 2004.

25. Frisch, M. J.; Trucks, G. W.; Schlegel, H. B.; Scuseria, G. E.; Robb, M. A.; Cheeseman, J. R.; Montgomery, J. A. Jr.; Vreven, T.; Kudin, K. N.; Burant, J. C.; Millam, J. M.; Iyengar, S. S.; Tomasi, J.; Barone, V.; Mennucci, B.; Cossi, M.; Scalmani, G.; Rega, N.; Petersson, G. A.; Nakatsuji, H.; Hada, M.; Ehara, M.; Toyota, K.; Fukuda, R.; Hasegawa, J.; Ishida, M.; Nakajima, T.; Honda, Y.; Kitao, O.; Nakai, H.; Klene, M.; Li, X.; Knox, J. E.; Hratchian, H. P.; Cross, J. B.; Adamo, C.; Jaramillo, J.; Gomperts, R.; Stratmann, R. E.; Yazyev, O.; Austin, A. J.; Cammi, R.; Pomelli, C.; Ochterski, J. W.; Ayala, P. Y.; Morokuma, K.; Voth, G. A.; Salvador, P.; Dannenberg, J. J.; Zakrzewski, V. G.; Dapprich, S.; Daniels, A. D.; Strain, M. C.; Farkas, O.; Malick, D. K.; Rabuck, A. D.; Raghavachari, K.; Foresman, J. B.; Ortiz, J. V.; Cui, Q.; Baboul, A. G.; Clifford, S.; Cioslowski, J.; Stefanov, B. B.; Liu, G.; Liashenko, A.; Piskorz, P.; Komaromi, I.; Martin, R. L.; Fox, D. J.; Keith, T.; Al-Laham, M. A.; Peng, C. Y.; Nanayakkara, A.; Challacombe, M.; Gill, P.

M. W.; Johnson, B.; Chen, W.; Wong, M. W.; Gonzalez, C.; Pople, J. A.; Gaussian, Inc.: Pittsburgh, PA, 2003.

26. S. Miertus, E. Scrocco, J. Tomasi, *Chem. Phys*. 1981, **55**, 117.

27. (a) A. Schäfer, H. Horn, R. Ahlrichs, *J. Chem. Phys.* 1992, **97**, 2571; (b) A. Schafer, C. Huber, R. Ahlrichs, *J. Chem. Phys.* 1994, **100**, 5829.

28. J. P. Perdew, J. A. Chevary, S. H. Vosko, K. A. Jackson, M. R. Pederson, D. J. Singh, C. Fiolhais, *Phys. Rev. B*, 1992, **46**, 6671.

29. (a) W. J. Hehre, R. Ditchfield, J.A. Pople, *J. Chem. Phys.* 1972, **56**, 2257; (b) M. M. Francl, W. J. Petro, W. J. Hehre, J. S. Binkley, M. S. Gordon, D. J. DeFrees, J.A. Pople, *J. Chem. Phys.* 1982, **77**, 3654.

30. M. P. Waller, H. Braun, N. Hojdis, M. Bühl, *J. Chem. Theory Comput.* 2007, **3**, 2234.

31. A. R. Allouche, Gabedit is a free Graphical User Interface for Computational Chemistry Packages. It is available from http://gabedit.sourceforge.net/.

Chapter 3, Part 1

Ruthenium Nitrosyls Derived from a Tetradentate Ligands with Dicarboxamido-N and Phosphine-P Donors

3.1.1 Background

In this chapter, we describe the development of $\{RuNO\}^6$ nitrosyls derived from strategically chosen ligand frames. The first few ruthenium nitrosyls developed in our lab (such as $[(PaPy_3)Ru(NO)]^{2+}$ discussed in Ch. 2) all contained ligands with carboxamido-N and pyridine-N donor groups. However, we discoved that such $\{RuNO\}^6$ nitrosyls only release NO upon exposure to high energy UV light. We therefore became interested in designing new $\{RuNO\}^6$ nitrosysls derived from ligand frames that contain other donor atoms. Since we had previously shown the importance of the carboxamido-N donor in the photolability of $[(PaPy_3)Ru(NO)]^{2+}$, we decided to employ tetradentate dicarboxamido-N ligand frames with different donor atoms, such as phosphine-P or Phenolato-O donors.

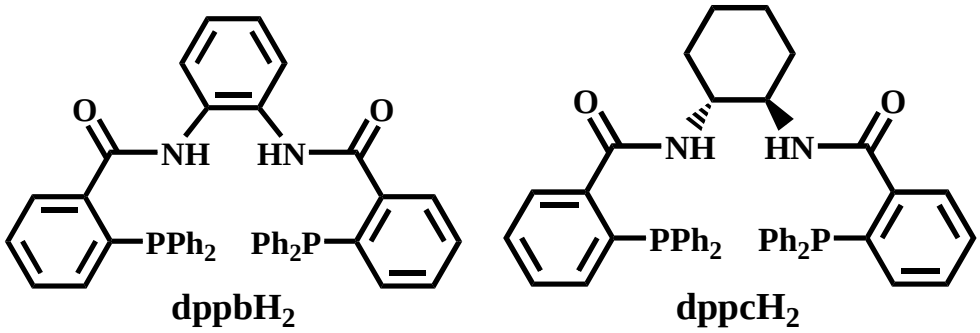

Figure 3.1.1. Tetradentate N_2P_2 ligand frames with carboxamide-N and phosphine-N donors

In the first set, the ligand will contain phosphine-P donors generating N_2P_2 chromophores. We have employed two ligand frameworks with two diphenylphosphine-P donors attached via amide bonds to either side of an *o*-phenylenedicarboxamide ($dppbH_2$, Figure 3.1.1)[2] or a (1*R*,2*R*)-*trans*-1,2-

diaminocyclohexane moiety ($dppcH_2$, Figure 3.1.1).[3] Although the chemistry of the Pd,[3,4] Pt,[3] and Rh[5] complexes of these ligands have been reported, the Ru nitrosyl chemistry of both remains unexplored. In $[(PaPy_3)Ru(NO)]^{2+}$, the deprotonated carboxamido N donors combined with pyridine groups provide extra stability to the Ru(III) center. Thus we were particularly interested in the role of phosphine-P donors in stabilizing either Ru(II) or Ru(III) centers in the resulting complex(es).

3.1.2 Synthesis of Phosphine Containing Ligand Frames

Both ligands frames were synthesized using the same reaction conditions. Starting with one equivalent of either *o*-phenylenedicarboxamide (for $dppbH_2$) or (1*R*,2*R*)-*trans*-1,2-diaminocyclohexane (for $dppcH_2$), dicyclohexylcarbodiimide (DCC) was used as an amide coupling reagent to attach two equivalents of 2-(diphenylphosphanyl)benzoic acid (Figure 3.1.2). Catalytic amounts of 4-(dimethylamino)pyridine (DMAP) were also added as a proton acceptor/donor to aid in the reaction. The order in which the reagents are added together greatly affects the

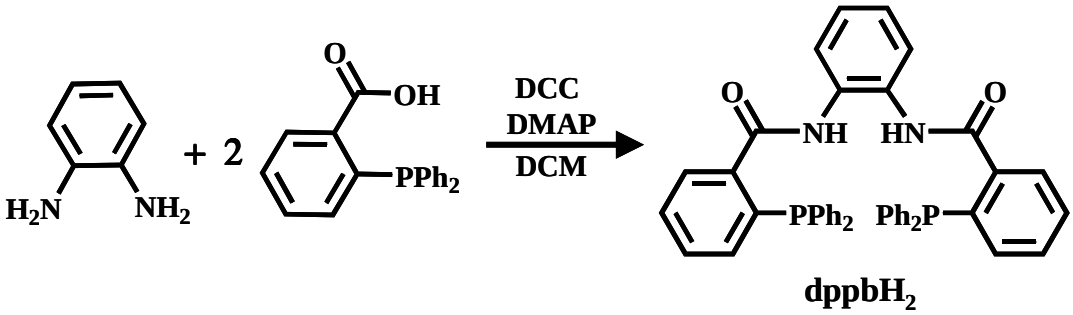

Figure 3.1.2. Reaction scheme of the $dppbH_2$ ligand frame

yield of these reactions. For the best results, the acid was allowed to react with the DCC and DMAP before the amine was added. This method resulted in yields around 65% while the yields reported in first published syntheses of these ligands were roughly 40% when DCC was added last.

3.1.3 Syntheses and X-Ray Structures of Metal Complexes

3.1.3.1 Characterization of [(dppcH_2)Ru(Cl)$_2$]

The metallation of a carboxamide ligand typically requires deprotonation with a base (such as NaH or NEt_3) in suitable solvent (DMF, EtOH, or MeCN) prior to its coordination to the metal centers. In the present case, dppcH_2 was deprotonated with NaH in DMF before the addition of $RuCl_3$. Upon heating, a green solution was generated. When the reaction mixture was allowed to reach refluxing temperature, Ruthenium carbonyl type stretching frequencies at 2060 and 1995 cm^{-1} were observed in the IR spectrum of the resulting reaction mixture. Therefore in later attempts, the reaction mixture was only allowed to reach 80ºC. Addition of NO(g) to the resulting solution caused a color change from dark green to orange and the IR spectrum of the reaction mixture revealed a new NO stretching frequency (ν_{NO}) at 1865 cm^{-1}. Attempts to crystallize this NO bound species resulted in only small orange crystals unsuitable for X-ray diffraction studies. These crystals formed over the course of just a few days and their IR spectrum (Figure 3.1.3) was very similar to that of the original reaction mixture, suggesting the NO bound nitrosyl was still intact. Some of these

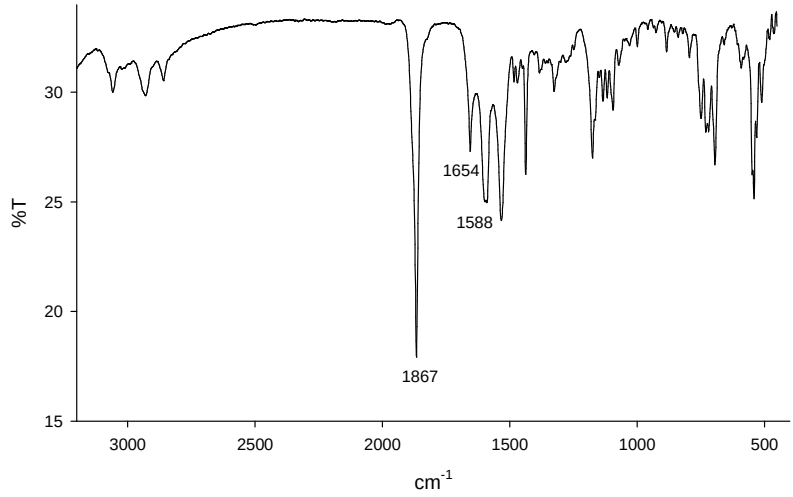

Figure 3.1.3. IR spectrum of small orange crystals of the nitrosyls species obtained from the $RuCl_3$ + $dppc^{2-}$ + NO(g) reaction mixture a few days after reaction (as a KBr pellet)

crystallization vials were stored in the dark over the course of a few weeks to a month and one large X-ray quality orange crystal was obtained. However, the X-ray structure revealed that the crystal was not of the NO bound species, but instead of a dichloro-species namely, $[(dppcH_2)Ru(Cl)_2]$.

The X-ray structure of $[(dppcH_2)Ru(Cl)_2]$ reveals that the $dppcH_2$ ligand frame is bound in the equatorial plane with two chloride atoms bound trans to each other in the axial plane (Figure 3.1.4). The $Ru–N_{(amide)}$ bonds (2.241(5) and 2.256(5) Å) are longer than those observed in the structure of $[(PaPy_3)Ru(NO)]^{2+}$ (1.901(2) Å) where the carboxamide-N donor in deprotonated.[6] This suggests that both carboxamide-N donor centers are protonated in $[(dppcH_2)Ru(Cl)_2]$. This idea is further supported by the tetrahedral geometry of the carboxamide-N donor centers. This is interesting considering the fact that the ligand was deprotonated prior to

reaction with the metal salt. In addition, no counter ion is observed in the structure pointing to an overall neutral charge of this complex. Thus the Ru(III) center must been reduced to Ru(II) in the resulting compound. It seems as though this compound is a decomposition product of the original nitrosyl compound identified as the main product by IR. Given the low stability of this nitrosyl compound and its lack of improved visible light absorption (orange color), we did not purse this species further.

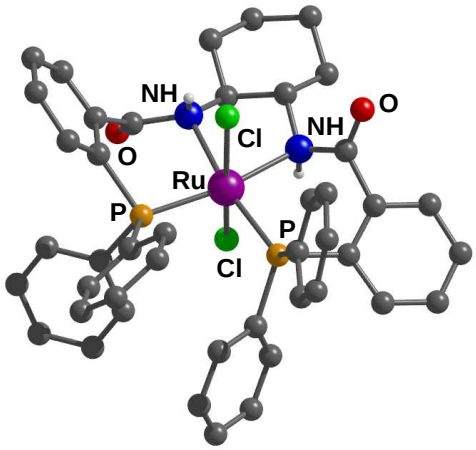

Figure 3.1.4. X-ray crystal structure of [(dppcH_2)Ru($Cl)_2$] with H atoms omitted (except for $N_{amido}H$) for the sake of clarity

3.1.3.2 Characterization of [(dppQ)Ru($Cl)_2$]

Reaction of the deprotonated ligand $dppb^{2-}$ (using NaH) with $RuCl_3$ in DMF generates a dark red solution upon heating (Figure 3.1.5). Subsequent cooling causes precipitation of a dark red solid from DMF. The structure and properties of this complex (vide infra) indicate that its formation is not just a simple complexation

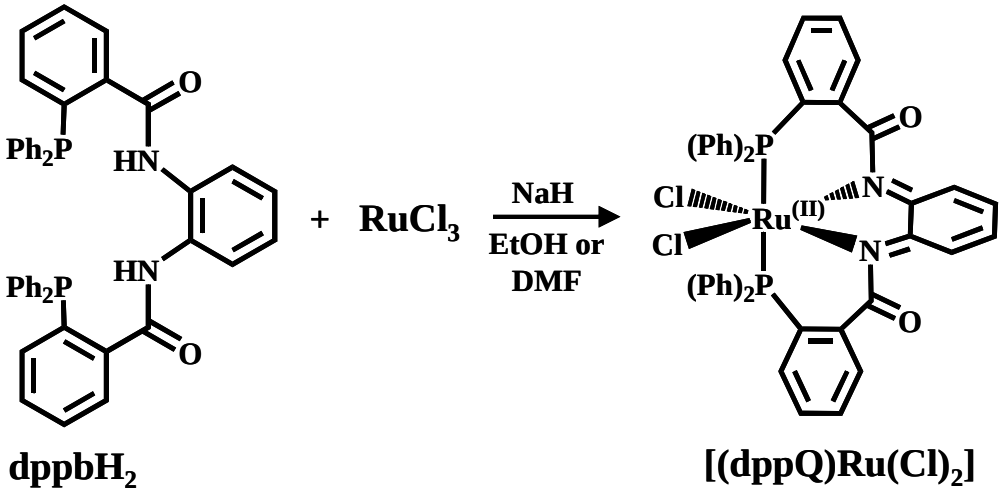

Figure 3.1.5. Reaction scheme of [(dppQ)Ru(Cl)$_2$]

reaction, rather an unexpected redox reaction takes place when dppbH$_2$ reacts with RuCl$_3$. As shown below, the Ru(III) center appears to be reduced to Ru(II) in the final product with concomitant oxidation of the *o*-phenylenediamine (opda) portion of the ligand to *o*-benzoquinonediimine (bqdi) moiety. As a result, instead of a dppb^{2-} ligand bound to Ru(III) center (as desired), one obtains a Ru(II) complex [(dppQ)Ru(Cl)$_2$] in which the opda moiety of dppb^{2-} is modified to a quinonoid (Q)-type ligand dppQ and coordinated to the Ru(II) center via two imine N and two phosphine P atoms.

When the above reaction is preformed in the absence of oxygen, there is a moderate yield of [(dppQ)Ru(Cl)$_2$], suggesting a metal-ligand coupled redox mechanism is most possibly responsible for the formation of [(dppQ)Ru(Cl)$_2$]. Indeed, when the reaction is carried out in the presence of air, the yield of [(dppQ)Ru(Cl)$_2$] increases significantly. This increase suggests that oxygen

facilitates the 2 electron oxidation of the bound ligand. Oxidation of bound opda ligands coordinated to Fe(II) or Ru(II) metal centers forming such complexes as $[Fe(bqdi)_3]^{2+}$ and $[Ru(bpy)_2(bqdi)]^{2+}$ has been reported previously.[7,8] Additionally, opda ligands have been shown to react with Ru(III) in the presence of air forming several Ru(II) bqdi complexes where the metal center and oxygen are thought to be involved in the redox reaction.[9,10]

Interestingly, the tetradentate ligand frame in $[(dppQ)Ru(Cl)_2]$ is not bound in a planar fashion (Figure 3.1.6). The X-ray structure of $[(dppQ)Ru(Cl)_2]$ reveals that the bulky diphenylphosphine ends of the ligand frame are coordinated trans to one another in the axial positions while the two imine Ns of the bqdi moiety occupy equatorial positions. The cyclohexane group in $[(dppcH_2)Ru(Cl)_2]$ projects the carboamide groups in opposite directions providing more room for the diphenyl-

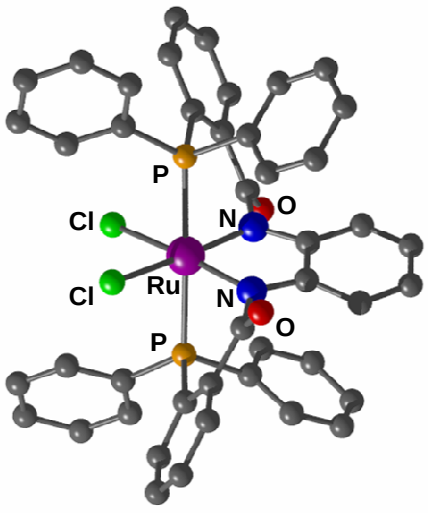

Figure 3.1.6. X-ray crystal structure of $[(dppQ)Ru(Cl)_2]$ with H atoms omitted for the sake of clarity

phosphine groups to bind in a cis configuration. However in the bqdi group of [(dppQ)Ru(Cl)$_2$], the imine groups are in a planar arrangement forcing the diphenylphosphine groups to bind in a trans configuration. Thus, the two Cl^- donors are coordinated in the equatorial plane, *cis* to one another. Close examination of the bond lengths of the bqdi ring in [(dppQ)Ru(Cl)$_2$] (Figure 3.1.7) reveals that the C(3)-C(4) and C(5)-C(6) distances are shorter (1.336(7) and 1.353(7) Å respectively) compared to the rest of C-C distances of the ring (all in the range of 1.408(7) to 1.439(7) Å). This distance distribution in addition to two imine double bonds (N(1)-C(2) = 1.361(7) Å and N(2)-C(7) = 1.357(6) Å) indicates a quinonoid form of the ligated bqdi moiety.

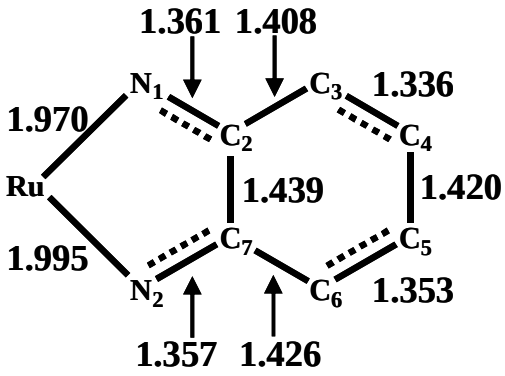

Figure 3.1.7. Bond distances (Å) within the bqdi portion of the ligand in [(dppQ)Ru(Cl)$_2$]

3.1.3.3 Characterization of [(NO_2dppQ)Ru(Cl)$_2$]

Although Ru(II) precursors generally require nitrite salts and acids to afford {Ru-NO}^{6} nitrosyls,[11-13] there was one report on the formation of a {Ru-NO}^{6} nitrosyl from a Ru(II) starting complex *cis*-[$RuCl_2$(dcype)(bpy)] (dcype = 1,2-

bis(dicyclohexylphosphino)ethane) via direct reaction with NO(g) in dichloromethane.[14] Interestingly, in the present case, passage of NO(g) through a solution of [(dppQ)Ru(Cl)$_2$] in DMF (previously deoxygenated) at room or elevated (90 ^{o}C) temperature does not afford any metal nitrosyl. Instead, the bqdi moiety of the ligand undergoes a nitration reaction, forming the ring-substituted product [(NO$_2$dppQ)Ru(Cl)$_2$] (Figure 3.1.8). The X-ray structure of [(NO$_2$dppQ)Ru(Cl)$_2$] (Figure 3.1.9) reveals that nitration of the bqdi ring does not alter the metric parameters of the bqdi moiety. Thus, the quinonoid moiety remains intact upon substitution of the

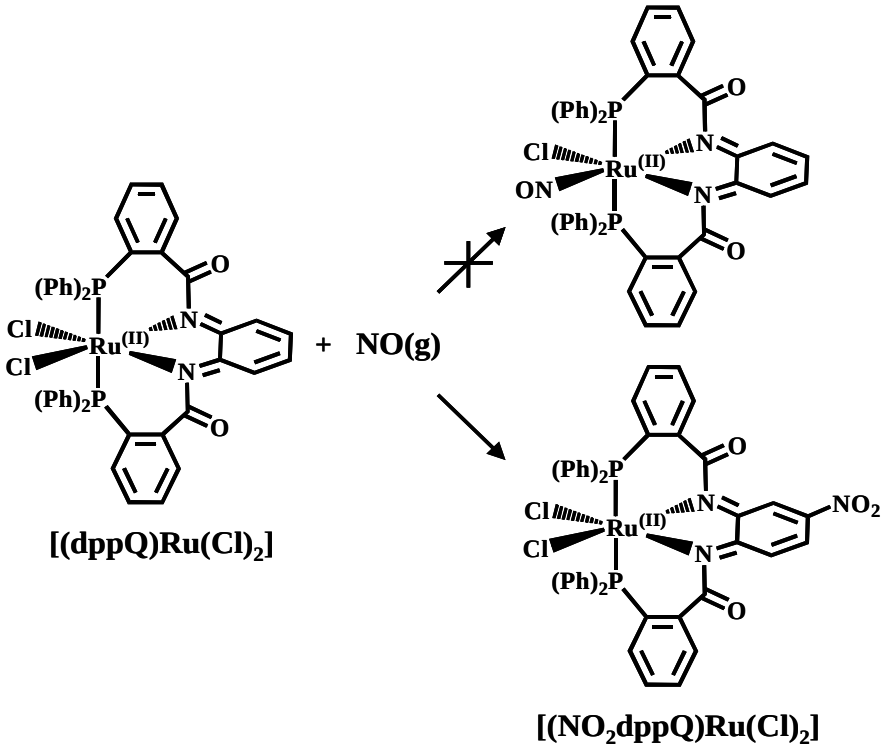

Figure 3.1.8. Reactivity of [(dppQ)Ru(Cl)$_2$] with NO(g)

ring. The Ru-N_{imine} bond lengths also show no significant changes upon nitration of the ring. However the IR spectrum of [$(NO_2dppQ)Ru(Cl)_2$] exhibits two distinct ν_{CO} bands while that of [$(dppQ)Ru(Cl)_2$] only has one. The two stretching frequencies presumably arise from the breakdown of ligand symmetry upon addition of the NO_2 group on the bqdi moiety. A strong band at 1334 cm^{-1} also confirms the presence of the NO_2 group in [$(NO_2dppQ)Ru(Cl)_2$].

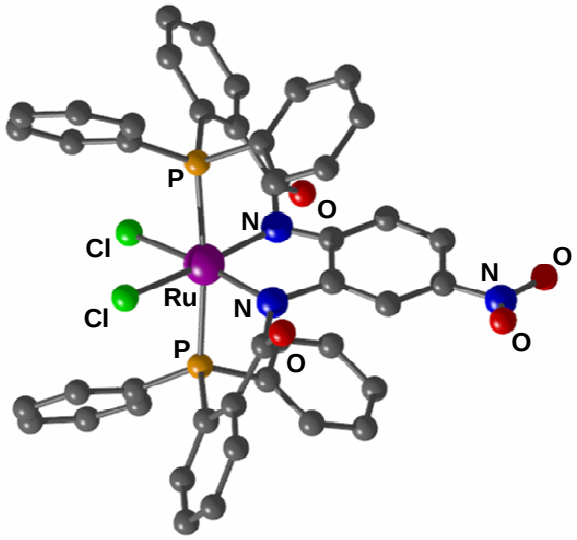

Figure 3.1.9. X-ray crystal structure of [$(NO_2dppQ)Ru(Cl)_2$] with H atoms omitted for the sake of clarity

We have previously reported that when a solution of the {Fe-NO}^{6} nitrosyl [$(bpb)Fe(NO)(NO_2)$] in DMF was exposed to air, a similar ring-nitrated product [$(NO_2bpb)Fe(NO_3)(DMF)$] was obtained.[15] In addition, Ford and co-workers have convincingly demonstrated that Ru(II) porphyrins disproportionate NO to NO_2, N_2O_3, and other reactive nitrogen oxide species capable of ligand modification.[16] Since the

present ring-nitrated species [$(NO_2$dppQ)Ru$(Cl)_2$] is obtained in the absence of air, we believe the nitration of the bqdi moiety of [(dppQ)Ru$(Cl)_2$] is facilitated by NO disproportionation.

3.1.4 Redox Properties

It is well known that phenylenediamine moiety can access multiple redox states when coordinated to a metal center.[7-10] As shown below, phenylenediamine can exist in its fully reduced $(opda)^{2-}$, semiquinone $(sqdi)^{-}$, or fully oxidized (bqdi) forms (Figure 3.1.10). For this reason, metal complexes derived from phenylenediamine ligands are known to exhibit rich redox chemistry. Since the presence of a redox active Ru center can also give rise to reversible redox processes,

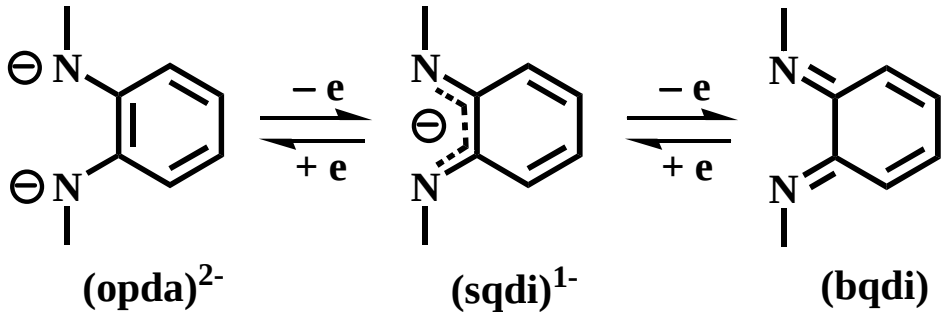

Figure 3.1.10. The various oxidation states of the *o*-phenylenediamine moiety

we have investigated the redox behavior of [(dppQ)Ru$(Cl)_2$]. In DMF, [(dppQ)Ru$(Cl)_2$] exhibits a reversible process **A** at a relatively high positive potential with $E_{1/2}$ = +0.90 V (vs aq. SCE, Figure 3.1.11). For a related bqdi complex namely,

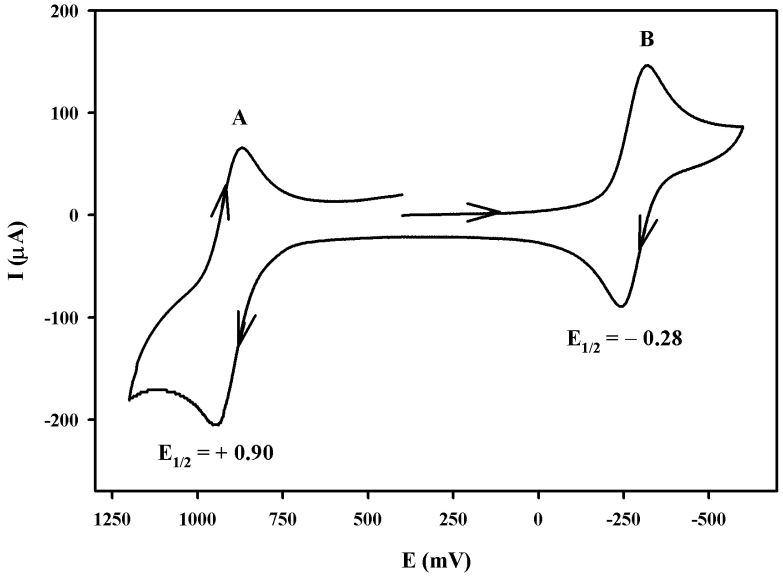

Figure 3.1.11. Cyclic voltammogram of $[(dppQ)Ru(Cl)_2]$ in DMF (0.10 M NEt_4ClO_4, scan rate = 50mV/s). Halfwave potentials ($E_{1/2}$) values are indicated vs aqueous SCE.

$[Ru(bpy)_2(bqdi)](PF_6)_2$, a similar redox process with $E_{1/2}$ = +1.35 V (vs aq. SCE) has been assigned to Ru(II)/Ru(III) couple by Lever and coworkers.[8d] We believe that the process **A** is also related to the Ru(II)/Ru(III) couple of $[(dppQ)Ru(Cl)_2]$. The lowered $E_{1/2}$ value of $[(dppQ)Ru(Cl)_2]$ presumably arises from the presence of coordinated Cl^- ligands in $[(dppQ)Ru(Cl)_2]$. Indeed, a complex containing a similar $N_2P_2Cl_2$ donor set, $Ru(PPh_3)_2(papm)Cl_2$ (papm = 2(phenylazo)pyrimide), has a Ru(II)/Ru(III) redox couple with $E_{1/2}$ = +0.897 V.[17] The other reversible process **B**, observed in the cyclic voltammogram of $[(dppQ)Ru(Cl)_2]$ with $E_{1/2}$ = –0.28 V (vs aq. SCE), is related to the bqdi/sqdi couple. A similar redox process with $E_{1/2}$ = –0.47 V (vs aq. SCE) has been noted for $[Ru(bpy)_2(bqdi)](PF_6)_2$.[8d] Both redox processes **A**

and **B** of Figure 3.1.11 are reversible and can be cycled several times without any loss of current heights. There is an additional irreversible reduction process at much more negative potential (E_p = –0.90 V; Figure S5, Supporting Information) which we assign to further reduction of sqdi to opda moiety.

The reaction of NO(g) with [(dppQ)Ru(Cl)$_2$] provides further evidence in favor of the presence of Ru(II) in [(dppQ)Ru(Cl)$_2$]. Close examination of literature reveals that NO(g) readily reacts with Ru(III) metal centers to form {Ru-NO}^{6} nitrosyls.[18] In contrast, very few Ru(II) species react with NO(g). In the present work, the reaction of [(dppQ)Ru(Cl)$_2$] with NO(g) has been closely monitored under several different reaction conditions. Addition of various amounts of NO(g) to solutions of [(dppQ)Ru(Cl)$_2$] in DMF at ambient *or* elevated temperatures (25-90 ^{o}C), under light *or* dark conditions did not produce any material that exhibits a ν_{NO} stretching band in the 1750-1950 cm^{-1} range of the IR spectrum.[18] Even when [(dppQ)Ru(Cl)$_2$] is treated with $AgBF_4$ (in order to remove a bound Cl^-) before the addition of NO(g), no IR band due to ν_{NO} is observed. If the metal center in [(dppQ)Ru(Cl)$_2$] were effectively Ru(III), one would expect to observe the formation of a {Ru-NO}^{6} nitrosyl. Instead, the reaction of [(dppQ)Ru(Cl)$_2$] with NO(g) affords [(NO_2dppQ)Ru(Cl)$_2$] in which the bqdi portion of the ligand is nitrated.

3.1.5 Conclusion

Collectively, the chemistry discussed above indicates that the combination of

carboxamide-N and phosphine-P donors in $dppcH_2$ and $dppbH_2$ leads to metal center reduction reactions and isolation of the Ru(II) complexes, [($dppcH_2$)Ru($Cl)_2$] and [(dppQ)Ru($Cl)_2$], in which the carboxamide-N atoms act as neutral donors. Since phosphine ligands provide stability to lower valent metal centers such as Ru(II), the presence of such donors facilitates reduction of the metal center with concomitant oxidation of the carboxamide-N atoms of the ligand frame. This results in protonation of the carboxamido-N in [($dppcH_2$)Ru($Cl)_2$] and formation of the bqdi moiety in [(dppQ)Ru($Cl)_2$]. Since bqdi is a good π-acceptor, it further stabilizes the reduced product, thus driving the reaction forward. In contrast, the redox chemistry observed with the cyclohexane containing ligand frame is less favored, taking several days to occur. This reactivity is notable since such redox activity is *not observed* with other analogous ligands bearing the opda moiety. For example, ligands like $bpbH_2$ (N_4),[21] H_4L (N_2O_2),[20,21] or $PhPepSH_4$ (N_2S_2)[22] readily bind various metal centers (Ru, Fe, Ni) without any redox activity. These findings clearly show that the identity of the donor atoms (N, P, O, S) dictates the redox status of the metal centers in complexes derived from such tetradentate ligands.

Initially, an orange NO bound species was obtained from the reaction of $RuCl_3$, $dppc^{2-}$, and NO(g). However, its lack of any significant absorption of low energy visible light absorption led us to abandon any further attempts to characterize this nitrosyl. However, given the strong visible light absorption bands of [(dppQ)Ru($Cl)_2$] in the 500-600 nm region, we were interested to see if we could generated an NO bound species that might release NO upon exposure to visible light.

Unfortunately, reaction of NO(g) with [(dppQ)Ru(Cl)$_2$] does not lead to formation of the metal nitrosyl; instead, the bqdi ring is nitrated and one obtains [(NO_2dppQ)Ru(Cl)$_2$] as the sole product. Collectively, the results indicate that the combination of carboxamide unit with phosphine donors does not afford in {RuNO}^{6} nitrosyls that can release NO upon exposure to low energy visible light.

3.1.6 Experimental Section

3.1.6.1 Syntheses of Compounds

Materials. NO gas was purchased from Spectra Gases Inc. and was purified by passing through a long KOH column prior to use. $RuCl_3$•xH_2O (Aldrich Chemical Co.) was treated several times with concentrated HCl to prepare the starting metal salt, $RuCl_3$•$3H_2O$. The solvents were dried by standard techniques and distilled. All other chemicals were purchased from Aldrich Chemical Co. and used without further purification.

Synthesis of dppcH_2. A batch of 0.500 g (1.63 mmol) of 2-(diphenylphosphino)benzoic acid along with 0.352 g (1.708 mmol) of *N*,*N*-dicyclohexylcarbodiimide (DCC) and 0.010 g (0.082 mmol) of 4-(dimethylamino) pyridine (DMAP) was dissolved in 15 mL of dichloromethane. Next, a solution of 0.088 g (0.771 mmol) of *R*,*R*-trans diaminocyclohexane in 5 mL of dichloromethane was slowly added to it. The turbid solution thus obtained was stirred at room temperature for 6 h. The light yellow solution was then filtered through a Celite pad and the filtrate was dried. The resulting yellow solid was stirred in 30 mL of ethyl

acetate for 1 h to remove any impurity. The white product was finally collected by filtration and washed several times with ethanol to remove any remaining urea and dried in vacuo. Yield: 0.36 g (68%). Selected IR frequencies (KBr disk, cm^{-1}): 3280 (w, ν_{NH}), 3292 (w, ν_{NH}), 2928 (w), 1637 (vs, ν_{CO}), 1528 (m), 1434 (w), 1226 (w), 1091 (w), 751 (m), 699 (m), 505 (w).

Synthesis of dppbH$_2$. A batch of 0.500 g (1.63 mmol) of 2-(diphenylphosphino)benzoic acid along with 0.352 g (1.708 mmol) of *N*,*N*-dicyclohexylcarbodiimide (DCC) and 0.010 g (0.082 mmol) of 4-(dimethylamino) pyridine (DMAP) was dissolved in 15 mL of dichloromethane. Next, a solution of 0.084 g (0.778 mmol) of *o*-phenylenediamine in 5 mL of dichloromethane was slowly added to it. The turbid solution thus obtained was stirred at room temperature for 6 h. The light yellow solution was then filtered through a Celite pad and the filtrate was dried. The resulting yellow solid was stirred in 30 mL of ethyl acetate for 1 h to remove any impurity. The white product was finally collected by filtration and washed several times with ethanol to remove any remaining urea and dried in vacuo. Yield: 0.36 g (68%). Selected IR frequencies (KBr disk, cm^{-1}): 3320 (w, ν_{NH}), 3051(w), 2927 (w), 1640 (vs, ν_{CO}), 1592 (m), 1524 (vs), 1512 (vs), 1486 (s), 1433 (s), 1314 (m), 1089 (w), 744 (vs), 695 (vs), 500 (w). ^{1}H NMR in $CDCl_3$, δ from TMS: 8.45 (s 2H), 7.75 (dd 2H), 7.39-7.17 (m 26H), 7.2-7.11(dd 2H), 7.00-6.98 (dd 2H).

Synthesis of [(dppQ)Ru(Cl)$_2$]. Method A. A batch of 100 mg (0.146 mmol) of dppbH$_2$ was dissolved in 20 mL of DMF and deprotonated with 2.2 equiv of NaH (8 mg, 0.321 mmol). A solution of 38 mg of $RuCl_3 \cdot 3H_2O$ (0.146 mmol) in 5 mL of

DMF was then added to it when the color turned to green. The reaction mixture was then heated at 100 °C for 2 h. Next, the dark reddish purple mixture was concentrated to 15 mL and stored at 0°C for 12 h. The dark red solid thus obtained was collected by filtration, washed with 2 x 5 mL of diethyl ether and dried in vacuo. Yield: 30 mg (24%). Vapor diffusion of pentane into a solution of this solid dissolved in chloroform afforded dark red crystalline plates, suitable for X-ray studies. Selected IR frequencies (KBr disk, cm^{-1}): 3050 (w), 1691(vs, ν_{CO}), 1582 (w), 1521 (w), 1481 (w), 1434 (s), 1261 (s), 1217 (vs), 1151 (w), 1128 (m), 1095 (s), 1017 (s), 880 (m), 868 (m), 747 (s), 694 (s), 520 (s). Electronic absorption spectrum in $CHCl_3$, λ_{max} in nm (ε in M^{-1} cm^{-1}): 260 (39 000), 460 (8 700), 530 (5 000). ^1H NMR in $CDCl_3$, δ from TMS: 8.76 (d 2H), 7.74 (q 4H), 7.70 (t 2H), 7.5 (t 2H), 7.42 (t 2H), 7.33 (t 4H), 7.04 (t 4H), 6.96 (t 4H), 6.81 (m 2H), 6.59 (m 2H), 6.53 (q 4H). ESI-MS: m/z 855 (M^+), 819 ($M - Cl^+$).

Method B. A batch of 38 mg (0.146 mmol) of $RuCl_3 \bullet 3H_2O$ was dissolved in 5 mL of EtOH and the orange-red solution was heated to reflux for 3 h. The resulting dark green solution was then added to a slurry of 100 mg (0.146 mmol) of $dppbH_2$ in 5 mL of EtOH containing 0.1 mL of Et_3N. A slow stream of air was bubbled directly through this mixture while heating it to reflux temperature. A dark red-brown precipitate was noted within 3 h. The solution was cooled and the precipitate was collected by filtration. Next, the crude product was extracted into chloroform (20 mL). Diffusion of pentane into this chloroform solution afforded 80 mg (65% yield) of $[(dppQ)Ru(Cl)_2]$.

Synthesis of [(NO_2dppQ)Ru($Cl)_2$]. A slurry of 25 mg (0.037 mmol) of [(dppQ)Ru($Cl)_2$] in 10 ml of DMF was thoroughly degassed and then heated to 100°C to obtain a dark red solution. A slow stream of purified NO gas was passed through this hot solution for 1 h when the color of the solution changed to orange red. The solvent was removed to isolate a dark orange-red solid (yield: 89%). Diffusion of pentane into a solution of this solid in $CHCl_3$ afforded red block crystals of [(NO_2dppQ)Ru($Cl)_2$]. Selected IR frequencies (KBr disk, cm^{-1}): 2924 (w), 1682 (m, ν_{CO}), 1665 (m, ν_{CO}), 1580 (w), 1508 (m), 1435 (m), 1334 (s, ν_{NO2}), 1278 (m), 1261 (m), 1218 (vs), 1128 (w), 1095 (m), 1015 (m), 742 (vs), 695 (vs), 527 (m), 513 (m). Electronic absorption spectrum in $CHCl_3$, λ_{max} in nm (ε in M^{-1} cm^{-1}): 260 (34 000), 365 (8 000), 450 (8 000), 485 (9500). ^{1}H NMR in $CDCl_3$, δ from TMS: 8.84 (d 1H), 8.81 (d 1H), 7.78 (t 1H), 7,76 (t 1H), 7.64 (m 4H), 7.56 (s 1H), 7.55 (d 1H), 7.53 (d 1H), 7.45 (t 2H), 7.31 (t 4H), 7.21 (d 1H), 7.07-6.96 (m 8H), 6.86 (d 1 H), 6.49 (d 2H), 6.45 (d 2H). ESI-MS: m/z 900 (M^+), 864 ($M - Cl^+$).

3.1.6.2 Experimental Data: ^{1}H-NMR and IR Spectra

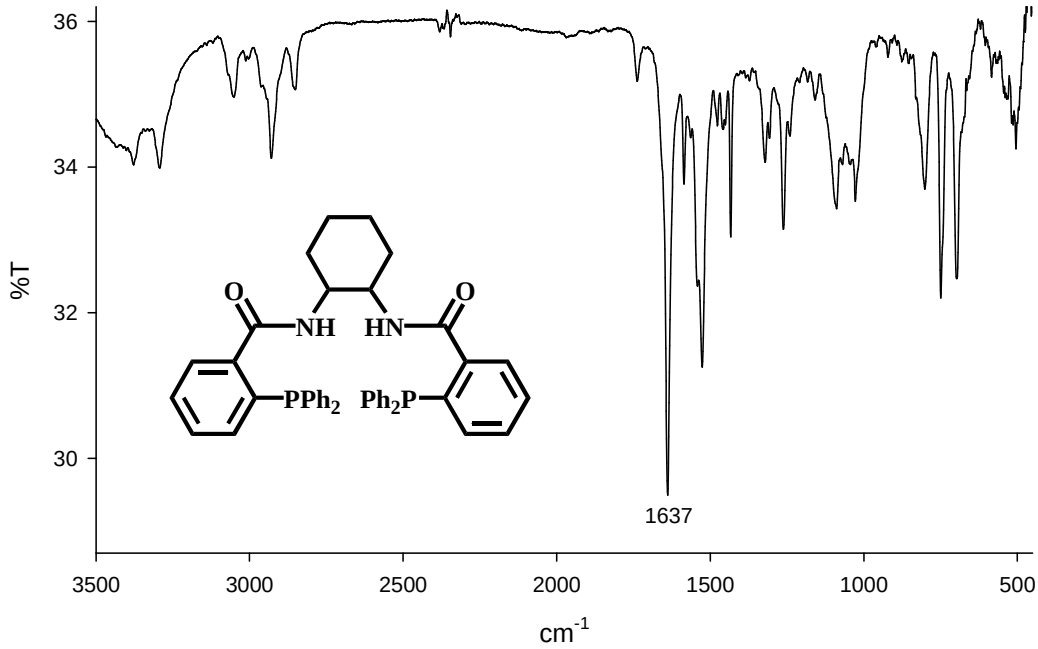

Figure 3.1.12. IR spectrum of $dppcH_2$ in KBr pellet

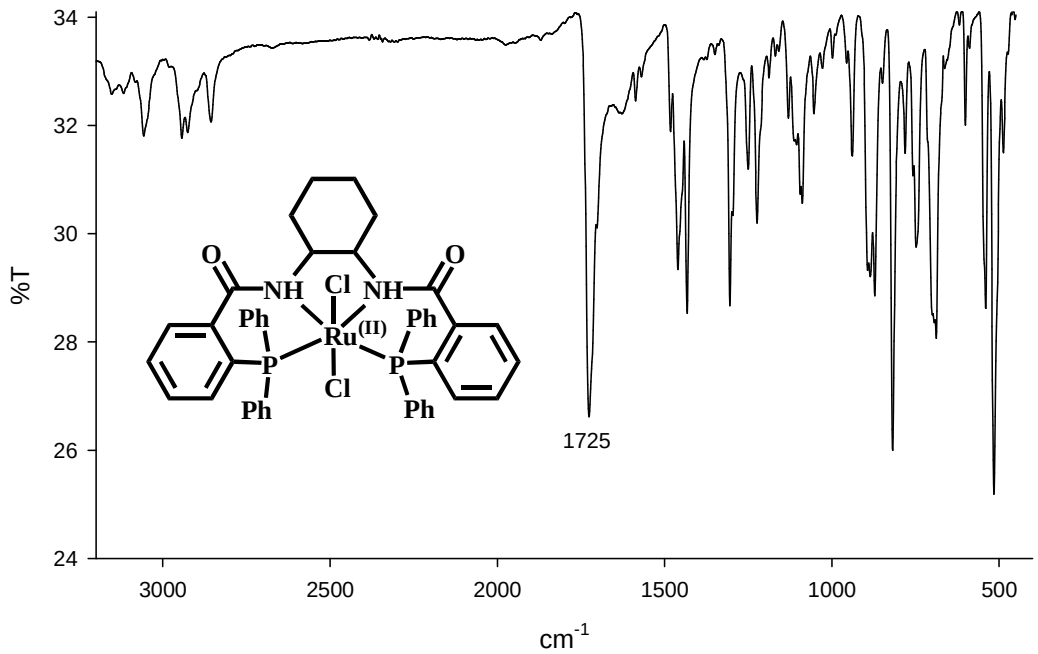

Figure 3.1.13. IR spectrum of $[(dppcH_2)Ru(Cl)_2]$ in KBr pellet

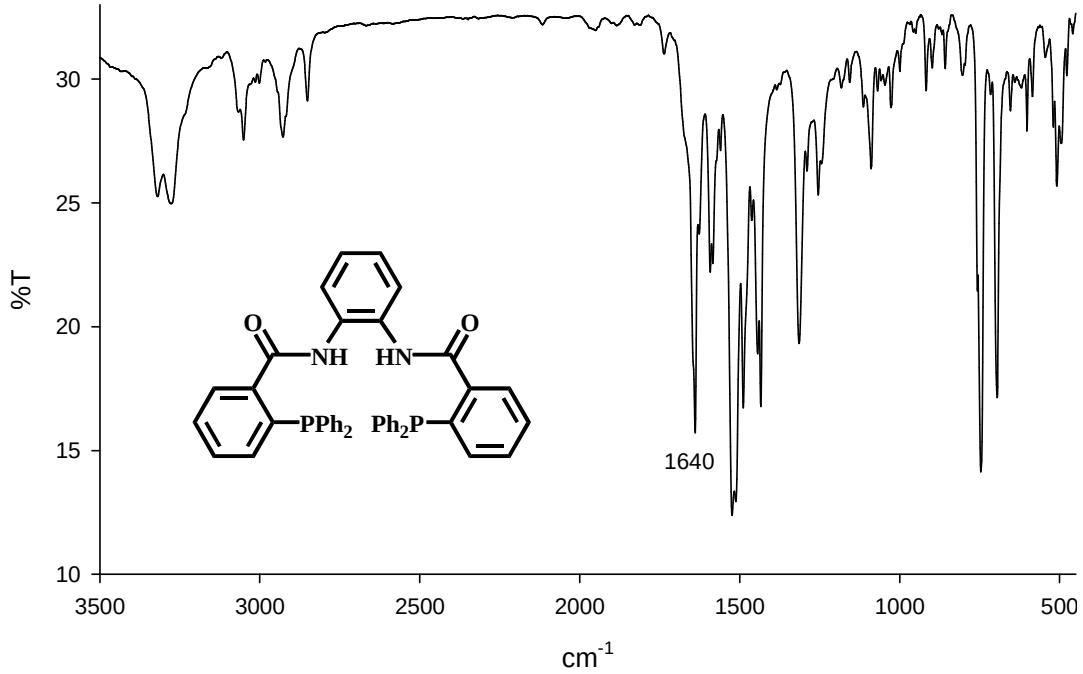

Figure 3.1.14. IR spectrum of $dppbH_2$ in KBr pellet

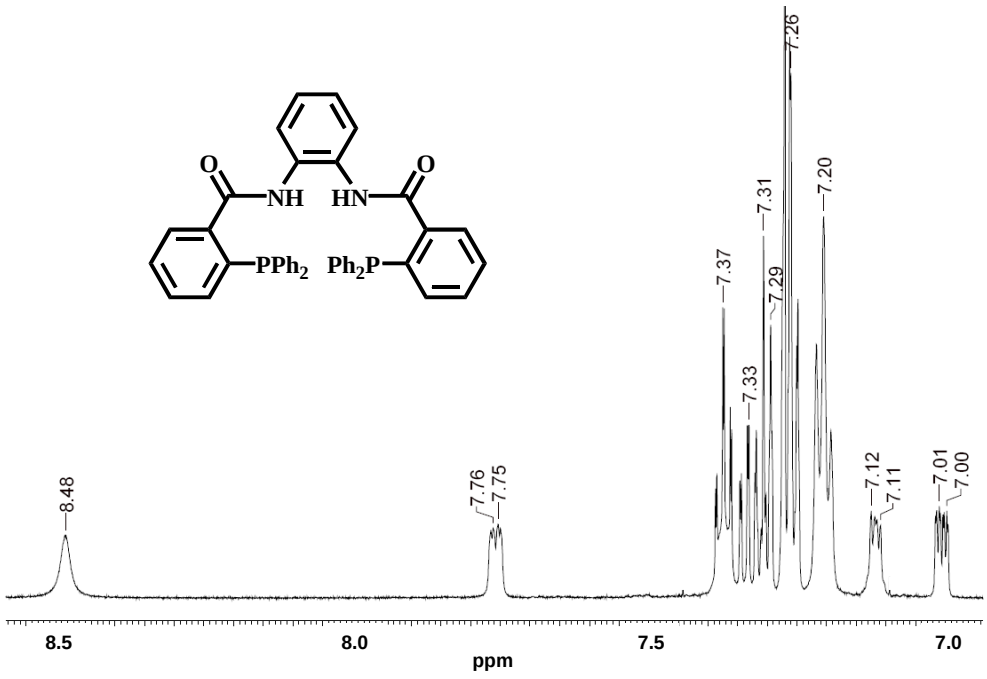

Figure 3.1.15. ^{1}H-NMR spectrum (6.9-8.5 ppm) of $dppbH_2$ in $CDCl_3$ at 298 K

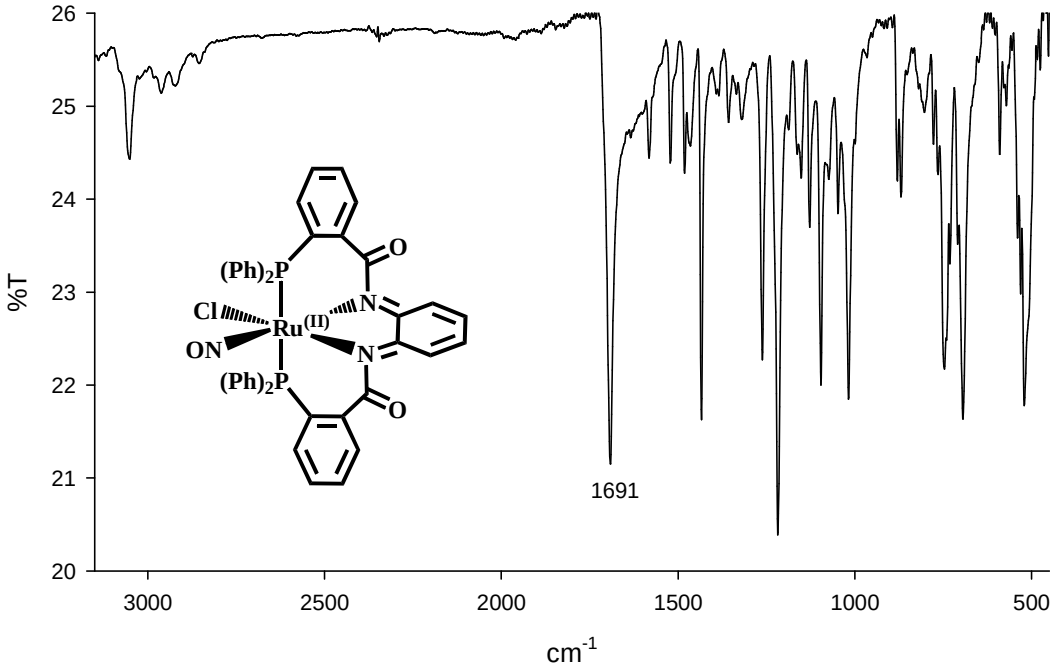

Figure 3.1.16. IR spectrum of [(dppQ)Ru(Cl)$_2$] in KBr pellet

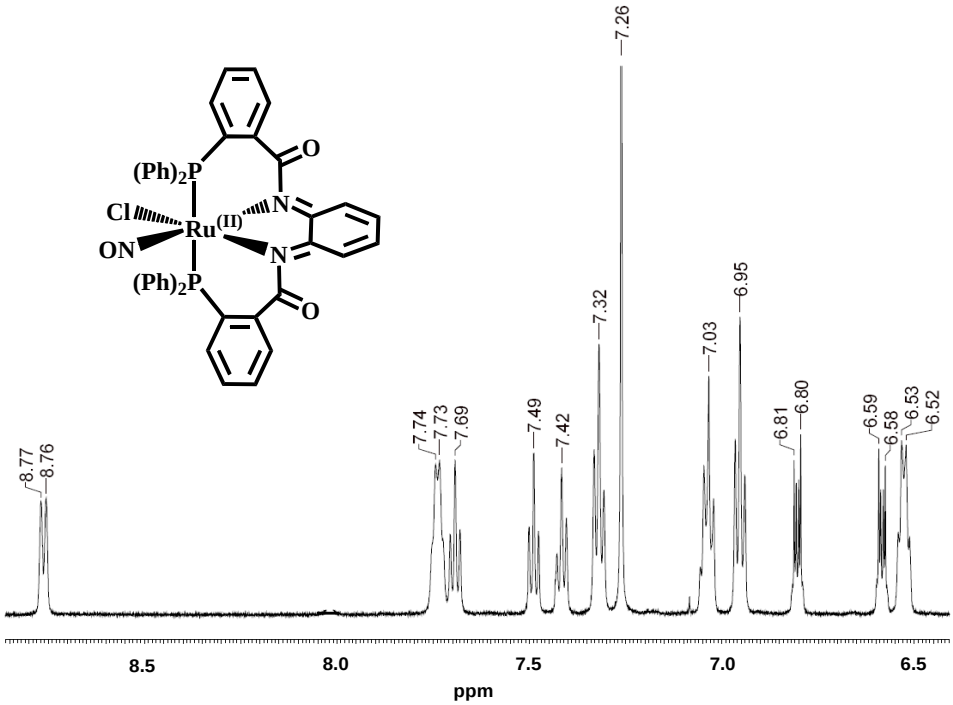

Figure 3.1.17. ^{1}H-NMR spectrum (6.9-8.5 ppm) of [(dppQ)Ru(Cl)$_2$] in $CDCl_3$ at 298 K

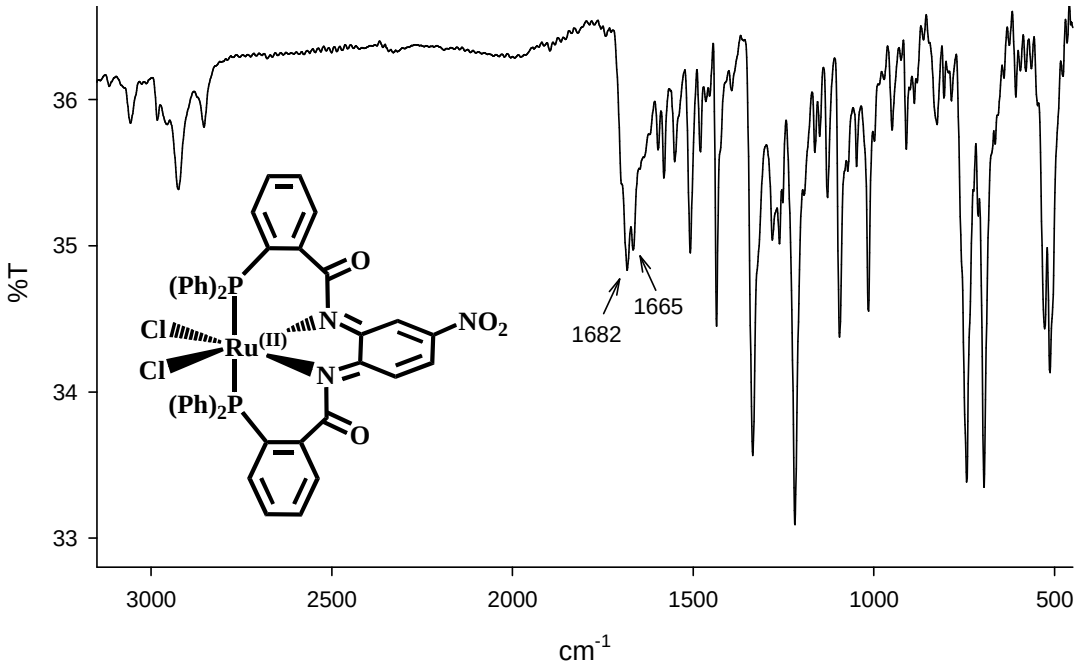

Figure 3.1.18. IR spectrum of $[(NO_2dppQ)Ru(Cl)_2]$ in KBr pellet

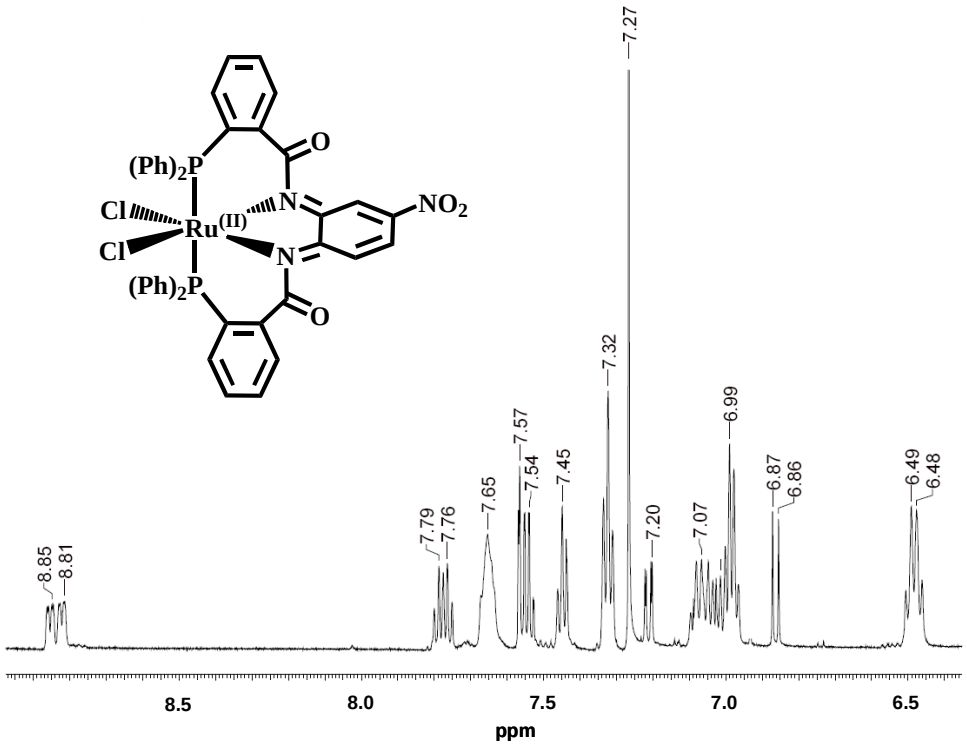

Figure 3.1.19. ^{1}H-NMR spectrum (6.4-9.0 ppm) of $[(NO_2dppQ)Ru(Cl)_2]$ in $CDCl_3$ at 298 K

3.1.7 References

1. Rose, M. J.; Olmstead, M. M.; Mascharak, P. K. *Polyhedron* **2007**, *26*, 4713.

2. Trost, B. M.; Van Vranken D. L.; Binge C. *J . Am. Chem. Soc.* **1992**, *114*, 9327.

3. Burger, S.; Therrien, B.; Süss-Fink, G. *Eur. J. Inorg. Chem.* **2003**, *17*, 3099-3103.

4. Chahen, L.; Karmazin-Brelot, L.; Süss-Fink, G. *Inorg. Chem. Comm*. **2006**, *9*, 1151.

5. Burger, S.; Therrien, B.; Süss-Fink, G. *Helv. Chim. Acta*. **2005**, *88*, 478.

6. Patra, A. K.; Olmstead, M. M; Mascharak, P. K. *Inorg. Chem.* **2003**, *42*, 7363.

7. Warren, L. F. *Inorg. Chem.* **1977**, *16*, 2814.

8. (a) Rusanova, J.; Rusanov, E.; Gorelsky, S. I.; Christendat, D.; Popescu, R.; Farah, A. A.; Beaulac, R.; Reber, C.; Lever, A. B. P. *Inorg. Chem.* **2006**, *45*, 6246. (b) Metcalfe, R. A.; Lever, A. B. P. *Inorg. Chem.* **1997**. *36*, 4762. (c) Masui, H.; Lever, A. B. P.; Dodsworth, E. S. *Inorg. Chem.* **1993**,*32*, 258. (d) Masui, H.; Lever, A. B. P.; Auburn, P. R. *Inorg. Chem.* **1991**. *30*, 2402.

9. (a) Milliken, B.; Borer, L.; Russell, J.; Bilich, M.; Olmstead, M. M. *Inorg. Chim. Acta.* **2003**, 348, 212. (b) Maji, S.; Patra, S.; Chakraborty, S.; Janardanan, D.; Mobin, S. M.; Sunoj, R. B.; Lahiri, G. K. *Eur. J. Inorg. Chem.* **2007**, 314. (c) Cheng, H.; Peng, S. *Inorg. Chim. Acta*. **1990**, *169*, 23.

10. (a) Jüstel, T.; Bendix, J.; Metzler-Nolte, N.; Weyhermüller, W.; Nuber, B.;

Wieghardt, K. *Inorg. Chem.* **1998**, *37*, 35. (b) Mitra, K. N.; Majumdar, P.; Peng, S.; Castinẽiras, A.; Goswami, S. *Chem. Commum.* **1997**, 1267.

11. Rose, M. J.; Patra, A. K.; Alcid, E. A.; Olmstead, M. M.; Mascharak, P. K. *Inorg. Chem.* **2007**. *46*, 2328.

12. (a) Gomes, M. G.; Davanzo, C. U.; Silva, S. C.; Lopes, L. G. F.; Santos, P. S.; Franco, D. W. *J. Chem. Soc., Dalton Trans*. **1998**, 601. (b) Pipes, D. W.; Meyer, T. J. *Inorg. Chem*. **1984**, *23*, 2466. (c) Callahan, R. W.; Meyer, T. J. *Inorg. Chem*. **1977**, *16*, 574.

13. (a) Sauaia, M. G.; da Silva, R. S. *Trans. Met. Chem*. **2003**, *28*, 254. (b) Nagao, H.; Ooyama, D.; Hirano, T.; Naoi, H.; Shimada, M.; Sasaki, S.; Nagao, N.; Mukaida, M.; Oi, T. *Inorg. Chim. Acta* **2001**, *320*, 60.

14. Von Poelhsitz, G.; Bogado, A. L.; de Souza, G. D.; Rodrigues-Filho, E.; Batista, A. A.; de Araujo, M. P. *Inorg. Chem. Commun*. **2007**, *10*, 133.

15. Patra, A. K; Rose, M. J.; Olmsted, M. M.; Mascharak, P. K. *J. Am. Chem. Soc.* **2004**, *126***,** 4780.

16. Lorković, I. M.; Ford, P. C. *Inorg. Chem.* **1999**, *38*, 1467.

17. Santra, P. K.; Sinha, C.; Sheen, W.; Liao, F.; Lu, T. *Polyhedron* **2001,** *20*, 599.

18. Rose, M. J.; Mascharak, P. K. *Coord. Chem. Rev.* **2008**, *252*. 2093.

19. Patra, A. K.; Rose, M. J.; Murphy, K. M.; Olmstead, M. M.; Mascharak, P. K. *Inorg. Chem.* **2004**, *43*, 4487.

20. (a) Patra A. K.; Ray, M.; Mukherjee, R. *Inorg. Chem* **2000**, *39*, 652. (b) Mukherjee, R. N.; Ray, M. *Polyhedron*, **1992**, *11*, 2929.

21. Stephens, F. S.; Vagg, R. S. *Inorg. Chim. Acta.* **1986**, *120*, 165.

22. (a) Harrop, T. C.; Olmstead, M. M.; Mascharak, P. K. *Inorg. Chem.* **2006**, *43*, 3424. (b) Harrop, T. C.; Olmstead, M. M.; Mascharak, P. K. *Inorg. Chem.* **2005**, *44*, 6918.

Chapter 3, Part 2

Ruthenium Nitrosyls Derived from Tetradentate Ligands with Dicarboxamido-N and Phenolato-O Donors

3.2.1 Background

Theoretical studies on simple $\{RuNO\}^6$ nitrosyls,[1] such as $[Ru(NH_3)_5NO]^{3+}$ and $[Ru(NH_3)_4(Cl)NO]^{2+}$, suggest that the photolability of these complexes are likely initiated by a high energy (~330 nm) $d\pi(Ru) \rightarrow \pi^*(NO)$ transition.[2,3] However, over the years, our group and others have identified several ligand characteristics that increase the efficiency of NO release from the resulting ruthenium nitrosyls.[4,5] For example, the use of charged ligands like Cl^- compared to neutral ligands like H_2O or pyridine accelerates the release of NO in [(salen)Ru(NO)(Cl)] and $[(Me_2bpb)Ru(NO)(Cl)]$.[6,7] The use of strong σ–donating anionic donors such as carboxamido-N or phenolato-O has been shown to enhance the photolability in these ruthenium nitrosyls.[4] Indeed, results of theoretical studies indicate that the metal-to-ligand charge transfer (MLCT) transitions observed in the electronic absorption spectra of [(salen)Ru(NO)(Cl)] and $[((OMe)_2bQb)Ru(NO)(Cl)]$ are not purely $d\pi(Ru) \rightarrow \pi^*(NO)$ in character but mixed transitions which include some (phenoxo) $\rightarrow \pi^*(NO)$ and (carboxamide) $\rightarrow \pi^*(NO)$ character, respectively.[8,9] It is therefore evident that the photolability of designed $\{RuNO\}^6$ nitrosyls can be modulated by careful choice of ligand(s).

Scrutiny of the known photosensitive $\{RuNO\}^6$ nitrosyls reveals that apart from NH_3,[10] most of the nitrosyls contain pyridine-N,[11] phenolato-O,[6,12] and carboxamido-N[7,13] donors around the metal center. However, there are a limited number of theoretical studies on closely related ruthenium nitrosyls that contain systematically modified multidentate ligands to examine the effects of these donors.

We therefore became interested in examining the effects of tetradentate ligands that combine anionic carboxamido-N and phenolato-O donors along with neutral pyridine-N donors. Using density functional theory (DFT) and time dependent DFT calculations on the resulting nitroysls we also attempted to gain insight into the specific donor atoms involved in the absorption of lower energy light leading to the photorelease of NO. We used the same tetradentate dicarboxamido-N ligand framework with two open sites as described in the last section. However, now we have incorporated charged phenolato-O donors and/or neutral pyridine donor atoms in the open sites generating three new ligand frames containing two, three, or four negatively charged donors, namely 1,2-bis(pyridine-2-carboxamido)benzene (H_2bpb),[14] 1-(2-hydroxybenzamido)-2-(2-pyridinecarbox-amido)benzene (H_3hypyb), [15,16] and 1,2-bis(2-hydroxybenzamido)benzene (H_4hybeb)[16] respectively (Figure 3.2.1). Since the incorporation of soft/neutral phosphine-P donors ultimately stabilized a Ru(II) center which was unable to form the desired nitrosyls, we were interested to determine the effects of increasing the strength and negative charge of the ligand frame on the resulting Ru complexes.

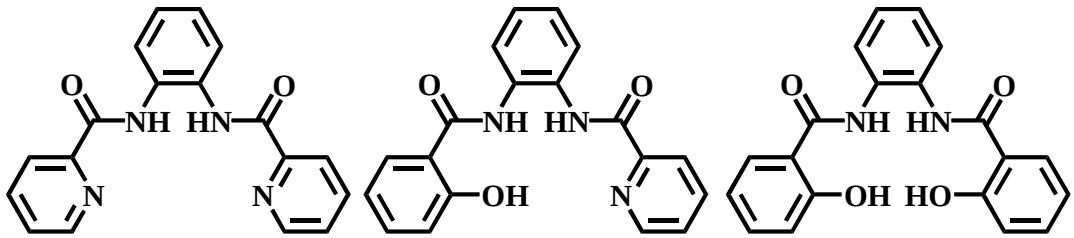

Figure 3.2.1. Tetradentate dicarboxamido-N ligands with two, three, or four anionic donor atoms (upon deprotonation)

3.2.2 Syntheses of Phenolate Containing Ligand Frames

We have modified the original synthetic procedures of both 1,2-bis(2-hydroxyben-zamido)benzene (H_4hybeb) and 1-(2-hydroxybenzamido)-2-(2-pyridinecarbox-amido)benzene (H_3hypyb) to improve the yields of these ligands. Previously in our lab, Todd Harrop and Elizabeth Espinoza attempted to synthesize an asymmetric tetradentate ligand frame containing two carboxamides, one pyridine, and one thiophenol donor group. Unfortunately, such attempts were unsuccessful. However, the synthetic steps nevertheless afforded some tips in the synthesis of the asymmetric H_3hypyb ligand frame. For example, picolinic acid was first converted into the acid chloride upon treatment with thionyl chloride. The acid chloride was then combined with 2-nitroaniline to afford Hpycan (Figure 3.2.2). Next the nitro

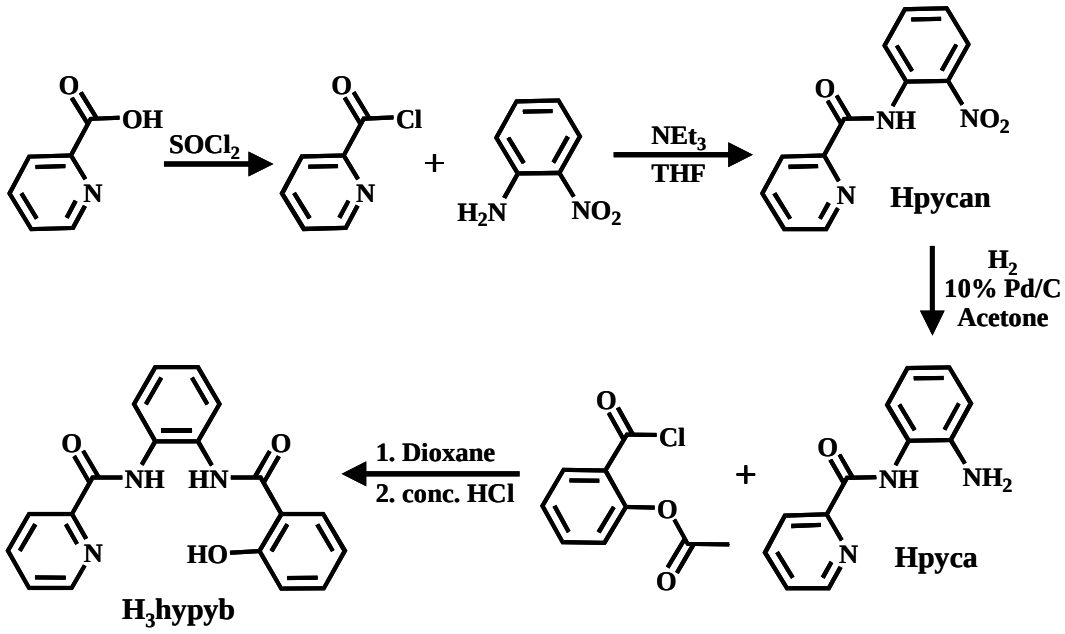

Figure 3.2.2. Reaction scheme of the H_3hypyb ligand frame

group of Hpycan was reduced to a primary amine generating Hpyca with H_2 in the presence of 10% Pd/C. The final step in the synthesis of H_3hypyb involves the addition of acetylsalicyloyl chloride. The desired phenolate moiety is protected to insure it does not react with the acid chloride of another molecule during this step. Once the desired amide bond has formed, treatment with conc. HCl deprotects the phenolate group to give the final product.

Since H_4hybeb is not an unsymmetrical ligand like H_3hypyb, there are considerably fewer steps in its synthesis. Instead of using 2-nitroaniline, 1,2-phenylenediamine can be directly reacted with two equivalents of the protected phenolate (acetylsalicyloyl chloride, Figure 3.2.3). Next both phenolate groups are deprotected by addition of conc. HCl resulting in the formation of H_4hybeb.

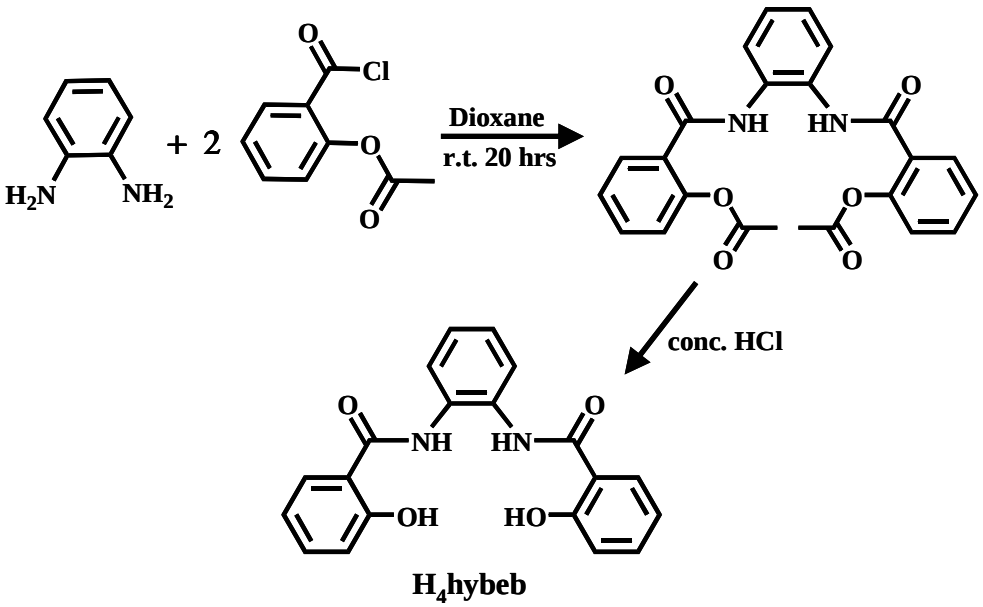

Figure 3.2.3. Reaction scheme for the synthesis of the H_3hybeb ligand frame

3.2.3 Syntheses and X-Ray Structures of Metal Complexes

3.2.3.1 Characterization of $[(hypyb)Ru(NO)(OEt)]^{-}$

One of the first $\{RuNO\}^6$ nitrosyls synthesized in our lab was derived from the H_2bpb ligand frame by the reaction of $RuCl_3$ with the deprotonated (with NaH) ligand in DMF followed by the addition of NO(g) resulting in $[(bpb)Ru(NO)(Cl)]$.[3] However, as we included phenolato-O donors in the ligand frame, this method did not afford the desired nitrosyls. After several attempts, it became evident that some of the reaction conditions needed to be changed. We first decided to switch solvents from DMF to EtOH. We had previously synthesized a few ruthenium nitrosyls derived from pentadentate carboxamide and pyridine containing ligand frames ($[(PaPy_3)Ru(NO)]^{2+}$ and $[(Py_3P)Ru(NO)]^{+}$) using ethanol as the solvent.[13] In this procedure, $RuCl_3$ was heated to reflux in ethanol generating the "green solution". Separately, the H_3hypyb ligand frame was deprotonated with NaH also in EtOH. Reaction of the two solutions followed by addition of NO(g) resulted in moderate yields of the final product as the ethanolate (-OEt) bound species, namely $[(hypyb)Ru(NO)(OEt)]^{-}$. It is thus evident that in ethanol, the ethanolate-bound nitrosyls are the predominant products particularly under the basic conditions (NaH) of the synthetic procedures. During the synthesis of the corresponding $[hybeb]^{4-}$ containing $\{RuNO\}^6$ nitrosyl an improved method of synthesis (describe below) was discovered and also used to increase the yields of $[(hypyb)Ru(NO)(OEt)]^{-}$.

Originally the final product was first isolated as the sodium salt. However

exchange of the counter ion by treatment with PPh_4Cl help the formation of X-ray quality crystals of the resulting (PPh_4)[(hypyb)Ru(NO)(OEt)]. In (PPh_4)[(hypyb)Ru(NO)(OEt)] (Figure 3.2.4) the deprotonated $[hypyb]^{3-}$ ligand is bound to the ruthenium center in the equatorial plane and the phenolato moiety is slightly out of the plane of the rest of ligand resulting in a slightly distorted octahedral geometry. The $Ru\text{-}O_{phenoxo}$ and $Ru\text{-}N_{amide}$ bond distances (2.024 and 2.019 Å respectively) on the right side of the ligand frame (as shown in Figure 3.2.4) are similar to those noted in $[(hybeb)Ru(NO)(OEt)]^{2-}$. Similarly, the $Ru\text{-}N_{amide}$ bond distance (1.985 Å) next to the pyridine moiety (on the left side of the ligand in Figure 3.2.4) is comparable to that noted for [(bpb)Ru(NO)(OEt)] (1.986 Å). However, the $Ru\text{-}N_{py}$ distance of (PPh_4)[(hypyb)Ru(NO)(OEt)] (2.107 Å) is shorter than the same bond distance in [(bpb)Ru(NO)(OEt)] (avg value 2.130 Å). This difference probably arises from distortions caused by the asymmetry of the ligand frame in

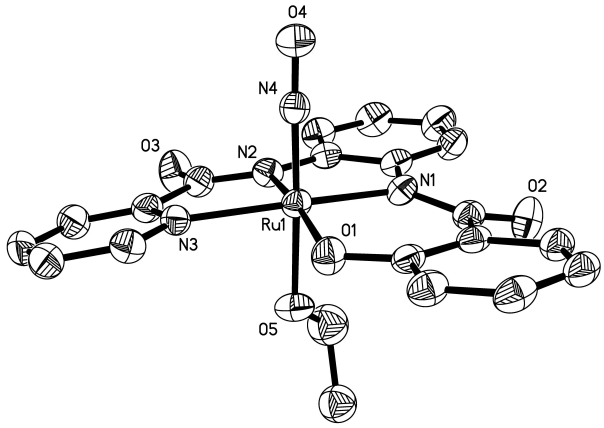

Figure 3.2.4. Thermal ellipsoid (probability level 50%) plot of $[(hypyb)Ru(OEt)]^-$ with select atom-labeling. H atoms are omitted for the sake of clarity.

(PPh_4)[(hypyb)Ru(NO)(OEt)]. The EtO^- ligand is bound trans to NO in the axial positions. The Ru-OEt and Ru-NO bond distances (1.973 and 1.738 Å respectively) of (PPh_4)[(hypyb)Ru(NO)(OEt)] are within the range of other ruthenium nitrosyls and the Ru-NO bond angle (177.6°) is almost linear, as expected for a $\{Ru\text{-}NO\}^6$ nitrosyl.

3.2.3.2 Characterization of $[(hybeb)Ru(NO)(OEt)]^{2-}$

Using either DMF or EtOH (as describe above for $[(hypyb)Ru(NO)(OEt)]^-$), we were unable to obtain good yields of either Cl- or OEt-bound species of the desired $[hybeb]^{4-}$ containing ruthenium nitrosyl. However, reactions using EtOH at least resulted in some of the desired product with OEt-bound while reactions done in DMF did not afford any of the desired product. Thus we decided to keep EtOH as the solvent while switching the starting metal salt from $RuCl_3$ to $RuNOCl_3$. Reaction of the $[hybeb]^{4-}$ ligand frame (deprotonated with NaH) with $RuNOCl_3$ in EtOH resulted in increased yields of the OEt-bound product, $[(hybeb)Ru(NO)(OEt)]^{2-}$. In addition, this procedure also increased the yields of $[(hypyb)Ru(NO)(OEt)]^-$. We believe that in such reactions, the trans effect of the Ru-bound NO moiety helps drive the formation of the OEt-bound product with the preferred O-donor (vs Cl-donor) trans to NO. This preference for O-donors trans to NO is supported by fact that the majority of the X-ray structures of Ru nitrosyls found in the Cambridge Crystal Structure Database do indeed contain an O-donor bound trans to NO.[17]

The $[(hybeb)Ru(NO)(OEt)]^{2-}$ product was first isolated as the sodium salt as

was also the case for $[(hypyb)Ru(NO)(OEt)]^{-}$. This time we were able to isolate X-ray quality crystals of $[(hybeb)Ru(NO)(OEt)]^{2-}$ by treatment with NEt_4Cl. Interestingly, the resulting X-Ray structure revealed only partial counter ion exchange with 1.5 and 0.5 equivalents of NEt_4^+ and Na^+ respectively, in the final structure ($(NEt_4)_{1.5}(Na)_{0.5}[(hybeb)Ru(NO)(OEt)]$). The structure of the anion of $[(hybeb)Ru(NO)(OEt)]^{2-}$ (Figure 3.2.5) reveals the ruthenium center in a slightly distorted octahedral geometry with one of the phenolato moieties raised slightly above the rest of the $[hybeb]^{4-}$ ligand frame in the equatorial plane, as was also seen for $[(hypyb)Ru(NO)(OEt)]^{-}$. A similar distortion is seen in ruthenium nitrosyls containing $[salophen]^{2-}$ type ligands.[4] The average Ru-N_{amide} bond distance (2.022 Å) of $[(hybeb)Ru(NO)(OEt)]^{2-}$ is longer than that found for [(bpb)Ru(NO)(OEt)] presumably due to increase in charge in the equatorial plane of the ligand frame. Similarly, the average Ru-$O_{phenoxo}$ bond distance (2.028 Å) is slightly longer than that noted for [(^{t}Bu$_2$salophen)Ru(NO)(Cl)] (2.022 Å, ^{t}Bu$_2$salophen = *N*,*N*′-1,2-phenylene-

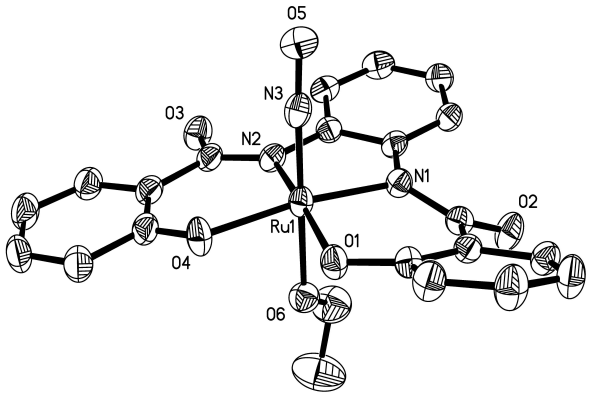

Figure 3.2.5. Thermal ellipsoid (probability level 50%) plot of $[(hybeb)Ru(OEt)]^{2-}$ with select atom-labeling. H atoms are omitted for the sake of clarity.

diaminebis(3-*tert*-butylsalicylideneiminato) dianion) [6] which contains neutral imine-N donors in place of the charged carboxamido-N donors. In $[(hybeb)Ru(NO)(OEt)]^{2-}$, the Ru-NO distance (1.733 Å) as well as the Ru-NO bond angle (170.5°) are as expected for this type of $\{Ru\text{-}NO\}^6$ nitrosyls.

3.2.3.3 Characterization of [(bpb)Ru(NO)(OEt)]

As expected, the reaction of the $[bpb]^{2-}$ ligand frame (deprotonated with NaH) with $RuNOCl_3$ in EtOH also resulted in the OEt-bound product, [(bpb)Ru(NO)(OEt)] in good yield. Since we were also able to synthesis the Cl-bound species, [(bpb)Ru(NO)(Cl)], we were interested to see if we could exchange the Cl-donor for OEt^- by refluxing [(bpb)Ru(NO)(Cl)] in EtOH in the presence of triethylamine (as base). This exchange worked well since the Cl^- ion is a better leaving group and allowed EtOH to bind trans to NO. Once bound, the pKa of the EtOH moiety greatly increases resulting in its deprotonation in the basic solution and formation of the final OEt-bound species and NEt_4Cl. This supports that fact that the Ru-NO moiety prefers O-bound donors trans to NO. In addition, it also clearly shows that the presence of a protic solvent and base give rise to deprotonated solvent bound species. This is not surprising since we have also synthesized $[(Me_2bpb)Ru(NO)(OH)]$ and $[(Me_2bQb)Ru(NO)(OH)]$ in moist MeCN in presence of aniline.[18] Clearly, presence of a protic solvent and a base give rise to the HO- or EtO-bound nitrosyls in this type of reaction.

The X-ray structure of [(bpb)Ru(NO)(OEt)] contains a 2-fold symmetry (Figure 3.2.6) as the bond distances and angles related to the $[bpb]^{2-}$ ligand are the same for each side of the symmetric ligand frame. The Ru-N_{amide} (1.986Å) and Ru-N_{py} (2.130 Å) bond distances of [(bpb)Ru(NO)(OEt)] are very similar to those of [(bpb)Ru(NO)(Cl)] (1.990 and 2.131 Å respectively).[7] Interestingly, the presence of neutral pyridine-N donors vs. charged phenolato-O donors appears to have decreased the Ru-N(O) (1.153 Å) bond distance of [(bpb)Ru(NO)(OEt)] compared to that of $[(hypyb)Ru(NO)(OEt)]^{-}$ (1.161 Å) and even further compared to that of $[(hybeb)Ru(NO)(OEt)]^{2-}$ (1.174 Å). A related trend in the NO stretching frequency

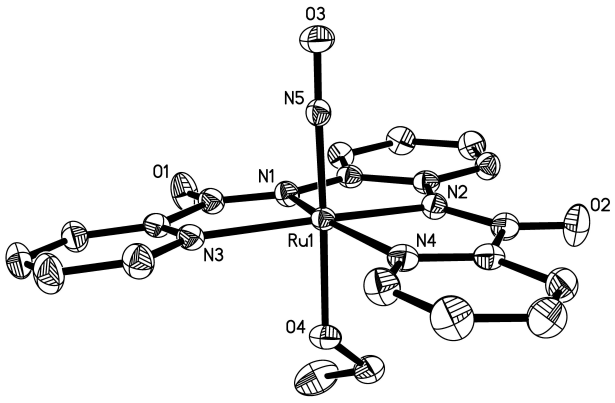

Figure 3.2.6. Thermal ellipsoid (probability level 50%) plot of [(bpb)Ru(NO)(OEt] with select atom-labeling. H atoms are omitted for the sake of clarity.

(ν_{NO}) of these nitroyls was also observed. As the charge on the deprotonated ligand decreases from $[hybeb]^{4-}$ to $[hypyb]^{3-}$ to $[bpb]^{2-}$, the corresponding ruthenium nitrosyls display NO stretching frequencies (ν_{NO}) of increasing energy ($[(hybeb)Ru(NO)(OEt)]^{2-}$, ν_{NO} = 1783; $[(hypyb)Ru(NO)(OEt)]^{-}$ ν_{NO} = 1793;

[(bpb)Ru(NO)(OEt)], ν_{NO} = 1838). Both trends suggests an increase in metal to (NO)π^* pi-backbonding as the overall charge of the complex increases.

3.2.4 NO Photolability of Metal Nitrosyls

Exposure of solutions of all three nitrosyls to low power UV light causes rapid release of NO (as evidenced by the responses of an NO-sensitive electrode). In order to study the effects of combining carboxamido-N and phenolato-O donors on the efficiency of NO photolability in this type of $\{Ru\text{-}NO\}^6$ nitrosyl, we have measured the quantum yield values of NO photorelease for $[(hybeb)Ru(NO)(OEt)]^{2-}$, $[(hypyb)Ru(NO)(OEt)]^{-}$, and [(bpb)Ru(NO)(OEt)] under similar conditions at both 300 and 400 nm. In MeCN, the quantum yield values at 300 nm (ϕ_{300}) for $[(hybeb)Ru(NO)(OEt)]^{2-}$, $[(hypyb)Ru(NO)(OEt)]^{-}$, and [(bpb)Ru(NO)(OEt)] are 2.5%, 6.7%, and 5.1% respectively. The addition of one phenolato-O donor in $[(hypyb)Ru(NO)(OEt)]^{-}$ slightly increases its quantum yield above that of [(bpb)Ru(NO)(OEt)] which contains no phenolato-O donors. Interestingly, the addition of a second phenolato-O donor, in $[(hybeb)Ru(NO)(OEt)]^{2-}$, lowers the quantum yield value below that of [(bpb)Ru(NO)(OEt)]. When exposed to lower energy light (400 nm), only $[(hypyb)Ru(NO)(OEt)]^{-}$ and [(bpb)Ru(NO)(OEt)] (which contain lower energy absorption bands at 420 and 380 nm, respectively) are photoactive. The quantum yield values measured at 400 nm (ϕ_{400}) for

(hypyb)Ru(NO)(OEt)]$^{-}$ (0.8%) and [(bpb)Ru(NO)(OEt)] (1.4%) reveal that both are less efficient NO donors when they are exposed to low energy light.

3.2.5 DFT and TDDFT Calculations

To elucidate how changes in the ligand frame affect the absorption of lower energy light leading to the photorelease of NO, DFT and TDDFT calculations were preformed on [(hybeb)Ru(NO)(OEt)]$^{2-}$, [(hypyb)Ru(NO)(OEt)]$^{-}$, and [(bpb)Ru(NO)(OEt)]. For comparison the DFT and TDDFT results of a related {RuNO}^{6} nitrosyl, namely [((OMe)$_2$bQb)Ru(NO)(Cl)], have also been included. This nitrosyl also contains a dicarboxamide tetradentate ligand frame where the remaining two donor sites are quinoline-N donors. In addition, aromatic ring substitution of the phenylenedicarboxamide portion of the ligand frame has been performed to alter the electron donating capacities of the carboxamido-N donor centers. The DFT and TDDFT results for these nitrosyls are combined in Figure 3.2.7 for comparison. The lowest 20 calculated energy transitions of each nitrosyls are shown as a bar graph in the top panel of Figure 3.2.7. The height of each bar corresponds to the calculated oscillator strength of each transition. The experimental electronic absorption spectrum of each complex (solid lines) and the spectra derived from the calculated data using Lorentzian broadening (dashed lines) are also shown for comparison in the top panel of Figure 3.2.7.[19] The relative intensities and wavelengths of the calculated data match very well with the corresponding experimental data and thus support the theoretical treatment. The bottom panel of

Figure 3.2.7 diaplays the molecular orbital (MO) energy diagrams for these nitrosyls. The lowest energy transitions of appreciable oscillator strength for each complex are highlighted in red and the orbitals involved in those transitions are shown at their corresponding energy levels.

The lowest energy transitions of [(bpb)Ru(NO)(OEt)], $[(hypyb)Ru(NO)(OEt)]^{-}$, and $[((OMe)_2bQb)Ru(NO)(Cl)]$ all originate from their HOMO's which are predominately derived from orbitals located on the carboxamido-N donor atoms and delocalized over the phenylenediamine (π(PDA)) portion of each ligand frame. These orbitals also contain some dπ(Ru)-π(NO) bonding (π(RuNO)) character. Interestingly, the HOMO of $[(hypyb)Ru(NO)(OEt)]^{-}$ has some phenolato π-orbital (π(PhO)) character in addition to the π(PDA) and is 0.46 eV higher in energy than the HOMO of [(bpb)Ru(NO)(OEt)] which has no phenolato donors. While $[((OMe)_2bQb)Ru(NO)(Cl)]$ also has no phenolato donors, the incorporation of methoxy groups causes a similar 0.41 eV rise in the energy of its HOMO compared to the HOMO of [(bpb)Ru(NO)(OEt)]. In the case of $[(hybeb)Ru(NO)(OEt)]^{2-}$, incorporation of two phenolato donors further raises the energy of its HOMO by an additional 0.41 eV above that of $[(hypyb)Ru(NO)(OEt)]^{-}$. Thus increasing the donor strength of the ligand (a) by addition of phenolate group(s) or (b) via ring substitution both raises the energy of the HOMO in these types of nitrosyls. Such changes bring about red-shifts in the low energy transitions of $[(hypyb)Ru(NO)(OEt)]^{-}$ and $[((OMe)_2bQb)Ru(NO)(Cl)]$ because their HOMO's are involved in those transitions

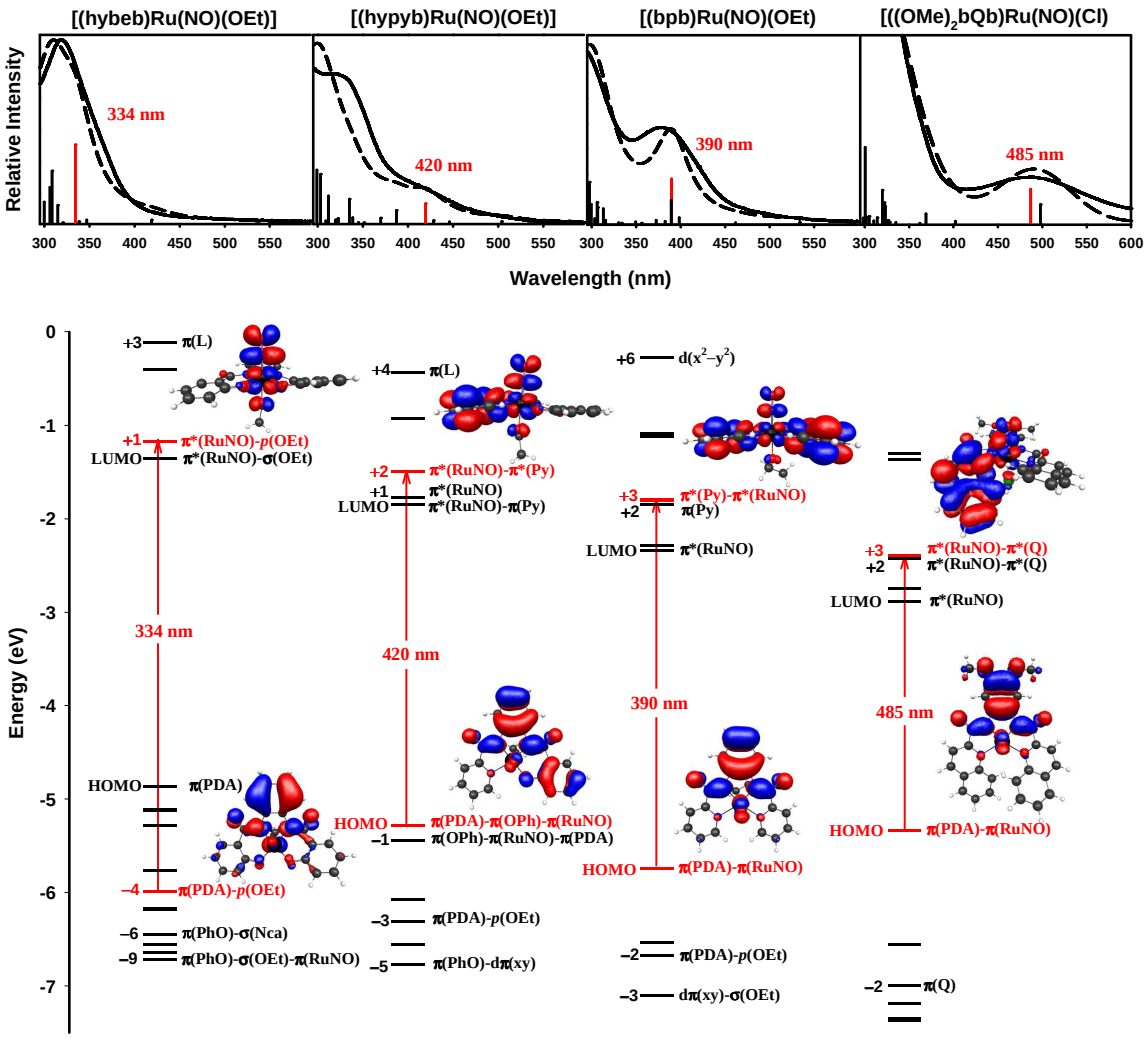

Figure 3.2.7. (Top) TDDFT calculated energy transitions and oscillator strengths (shown as vertical lines, red = major low energy transition), experimental (solid lines) and calculated (dashed lines) electronic absorption spectra. (Bottom) Calculated HOMO/ LUMO energy diagrams of $[(hybeb)Ru(NO)(OEt)]^{2-}$, $[(hypyb)Ru(NO)(OEt)]^{-}$, [(bpb)Ru(NO)(OEt)], and $[((OMe)_2bQb)Ru(NO)(Cl)]$ (left to right). The most prominent MOs involved in the lowest energy transitions (labeled in red) and their diagrams are shown. Other orbitals involved in TDDFT calculated transitions are labeled in black.

(Figure 3.2.7). However, the lowest energy transition observed in the calculated spectrum of $[(hybeb)Ru(NO)(OEt)]^{2-}$ originates from the HOMO-4, thus explaining its lack of red-shift despite the presence of four strong σ-donors (Figure 3.2.7).

The LUMO and LUMO+1 for each of the four nitrosyls are predominantly orbitals with dπ(Ru)-π*(NO) antibonding character (abbreviated as π*(RuNO) in Figure 3.2.7). At slightly higher energy, there are unoccupied orbitals with considerable mixing of the π*(RuNO) orbitals with pyridine (π(py)) or quinoline (π(Q)) character in [(bpb)Ru(NO)(OEt)] (LUMO+3), $[(hypyb)Ru(NO)(OEt)]^{-}$ (LUMO+2), and $[((OMe)_2bQb)Ru(NO)(Cl)]$ (LUMO+3) respectively. The lowest energy transitions observed for the pyridine- and quinoline-containing nitrosyls excite an electron into these π*(RuNO)-π*(py/Q) mixed orbitals. Interestingly, this mixing lowers the energy of these orbitals compared to the pure π*(RuNO) orbital of $[(hybeb)Ru(NO)(OEt)]^{2-}$ (LUMO+1) which is involved in its lowest energy transition. Consequently, the π*(RuNO)-π*(py/Q) mixed orbitals of $[(hypyb)Ru(NO)(OEt)]^{-}$ (with one pyridine), [(bpb)Ru(NO)(OEt)] (with two pyridine), and $[((OMe)_2bQb)Ru(NO)(Cl)]$ (with two quinoline) are 0.33 eV, 0.63 eV, and 1.22 eV lower in energy than the pure π*(RuNO) orbital of $[(hybeb)Ru(NO)(OEt)]^{2-}$ (with no pyridine or quinoline donors). Both pyridine-N and quinoline-N are considered electron-withdrawing groups and the added conjugation of quinoline moieties makes it slightly more electron-accepting. Conversely, phenolate moieties are considered more electron-donating in character. Thus as the number or strength of the electron-withdrawing groups are increased, the energy of

the π*(RuNO)-π*(py/Q) mixed orbitals of these nitrosyls are lowered. This finding explains the red-shift in the low energy transitions of the pyridine- and quinoline-containing nitrosyls.

Overall, the TDDFT results strongly suggest that increase in the electron donating ability of the donor groups in the ligand frame raises the energy of the HOMO while the energies of the lowest unoccupied orbitals are lowered when the electron accepting abilities of the donor groups are increased. Thus the energy gap between the occupied and unoccupied orbitals can be altered in a predictable fashion (and shifting the electronic transitions to lower energy) through correct mixing of donor groups. That [((OMe)$_2$bQb)Ru(NO)(Cl)] has the lowest energy absorption band in this series of {RuNO}^{6} nitrosyls supports this conclusion.

The low energy transitions of [(hybeb)Ru(NO)(OEt)]$^{2-}$ and [(hypyb)Ru(NO)(OEt)]$^-$ both end in orbitals with high contributions from dπ(Ru)-π*(NO) antibonding orbitals. Since [(hybeb)Ru(NO)(OEt)]$^{2-}$ has no pyridine or quinoline donors, its low energy transition excites an electron into an orbital (LUMO+1) that is primarily dπ(Ru)-π*(NO) antibonding in character with 43% Ru and 49% NO. The addition of one pyridine donor in [(hypyb)Ru(NO)(OEt)]$^-$ moderately lowers the overall amount of dπ(Ru)-π*(NO) antibonding character to 24% Ru and 21% NO (in its LUMO+2). A direct mechanism of NO photorelease through these singlet metal–NO antibonding excited states therefore seems possible for these two nitrosyls. However, when additional pyridine and quinoline donors are added in [(bpb)Ru(NO)(OEt)] and [((OMe)$_2$bQb)Ru(NO)(Cl)], such direct pathways

become less likely as the low energy transitions go to orbitals with more pyridine and quinoline character than dπ(Ru)-π*(NO) antibonding character. For example, the percentages of Ru and NO character in the LUMO+3 orbitals of [(bpb)Ru(NO)(OEt)] and [((OMe)$_2$bQb)Ru(NO)(Cl)] are only 10-14% for each. This is similar to the low energy transitions observed for [(PaPy$_3$)Mn(NO)]$^+$ which end in pyridine-centered orbitals with a low contribution from the dπ(Mn) orbitals. Therefore it seem likely that these {RuNO}^{6} nitrosyls also undergo an intersystem crossing into the corresponding Ru–NO antibonding triplet excited states, which, due to extended life times, are expected to be much more efficient in the photodissociation of NO.

Optimization of the lowest energy triplet state of [(bpb)Ru(NO)(OEt)] reveals an elongated Ru-NO bond (1.926 Å) compared to that observed in the corresponding singlet state (1.742 Å). In addition, the linear Ru-N-O bond angle in the singlet state (177°) becomes significantly bent in the geometry-optimized triplet state (138°). These changes in geometry suggest a Ru(II)-NO$^+$ to Ru(III)-NO$^\bullet$ transformation during the singlet to triplet state intersystem crossing. Such a change in electronic distribution decreases the extent of π-back bonding in the triplet state causing the observed bending of the Ru-N-O bond which is characteristic of Ru(III)-NO$^\bullet$ moieties. Franco and co-workers have suggested that efficient interconversion and intersystem crossing to lower energy triplet excited states can occur in ruthenium nitrosyls and rapid solvation of such triplet species could be competitive with other deactivation pathways and account for NO photolability.[3]

3.2.6 Conclusions

The TDDFT results reveal that the calculated electronic transitions of the photoactive metal nitrosyls in the region of 350-500 nm all originate from molecular orbitals with significant carboxamido character. When such transitions excite electrons into orbitals with significant metal-NO antibonding character, the metal-NO bond is weakened and thus NO release could occur in the initially excited singlet state. This appears to be the case for $[(hybeb)Ru(NO)(OEt)]^{2-}$ and $[(hypyb)Ru(NO)(OEt)]^{-}$. When the number and/or strength of the carboxamido-N donors in the ruthenium nitrosyls is increased with concomitant addition of electron-withdrawing donor groups like pyridine and quinoline in [(bpb)Ru(NO)(OEt)] and $[((OMe)_2bQb)Ru(NO)(Cl)]$, their low energy transitions begin to possess more carboxamido → py/Q character. Thus it is more likely that the NO photolability of these nitrosyls occurs via intersystem crossing into low-lying π(Ru)-π*(NO) antibonding triplet states.

The results also indicate that NO photolability of ruthenium nitrosyls with visible light can be achieved via smart ligand design. These studies have revealed that the addition of phenolato-O donors raises the energy of the highest occupied MOs while addition of pyridine donors lowers the energy of the lowest unoccupied MOs. Thus $[(hypyb)Ru(NO)(OEt)]^{-}$ which contains both phenolato and pyridine donors has the lowest energy transition (of the phenolate and/or pyridine containing compounds) from an occupied orbital with phenolato character into an orbital with pyridine character. In addition, complex $[(hybeb)Ru(NO)(OEt)]^{2-}$ which has all

charged (electron-donating) donors and no electron-accepting groups exhibits only high energy transitions. Thus it becomes apparent that the correct mix of electron-accepting and electron-donating groups in the ligand frame promotes the absorption of lower energy light (and concomitant NO photolability) in this type of ruthenium nitrosyls derived from designed ligands. This point is confirmed by [((OMe)$_2$bQb)Ru(NO)(Cl)] where the addition of electron withdrawing quinoline groups and electron donating OMe substituents has lower the energy of its electronic transitions even further.

3.2.7 Computational Method

DFT calculations were carried out using the double-zeta basis set 6-311G* for all atoms except Ru, for which the quasi-relativistic Stuttgart-Dresden effective core potential (ECP) was implemented. Calculations were carried out with the aid of the program PC-GAMESS [20] using the hybrid functional PBE0. In the first publication from our lab that contained DFT calculations on {RuNO}^{6} nitrosyls ([((OMe)$_2$bQb)Ru(NO)(Cl)] and ([((OMe)$_2$bQb)Ru(NO)(Dye)], Dye = Resf, Thln, and Seln), the functional B3PW91 was used. B3PW91 is a hybrid functional which (along with Stuttgart Ru-ECP) has been shown to be accurate for second-row transition metals.[21] Unfortunately, the TDDFT calculations using this functional and basis set combination did not match well with the experimental electronic absorption spectra. Thus we only reported the specific details of the DFT calculated MO energy diagrams in that first publication. In our later attempts (discussed above) to generate

TDDFT calculated electronic absorption spectra that are consistent with the experimental spectra, we tried different functionals such as B3LYP and PBE0. These results were similar to those obtained using B3PW91 and gave calculated spectra that were significantly red-shifted. Only when solvent effects were added using the Polarized Continuum Model (PCM) with the PBE0 functional did we obtain results with the correct energy shift.[22] Interestingly, the type of solvent added (MeCN, H_2O, EtOH) dramatically affected the calculated spectra in contrast to experimental spectra which are only slightly affected by differences in solvent. We found that using the EtOH PCM solvent effect gave calculated results most similar to the experimental spectra for all of our $\{RuNO\}^6$ nitrosyls regardless of the solvent the spectra were taken in. The X-ray coordinates of the nitrosyls were used as a starting point for each geometry optimization and molecular orbital (MO) energy level analysis. MOs were visualized in MacMolPlt for analysis.[23] Graphical representations of TDDFT data were created by ChemCraft Software.[24]

3.2.8 Experimental Section

3.2.8.1 Syntheses of Compounds

Materials. All chemicals were purchased from Aldrich Chemical Co. and used without further purification except for the acetylsalicyloyl chloride and quinaldic acid which were purchased from Acros Organics. The solvents were dried by standard techniques and distilled prior to use.

Syntheses of Ligands. The ligand 1,2-bis(pyridine-2-carboxamido)benzene (H_2bpb) was synthesized by following literature procedure.[25]

1,2-bis(2-hydroxybenzamido)benzene (H_4hybeb). To a solution containing 500 mg (4.6 mmol) phenylenediamine in 5 mL of dioxane was slowly added 1.83 g (9.3 mmol) of neat acetylsalicyloyl chloride. The mixture was allowed to stir for 20 h at room temperature at which point, 1 mL of conc HCl was slowly added to the solution. The pink solution was stirred for an additional 20 h, followed by addition of 40 mL of water resulting in a white precipitate. The product was filtered, washed several times with water and MeCN to remove impurities, and dried in vacuo. Yield: 1.29 g (80%). Selected IR frequencies (KBr disk, cm^{-1}): 3281 (ν_{NH}, w), 3049 (w), 1640 ($\nu_{C=O}$, m), 1591 (m), 1533 (vs), 1496 (s), 1313 (m), 1223 (m), 751 (s). ^{1}H NMR (500 MHz, $(CD_3)_2SO$, δ from TMS): 11.74 (s, 2H), 10.42 (s, 2H), 8.01 (d, 2H), 8.81 (t, 2H), 7.42 (t, 2H), 7.28 (dd, 2H), 6.96 (t, 4H).

***N*-(2-Nitrophenyl)pyridine-2carboxamide) (Hpycan).** A batch of 1.00 g (8 mmol) of picolinic acid was weighed out into a 50 mL round bottom flask and 10 mL of thionyl chloride was added. The resulting solution changed from white to green in color. It was then heated to reflux for 3 h when the color of the solution changed to a burgundy red. Next, the excess solvent was removed and the resulting red solid was triturated 3 times with dichloromethane. The solid was then dissolved in 100 mL of THF and added dropwise to a solution containing 1.76 g (16 mmol) of triethylamine and 1.21 g (8 mmol) of 2-nitroaniline also in 100 mL of THF. The solution was stirred for 20 h and the resulting NEt_3•HCl was filtered off using a Celite pad. The

filtrate was condensed to half the original volume and cooled to -20° C causing the product to precipitate. The filtered product was washed 3 times each with cold ethanol and diethyl ether and dried in vacuo. Yield: 1.7 g (80%). Selected IR Frequencies (KBr disk, cm^{-1}): 3276 (ν_{NH}, m), 1690 ($\nu_{C=O}$, s), 1606 (s), 1580 (s), 1497 (vs), 1446 (s), 1423 (s), 1341 (s), 1271 (s), 1148 (m), 787 (m), 743 (s), 686 (m). ^{1}H NMR (500 MHz, $CDCl_3$, δ from TMS): 12.78 **(**s, 1 H), 9.06 (d, 1H), 8,76 (d, 1H), 8.30 (t, 2H), 7.95 (t, 1H), 7.74 (t, 1H), 7.54 (dd, 1H), 7.24 (t, 1H).

***N*-(2-Aminophenyl)pyridine-2-carboxamide (Hpyca).** A solution of 5.00 g (20.6 mmol) of Hpycan and 30 wt% of hydrogenation catalyst (10% Pd on activated carbon) was prepared in 150 mL of acetone. Dihydrogen was admitted to the reaction vessel and the mixture was stirred for 16 h under 45 atmos pressure of dihydrogen. The reaction product was then separated from the catalyst by filtration using a Celite pad and the filtrate was evaporated to dryness to yield an yellow-brown oil. The oil was dissolved in dichloromethane and hexane was slowly added under vigorous magnetic stirring until a slight precipitate formed. This solution was refrigerated overnight to allow more yellow product to precipitate. The precipitate was filtered, washed with hexane, and dried in vacuo. Yield: 3.95 g (90%). Selected IR Frequencies (KBr disk, cm^{-1}): 3387 (ν_{NH}, m), 3314 (ν_{NH}, m), 1667 ($\nu_{C=O}$, s), 1629 ($\nu_{C=O}$, m), 1588 (m), 1527 (vs), 1453 (m), 1431 (m), 1315 (m), 761 (s), 696 (m), 970 (m). ^{1}H NMR (500 MHz, $CDCl_3$, δ from TMS): 10.89 **(**s, 1 H), 8.64 (d, 1H), 8.31 (d, 1H), 7.92 (t, 1H), 7.50 (d, 2H), 7.10 (t, 1H), 6.87 (t, 2H), 3.89 (s, 2 H).

1-(2-hydroxybenzamido)-2-(2-pyridinecarboxamido)benzene (H_3hypyb). A batch of 460 mg (2.4 mmol) of neat acetylsalicyloyl chloride was slowly added to a solution containing 500 mg (2.4 mmol) of Hpyca dissolved in 5 mL of dioxane. After the mixture was stirred for 20 h at room temperature, 1 mL of conc HCl was slowly added to the solution. The orange solution was stirred for 20 h followed by addition of 40 mL of water added dropwise to the stirred solution. The resulting white precipitate was filtered, washed several times with water, and dried in vacuo. Yield: 800 mg (75%). Selected IR frequencies (KBr disk, cm^{-1}): 3252 (ν_{NH}, m), 3058 (w), 1665 ($\nu_{C=O}$, s), 1641 ($\nu_{C=O}$, s), 1593 (s), 1544 (vs), 1518 (vs), 1491 (s), 1339 (m), 1227 (m), 751 (vs), 692 (m). ^{1}H NMR (500 MHz, $(CD_3)_2SO$, δ from TMS): 11.58 (s, 1H), 10.55 (s, 1H), 10.46 (s, 1H), 8.59 (d, 1H), 8.14 (d, 1H), 8.04 (t, 1H), 7.99 (d, 1H), 7.86 (d, 1H), 7.69 (d, 1H), 7.64 (t, 1H), 7.42 (t, 1H), 7.29 (dt, 2H), 6.96 (t, 2H).

Syntheses of Metal Complexes. $(NEt_4)_2$[(hybeb)Ru(NO)(OEt)]. A slurry containing 100 mg (0.3 mmol) of H_4hybeb and 200 mg (1.2 mmol) NEt_4Cl in 15 mL of ethanol was treated with 35 mg (1.4 mmol) of NaH under dinitrogen. The solution was then filtered to remove NaCl, producing a clear tan solution of the deprotonated ligand. Subsequently, 68 mg (0.3 mmol) of $RuNOCl_3$ dissolved in 10 mL of degassed ethanol was added to the reaction flask under dinitrogen via cannula generating an orange brown solution. The solution was heated under refluxing condition for 24 h and then cooled to room temperature. The solution was concentrated and cooled to -20° C. Upon addition of 5 mL of diethyl ether to the cold solution, an orange solid precipitated. The solid was filtered and washed several

times with diethyl ether and dried in vacuo. Yield: 52 mg (25%). Selected IR frequencies (KBr disk, cm^{-1}): 2982 (w), 1783 (ν_{NO}, s), 1594 ($\nu_{C=O}$, s), 1558 (s), 1526 (m), 1465 (vs), 1438 (vs), 1347 (vs), 1259 (m), 1034 (ν_{CO}, w), 761 (m). ^{1}H NMR (500 MHz, $(CD_3)_2SO$, δ from TMS): 9.08 (dd, 2H, J = 6 & 4 Hz), 8.12 (d, 2H, J = 8 Hz), 7.01 (t, 2H, J = 8 Hz), 6.77 (d, 2H, J = 8 Hz), 6.69 (dd, 2H, J = 6 & 4 Hz), 6.44 (t, 2H, J = 8 Hz), 3.37 (q, 2H, J = 7 Hz), 3.17 (q, 12H, J = 7 Hz), 1.13 (t, 18H, J = 7 Hz), 0.48 (t, 3H, J = 7 Hz). Electronic absorption spectrum, λ_{max}, nm (ε, M^{-1} cm^{-1}) in EtOH: 320 (23 270) and in MeCN: 325 (25 000).

(PPh_4)[(hypyb)Ru(NO)(OEt)]. A batch of 100 mg (0.3 mmol) of H_3hypyb was dissolved in 5 mL of ethanol and mixed with a solution containing 29 mg (1.2 mmol) of NaH in 5 mL ethanol to generate a light yellow solution. To this solution, 71 mg (0.3 mmol) of $RuNOCl_3$ dissolved in 5 mL of ethanol was added dropwise and the mixture was heated to reflux for 5 h. The resulting dark red brown solution was then treated with 135 mg (0.4 mmol) of PPh_4Cl. Subsequently, the solvent was removed and replaced with MeCN to filter off solid NaCl. About 5 mL of diethyl ether was added and the solution was cooled to -20° C. The mixture was filtered after 24 h to remove small quantity of an impurity. The filtrate, upon further cooling, afforded the desired product as an orange powder. The product was filtered and washed several times with diethyl ether and dried in vacuo. Yield: 120 mg (45%). Selected IR Frequencies (KBr disk, cm^{-1}): 3052(w), 1793 (ν_{NO}, vs), 1625 ($\nu_{C=O}$, vs), 1593 ($\nu_{C=O}$, vs), 1557 (vs), 1534 (s), 1462 (vs), 1436 (vs), 1342 (vs), 1108 (vs), 1042 (ν_{CO}, m), 756 (vs), 723 (vs), 688 (s), 526 (vs). ^{1}H NMR (500 MHz, $CDCl_3$, δ from

TMS): 9.06 (d, 1H, J = 8 Hz), 8.77 (d, 1H, J = 8 Hz), 8.60 (d, 1H, J = 8 Hz), 8.28 (t, 1H, J = 8 Hz), 8.15 (d, 1H, J = 8 Hz), 8.11 (d, 1H, J = 8 Hz), 7.96 (t, 4H, J = 8 Hz), 7.82 (m, 9H), 7.73 (dd, 8H, J = 1 & 8 Hz), 7.05 (t, 1H, J = 8 Hz), 6.86 (d, 1H, J = 8 Hz), 6.81 (t, 2H, J = 8 Hz), 6.46 (t, 1H, J = 8 Hz), 3.42 (q, 2H, J = 7 Hz), 0.38 (t, 3H, J = 7 Hz). Electronic absorption spectrum, λ_{max}, nm (ε, M^{-1} cm^{-1}) in EtOH: 315 (10 700) and in MeCN: 315 (9 250).

[Ru(bpb)(NO)(OEt)]. A slurry of 100 mg (0.3 mmol) of H_2bpb in 10 mL of ethanol was deprotonated via addition of 23 mg (0.9 mmol) of NaH dissolved in 5 mL of ethanol. A solution containing 74 mg (0.31 mmol) of $RuNOCl_3$ in 10 mL of ethanol was added to the flask containing the deprotonated ligand. The resulting dark orange solution was heated at reflux temp for 10 h. The solution was then cooled to -20° C to precipitate impurities and filtration. The filtrate was then concentrated and 5 mL of diethyl ether was added. Upon cooling, the target complex precipitated out as an orange solid which was filtered, washed several times with diethyl ether, and dried in vacuo. Yield: 62 mg (40%). Selected IR Frequencies (KBr disk, cm^{-1}): 2923(w), 1838 (ν_{NO}, s), 1632 ($\nu_{C=O}$, vs), 1595 (s), 1472 (s), 1356 (s), 1286 (m), 1047 (ν_{CO}, m), 782 (w), 752 (m), 683 (w) 502 (w). ^{1}H NMR (500 MHz, $(CD_3)_2SO$, δ from TMS): 9.34 (d, 2H, J = 6 Hz), 8.54 (dd, 2H, J = 6 & 4 Hz), 8.38 (t, 2H, J = 8 Hz), 8.19 (d, 2H, J = 8 Hz), 7.93 (t, 2H, J = 6 Hz), 7.08 (dd, 2H, J = 6 & 4 Hz), 3.34 (q, 2H, J = 7 Hz), 0.30 (t, 3H, J = 7 Hz). Electronic absorption spectrum, λ_{max}, nm (ε, M^{-1} cm^{-1}) in EtOH: 380 (7 680) and in MeCN: 380 (9 800).

3.2.8.2 Experimental Data: ^{1}H-NMR and IR Spectra

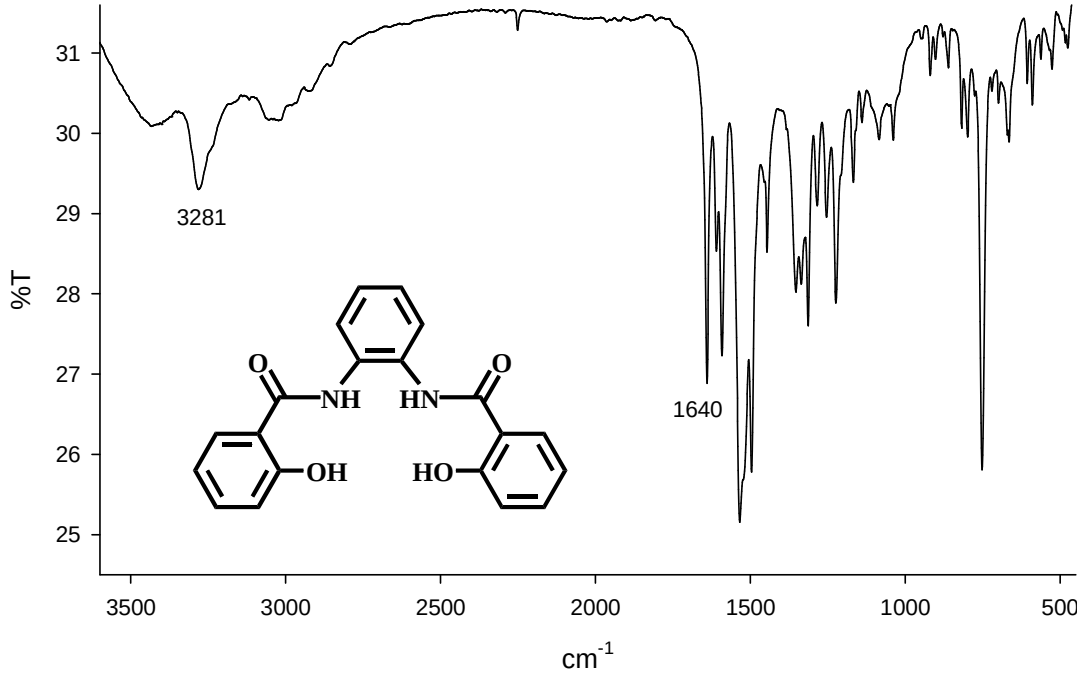

Figure 3.2.8. IR spectrum of H_4hybeb in KBr pellet

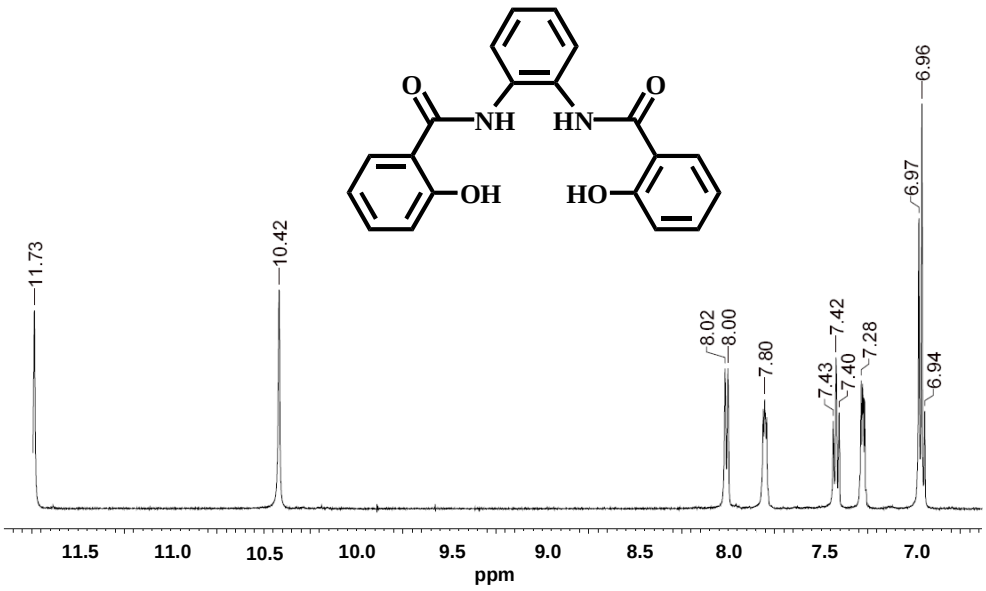

Figure 3.2.9. ^{1}H-NMR spectrum (6.7-11.9 ppm) of H_4hybeb in $((CD_3)_2SO)$ at 298 K

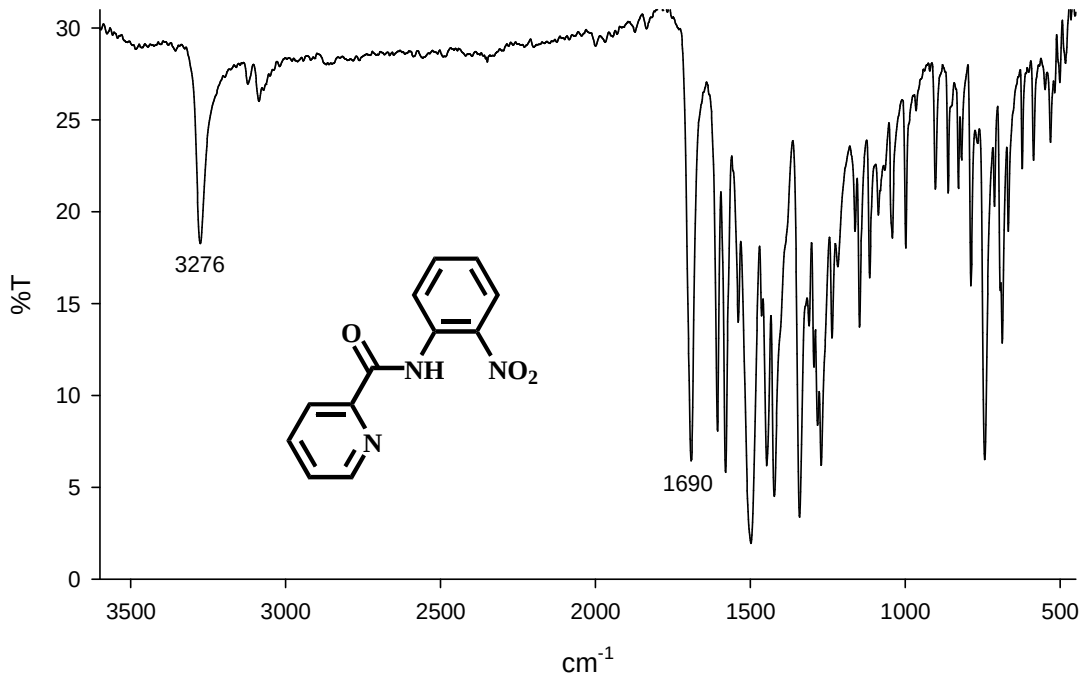

Figure 3.2.10. IR spectrum of Hpycan in KBr pellet

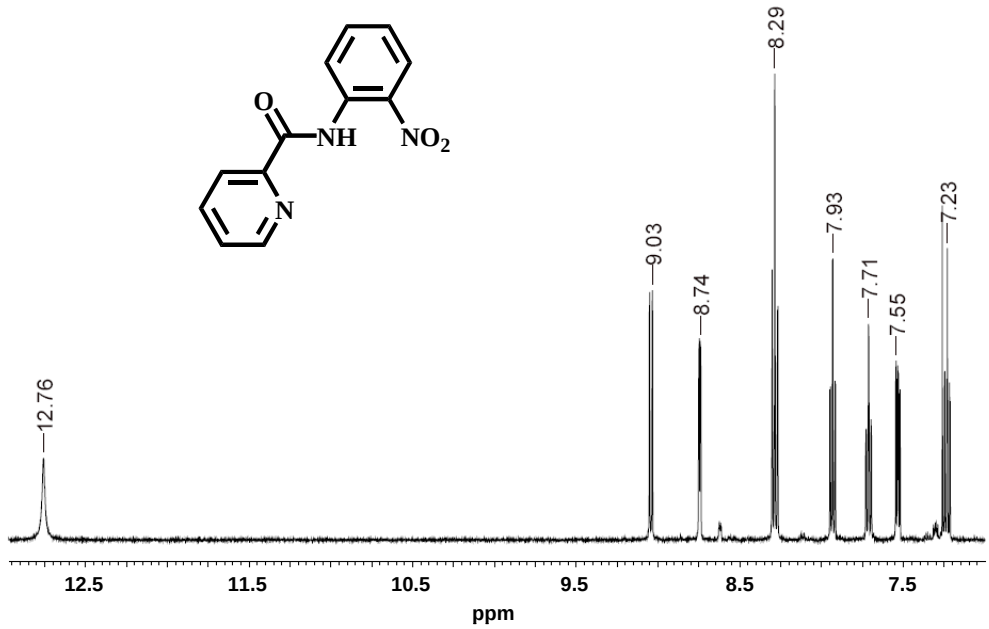

Figure 3.2.11. ^{1}H-NMR spectrum (7.0-13.0 ppm) of Hpycan in $CDCl_3$ at 298 K

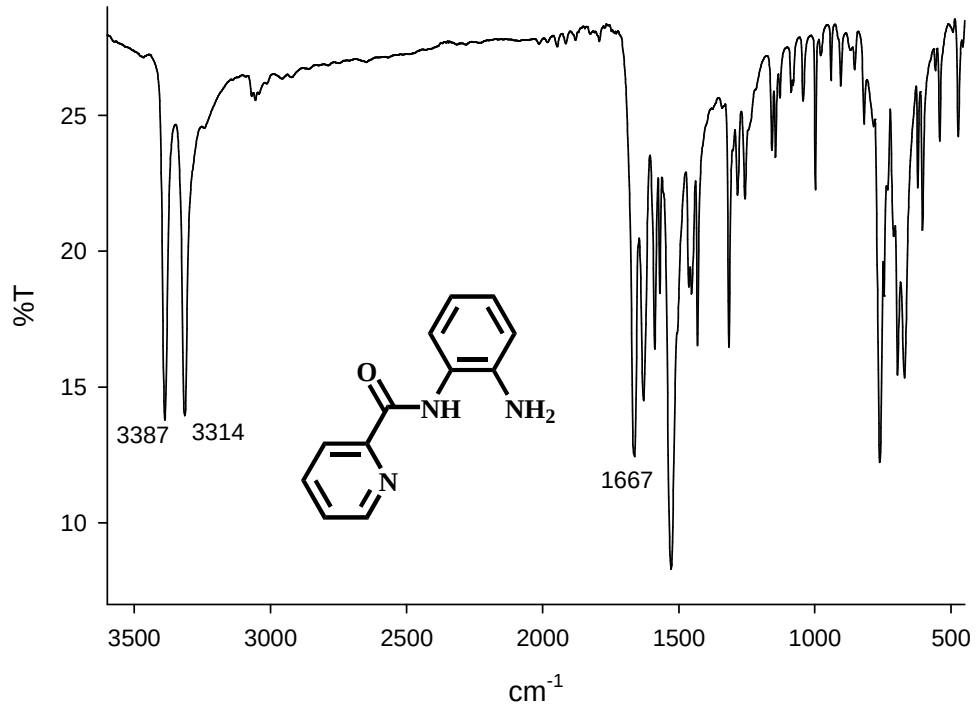

Figure 3.2.12. IR spectrum of Hpyca in KBr pellet

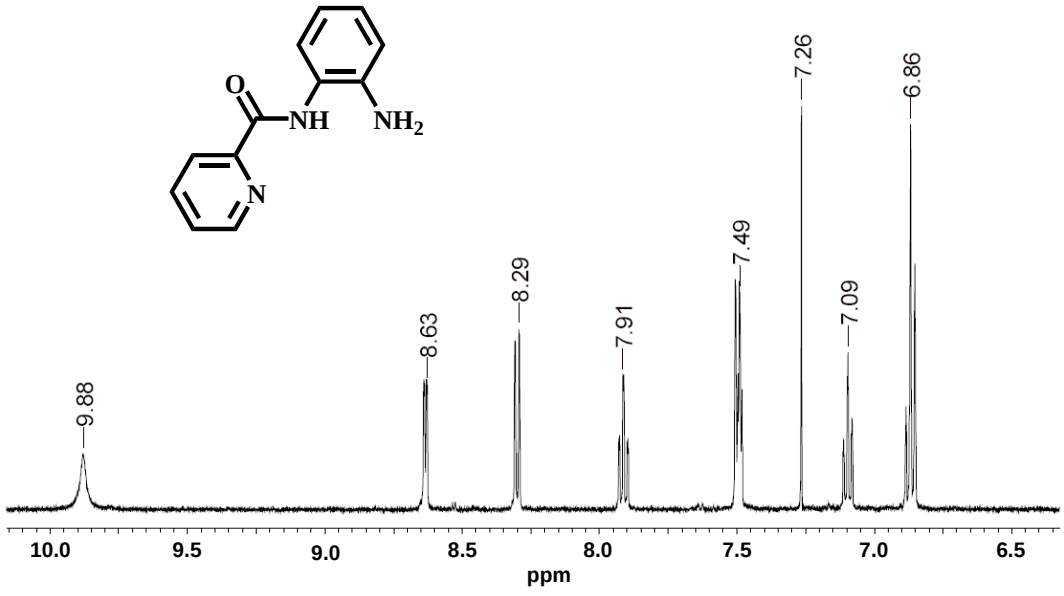

Figure 3.2.13. ^{1}H-NMR spectrum (6.2-10.2 ppm) of Hpyca in $CDCl_3$ at 298 K

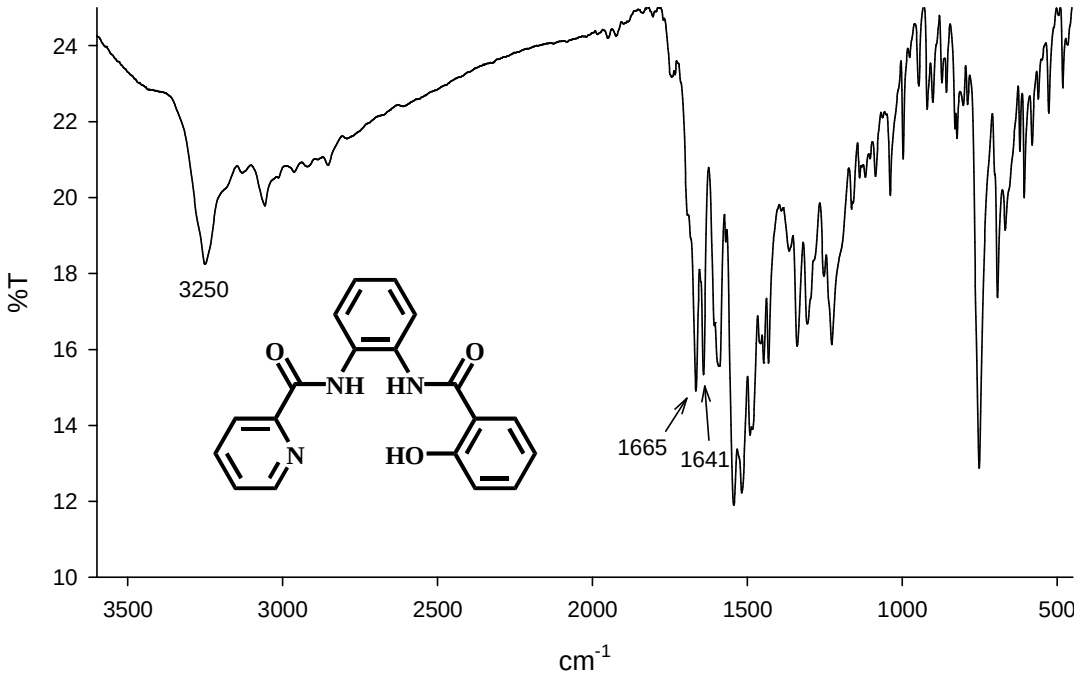

Figure 3.2.14. IR spectrum of H_3hypyb in KBr pellet

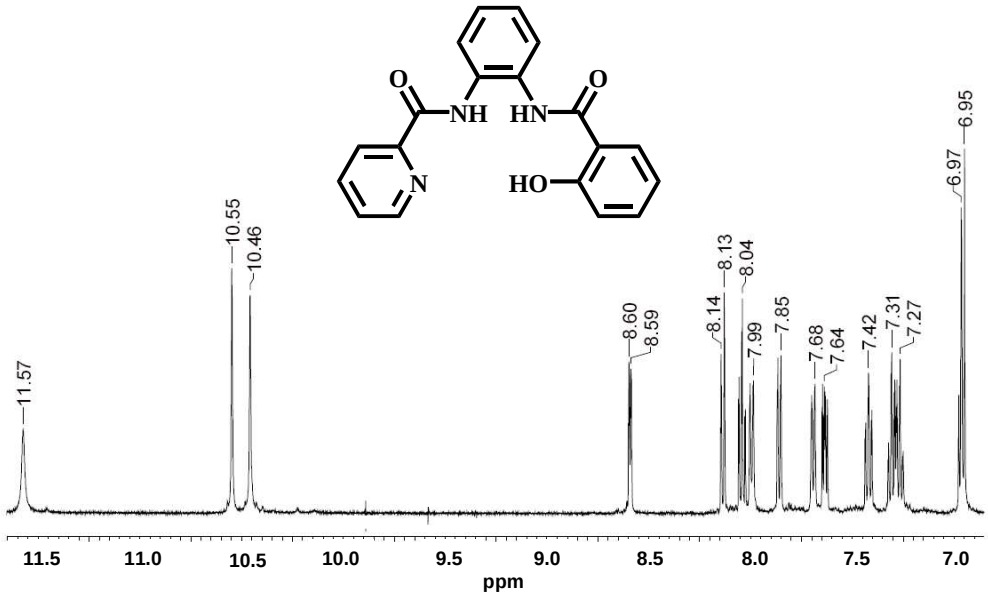

Figure 3.2.15. ^{1}H-NMR spectrum (6.9-11.6 ppm) of H_3hypyb in $(CD_3)_2SO$ at 298 K

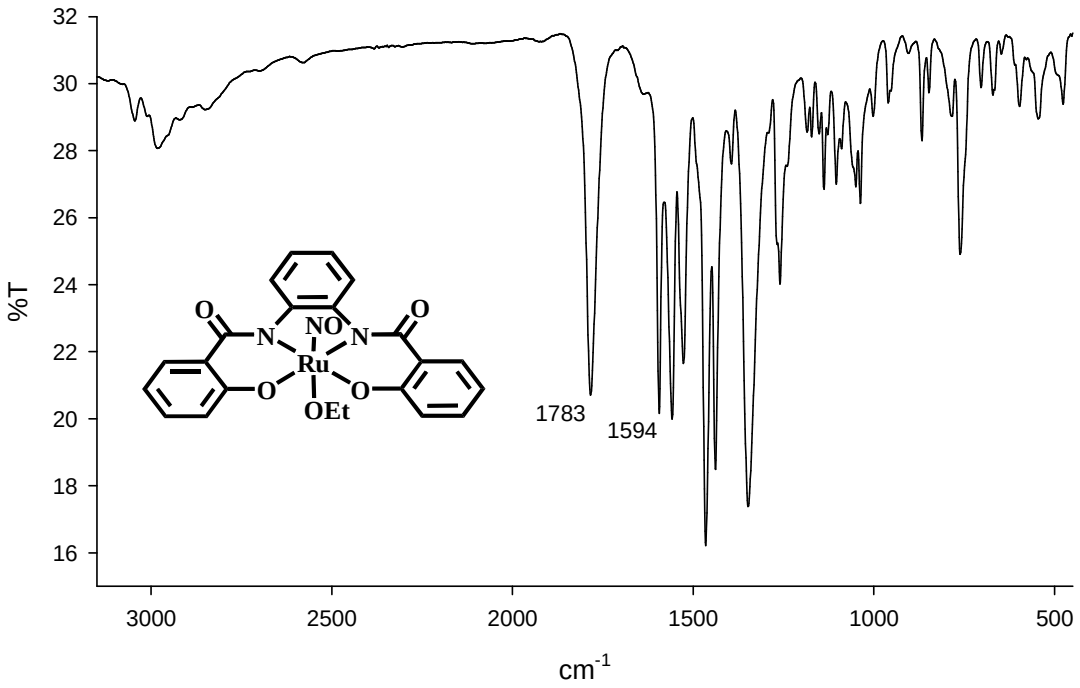

Figure 3.2.16. IR spectrum of $(NEt_4)_2$[(hybeb)Ru(NO)(OEt)] in KBr pellet

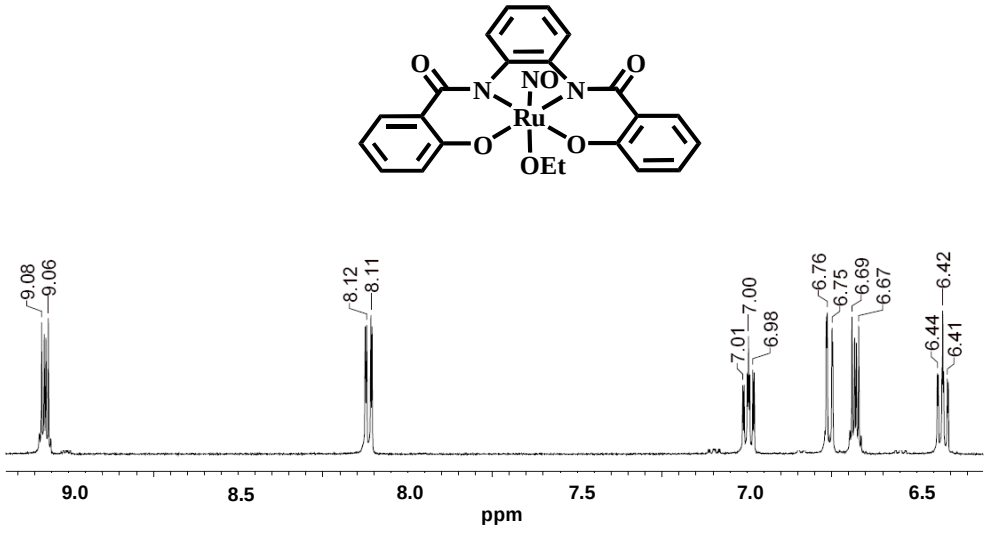

Figure 3.2.17. ^{1}H-NMR spectrum (6.3-9.2 ppm) of $(NEt_4)_2$[(hybeb)Ru(NO)(OEt)] in $(CD_3)_2SO$ at 298 K

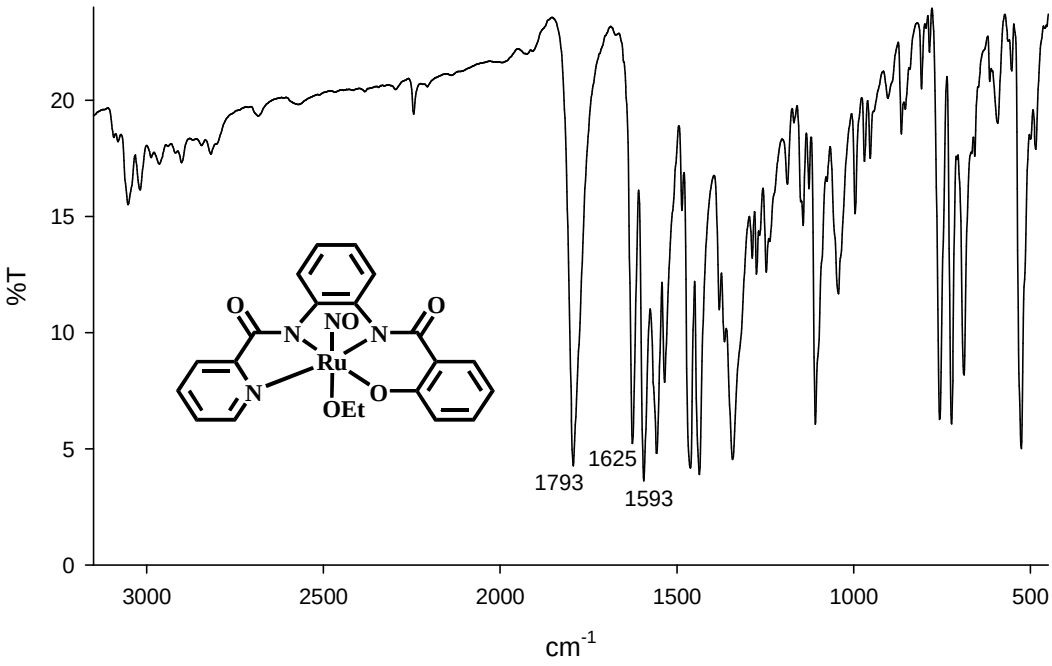

Figure 3.2.18. IR spectrum of (PPh_4)[(hypyb)Ru(NO)(OEt)] in KBr pellet

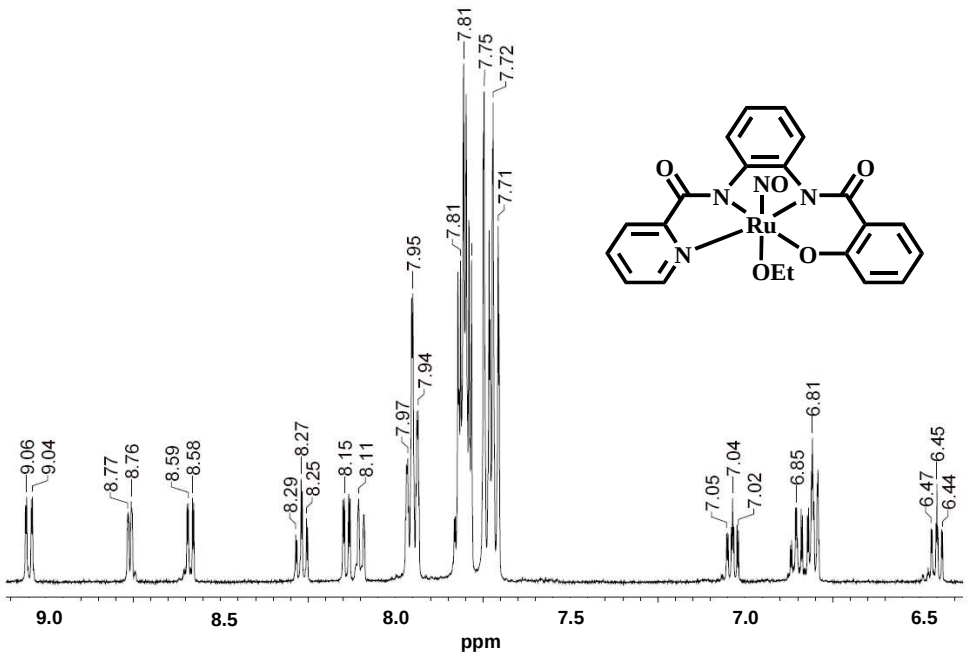

Figure 3.2.19. ^{1}H-NMR spectrum (6.4-9.1 ppm) of (PPh_4)[(hypyb)Ru(NO)(OEt)] in $(CD_3)_2SO$ at 298 K

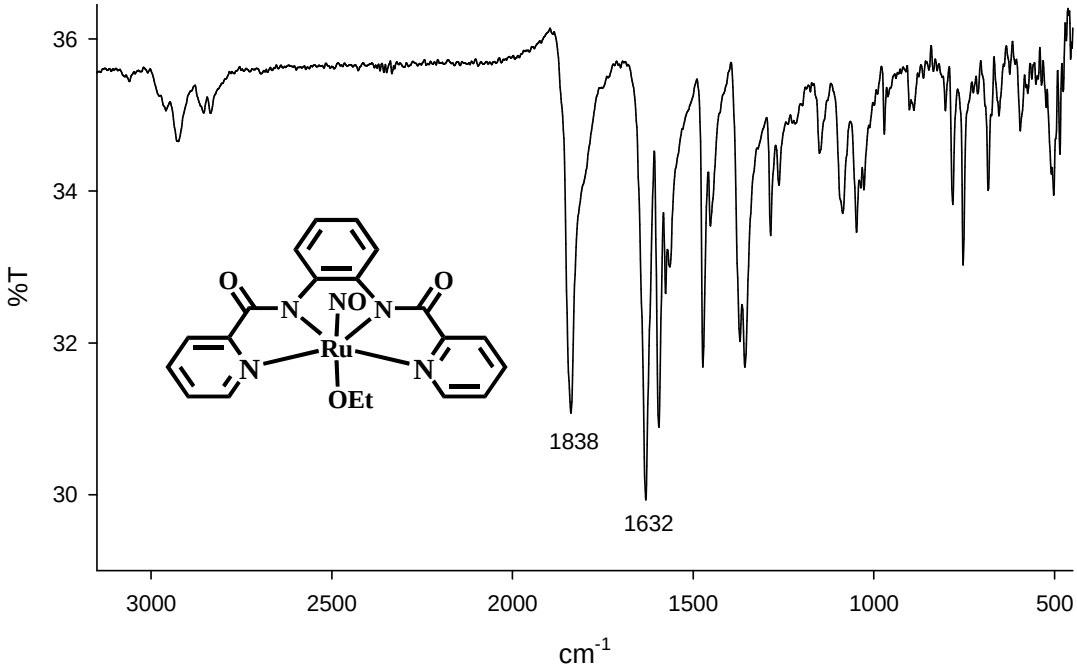

Figure 3.2.20. IR spectrum of [(bpb)Ru(NO)(OEt)] in KBr pellet

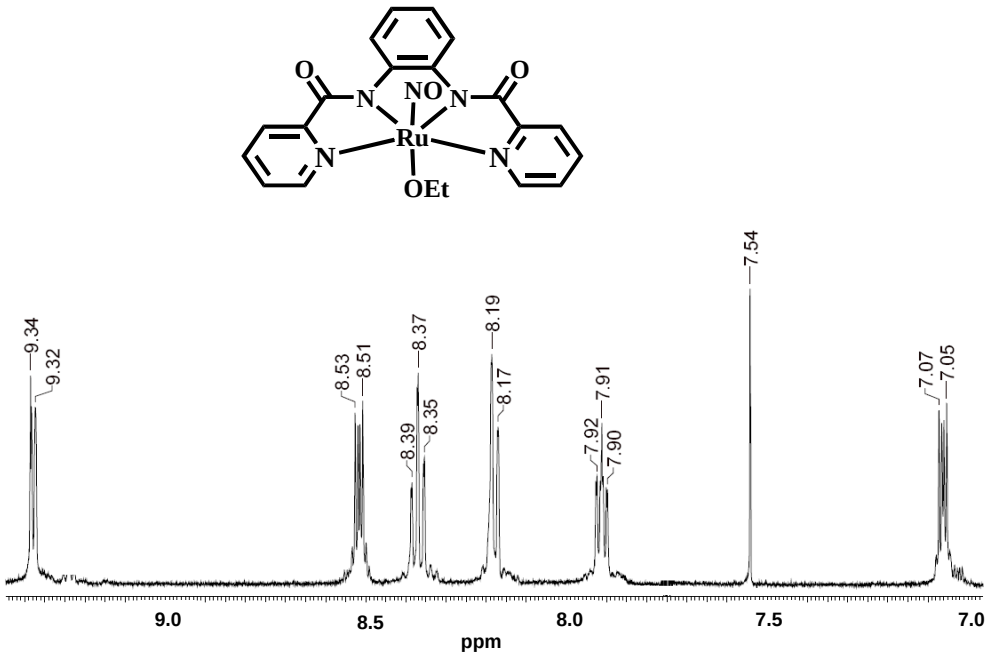

Figure 3.2.21. ^{1}H-NMR spectrum (7.0-9.5 ppm) of [(bpb)Ru(NO)(OEt)] in $(CD_3)_2SO$ at 298 K

3.2.9 References

1. The $\{M\text{-}NO\}^n$ notation used in this paper is that of Feltham and Enemark. See Enemark, J. H.; Feltham, R. D. *Coord. Chem. Rev.* **1974**, *13*, 339.

2. Groelsky, S. I.; da Silva, S. C.; Lever, A. B. P.; Franco, D. W. *Inorg. Chim. Acta.* **2000**, *30*, 689.

3. Tfouni, E.; Krieger, M.; McGarvey, B. R.; Franco, D. W. *Coord. Chem. Rev.* **2003**, *236*, 5769.

4. (a) Rose, M. J.; Mascharak, P. K. *Coord. Chem. Rev*. **2008**, *252*, 2093. (b) Rose, M. J.; Mascharak, P. K. *Curr. Opin. Chem. Biol*. **2008**, *12*, 238.

5. (a) Ford, P. C.; Lorkovic, I. M. *Chem. Rev*. **2002**, *102*, 993. (b) Ford, P. C.; Bourassa, J.; Miranda, K.; Lee, B.; Lorkovic, I.; Boggs, S.; Kudo, S.; Laverman, L. *Coord. Chem. Rev.* **1998**, *171*, 185.

6. Works, C. F.; Jocher, C. J.; Bart, G. D.; Bu, X.; Ford, P. C. *Inorg. Chem*. **2002**, 41, 3728.

7. Patra, A. K.; Rose, M. J.; Murphy, K. M.; Olmstead, M. M.; Mascharak, P. K. *Inorg. Chem.* **2004**, *43*, 4487.

8. Sizova, O. V.; Ivanova, N. V.; Sizov, V. V.; Nikol'skii, A. B. *Russ. J. Gen. Chem.* **2004,** *74*, 481.

9. Rose, M. J.; Mascharak, P. K. *Inorg. Chem.* **2009**, *48*, 6904.

10. (a) Carlos, R. M.; Cardoso, D. R.; Castellano, E. E.; Osti, R. Z.; Camargo, A. J.; Macedo, L. G.; Franco, D. W. *J. Am. Chem. Soc.* **2004**, *126*, 2546. (b) Lang,

D. R.; Davis, J. A.; Lopes, L. G. F.; Ferro, A. A.; Vasconcellos, L. C. G.; Franco, D. W.; Tfouni, E.; Wieraszko, A.; Clarke, M. J. *Inorg. Chem.* **2000**, *39*, 2294. (c) da S. S. Borges, S.; Davanzo, C. U.; Castellano, E. E.; Z-Schpector, J.; Silva, S. C.; Franco, D. W. *Inorg. Chem.* **1998**, *37*, 2670 (d) Allen, A. D.; Bottomley, F.; Harris, R. D.; Reinslau, V. P.; Senoff, C.V. *Inorg. Synth.* **1970**, *12*, 2.

11. (a) Patra, A. K.; Olmstead, M. M; Mascharak, P. K. *Inorg. Chem.* **2003**, *42*, 7363. (b) Ko, P.; Chen, T.; Zhu, J.; Cheng, K.; Peng, S.; Che, C. *J. Chem. Soc. Dalton Trans.* **1995**, *1*, 215. (c) Pipes, D. W.; Meyer, T. J. *Inorg. Chem.* **1984**, *23*, 2466.

12. (a) Leung, W.; Chan, E. Y. Y.; Chow, E. K. F.; Williams, I. D.; Peng, S. *J. Chem. Soc. Dalton Trans*. **1996**, *15*, 1229. (b) Odenkirk, W.; Rheingold, A. L.; Bosnich, B. *J. Am. Chem. Soc.* **1992**, *114*, 6392.

13. (a) Rose, M. J.; Patra, A. K.; Alcid, E. A.; Olmstead, M. M.; Mascharak, P. K. *Inorg. Chem.* **2007**. *46*, 2328. (b) Rose, M. J.; Olmstead, M. M.; Mascharak, P. K. *Polyhedron* **2007**, *26*, 4713.

14. Barnes, D. J.; Chapman, R. L.; Vagg, R. S.; Watton, E. C. *J. Chem. Eng. Data* **1978**, *23*, 349.

15. Keramidas, A. D.; Papaioannou, A. B.; Vlahos, A.; Kabanos, T. A.; Bonas, G.; Makriyannis, A.; Rapropoulou, Terzis, A. *Inorg. Chem*. **1996**, 35, 357.

16. Hanson, G. R.; Kabanos, T. A.; Keramidas, A. D.; Mentzafos, D; Terzis, A. *Inorg. Chem*. **1992**, 31, 2587.

17. Allen, F. H. *Acta Cryst.* **2002**, *B58*, 380.

18. Rose, M. J.; Fry, N. L.; Marlow, R.; Hink, L.; Mascharak, P. K. *J. Am. Chem. Soc.* **2008**, *130*, 8834.

19. Nazeeruddin, M. K.; De Angelis, F.; Fantacci, S.; Selloni, A.; Viscardi, G.; Liska, P.; Ito, S.; Takeru, B.; Grätzel, M. *J. Am. Chem. Soc.* **2005**, *127*, 16835.

20. Nemukhin, A. V.; Grigorenko, B. L.; Granovsky, A. A. *Moscow Univ. Chem. Bull.* **2004**, *45*, 75.

21. Waller, M. P.; Braun, H.; Hojdis, N.; Bühl, M. J. *Chem. Theory Comput.* **2007**, 3, 2234.

22. Miertus, S.; Scrocco, E.; Tomasi, J. *Chem. Phys.* **1981**, *55*, 117.

23. Waller, M. P.; Braun, H.; Hojdis, N.; Bühl, M. *J. Chem. Theory Comput.* **2007**, *3*, 2234.

24. Zhurko, G. A. ChemCraft Software Version 1.6 (http://www.chemcraftprog.com)

25. Barnes, D. J.; Chapman, R. L.; Vagg, R. S.; Watton, E. C. *J. Chem. Engin. Data* **1978**, *23*, 349.

Chapter 4

Fluorescent Dye Bound Ruthenium Nitrosyls

4.1 Introduction

Although alteration of ligand frames allowed us to achieve good sensitivity of the designed $\{RuNO\}^6$ nitrosyls to visible light, the quantum yield values of NO photorelease with 500 nm light (ϕ_{500}) for these nitrosyls remained somewhat modest, in the range of 0.010-0.030. In an effort to further increase the visible light absorption by our ruthenium nitrosyls and enhance their ϕ_{500} values, we adopted a new strategy of attaching dye chromophores (as light-harvesting units) to these nitrosyls and determined their effects on the NO photolability of the resulting dye-bound nitrosyls under visible light. Previously, Ford and coworkers have connected chromophores like protoporphyrin IX ($\lambda_{max} \approx 400$ nm) and fluorescein ($\lambda_{max} \approx 450$ nm) via $(CH_2)_n$ linkers to Roussin's salt esters (generating PPIX-RSE or Fluor-RSE).[1,2] This indirect dye attachment led to moderate improvement in the quantum yield of NO photolability (ϕ in the range of 0.00025-0.00052). We decided to improve upon this strategy by *directly conjugating* selected visible light-absorbing chromophores to the [RuNO] unit to enhance the sensitivity of our ruthenium nitrosyls to visible light.[3,4]

In previous work from this laboratory, the tricyclic phenoxazin dye Resorufin (Resf) with a phenolato moiety was employed for direct metal conjugation. A series of $\{RuNO\}^6$ nitrosyls with various dicarboxamide tetradentate ligands, namely [(Me_2-bpb)Ru(NO)(Cl)], [(Me_2bQb)Ru(NO)(Cl)], and [(($OMe)_2$bQb)Ru(NO)(Cl)] were sensitized to 500 nm visible light via substitution of the chloride ligand with Resf (Figure 4.1).[5] While the resulting resorufin-bound nitrosyls all exhibit absorption

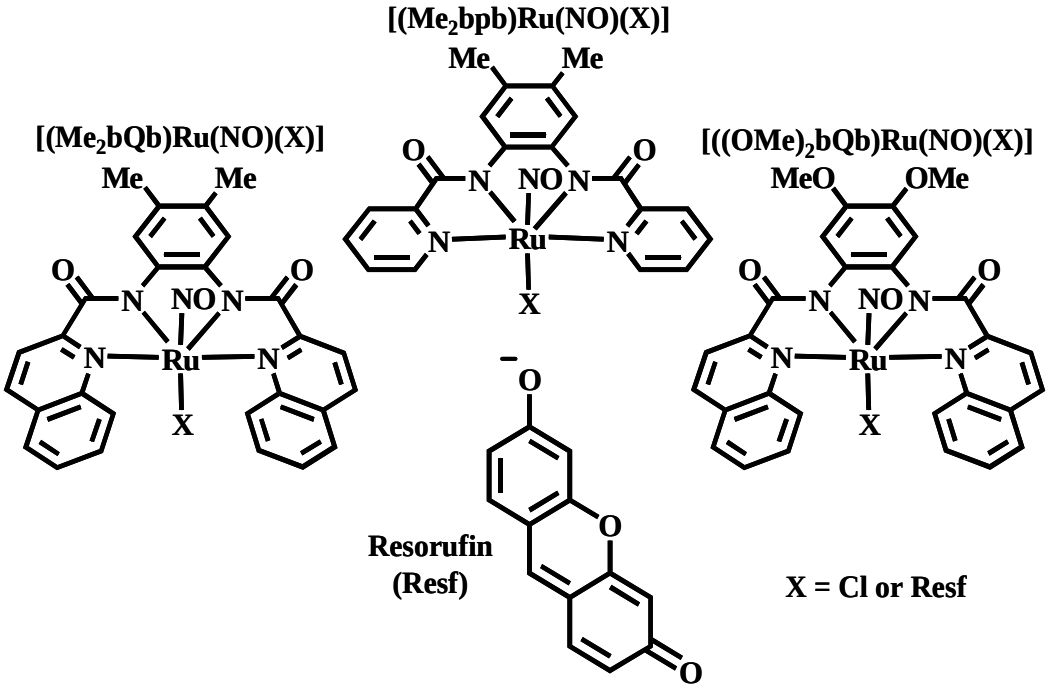

Figure 4.1. Ruthenium nitrosyls derived from $[Me_2bpb]^{2-}$, $[Me_2bQb]^{2-}$, or $[(OMe)_2bQb]^{2-}$ ligand frames with chloride or resorufin bound trans to NO

bands with λ_{max} of 500nm, their efficiencies of NO photorelease upon exposure to 500 nm light can be modulated by rational substitutions in the in-plane ligand frame. For example, substitution of the pyridine donors in the ligand frame of [(Me_2-bpb)Ru(NO)(Resf)] with quinoline donors in [(Me_2bQb)Ru(NO)(Resf)] and substitution of the methyl groups with more electron donating methoxy groups in [((OMe)$_2$bQb)Ru(NO)(Resf)] both result in higher quantum yield values at 500 nm ($\phi_{500} \approx 0.05$, 0.10, and 0.20, respectively).[5b] The different ligand frames also lead to differences in the stabilities of the resorufin-bound nitrosyls in solution. For example, both quinoline containing [(Me_2bQb)Ru(NO)(Resf)] and [((OMe)$_2$bQb)-Ru(NO)(Resf)] have reduced stability in aqueous solutions compared to

[(Me_2bpb)Ru(NO)(Resf)] which comprises pyridine donors. Close examination of the structural features of these nitrosyls revealed that the ligand frames containing the quinoline donors (H_2R_2bQb) bind the {RuNO}^{6} center in a twisted fashion due to steric interactions between the two quinoline moeities in the equatorial plane (Figure 4.2). In order to probe the effect(s) of this twist on the stability and NO photolability of the resorufin-bound {RuNO}^{6} nitrosyls, we have now designed new dicarboxamide ligands containing methoxy-substituted phenylenediamine rings combined with pyridine ($H_2(OMe)_2$bpb) or 1-isoquinoline ($H_2(OMe)_2$IQ1) donors and methyl-substituted phenylenediamine rings combined with 3-isoquinoline (H_2Me_2IQ3) or 1-isoquinoline ($H_2(OMe)_2$IQ1) donors (Figure 4.3).

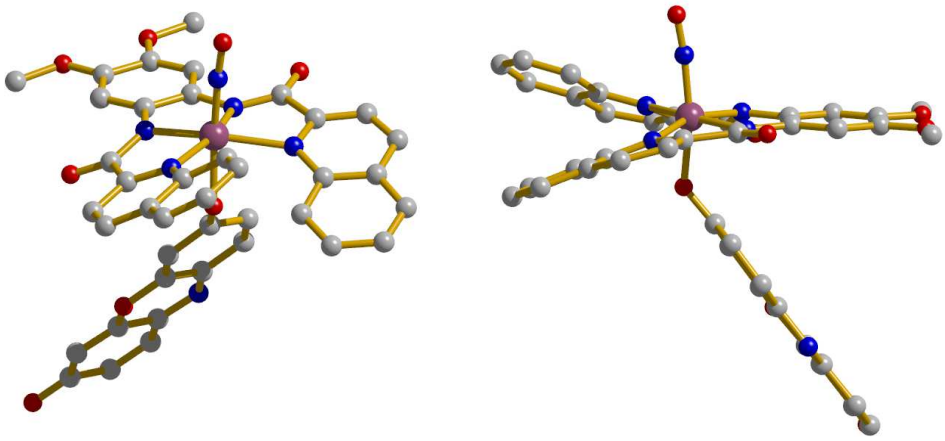

Figure 4.2. X-ray structure of [(($OMe)_2$bQb)Ru(NO)(Resf)] from front angle (left) and side angle (right) displaying twist of the in plane tetradentate ligand. H atoms are omitted for the sake of clarity.

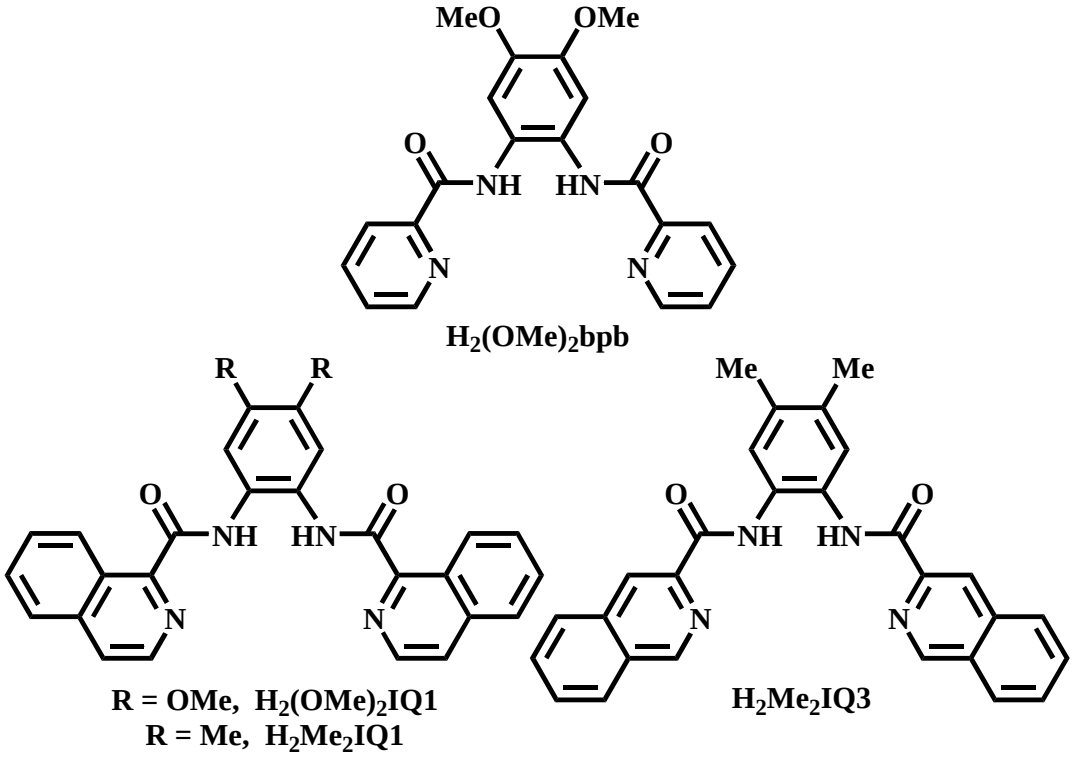

Figure 4.3. Methyl- and methoxy-substituted tetradentate dicarboxamide ligands with pyridine, 1-isoquinoline, or 3-isoquinoline donors

Free resorufin is a very efficient fluorophore that exhibits red fluorescence upon light exposure. Although the fluorescence of the free dye is partly quenched when Resf is directly attached to the Ru-center of the {RuNO}^{6} nitrosyls, the residual fluorescence of [(Me_2bpb)Ru(NO)(Resf)] is enough to visualize the complex in cellular matrices.[5b] This allowed us to track the NO donor within the biological targets. In order to extend this concept further and develop new trackable NO donors, we chose fluorescein as the next chromophore (Figure 4.4). Fluorescein is a green fluorescent dye commonly used for biological studies.[6,7] We were interested to see how attachment of fluorescein derivatives such as fluorescein ethyl ester (FlEt) and

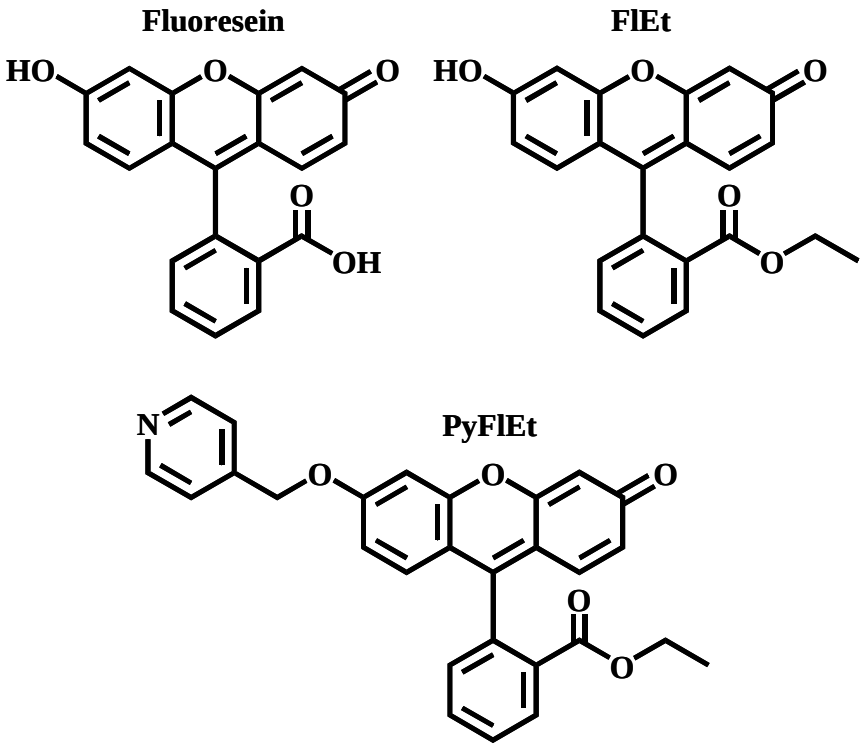

Figure 4.4. Fluorescein dye and its derivatives fluorescein ethyl ester (FlEt) and 4-(pyridinyloxy)-fluorescein ethyl ester (PyFlEt)

4-(pyridinyloxy)-fluorescein ethyl ester (PyFlEt) to the Ru center of our designed ruthenium nitrosyls would affect the fluorescence and NO photolability of the resulting nitrosyls upon exposure to 500 nm light (Figure 4.4).

4.2 Syntheses of Planar Ligand Frames

In order to remove the twist of the bQb^{2-} ligand frame in the equatorial planes of [$(Me_2bQb)Ru(NO)(Cl)$] and [$((OMe)_2bQb)Ru(NO)(Cl)$]**,** we selected the more spread-out 1-isoquinoline or 3-isoquinoline groups in the designed ligands

$H_2(OMe)_2IQ1$, H_2Me_2IQ1, and H_2Me_2IQ3. Such a change does not affect the extended conjugation in the ligand frame, yet ensures removal of the twist in the coordinated equatorial plane ligand frame of the nitrosyls with minimum changes in other parameters (Figure 4.5). To complete the investigation on the effect(s) of the twist, we also designed the methoxy substituted pyridine-based ligand, $H_2(OMe)_2bpb$. When coordinated, the pyridine rings of this ligand remain far apart in the equatorial plane of the nitrosyls and hence no steric interaction between them is expected.

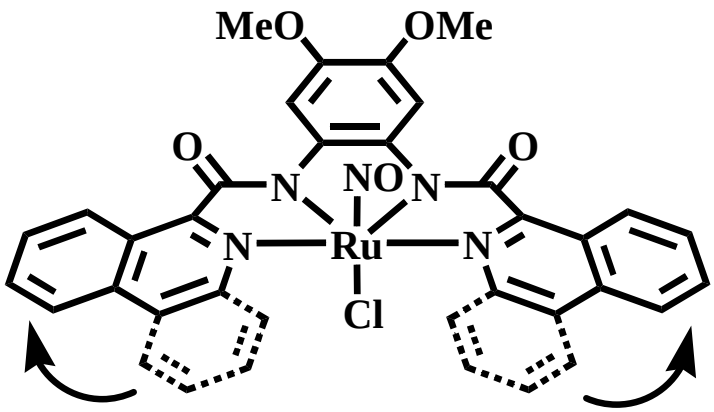

Figure 4.5. The design of the new ligand $(OMe)_2IQ1$, intended for relieving twist in the equatorial plane of these $\{RuNO\}^6$ nitrosyls

All four of the new ligand frames were synthesized using similar reaction conditions to those of H_2Me_2bQb and $H_2(OMe)_2bQb$ in which triphenyl phosphite acts as the amide coupling reagent in pyridine.[8,5b] Specifically, the methyl-substituted ligand frames H_2Me_2IQ1 and H_2Me_2IQ3, were synthesized by reaction of one equiv of 4,5-dimethyl-1,2-phenylenediamine with 2 equiv of either 1-isoquinolinecarboxylic acid or 3-isoquinolinecarboxylic acid, respectively. Synthesis

of the methoxy-substituted ligand frames, first requires the preparation of l,2-dimethoxy-4,5-phenylenediamine via reduction of l,2-dimethoxy-4,5-dinitrobenzene with excess hydrazine over Pd/C (Figure 4.6).[9] The resulting diamine (which is air sensitive) is then immediately reacted with 2 equiv of either picolinic acid or 1-isoquinolinecarboxylic acid to afford $H_2(OMe)_2bpb$ and $H_2(OMe)_2IQ1$, respectively.

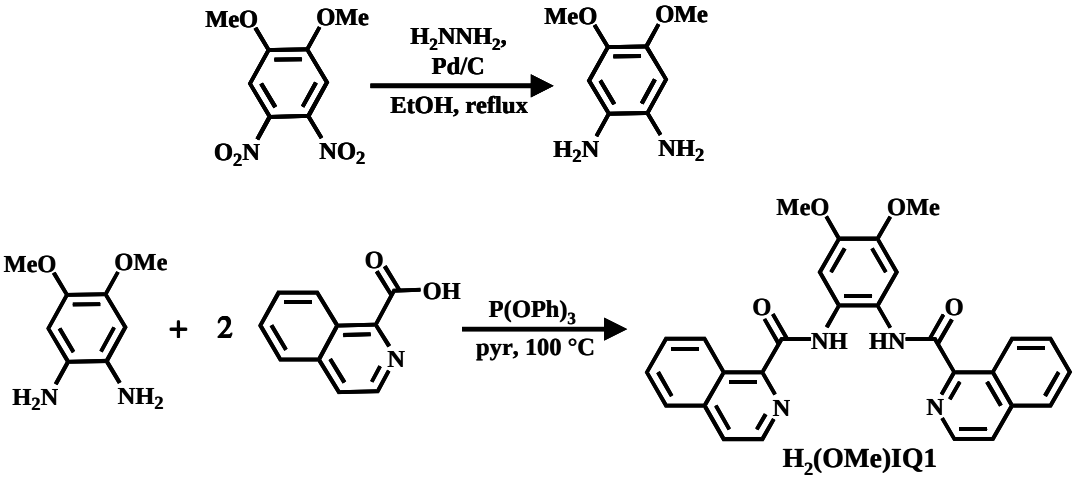

Figure 4.6. Reaction scheme of the $H_2(OMe)IQ1$ ligand frame

The pyridine containing ligand $H_2(OMe)_2bpb$ is isolated as a white solid similar to H_2Me_2bpb while the added conjugation of 1-isoquinoline moieties results in both H_2Me_2IQ1 and $H_2(OMe)_2IQ1$ a bright yellow color similar to $H_2(OMe)_2bQb$. Interestingly in case of 3-isoquinoline, there is no added color as H_2Me_2IQ3 is a white solid. A similar trend holds true when comparing the absorption band λ_{max} of the

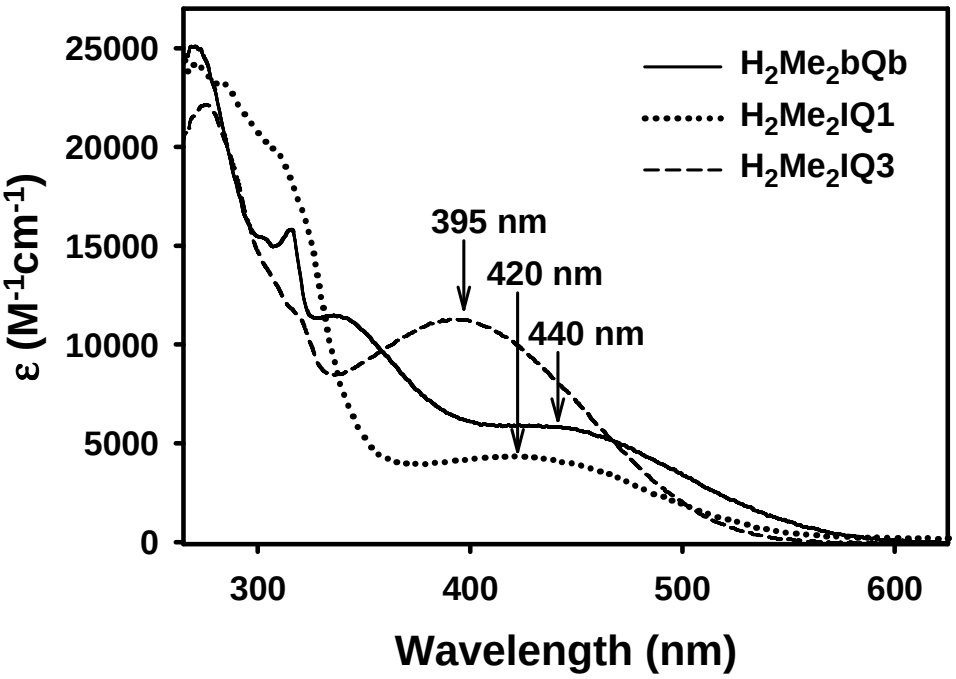

Figure 4.7. Electronic absorption spectra of the methyl-substituted quinoline containing ligand frames deprotonated with NaH in DMF

methyl-substitued ligand frames in their deprotonated form (deprotonated with 2 equiv of NaH in DMF, Figure 4.7). H_2Me_2IQ3 has the highest energy absorption band with its λ_{max} at 395 nm while the λ_{max} of both H_2Me_2IQ1 and $H_2(OMe)_2bQb$ are red-shifted to 420 and 440 nm, respectively. However the absorption band of H_2Me_2IQ3 is more intense than those of H_2Me_2IQ1 and $H_2(OMe)_2bQb$.

4.3 Syntheses and Characterization of Cl-Bound Metal Nitroyls

Reaction of $RuCl_3$ with the deprotonated (with NaH) dicarboxamide ligands in *N*,*N*-dimethylformamide (DMF) followed by the addition of NO(g) afords the

corresponding chloride bond species. The resulting nitroysls with methoxy-substituted ligand frames, namely [((OMe)$_2$bpb)Ru(NO)(Cl)] and [((OMe)$_2$IQ1)Ru-(NO)(Cl)], were isolated as pure compounds in good yield by removing the DMF and extracting the residues with MeCN. However, we were unable to obtain analytically pure samples of [(Me$_2$IQ1)Ru(NO)(Cl)] and [(Me$_2$IQ3)Ru(NO)(Cl)]. Given the supior absorption properties and ease of purification of the nitrosyls derived from the methoxy-substituted ligand frames, we decided to put all of our effort into the characterization of [((OMe)$_2$bpb)Ru(NO)(Cl)] and [((OMe)$_2$IQ1)Ru(NO)(Cl)].

4.3.1 Structure of [((OMe)$_2$bpb)Ru(NO)(Cl)]

The ^{1}H-NMR and IR spectra of [((OMe)$_2$bpb)Ru(NO)(Cl)] both confirm formation of the desired nitrosyl. For example, the carbonyl stretching frequency ($\nu_{C=O}$) of the free ligand H$_2$(OMe)$_2$bpb (1676 cm^{-1}) shifts to lower energy upon formation of complex (1631 cm^{-1}) and the complex exhibits its NO stretching frequency (ν_{NO}) at 1845 cm^{-1}, which is typical for neutral {RuNO}^{6} nitrosyl containing dicarboxamide tetradentate ligands and a trans Cl$^-$ ligand. In addition, we expect the [(OMe)$_2$bpb]$^{2-}$ ligand frame of [((OMe)$_2$bpb)Ru(NO)(Cl)] to be bound in a similarly planar fashion to that of the related Resf-bound nitrosyl (as evidenced by the X-ray structure of [((OMe)$_2$bpb)Ru(NO)(Resf)], vide infra).

4.3.2 X-ray Structure of [((OMe)$_2$IQ1)Ru(NO)(Cl)]

The X-ray structure of [((OMe)$_2$IQ1)Ru(NO)(Cl)] confirms that the presence of 1-isoquinoline moieties in [(OMe)$_2$IQ1]$^{2-}$ instead of regular quinoline (as in [(OMe)$_2$bQb]$^{2-}$) allows the ligand to remain *strictly planar* when bound to the ruthenium center in equatorial plane (Figure 4.8). This is in contrast to the steric

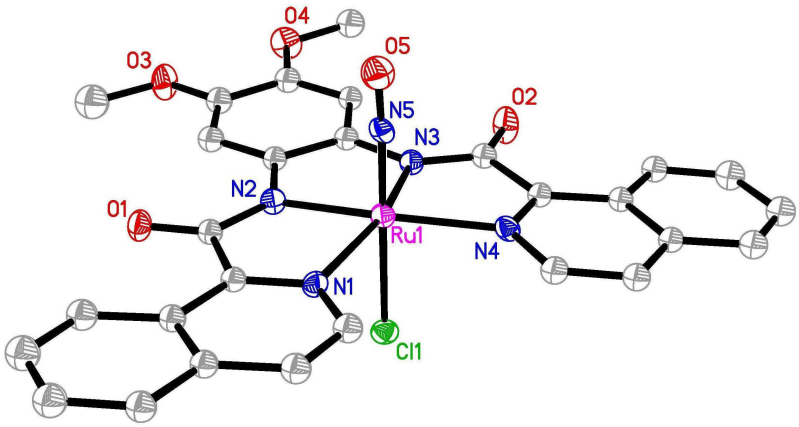

Figure 4.8. Thermal ellipsoid (probability level 50%) plot of [((OMe)$_2$IQ1)Ru(NO)(Cl)] with select atom-labeling. H atoms are omitted for the sake of clarity.

interaction of the extended quinoline groups in the (OMe)$_2$bQb^{2-} ligand of [((OMe)$_2$bQb)Ru(NO)(Cl)] that led to the twisting of the ligand (~ 35°) as noted in our previous work (Figure 4.9).[5] A chloride ligand is bound trans to NO in the axial positions generating a nearly octahedral geometry in the structure of [((OMe)$_2$IQ1)Ru(NO)(Cl)]. Examination of bond lengths reveals that the Ru–N5(O) (1.735(3) Å) and N5–O5 (1.153(3) Å) bond lengths of [((OMe)$_2$IQ1)Ru(NO)(Cl)] are very similar to those of [((OMe)$_2$bQb)Ru(NO)(Cl)] (1.7457(18) and 1.148(2) Å [5b]

respectively). Both nitrosyls contain almost linear Ru–N5–O5 bond angles ([((OMe)$_2$bQb)Ru(NO)(Cl)] =175.73(19) Å [5b]; [((OMe)$_2$IQ1)Ru(NO)(Cl)] = 175.9(2) Å), typical of {RuNO}^{6} nitrosyls.

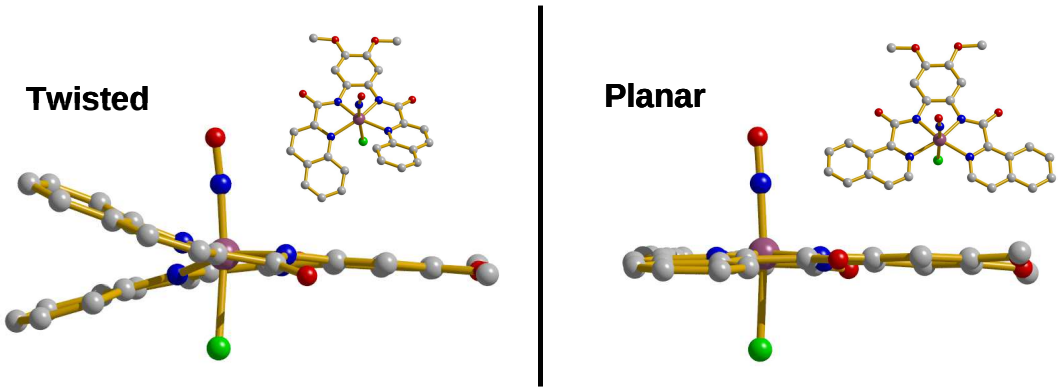

Figure 4.9. X-ray structures of [((OMe)$_2$bQb)Ru(NO)(Cl)] (left) and [((OMe)$_2$IQ1)Ru(NO)(Cl)] (right), displaying the differing amounts of twist in their in-plane ligand frames

4.3.3 Comparison of Electronic Absorption Spectra of the Cl-bound Ruthenium Nitroyls

Substitution of the aromatic ring(s) of the ligand frame alter the electron-donating and accepting capacities of the donor centers in the series of ruthenium nitrosyls with ligands containing electron donating groups of increasing strength (H, Me, OMe) on the phenylenediamine region of the ligand frame, namely [(bpb)Ru(NO)(Cl)],[8] [(Me$_2$bpb)Ru(NO)(Cl)],[8] and [((OMe)$_2$bpb)Ru(NO)(Cl)]. The photoband of the these {RuNO}^{6} nitrosyl is systematically shifted from 380 nm to 395 nm to 420 nm respectively (Figure 4.10). The basis of this phenomenon can be understood with the help of the previously described TDDFT study (Ch.3, part 2), in which the photoband of ruthenium nitrosyls with bpb^{2-} type ligand frames was

assigned to a π(PDA)–π(RuNO) → π*(RuNO)π(Py) transition. Such a transition would indeed require less energy with the addition of electron donating groups of increasing strength on the PDA moiety. This set of $\{RuNO\}^6$ nitrosyls clearly demonstrates that the π(PDA)–π(RuNO) → π*(RuNO)π(Py) transition can be readily manipulated by appropriate substitution on the ligand frame. In addition, the extinction coefficient (ε) of the photoband also increases significantly when a strongly electron-donating group (like OMe) is added to the PDA moiety. Thus, $[((OMe)_2bpb)Ru(NO)(Cl)]$ exhibits an ε value of 7 800 $M^{-1}cm^{-1}$ which is greater than the ε value of [(bpb)Ru(NO)(Cl)]
(5 100 $M^{-1}cm^{-1}$).[8]

Just as the position of the photoband of the $\{RuNO\}^6$ nitrosyls can be adjusted via substitution, extension of conjugation through replacement of the pyridine rings with either quinoline (Q) or 1-isoqulinoline (IQ1) moieties can also lead to enhanced sensitivity to visible light (Figure 4.11). For example, the addition of Q in $[((OMe)_2bQb)Ru(NO)(Cl)]$ (490 nm) results in a 70 nm red shift in the absorption maximum (λ_{max}) of the photoband compared to that of $[((OMe)_2bpb)Ru(NO)(Cl)]$ (420 nm). With the use of IQ1 in $[((OMe)_2IQ1)Ru(NO)(Cl)]$ (475 nm), there is a more modest red shift of 55 nm. When the ε values of the Cl-bound {RuNO} are compared, another interesting trend becomes evident. As the twist of the bound Q-based ligand frames is relieved and the electron-donating effects of the substituents are increased, the overall ε values of the photobands of the nitrosyls (in the 350-600

nm region, Figure 12) increase substantially. As a result, [((OMe)$_2$IQ1)Ru(NO)(Cl)] exhibits the highest ε value (8 700 M^{-1} cm^{-1}).

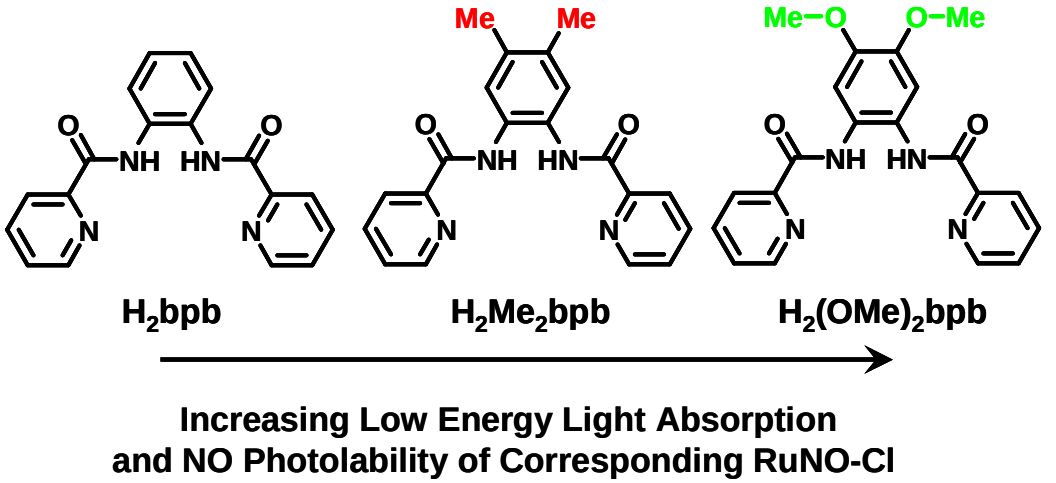

Figure 4.10. Dicarboxamide tetradentate ligands with substituents of increasing electron donor strength (H < Me < OMe)

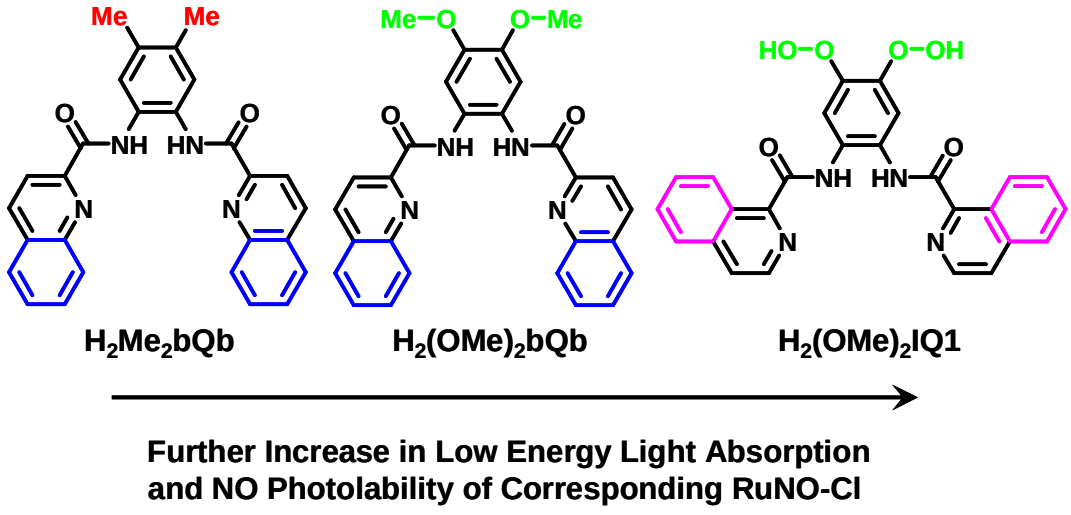

Figure 4.11. Dicarboxamide tetradentate ligands with Me or OMe substituents and extended conjugation (quinoline or 1-isoquinoline moieties in place of pyridine)

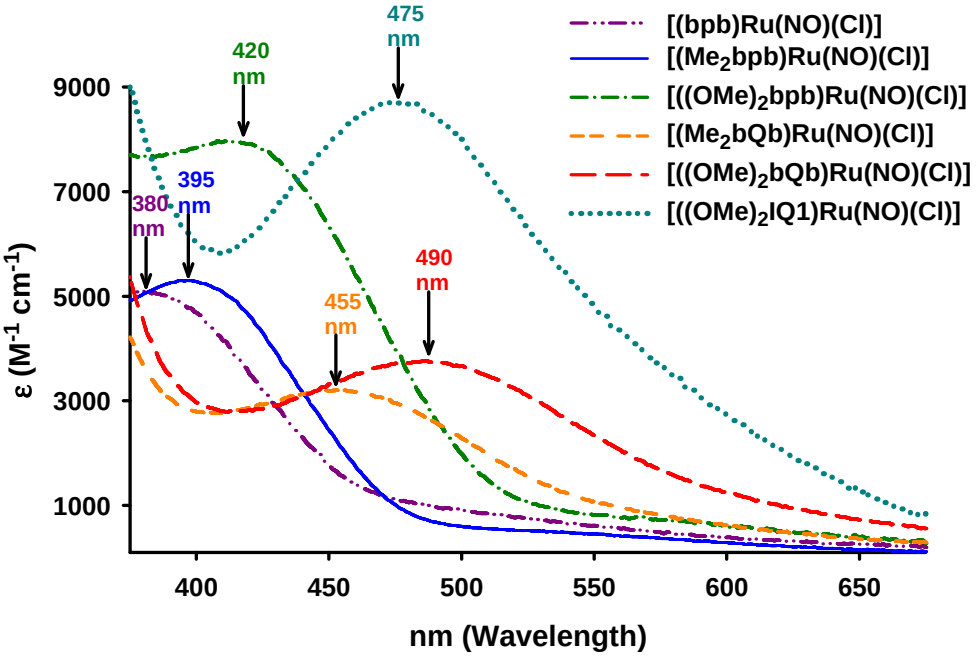

Figure 4.12. Electronic absorption spectra of chloride bound $\{RuNO\}^6$ nitrosyls displaying a systematic red shift and increase in ε values of the photoband as the ligand frame is changed

4.4 Syntheses of Fluorescein Dye Derivatives

4.4.1 Characterization of Fluorescein Ethyl Ester

In order to synthesize a fluorescein-bound ruthenium nitrosyl, the structure of the dye molecule had to be considered. For example, fluorescein has a phenolato-O as well as a carboxylato-O donor center both of which are capable of binding to the metal center. Indeed, initial attempts to combine fluorescein with our designed ruthenium nitrosyls resulted in a mixture of products. To circumvent this problem, we decided to protect one of the metal binding sites of the fluorescein dye. Simple treatment of fluorescein with concentrated sulfuric acid in ethanol resulted in

conversion of the carboxylic acid into an ethyl ester derivative of fluorescien (FlEt) in which only the phenolato-O donor is available for metal binding. The new alkyl proton signals (4.01 (q 2H) and 0.92 (t 3H) ppm in $CDCl_3$) in the ^1H NMR of resulting product are indicative of formation of the ethyl ester product. The ethyl ester group of FlEt is also beneficial since it could be used to attach different cell targeting moieties such as peptides or antibodies providing more site specificity to these $\{RuNO\}^6$ nitrosyls.

4.4.2 Characterization of PyFlEt

We decided to further derivatize FlEt by adding a 4-(pyridinyloxy) linker off the phenolate group of FlEt (PyFlEt) that can bind the metal center through the pyridine-N donor. We were interested to see how adding this type of linker would affect the fluorescence and NO photolability of the resulting PyFlEt-bound $\{RuNO\}^6$ nitrosyl compared to the corresponding nitrosyl with FlEt bound directly to the Ru-center. We employed a Mitsunobu type reaction for the synthesis of PyFlEt (4-(pyridinyloxy)-fluorescein ethyl ester, Figure 4.13). In this reaction, triphenylphosphine (TPP) activates diethyl azodicarboxylate (DEAD) which then deprotonates the phenol moiety of FlEt. Next the triphenylphosphine group is transferred from DEAD to the oxygen atom of 4-pyridylcarbinol resulting in an oxyphosphonium ion which activates it toward reaction with the deprodonated FlEt. The final PyFlEt product precipitates as a yellow solid while the side products, diethyl 1,2-hydrazinedicarboxylate and triphenylphosphine oxide, stay in solution. We found that excess TPP, DEAD, and 4-pyridylcarbinol (5 equiv of each) was

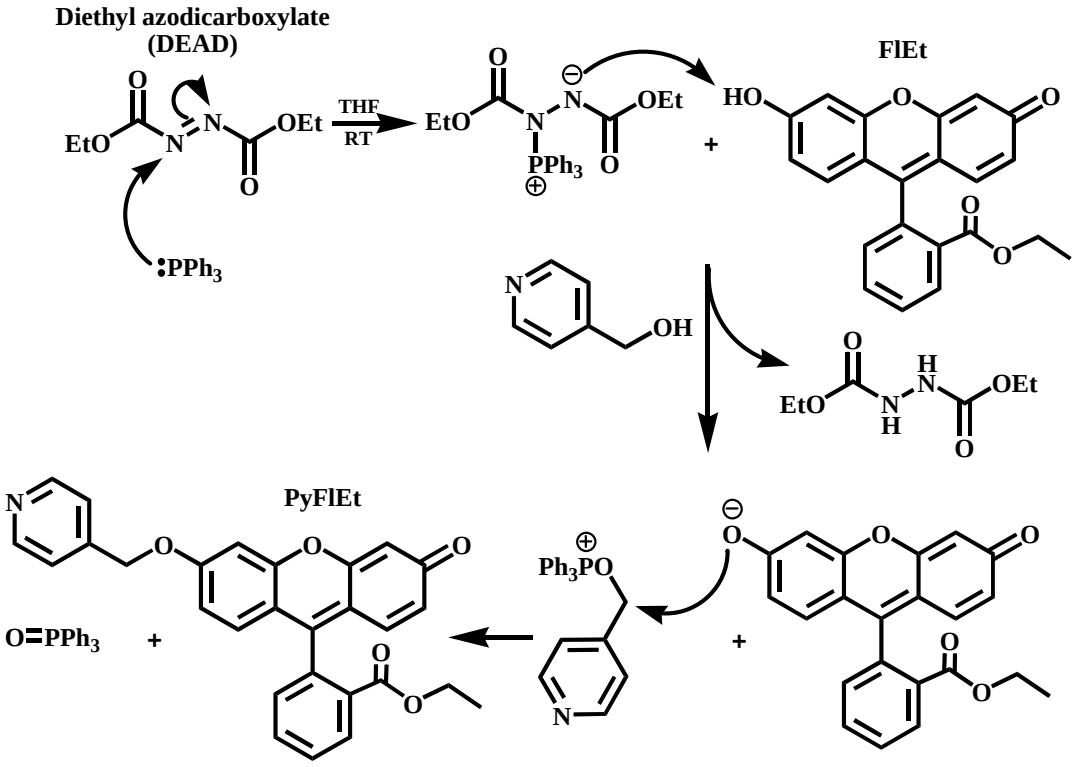

Figure 4.13. Reaction scheme of the fluorescein derivative 4-(pyridinyloxy)-fluorescein ethyl ester (PyFlEt) synthesized from fluorescein ethyl ester (FlEt)

necessary to drive the reaction with FlEt (1 equiv) which led to an 80% yield of PyFlEt. New aromatic proton signals corresponding to a pyridine group (8.653 (d 2H) and 7.359 (d 2H) ppm in $CDCl_3$) and a singlet proton signal (5.20 (s 2H) ppm in $CDCl_3$), corresponding to the alkyl group of 4-pyridinyloxy confirmed the formation of PyFlEt.

4.5 Syntheses and Structures of Dye Conjugated Metal Nitrosyls

The ligand frames H_2Me_2bpb, $H_2(OMe)_2bpb$, and $H_2(OMe)_2IQ1$ were strategically chosen for the syntheses of dye-bound nitrosyls due to their planarity

when bound to the ruthenium center. This allows ample room for binding of the bulky dyes trans to NO in the resulting dye-bound $\{RuNO\}^6$ nitrosyls namely, [((OMe)$_2$bpb)Ru(NO)(Resf)], [((OMe)$_2$IQ1)Ru(NO)(Resf)], [(Me$_2$bpb)Ru(NO)-(FlEt)], [((OMe)$_2$IQ1)Ru(NO)(FlEt)], and [((OMe)$_2$IQ1)Ru(NO)(PyFlEt)](BF_4). Reaction of chloro-bound $\{RuNO\}^6$ nitrosyls with $AgBF_4$ in MeCN results in the formation of the MeCN-bound intermediates which are primed for binding by the various dye chromophores to the Ru-center. The neutral chloro-bound starting nitrosyls are typically not very soluble in MeCN. Therefore such reaction typically require several hours at reflux temperature to achieve the formation of the MeCN-bound nitrosyl. In previous work, the resulting AgCl(s) was filter off from the MeCN solution before addition of the dye. However, we found that we could never get full reaction of the chloro-bound nitrosyls and the unreacted material would be filtered off with the AgCl. Since the AgCl is very insoluble in MeCN and thus unlikely to interfere with the dye reaction, we decided to not filter it off thus allowing the unreacted starting material a chance to react once the dye was added. The phenol groups of both Resf and FlEt were deprotonated with NaH before addition to the metal while PyFlEt was added as is. The presence of the dye appears to help drive the reaction of the chloro-bound nitrosyls with $AgBF_4$ which opens up the metal binding site for the dye. Thus we found that addition of the dye molecules shortly after addition of $AgBF_4$ gave much higher yields of the dye-bound species.

In general, the quinoline containing Resf- and FlEt-bound $\{RuNO\}^6$ nitrosyls tend to be more insoluble in MeCN than the pyridine contain species while the

PyFlEt-bound nitrosyl is completely soluble in MeCN. The neutral PyFlEt donor leads to an overall 1+ charge of [((OMe)$_2$IQ1)Ru(NO)(PyFlEt)](BF$_4$) which increases its solubility compared to that of the neutral Resf- and FlEt-bound {RuNO}^{6} nitrosyls. For example, [((OMe)$_2$IQ1)Ru(NO)(PyFlEt)](BF$_4$) was completely soluble at high concentration in MeCN at 4^o C as expected for a charged complex. Thus [((OMe)$_2$IQ1)Ru(NO)(PyFlEt)](BF$_4$) was finally isolated by removal of MeCN in vacuo and the resulting solid was thoroughly washed with THF. Conversly both [((OMe)$_2$IQ1)Ru(NO)(Resf)] and [((OMe)$_2$IQ1)Ru(NO)(FlEt)] precipitate from room temperature MeCN while [((OMe)$_2$bpb)Ru(NO)(Resf)] and [(Me$_2$bpb)Ru(NO)(FlEt)] only precipitate from MeCN solutions at low temperature. Since [((OMe)$_2$bpb)Ru(NO)(Resf)] and [(Me$_2$bpb)Ru(NO)(FlEt)] are more soluble, the AgCl impurities can be removed by filtration at room temperature. The filtrate can then be concentrated and cooled inorder to isolate the dye-bound species. However, in the case of [((OMe)$_2$IQ1)Ru(NO)(Resf)] and [((OMe)$_2$IQ1)Ru(NO)(FlEt)], the AlCl can not be filtered off without also filtering off the dye-bound products. Thus the dye-bound nitrosyls were extracted from the AgCl mixture with CH_2Cl_2.

4.5.1 Characterization of [((OMe)$_2$bpb)Ru(NO)(Resf)]

The X-ray structure of [((OMe)$_2$bpb)Ru(NO)(Resf)] reveals that the tetradentate (OMe)$_2$bpb^{2-} ligand frame remains bound to the ruthenium center in a planar fashion after Resf is bound (Figure 4.14). The pseudooctahedral structure is completed with the phenolato-O bound resorufin dye trans to NO at the axial

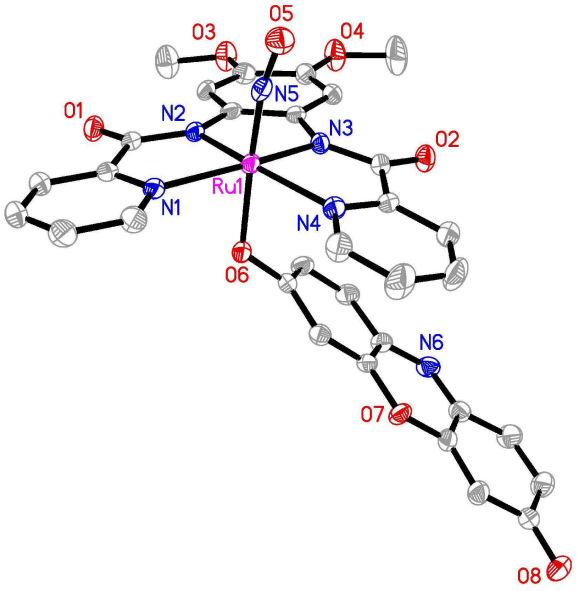

Figure 4.14. Thermal ellipsoid (probability level 50%) plot of [((OMe)$_2$bpb)Ru(NO)(Resf)] with select atom-labeling. H atoms are omitted for the sake of clarity.

positions. The Ru–N5–O5 bond angle is slightly bent at 169.3(3)°. The substitution of methoxy groups in [((OMe)$_2$bpb)Ru(NO)(Resf)] compared to methyl groups in [(Me$_2$bpb)Ru(NO)(Resf)] does little to alter the overall geometry of the two structures. In both cases, the resorufin dye is tilted away from the equatorial plane with ~120^o Ru–O6–C(Resf) bond angles ([(Me$_2$bpb)Ru(NO)(Resf)] = 128.46(11)°, [5] [((OMe)$_2$bpb)Ru(NO)(Resf)] = 126.0(3)°) implying that the bound oxygen is more sp^2 than sp^3 hybridized. The dye is positioned in such a way that it is directly below one of the pyridine rings of the equatorial ligand and presumably provides favorable π-π interactions that stabilize the structures of both [(Me$_2$bpb)Ru(NO)(Resf)] and [((OMe)$_2$bpb)Ru(NO)(Resf)]. As a result, this pyridine ring is very slightly off the

plane of the rest of the ligand frame. The Ru–N5 (1.729(4) Å) and N5–O5 (1.169(4) Å) bonds lengths of [((OMe)$_2$bpb)Ru(NO)(Resf)] are also similar to those of [(Me$_2$bpb)Ru(NO)(Resf)] (1.7347(16) [5] and 1.159(2) Å respectively).

4.5.2 Characterization of [((OMe)$_2$IQ1)Ru(NO)(Resf)]

The (OMe)$_2$IQ1^{2-} ligand frame of [((OMe)$_2$IQ1)Ru(NO)(Resf)] is bound to the ruthenium center in the equatorial plane while the resorufin dye is trans to NO at the axial positions (Figure 4.15). Here also, the resorufin dye is bound through the phenolato-O and a similar tilt of the bound dye (Ru–O6–C(Resf) angle of 126.3(2)°) is observed. The position of the bound resorufin is such that the rings of the dye are aligned parallel to the rings of one of the 1-isoquinoline moieties in the (OMe)$_2$IQ1^{2-}

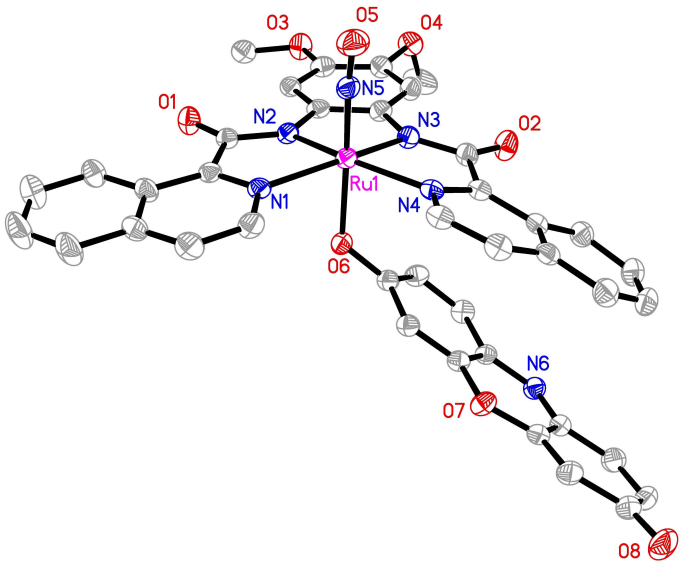

Figure 4.15. Thermal ellipsoid (probability level 50%) plot of [((OMe)$_2$IQ1)Ru(NO)(Resf)] with selected atom-labeling. H atoms are omitted for the sake of clarity.

ligand frame of [((OMe)$_2$IQ1)Ru(NO)(Resf)]. This π-π interaction causes the 1-isoquinoline moiety of (OMe)$_2$IQ1^{2-} to tilt *slightly* out of the plane of the rest of the tetradentate ligand frame. Despite this tilt of the ligand in the equatorial plane, [((OMe)$_2$IQ1)Ru(NO)(Resf)] is significantly more planar than that of [((OMe)$_2$bQb)Ru(NO)(Resf)] which contains the regular quinoline ligand, (OMe)$_2$bQb^{2-}. The Ru-NO unit in [((OMe)$_2$IQ1)Ru(NO)(Resf)] comprises Ru–N5(O) and N5–O5 bond lengths of 1.732(3) Å and 1.167(3) Å respectively which fall within the ranges observed in the other resorufin nitrosyls (1.729 –1.7425 Å and 1.154 –1.169 Å respectively).[5] In addition, the Ru–N5–O5 bond angle of [((OMe)$_2$IQ1)Ru(NO)(Resf)] is almost linear (176.5(3)°) as expected for a {RuNO}^{6} nitrosyl.

4.5.3 Characterization of [(Me$_2$bpb)Ru(NO)(FlEt)] and [((OMe)$_2$IQ1)Ru(NO)(FlEt)]

The structures of [(Me$_2$bpb)Ru(NO)(FlEt)] and [((OMe)$_2$IQ1)Ru(NO)(FlEt)] (Figure 4.16) have been confirmed with the aid of ^{1}H NMR, infrared (IR) spectroscopy, and mass spectrometry. IR spectra of [(Me$_2$bpb)Ru(NO)(FlEt)] and [((OMe)$_2$IQ1)-Ru(NO)(FlEt)] reveal the presence of NO and FlEt as evidenced by their NO stretching frequencies (ν_{NO}) at 1846 and 1832 cm^{-1} in addition to their FlEt carbonyl stretching frequencies (ν_{CO}) at 1715 and 1712 cm^{-1} respectively. The greater electron donating ability of the (OMe)$_2$IQ1 ligand frame causes an increase in

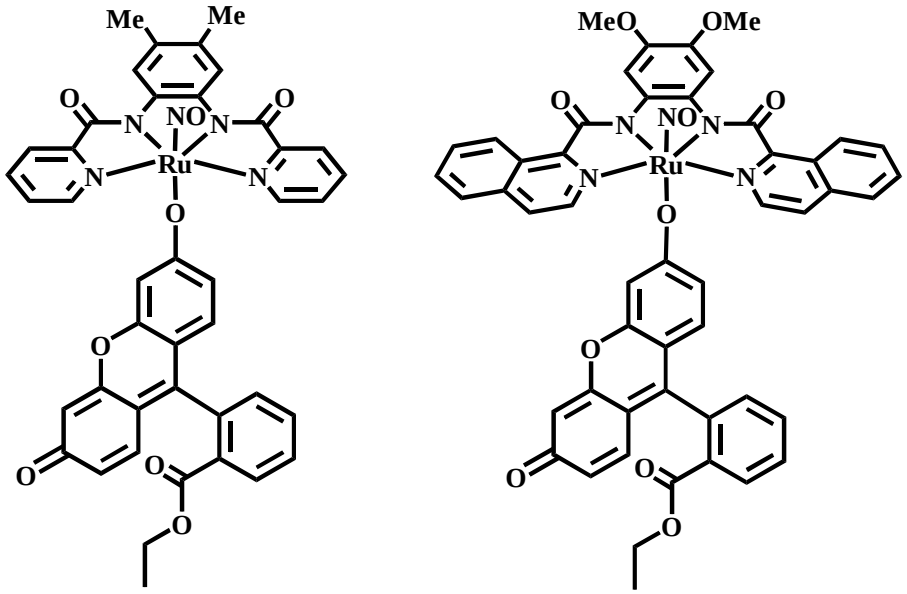

Figure 4.16. FlEt-Bound $\{RuNO\}^6$ Nitorsyls

electron density in the π^* level of the bound NO of [((OMe)$_2$IQ1)Ru(NO)(FlEt)] and is responsible for its lower ν_{NO} frequency.

Both complexes are diamagnetic and afford clean ^{1}H NMR spectra, as expected for $\{RuNO\}^6$ nitrosyls. The integration and number of the peaks observed in both ^{1}H-NMR spectra confirm the presence of Ru-bound FlEt. For example, in the ^{1}H-NMR spectrum of free FlEt there are several overlapping aromatic peaks that shift apart upon binding to the Ru center. Thus none of the 10 aromatic FlEt hydrogen peaks overlap with one another in the ^{1}H-NMR spectra of [(Me$_2$bpb)Ru(NO)(FlEt)] and [((OMe)$_2$IQ1)Ru(NO)(FlEt)] in $CDCl_3$. Similarly, several peaks corresponding to the hydrogen atoms on the ligand frame also shift upon dye binding. In addition, there is no evidence of either Cl-bound or free FlEt starting materials in either spectrum.

Interestingly, the CH_2 proton peaks of the ethyl ester group shift apart when the dye is bound to the metal center. Thus the ethyl ester tail must be pointing toward the metal complex.

4.5.4 Characterization of [((OMe)$_2$IQ1)Ru(NO)(PyFlEt)]

The structure of [((OMe)$_2$IQ1)Ru(NO)(PyFlEt)](BF$_4$) (Figure 4.17) was confirmed by ^{1}H NMR and infrared (IR) spectroscopy. The IR spectra of [((OMe)$_2$IQ1)Ru-(NO)(PyFlEt)](BF$_4$) contains and NO stretching frequencies (ν_{NO}) at 1880 cm^{-1}. This ν_{NO} is significantly blue-shifted compared those of both [((OMe)$_2$IQ1)Ru(NO)(Cl)] and [((OMe)$_2$IQ1)Ru(NO)(FlEt)] which have charged donors trans to NO. The greater electron accepting ability of the neutral pyridine-N donor of PyFlEt reduces the amount of π-backbonding into the π^* level of the bound NO of [((OMe)$_2$IQ1)Ru(NO)(PyFlEt)](BF$_4$) resulting in a shorter NO bound (i.e. higher ν_{NO} frequency). A clean ^{1}H-NMR spectrum of [((OMe)$_2$IQ1)Ru(NO)-(PyFlEt)](BF$_4$) agrees with a {RuNO}^{6} assignment for this nitrosyl. The integration and number of the peaks observed in the ^{1}H-NMR spectrum confirms the presence of Ru-bound PyFlEt. Several peaks corresponding to the hydrogen atoms on the ligand frame shift upon dye binding. Thus in the ^{1}H-NMR spectrum none of the aromatic peaks overlap with those observed in the ^{1}H-NMR spectra either [((OMe)$_2$IQ1)Ru(NO)(Cl)] or free PyFlEt. Similar to the the FlEt-bound nitrosyls, the CH_2 proton peaks of the ethyl ester group of PyFlEt shift apart when the dye is

bound to the metal center indicating some interaction between the ethyl ester tail the rest of the metal complex.

[((OMe)$_2$IQ1)Ru(NO)(PyFlEt)](BF$_4$)

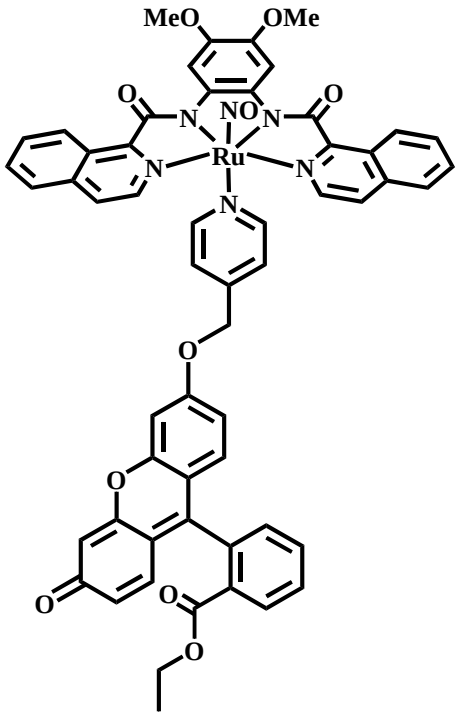

Figure 4.17. PyFlEt-bound {RuNO}^{6} nitrosyl

4.6 Comparison of the Electron Absorption Spectra of Free Dye, Cl-Bound, and Dye-Bound Metal Nitrosyls

Replacing the chloride ligands (trans to NO) with resorufin dye enhances the sensitivity of [((OMe)$_2$bpb)Ru(NO)(Resf)] and [((OMe)$_2$IQ1)Ru(NO)(Resf)] toward visible light. For example, the absorption spectra of both Resf-conjugates contain intense absorption bands at 500 nm (ε = 29 000 $M^{-1}cm^{-1}$ and 31 000 $M^{-1}cm^{-1}$

respectively in $CHCl_3$, Figure 4.18). Interestingly, the deprotonated form of the unbound dye ($Resf^-$) has an intense absorption band at 590 nm (ε = 105 000 $M^{-1}cm^{-1}$ in DMF). Upon coordination to the positively charged metal center, a blue shift of the dye band (with concomitant reduction in extinction coefficient) occurs in the nitrosyl-dye conjugates. We have previously assigned such changes to the loss of

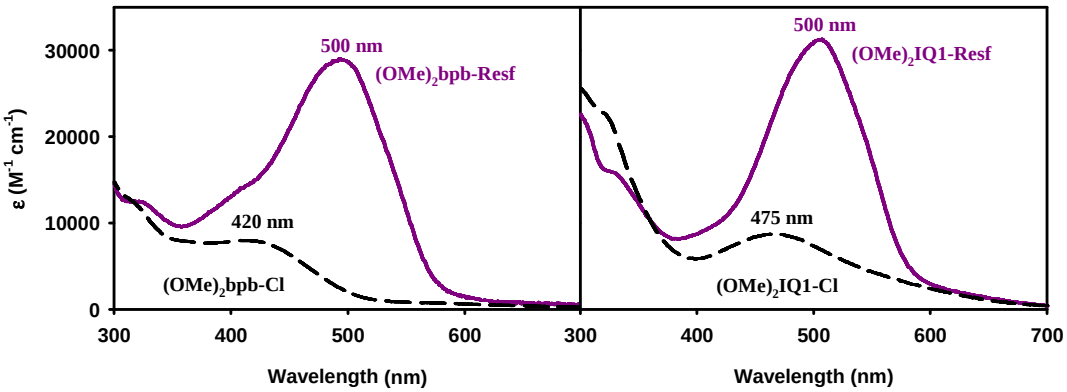

Figure 4.18. Electronic absorption spectra of [((OMe)$_2$bpb)Ru(NO)(Cl)] and [((OMe)$_2$bpb)Ru(NO)(Resf)] (left), and [((OMe)$_2$IQ1)Ru(NO)(Cl)] and [((OMe)$_2$IQ1)Ru(NO)(Resf)] (right) in $CHCl_3$

delocalization of negative charge over the heterocyclic π-system and the loss of overall symmetry of the dye upon coordination. Indeed, simple protonation of Resf also brings about similar changes in its electronic absorption spectrum (λ_{max} = 470 nm, ε = 20 000 $M^{-1}cm^{-1}$ in DMF).[3]

A comparison of the five Ru-Resf complexes reveals a uniform shift in the λ_{max} of the dye absorption band to 500 nm upon complexation. However, the ε-values of these complexes are greatly varied. For example, [(Me_2bpb)Ru(NO)(Resf)] and [(Me_2bQb)Ru(NO)(Resf)] both have ε-values around 12 000 $M^{-1}cm^{-1}$ [5b] while [((OMe)$_2$bQb)Ru(NO)(Resf)], [((OMe)$_2$bpb)Ru(NO)(Resf)], and [((OMe)$_2$IQ1)Ru-

(NO)(Resf)] have ε-values around 30 000 $M^{-1}cm^{-1}$ (Figure 4.19). The most apparent difference between the two sets of complexes is the presence of Me vs OMe substituents on the tetradentate ligand frame. It therefore appears that in these nitrosyl-dye conjugates, the substituents on the ligand frame have more pronounced effect on the overall capacity of light absorption compared to the twist of the frame in the equatorial plane.

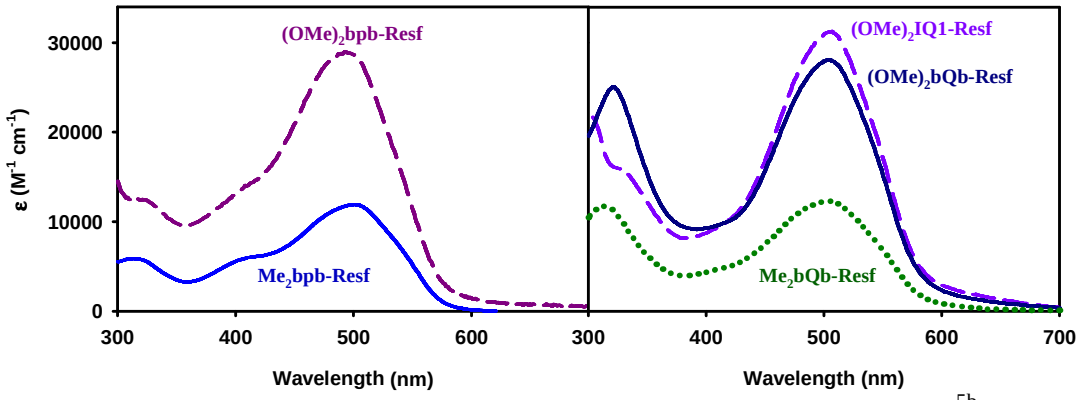

Figure 4.19. Electronic absorption spectra of [(Me_2bpb)Ru(NO)(Resf)] [5b] and [(($OMe)_2$bpb)Ru(NO)(Resf)] (left), and [(Me_2bQb)Ru(NO)(Resf)], [5b] [(($OMe)_2$bQb)Ru(NO)(Resf)], [5b] and [(($OMe)_2$IQ1)Ru(NO)(Resf)] (right) in $CHCl_3$

Since we utilized FlEt and PyFlEt (and not fluoroscein) as the light-harvesting chromophores in the second set of dye-bound nitrosyls, we first had to characterize the absorption spectra of these fluoroscein dye derivatives. Fortunately, the protection of the carboxylate group of fluoroscein (necessary for specific binding to the Ru center of the nitrosyl) in FlEt and PyFlEt did not eliminate the visible light absorption of these dyes (Figure 4.20). In its deprotonated form, $FlEt^-$ has an intense absorption

band at504 nm (ε = 80 000, in 50:50 MeCN/H_2O). Interestingly, there is a 50 nm blue-shift (to 454 nm) coupled with a reduction in intensity (ε = 20 000, in MeCN/

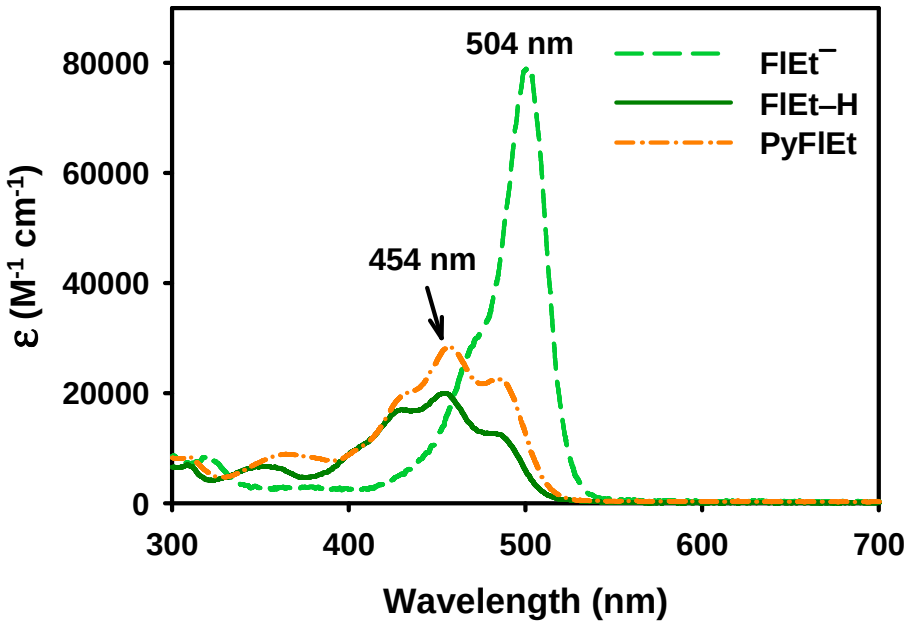

Figure 4.20. Electronic absorption spectra of fluorescein ethyl ester (FlEt, in 50:50 MeCN H_2O)**,** protonated FlEt-H (in MeCN/AcOH pH = 5), and 4-pyridinyloxy fluorescein ethyl ester (PyFlEt, in 50:50 MeCN H_2O)

AcOH) of this absorption band when FlEt is in its protonated state (FlEt-H, Figure 4.21). Addition of the 4-pyridinyloxy group causes a similar change in the absorption spectrum of PyFlEt. Therefore the spectra of FlEt-H and PyFlEt are almost exactly the same with three overlapping peaks centered at 454 nm (Figure 4.20). There is only a slight difference in the relative height of the three peaks in the spectra of the different dyes.

The attachment of FlEt in both [(Me_2bpb)Ru(NO)(FlEt)] and [(($OMe)_2$IQ1)Ru(NO)(FlEt)] significantly enhanced the amount of visible light

absorbed by these nitrosyls compared the corresponding Cl-bound nitrosyls. For example, the lowest energy absorbance band in the spectrum of [(Me_2bpb)-Ru(NO)(Cl)] [8] has a λ_{max} at 395 nm with an ε of 5 300 $M^{-1}cm^{-1}$ while the main absorption band of [(Me_2bpb)Ru(NO)(FlEt)] is centered at 475 nm with an extinction coefficient value of 24 000 $M^{-1}cm^{-1}$ (Figure 4.21). The electronic absorption spectrum

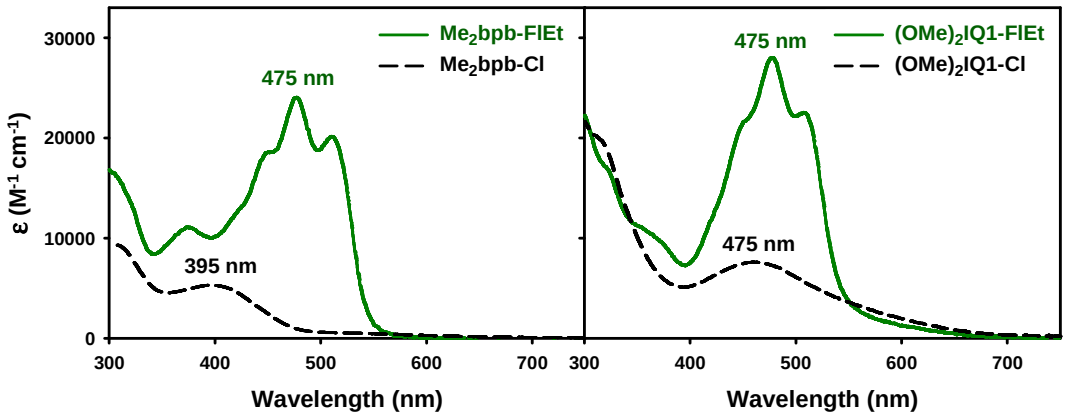

Figure 4.21. Electronic absorption spectra of [(Me_2bpb)Ru(NO)(Cl)] [8] and [(Me_2bpb)Ru(NO)(FlEt)] (left panel) and [(($OMe)_2$IQ1)Ru(NO)(Cl)] and [(($OMe)_2$IQ1)Ru(NO)(FlEt)] (right panel) in MeCN

[(($OMe)_2$IQ1)-Ru(NO)(FlEt)] is very similar to that of [(Me_2bpb)-Ru(NO)(FlEt)] with its main absorption band also centered at 475 nm (Figure 4.21). In addition, the general shapes of the absorption bands in both dye-bound spectra are very similar to that of FlEt-H, each containing three overlapping peaks in the visible region. The epsilon value at 475 nm for [(($OMe)_2$IQ1)Ru(NO)(FlEt)] (ε = 28 000 $M^{-1}cm^{-1}$) is slightly higher than that of [(Me_2bpb)Ru(NO)(FlEt)]. This is most possibly due to the greater overlap of the absorption band of [(($OMe)_2$IQ1)Ru(NO)(Cl)] (λ_{max} = 475 nm,

ε = 8700 M^{-1} cm^{-1}) with that of dye chromophore. In general, the large number of high ε values over a large range of wavelengths (400-550 nm) for both [(Me_2bpb)Ru(NO)(FlEt)] and [(($OMe)_2$IQ1)Ru(NO)(FlEt)] leads to a significant amount of visible light absorption by these dye-nitrosyl conjugates.

The shape and intensity of the absorption spectrum of the PyFlEt-bound nitrosyl [(($OMe)_2$IQ1)Ru(NO)(PyFlEt)](BF_4) is very similar to that of [(($OMe)_2$IQ1)Ru(NO)(FlEt)] except for a 20 nm blue-shift in λ_{max} of the low energy band (454 nm and 475 nm respectively, Figure 4.22). In addition, the shift, shape, and intensity of this absorption band in the spectrum of [(($OMe)_2$IQ1)Ru(NO)(PyFlEt)](BF_4) are all very similar to that of the free PyFlEt dye although the [(($OMe)_2$IQ1)Ru(NO)(PyFlEt)](BF_4) band is slightly wider (Figure 4.23). This is in contrast to what was found while comparing the absorption spectra of free FlEt or Resf with their corresponding $\{RuNO\}^6$ dye-bound nitrosyls which were less intense than the free dyes. This can be understood by that fact that the pyridine-N electrons (used to bind the Ru-center) of PyFlEt do not contribute to the aromaticity of the dye while the electrons of the phenolo-O do contribute to the aromaticity of both FlEt and Resf. Thus in the case of [(($OMe)_2$IQ1)Ru(NO)-(PyFlEt)](BF_4) there is not a blue-shift in λ_{max} or reduction in epsilone value of the lower energy band compared to the free dye as was seen for the Resf- and FlEt-bound nitrosyls.

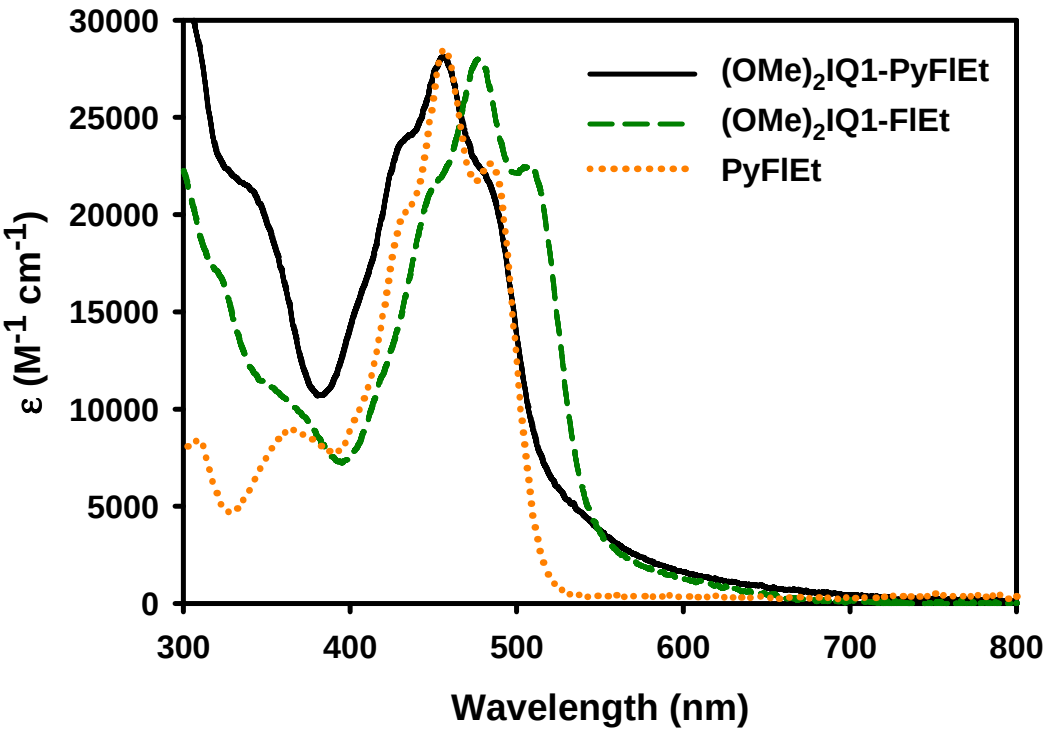

Figure 4.22. Electronic absorption spectra of [((OMe)$_2$IQ1)Ru(NO)(PyFlEt)](BF$_4$), [((OMe)$_2$IQ1)Ru(NO)(FlEt)] (in MeCN) and PyFlEt (in 50:50 MeCN-H$_2$O)

4.7 Stability of Dye-Bound Metal Nitrosyls in Aqueous Solvents

The dye-bound nitrosyls are indefinitely stable and do not lose their dye moeities when dissolved in weakly coordinating aprotic solvents like $CHCl_3$ and MeCN. However, in solvents like DMSO or in aqueous solutions (pH 5-7), the FlEt and Resf dye-bound nitrosyls slowly lose the bound dye over the course of several hours. The Ru-PyFlEt bond (via the pyridine-N) in [(OMe$_2$(IQ1)Ru(NO)(PyFlEt)]$^+$ appears to be much more stable than the corresponding Ru-Resf and Ru-FlEt bonds

(via phenolato-O) as $[(OMe_2(IQ1)Ru(NO)(PyFlEt)]^+$ has a greater stability in strongly coordinating solvents. Quantitative measurements of dye lose in the FlEt- and Resf-bound nitrosyls were attempted using UV-Vis spectroscopy. However such measurements were complicated by the overlapping absorption bands of the different bound/unbound dye species. For example, the absorption spectra of protonated Resf-H and FlEt-H are very similar to those of the corresponding Resf- and FlEt-bound nitrsoyls. On the other hand, the absorption spectra of deprotonated $Resf^-$ and $FlEt^-$ are red-shifted with a higher epsilon value compared to the corresponding absorption bands of the protonated dyes and dye-bound nitrosyls. Thus the appearance of this band provides an easy was to measure the amount of deprotonated free dye. However, as dye is lost and the concentration of protic solvent-bound nitrosyls increase, the acidity of the solution also increases. Therefore after a certain amount of time, both protonated and unprotonated free dye species are present in solution making the total amount of dye lost impossible to measure by UV-Vis. We therefore could only get a qualitative comparison of stability for these dye-bound nitrosyls by comparing the amount of unprotonated free dye in solution.

In the case of the Resf-bound nitrosyls, the $\{RuNO\}^6$ nitrosyls containing twisted quinoline ligands namely, $[(Me_2bQb)Ru(NO)(Resf)]$ and $[((OMe)_2bQb)Ru(NO)(Resf)]$**,** lose ~20% bound dye in 1h, while the planar $[((OMe)_2IQ1)Ru(NO)(Resf)]$ loses ~10% bound dye within the same time. The two pyridine-containing nitrosyls $[(Me_2bpb)Ru(NO)(Resf)]$ and $[((OMe)_2bpb)$-$Ru(NO)(Resf)]$ both lose less than 5% bound dye in 1h. The dye bound nitrosyls

derived from planar ligand frames with no twist thus exhibit increased stability in H_2O. While the stability of [((OMe)$_2$IQ1)Ru(NO)(Resf)] is improved compared to that of the {RuNO}^{6} nitrosyls with twisted quinoline ligand frames, it is still slightly less stable than the pyridine-containing nitrosyls [(Me$_2$bpb)Ru-(NO)(Resf)] and [((OMe)$_2$bpb)Ru(NO)(Resf)]. A similar tend was also observed for the FlEt-bound nitrosyls as the pridine-based [(Me$_2$bpb)Ru(NO)(FlEt)] was overall more stable than the quinioling containing [((OMe)$_2$IQ1)Ru(NO)(FlEt)]. Collectively, the results suggest that the use of planar pyridine-based ligand frames provides the most stability in these designed dye-tethered {RuNO}^{6} nitrosyls.

4.8 Comparison of the NO Photolability of Metal Nitrosyls

Exposure of solutions of the chloride-bound nitrosyls [((OMe)$_2$bpb)Ru(NO)(Cl)] and [((OMe)$_2$IQ1)Ru(NO)(Cl)] in DMF to visible light promotes rapid release of NO (as evidenced by the responses of an NO-sensitive electrode). The photo-dissociation of NO is accompanied by the formation of a solvent bound Ru(III) photoproduct (eq 1), which typically exhibits a low-energy

$$(L)Ru\text{-}NO + h\nu + solv \rightarrow (L)Ru(III)\text{-}solv + NO^{\bullet} \qquad (1)$$

absorption band in its electronic spectrum. This transition has previously been assigned to a ligand-to-metal charge transfer (LMCT) from the negatively charged ligand (in this case (OMe)$_2$bpb^{2-} or OMe)$_2$IQ1^{2-}) to the Ru(III) center.[10]

Comparison of the quantum yield (ϕ) values of NO photorelease (in DMF) upon exposure to monochromatic 500 nm light of these chloride-bound nitrosyls indicate that [((OMe)$_2$IQ1)Ru(NO)(Cl)] (0.035 ± 0.005) is a more efficient NO donor than [((OMe)$_2$bpb)Ru(NO)(Cl)] (0.010 ± 0.005). Comparison of these values (Table 4.1) with those measured under similar conditions for [(Me$_2$bpb)Ru(NO)(Cl)], [(Me$_2$bQb)Ru(NO)(Cl)], and [((OMe)$_2$bQb)Ru(NO)(Cl)] reveals a trend in the efficiency of NO photorelease of [(Me$_2$bpb)Ru(NO)(Cl)] < [(Me$_2$bQb)Ru(NO)(Cl)] = [((OMe)$_2$bpb)Ru(NO)(Cl)] < [((OMe)$_2$bQb)Ru(NO)(Cl)] < [((OMe)$_2$IQ1)Ru-(NO)(Cl)]. This result confirms that alterations in the equatorial ligand frame do lead to increased sensitivity to visible light in ruthenium nitrosyls. In particular, removal of the twist in the equatorial ligand frame leads to increased NO photolability as exemplified by the trend [((OMe)$_2$bQb)Ru(NO)(Cl)] < [((OMe)$_2$IQ1)Ru(NO)(Cl)].

In all the Resf-nitrosyl conjugates, the overlap of the photoband of the parent chloride-bound nitrosyls with the strong 500 nm Resf absorption band results in sensitization toward visible light. As changes in the equatorial ligand frames red-shift the photobands of the parent nitrosyls (more toward the 500 nm dye band), the extent of sensitization is increased due to overlap of the two transitions. Since alterations of the equatorial ligands also bring about enhancement in the ε values of the photoband of the parent nitrosyls (as shown in Figure 4.12), considerable overlap (in some cases merging) of the two bands lead to excellent sensitization, as in the case with [((OMe)$_2$bQb)Ru(NO)(Resf)] and [((OMe)$_2$IQ1)Ru(NO)(Resf)]. The enhanced visible light absorption provides considerably increased NO photolability with 500

Table 4.1. Summary of Absorption Parameters (λ_{max}, ε) and Quantum Yield (ϕ) Values of Selected Nitrosyls

Complexes	Quantum Yield ϕ (λ_{irr}, nm)	solvent	λ_{max}, nm (ε, $M^{-1}cm^{-1}$)
$[(Me_2bpb)Ru(NO)(Cl)]$ [a]	0.0008 ± 0.0002 (500)	DMF	395 (5 300)
$[(Me_2bQb)Ru(NO)(Cl)]$ [a]	0.010 ± 0.003 (500)	DMF	455 (3 200)
$[((OMe)_2bQb)Ru(NO)(Cl)]$ [b]	0.025 ± 0.003 (500)	DMF	490 (3750)
$[((OMe)_2bpb)Ru(NO)(Cl)]$	0.010 ± 0.005 (500)	DMF	420 (7 800)
$[((OMe)_2IQ1)Ru(NO)(Cl)]$	0.035 ± 0.005 (500)	DMF	475 (8 700)
[(Me bpb)Ru(NO)(Resf)] [b]	0.052 ± 0.008 (500)	DMF	500 (11 920)
$[(Me_2bQb)Ru(NO)(Resf)]$ [b]	0.102 ± 0.009 (500)	DMF	500 (12 300)
$[((OMe)_2bQb)Ru(NO)(Resf)]$ [b]	0.206 ± 0.008 (500)	DMF	500 (27 100)
$[(OMe_2bpb)Ru(NO)(Resf)]$	0.120 ± 0.008 (500)	DMF	500 (29 000)
$[(OMe_2IQ1)Ru(NO)(Resf)]$	0.271 ± 0.008 (500)	DMF	500 (31 000)
$[(Me_2bpb)Ru(NO)(FlEt)]$	0.306 ± 0.01 (500)	DMF	475 (24 000)
$[((OMe)_2IQ1)Ru(NO)(FlEt)]$	0.173 ± 0.01 (500)	DMF	475 (28 000)
$[((OMe)_2IQ1)Ru(NO)(PyFlEt)]^+$	0.02 ± 0.01 (500)	DMF	454 (28 000)
Roussin's Salt Ester (RSE) [c]	0.00019 ± 0.00005(546)	$CHCl_3$	364 (8 500)
PPIX-RSE [d]	0.00025 ± 0.00005(546)	$CHCl_3$	538 (10 200)
Fluor-RSE [e]	0.0036 ± 0.0005(436)	$MeCN/H_2O$	506 (72 200)

[a] ref 8, [b] ref 5b, [c] ref 11, [d] ref 2, [e] ref 1.

nm light in such cases. For example, the photoband of $[(Me_2bpb)Ru(NO)(Cl)]$ is at 395 nm and $[(Me_2bpb)Ru(NO)(Resf)]$ has a quantum yield value of 0.052 at 500 nm while the photoband of $[((OMe)_2IQ1)Ru(NO)(Cl)]$ is at 475 nm and $[((OMe)_2IQ1)Ru(NO)(Resf)]$ has a quantum yield value of 0.270 (Figure 4.23). However, when one compares $[((OMe)_2bQb)Ru(NO)(Resf)]$ (ϕ_{500} = 0.206) and has a

λ_{max} at 490 nm and [((OMe)$_2$IQ1)Ru(NO)(Cl)] at 475 nm, the greater intensity [((OMe)$_2$IQ1)Ru(NO)(Resf)] (ϕ_{500} = 0.270), even though [((OMe)$_2$bQb)Ru(NO)(Cl)] of the photoband of [((OMe)$_2$IQ1)Ru(NO)(Cl)] (ε = 8 700 M^{-1} cm^{-1}) leads to more overlap with the dye band compared to [((OMe)$_2$bQb)Ru(NO)(Cl)] (ε = 3 750 M^{-1} cm^{-1}). It is thus evident that the energy absorbed by the dye is transferred to the RuNO unit allowing enhanced photodissociation of NO under 500 nm light.

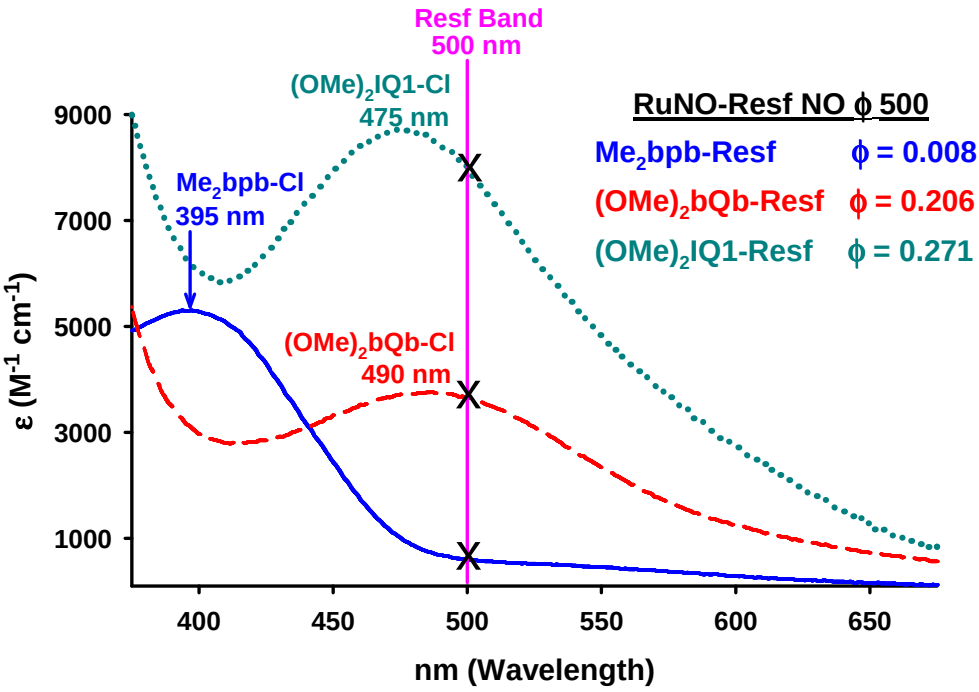

Figure 4.23. Electronic Absorption Spectra of [(Me$_2$bpb)Ru(NO)(Cl)], [((OMe)$_2$bQb)Ru(NO)(Cl)], and [((OMe)$_2$IQ1)Ru(NO)(Cl)]. Black X's represents points of overlap of RuNO-Cl photoband with the bound Resf absorption band at 500 nm. Larger overlap leads to higher quantum yield values of NO release in the corresponding RuNO-Resf nitorsyls (Inset).

Comparison of the quantum yield values for the FlEt-bound nitroyls [(Me$_2$bpb)Ru(NO)(FlEt)] and [((OMe)$_2$IQ1)Ru(NO)(FlEt)] compared to their parent

Cl-bound nitrosyls also reveals increased efficiency of NO release (see Table 4.1). For example, exposure [(Me_2bpb)Ru(NO)(Cl)] to 500 nm light results in a very low quantum yield (ϕ_{500}) value of 0.0008 while similar light exposure of [(Me_2bpb)Ru(NO)(FlEt)] leads to a significantly larger ϕ_{500} value of 0.30. Interestingly, [(Me_2bpb)Ru(NO)(FlEt)] has a larger ϕ_{500} compared to that of [(($OMe)_2$IQ1)Ru(NO)(FlEt)] (ϕ_{500} = 0.17). The opposite is true in case of the corresponding Resf-tethered {Ru-NO}^{6} nitrosyls as the ϕ_{500} value of the Resf-bound nitrosyls [($OMe)_2$IQ1)Ru(NO)(Resf)] is larger than that of [(Me_2bpb)Ru(NO)(Resf)] (Table 4.1). The increased absorption at 500 nm for [($OMe)_2$IQ1)Ru(NO)(Resf)] (compared to [(Me_2bpb)Ru(NO)(Resf)]) could account for its larger ϕ_{500} value. However, the same is not true for the FlEt-tethered nitrosyls. Despite similar extinction coefficient values, [(Me_2bpb)Ru(NO)(FlEt)] (ε_{500} = 19 000 $M^{-1}cm^{-1}$) exhibits a higher ϕ_{500} value than [(($OMe)_2$IQ1)Ru(NO)(FlEt)] (ε_{500} = 22 000 $M^{-1}cm^{-1}$).

In the case of [(($OMe)_2$IQ1)Ru(NO)(PyFlEt)](BF_4), while the attachment of the PyFlEt dye improves the amount of visible light absorbed by the compound, it does not improve the effiency of NO photorelease triggered by visible light. Thus it appears that the 4-pyridinyloxy linker does not allow the increased visible light absorbed by the dye to be used toward the NO photolabitlity of [(($OMe)_2$IQ1)Ru(NO)(PyFlEt)](BF_4). This confirms that the direct conjugation of Resf and FlEt to the Ru-center facilitates the transfer of energy from the dye into the RuNO unit which is necessary for the enhanced NO photolability in such dye-bound {RuNO}^{6} nitrosyls when exposed to visible light (Figure 4.24).

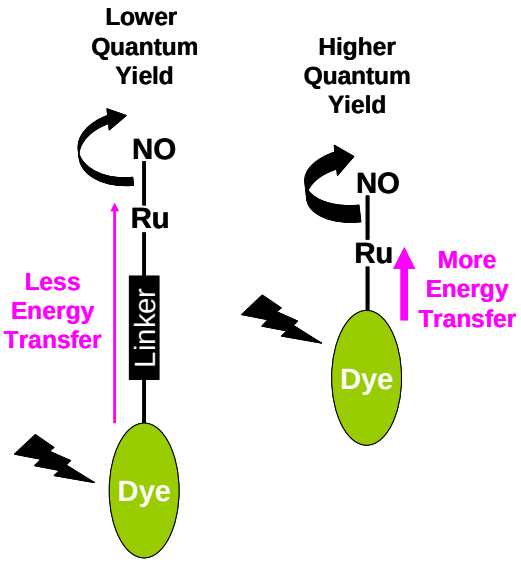

Figure 4.24. Ruthenium nitrosyls directly coordinated to a sensitizing dye chromophore (right) have higher quantum yields of NO photorelease than nitorsyls with the dye coordinated through a linker (left)

4.9 Fluorescence Properties of Free- and Bound-Dye Compounds

Given the intense fluorescence of free resorufin and fluorescein (ϕ_{fl} = 0.83 and 0.93), we were interested to see if the dye-bound nitrosyls also had fluorescent properties. Since fluorescein derivatives were used for these nitroyls, we first examined the fluorescent properties of FlEt and PyFlEt. The conversion of fluorescein into FlEt results in a 18% decrease in the fluorescence quantum yield of FlEt (ϕ_{fl} = 0.77, Table 4.2) compared to free fluorescein.[1] The added 4-pyridinyloxy linker in PyFlEt further quenches the fluorescence (ϕ_{fl} = 0.20, Table 4.2) by an additional 60%. Upon coordination of the dye chromophores to the $\{RuNO\}^6$ centers, the fluorescence is further quenched in all cases, presumably due to energy transfer

Table 4.2. Summary of Absorption and Emission Parameters (λ_{ex} = 480 nm) and Fluorescence Quantum Yield (ϕ_{fl}) Values of Selected Compounds in 50:50 MeCN/H_2O at pH 7

Compound	Absorbance λ_{max}	Emission λ_{max}	Fluorescence Quantum Yield ϕ_{fl}
Fluorescein	496 nm	518 nm	0.93 ± 0.02 [a]
FlEt	504 nm	526 nm	0.77 ± 0.02 [b]
PyFlEt	454 nm	520 nm	0.20 ± 0.02
[(Me_2bpb)Ru(NO)(FlEt)]	475 nm	526 nm	0.009 ± 0.002
[(($OMe)_2$IQ1)Ru(NO)(FlEt)]	475 nm	526 nm	0.017 ± 0.003
[(($OMe)_2$IQ1)Ru(NO)(PyFlEt)]$^+$	460 nm	525 nm	0.10 ± 0.02

[a] Measured in aqueous solution at pH 11.
[b] Measured in 50:50 mixture of MeCN/phosphate buffer at pH 7.4.

from the dye into the $\{RuNO\}^6$ unit. However, solutions of both [(($OMe)_2$bpb)Ru(NO)(Resf)] and [(($OMe)_2$IQ1)Ru(NO)-(Resf)] in MeCN sill exhibit broad red fluorescence emission bands of moderate intensity at 593 nm (Figure 4.25). Similar fluorescence properties have previously been observed with [(Me_2bpb)Ru(NO)(Resf)] for which the residual fluorescence was enough to monitor the location of the complex during targeted NO delivery to cancer cells.[18b] Similarly, the direct coordination of FlEt to the $\{RuNO\}^6$ center in both [(Me_2bpb)Ru(NO)(FlEt)] and [(($OMe)_2$IQ1)Ru(NO)(FlEt)] results in a low intensity fluorescence emission band at 526 nm (ϕ_{fl} = 0.009 and 0.017 respectively, Table 4.2). The fluorescence of [(($OMe)_2$IQ1)Ru(NO)(FlEt)](BF_4) (ϕ_{fl} = 0.10, Table 4.2) is

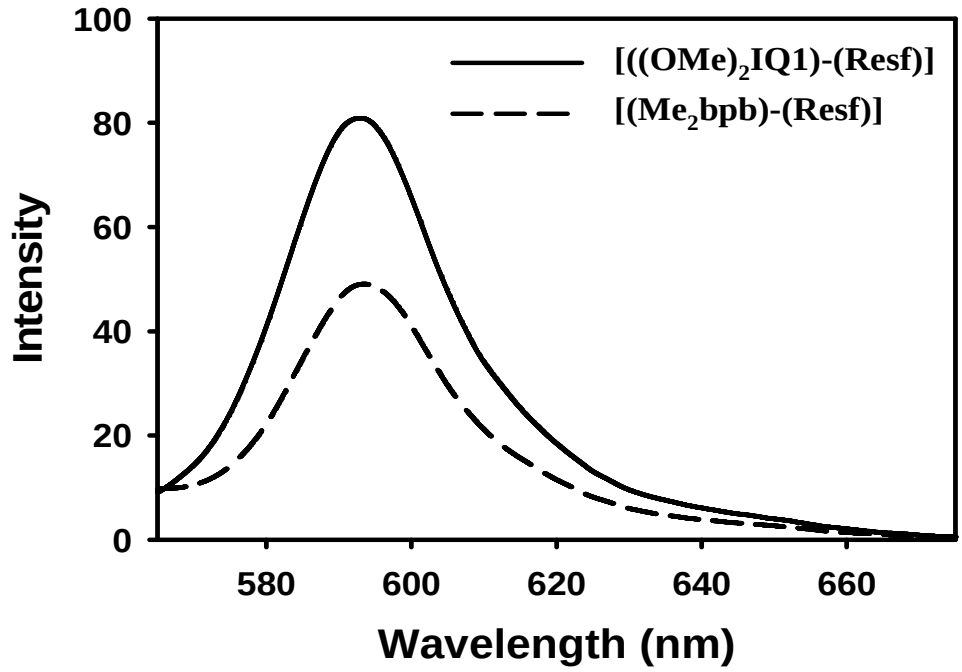

Figure 4.25. Fluorescence emission spectrum of [((OMe)$_2$IQ1)Ru(NO)(Resf)] and [(Me$_2$bpb)Ru(NO)(Resf)] in MeCN (λ_{ex}= 490 nm). Samples with same absorbance values at 490 nm were used.

higher than that of the FlEt-bound nitrosyls and quenched by only 50% compared to that of free PyFlEt. For comparison, the fluorescence of [((OMe)$_2$IQ1)Ru-(NO)(FlEt)] is quenched by 97% compared to that of free FlEt. It appears that the 4-pyridinyloxy linker decreases the amount of energy transferred from the dye to the Ru-center which decreases the amount of fluorescence quenching caused by metal binding. This finding is consistant with the lack of enhanced NO photolabilty in [((OMe)$_2$IQ1)Ru(NO)(PyFlEt)](BF$_4$). Therefore, the additional visible light absorbed by the dyes in the directly conjugated Resf and FlEt nitrosyls goes toward NO photorelease and not fluorescence while in the case of the PyFlEt-bound nitrosyl, the

additional absorbed visible light get released as fluorescence and the NO photolabilty remains unaffected.

4.10 Fluorescence Turn-Off and Turn-ON Signals

We found that light exposure of [(Me_2bpb)Ru(NO)(FlEt)] and [(($OMe)_2$IQ1)Ru(NO)(FlEt)] in 50:50 MeCN/H_2O (causing NO photorelease) resulted in a rapid increase in fluorescence of these solutions. When such solutions were kept in the dark, there was very little change in their fluorescence. In addition, no increase in fluorescence was observed when solutions of [(Me_2bpb)Ru(NO)(FlEt)] and [(($OMe)_2$IQ1)Ru(NO)(FlEt)] *in very dry solvents* (such as MeCN) were exposed to light. It thus became evident that these FlEt-bound $\{RuNO\}^6$ nitrosyls are light activated fluorescence turn-ON agents in the presence of water. Figure 4.26 shows the increase in fluorescence (λ_{ex} = 480 nm, λ_{em} = 526) of [(Me_2bpb)Ru(NO)(FlEt)] and [(($OMe)_2$IQ1)Ru(NO)(FlEt)] (in 50:50 MeCN/H_2O) observed after 1 min intervals of visible light exposure. There was a 27-fold fluorescence turn-ON for [(Me_2bpb)Ru(NO)(FlEt)] after 5 min of light exposure while in the case of [(($OMe)_2$IQ1)Ru(NO)(FlEt)], there was a 5-fold fluorescence increase under similar conditions. These findings follow a similar trend ([(Me_2bpb)Ru(NO)(FlEt)] > [(($OMe)_2$IQ1)Ru(NO)(FlEt)]) observed for the NO photolability of [(Me_2bpb)Ru(NO)(FlEt)] and [(($OMe)_2$IQ1)Ru(NO)(FlEt)]. The extent of fluorescence turn-ON therefore appears to correlate with the amount of light triggered NO release from these $\{RuNO\}^6$ nitrosyls.

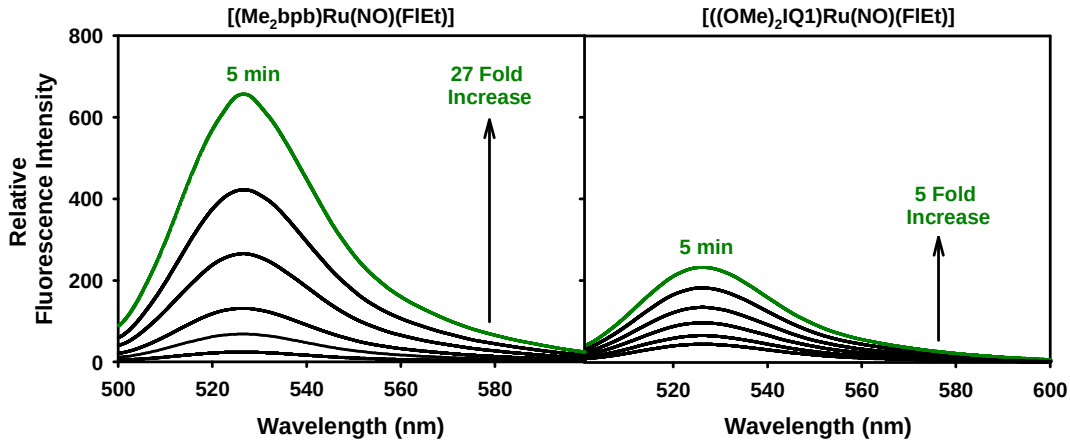

Figure 4.26. Changes in the fluorescence emission spectra upon 1 minute intervals of visible light illumination of [(Me_2bpb)Ru(NO)(FlEt)] (left panel) and [(($OMe)_2$IQ1)Ru(NO)(FlEt)] (right panel) in 50:50 H_2O/MeCN (λ_{ex}= 480 nm). Samples with absorbance values of 0.9 at 480 nm were used.

In order to understand the structural changes responsible for the increase in fluorescence we have employed ^{1}H-NMR spectroscopy to monitor the fate of [(Me_2bpb)Ru(NO)(FlEt)] and [(($OMe)_2$IQ1)Ru(NO)(FlEt)] upon light exposure in wet $CDCN_3$. When left in the dark for several hours, there are no changes in the ^{1}H-NMR spectra of both nitrosyls. However, exposure of the solutions of [(Me_2bpb)Ru(NO)(FlEt)] and [(($OMe)_2$IQ1)Ru(NO)(FlEt)] to visible light results in the appearance of new peaks consistent with those of free FlEt (Figure 4.27). This observation confirms that the increase in fluorescence observed upon light exposure is due to the release of FlEt.

We hypothesize that this release of FlEt arises due to the formation of a thermodynamically stable HO-bound Ru(III) photoproduct. When NO is bound, the

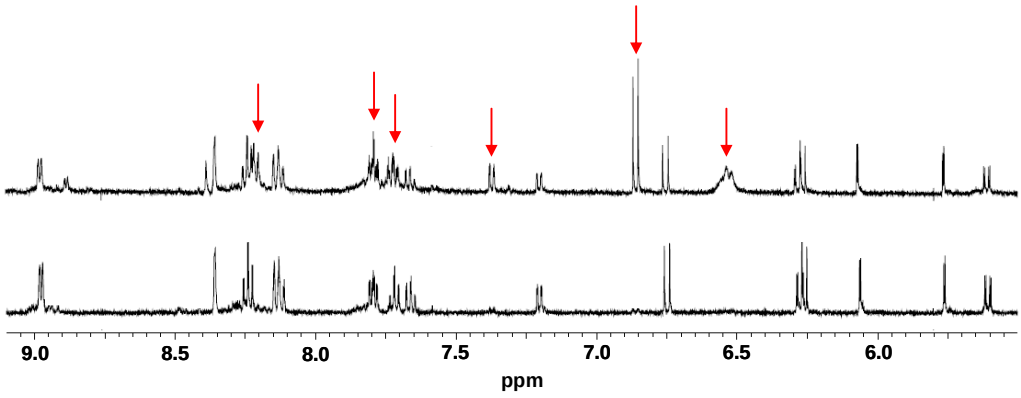

Figure 4.27. ^{1}H-NMR spectra (9.1-5.5 ppm) of [(Me_2bpb)Ru(NO)(FlEt)] in CD_3CN at 298 K kept in the dark (bottom) and after light exposure (top). Red arrow show new peaks of unbound FlEt dye.

Ru-center is thought to have more low-spin Ru(II) character. However once NO has been released, the Ru-center is converted into a low-spin Ru(III) species (strong EPR signal, vide infra) which is more susceptible to aquation (eq 2). The high Lewis acidity of the resulting water bound Ru(III) complex combined with the basic properties of $FlEt^-$ may eventually lead to the formation of the more stable [(L)Ru(III)(OH)(H_2O)] (L = Me_2bpb or $(OMe)_2$IQ1) photoproduct and FlEt-H (eq. 3).

$$[(L)Ru(NO)(FlEt)] \xrightarrow{H_2O} NO^{\bullet} + [(L)Ru^{3+}(H_2O)(FlEt)]^{+} \quad (2)$$

$$[(L)Ru^{3+}(H_2O)(FlEt)]^{+} \xrightarrow{H_2O} [(L)Ru^{3+}(H_2O)(OH)] + FlEt\text{-}H \quad (3)$$

(L = Me_2bpb or $(OMe)_2$IQ1)

This mechanism is confirmed by the lack of light-induced fluorescence turn-ON in dry non-aqueous solvents. The observation strongly implies that the FlEt dye in

[(Me_2bpb)Ru(NO)(FlEt)] and [(($OMe)_2$IQ1)Ru(NO)(FlEt)] stays bound to the Ru(III) center upon light exposure (and NO release) in the absence of water. The paramagnetism of the low-spin Ru(III) center in [(L)Ru(III)(FlEt)(solv)] (L = Me_2bpb or $(OMe)_2$IQ1) quenches the fluorescence of such photoproducts in dry solvents.

To confirm the 3+ oxidation state of ruthenium in the solvato species generated after complete photolysis of the diamagnetic {Ru-NO}^{6} nitrosyls [(Me_2bpb)Ru(NO)(FlEt)] and [(($OMe)_2$IQ1)Ru(NO)(FlEt)], EPR measurements were performed. Photoproducts of [(Me_2bpb)Ru(NO)(FlEt)] and [(($OMe)_2$IQ1)Ru-(NO)(FlEt)] generated in dry MeCN display axial EPR spectra (*g* values: 2.16 and 1.89 for [(Me_2bpb)Ru(NO)(FlEt)] and 2.18 and 1.90 for [(($OMe)_2$IQ1)Ru(NO)(FlEt)]) typical of low spin Ru(III). However, the spectra change when photolysis is done in the presence of water (*g* values: 2.19 and 1.88 for [(Me_2bpb)Ru(NO)(FlEt)] and 2.12 and 1.92 for [(($OMe)_2$IQ1)Ru(NO)(FlEt)]). Comparison of the EPR spectra of the photoproduct of [(Me_2bpb)Ru(NO)(FlEt)] in aqueous media with that of [(Me_2bpb)Ru(NO)(OH)] [22] after photolysis under similar conditions confirms such conclusion (similar spectra with identical g values). Collectively, these results support the hypothesis that the ultimate formation of OH-bound photoproduct [(L)Ru(III)(OH)(H_2O)] (L = Me_2bpb or $(OMe)_2$IQ1) drives the release of FlEt.

The {RuNO}^{6} nitrosyls with coordinated Resf dye chromophores display *turn-OFF* fluorescence signal once NO is released. The decrease in fluorescence has

been attributed to the formation of dye-bound Ru(III) photoproducts. The paramagnetic d^5 Ru(III) center is a very effective fluorescence quencher of the bound Resf in these photoproducts. In contrast, [(Me_2bpb)Ru(NO)(FlEt)] and [(($OMe)_2$IQ1)Ru(NO)(FlEt)] are the first example of ruthenium nitrosyls with a fluorescent *turn-ON* signal for NO release. Although a Ru(III) photoproduct is also produced in this case, the FlEt dye does not stay bound to the metal center. It becomes apparent that FlEt has a lower affinity for Ru(III) compared to that of Resf. Thus as NO leaves generating a Ru(III) photoproduct, FlEt is released and a fluorescence enhancement is noted instead of quenching (Figure 4.28).

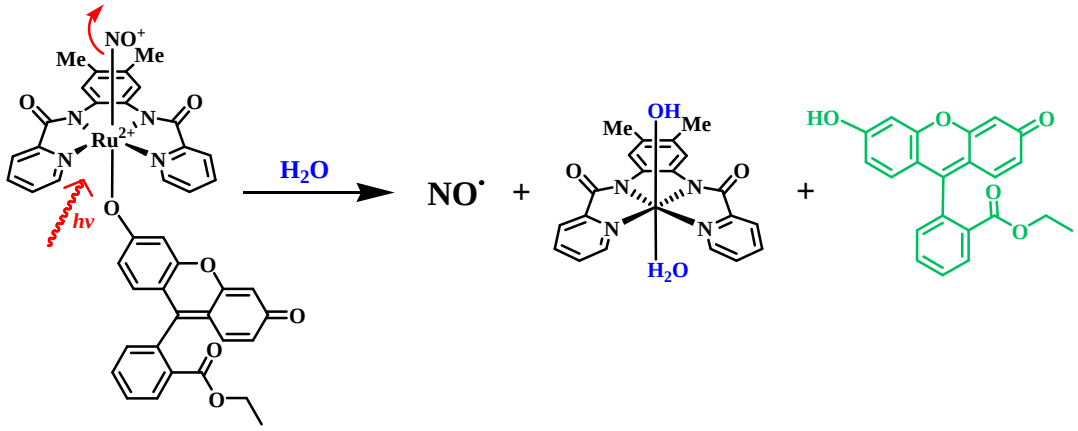

Figure 4.28. Purposed mechanism of light triggered fluorescence turn-on for [(Me_2bpb)Ru(NO)(FlEt)]

Recently, there have been several reports of fluorescent turn-ON sensors that signal the presence of NO.[12] For example, Lippard and coworkers have designed a Cu(II) fluorescein-based NO sensor CuFL (FL = 2-{2-chloro-6-hydroxy-5-[(2-methyl-quinolin-8-ylamino)-methyl]-3-oxo-3*H*-xanthen-9-yl}benzoic acid).[13] The FL

ligand is not fluorescent in its free or Cu(II)-bound form. However upon expose to NO, the Cu(II) center of CuFl is reduced to Cu(I) with concomitant *N*-nitrosylation of FL (FL-NO). The *N*-nitrosylation of the FL-NO ligand results in its displacement from the Cu(I) center and an increase in fluorescence. Indeed, CuFL has been successfully used to visualize NO generated from iNOS in murine macrophage cells and from cNOS in SK-N-SH human neuroblastoma cells.[13] However in the present case, our goal is to deliver exogenous NO to biological targets. With [(Me_2bpb)Ru(NO)(FlEt)] and [(($OMe)_2$IQ1)Ru(NO)(FlEt)], the release of NO (instead of NO binding) results in a fluorescent turn-ON signal which could clearly indicate NO delivery. This is a distinct advantage of the designed NO donors [(Me_2bpb)Ru(NO)(FlEt)] and [(($OMe)_2$IQ1)Ru(NO)(FlEt)].

4.11 Experimental Section

4.11.1 Syntheses of Compounds

Materials. NO gas was purchased from Spectra Gases Inc. and was purified by passing through a long KOH column prior to use. $RuCl_3$•*x*H_2O (Aldrich Chemical Co.) was treated several times with concentrated HCl to prepare the starting metal salt, $RuCl_3$•3H_2O. The solvents were dried by standard techniques and distilled. The starting complex [(Me_2bpb)Ru(NO)(Cl)] was synthesized by following the procedure previously reported by us.[8] The published procedure for Fluorescein ethyl ester was modified to obtain high yields of the pure dye.[1] 1-Isoquinoline was purchased from Wako Chemicals and the quinaldic acid was obtained from Acros Organics. 1,2-

dimethoxy-4,5-diaminobenzene was synthesized according to the published procedure.[9] Fluorescein and $AgBF_4$ were purchased from Fluka and Alfa-Aesar, respectively. All other chemicals were purchased from Aldrich Chemical Co. and used without further purification.

Synthesis of Ligands. 1,2-Bis(Isoquinoline-1-carboxamido)-4,5-dimethyl-benzene (H_2Me_2IQ1). A mixture of one equiv 4,5-dimethyl-1,2-phenylenediamine (0.5 g, 3.67 mmol), 2 equiv of 1-Isoquinolinecarboxylic acid (1.27 g, 7.33 mmol), and 2 equiv of $P(OPh)_3$ (2.28 g, 7.34 mmol) in 20 mL of pyridine was prepared. Upon heating at 100 °C for 3 hours the brown solution turned red. The cooled solution was partially condensed and further cooled to 4 °C overnight. The resulting orange precipitate was filtered and washed several times with EtOH and Et_2O and dried in vacuo. Yield: 0.89 g (55%). Selected IR frequencies (KBr disk, in cm^{-1}): 3248 (w, ν_{NH}), 1675 (s, $\nu_{C=O}$), 1661 (s, $\nu_{C=O}$), 1585 (s), 1532 (vs), 1484 (vs), 1452 (s), 1379 (s), 1134 (w), 831 (s), 735 (w), 636 (w). ^1H NMR in $CDCl_3$, δ from TMS: 10.48 (s 2H), 9.72 (d 2H), 8.43 (d 2H), 7.85 (d 2H), 7.80 (d 2H), 7.73 (m 4H), 7.70 (s 2H), 2.35 (s 6H).

1,2-Bis(Isoquinoline-3-carboxamido)-4,5-dimethylbenzene (H_2Me_2IQ3). A batch of 4,5-dimethyl-1,2-phenylenediamine (0.5 g, 3.67 mmol), of 3-Isoquinoline-carboxylic acid (1.27 g, 7.33 mmol), and of $P(OPh)_3$ (2.28 g, 7.34 mmol) was prepared in 15 mL of pyridine. The brown solution turned dark brownish-red upon heating for 3 hours at 100 °C. The solution was cooled and refrigerated at 4 °C overnight. The resulting white precipitate was filtered and washed several times with

EtOH and Et_2O and dried in vacuo. Yield: 0.68 g (42%). Selected IR frequencies (KBr disk, in cm^{-1}): 3307 (w, ν_{NH}), 1691 (vs, $\nu_{C=O}$), 1533 (s), 1490 (vs), 1443 (s), 758 (w). ^1H NMR in $CDCl_3$, δ from TMS: 10.39 (s 2H), 9.16 (s 2H), 8.75 (s 2H), 8.02 (m 4H), 7.79 (s 2H), 7.71 (m 4H), 2.36 (s 6H).

1,2-Bis(pyridine-2-carboxamido)-4,5-dimethoxybenzene ($H_2(OMe)_2$bpb). A mixture of 1,2-dimethoxy-4,5-diaminobenzene (0.51 g, 3.0 mmol), 2 equiv of picolinic acid (0.74 g, 6.0 mmol) and 2 equiv of $P(OPh)_3$ (1.87 g, 6.0 mmol) was dissolved in 20 mL of pyridine. The resulting green/brown solution turned amber after refluxing for 4 h. The solution was cooled and kept at 4°C over night. The resulting tan precipitate was filtered and washed with EtOH and Et_2O and dried in vacuo. Yield: 1.04 g (55%). Selected IR bands (KBr disk, in cm^{-1}): 3335 (w, ν_{NH}), 3285 (w), 1676 (s $\nu_{C=O}$), 1662 (s), 1609 (w), 1527 (s), 1504 (s), 1480 (m), 1350 (m), 1210 (vs), 1093 (m), 997 (m), 751 (m), 671 (m). ^1H NMR in $CDCl_3$, δ from TMS: 10.32 (s 2H), 8.57 (d 2H), 8.32 (d 2H), 7.91 (t 2H), 7.47 (m 4H), 3.94 (s 6H).

1,2-Bis(Isoquinoline-1-carboxamido)-4,5-dimethoxybenzene ($H_2(OMe)_2$IQ1). A solution containing 1 equiv of 1,2-dimethoxy-4,5-diaminobenzene (1.27 g, 7.56 mmol), 2 equiv of 1-Isoquinolinecarboxylic acid (2.62 g, 15.1 mmol), and 2 equiv of $P(OPh)_3$ (4.69 g, 15.1 mmol) was prepared in 40 mL of pyridine. The green solution turned bright red upon heating at 100 °C for 4 h. The solution was partially condensed and stored at 4 °C overnight. The resulting bright yellow-orange precipitate was filtered and washed several times with EtOH and Et_2O and dried in vacuo. Yield: 2.17 g (60%). Selected IR frequencies (KBr disk, in cm^{-1}):

3296 (w, ν_{NH}), 1682 (s, $\nu_{C=O}$), 1526 (vs), 1478 (s), 1334 (w), 1205 (s), 1108 (w). ^{1}H NMR in $CDCl_3$, δ from TMS: 10.46 (s 2H), 9.72 (d 2H), 8.40 (d 2H), 7.88 (d 2H), 7.82 (d 2H), 7.73 (t 4H), 7.53 (s H).

Fluorescein Ethyl Ester (FlEt). A slurry of Fluorescein (1.00g, 3.01 mmol) in 150 mL of EtOH was treated with 7 mL of sulfuric acid and heated to reflux temperature for 20 h in a 500 mL round bottom flask covered with aluminum foil. EtOH was then removed via rotary evaporation, leaving a bright yellow oil. The product was extracted into dichloromethane (DCM) via liquid-liquid extraction using DCM and water, and the DCM layer was washed with sodium bicarbonate (2.50g, 30.00 mmol) dissolved in 50mL of water. Finally, DCM was removed via rotary evaporation, leaving a red-orange solid. Yield: 0.97g (90%). Selected IR frequencies (KBr disk, in cm^{-1}): 1718 (m), 1640 (m), 1595 (vs), 1495 (s), 1460 (vs), 1384 (s), 1263 (vs), 1205 (s), 1107 (s). ^{1}H NMR in $CDCl_3$, δ from TMS: 8.72 (d 1H), 7.74 (t 1H), 7.69 (t 1H), 7.33 (d 1H), 6.99 (d 2H), 6.89 (s 2H), 6.81 (d 2H), 4.01 (q 2H), 0.92 (t 3H).

4-(Pyridinyloxy)-Fluorescein Ethyl Ester (PyFlEt). A batch of FlEt (0.750g, 2.08 mmol) was dissolved with 5 equiv each of triphenylphosphine (2.729g, 10.42 mmol) and 4-pyridylcarbinol (1.144g, 10.42 mmol) in 35 mL of THF. The solution was then cooled in a ice bath and treated with 5 equiv of diethyl azodicarboxylate (1.480g, 10.42 mmol) in 5 mL of THF, added dropwise. The resulting solution was then allowed to stir at room temp for 40 hours. The solution was then put in freezer to maximize precipitation of the orange solid which was

collected via gravity filtration and washed with MeCN. Yield: 0.753g (80%). Selected IR frequencies (KBr disk, in cm^{-1}): 1707 (m), 1643 (m), 1596 (vs), 1519 (s), 1450 (m), 1257 (s), 1208 (m), 1109 (m). H NMR in chloroform, δ from TMS: 8.653 (d 2H), 8.253 (d 1H), 7.732 (t 1H), 7.674 (t 1H), 7.359 (d 2H), 7.310 (d 1H), 6.993 (d 1H), 6.925 (d 1H), 6.862 (d 1H), 6.808 (d 1H), 6.536 (d 1H), 6.437 (s 1H), 5.20 (s 2H), 4.040 (q 2H), 0.971 (t 3H). UV/vis in MeCN, λ in nm (ε in M^{-1} cm^{-1}): 346 (7 500), 430 (18 700), 454 (20 800), 480 (12 600).

Syntheses of Metal Complexes. [((OMe)$_2$bpb)Ru(NO)(Cl)]. A pale yellow solution of $H_2(OMe)_2bpb$ (0.200 g, 0.53 mmol) in 20 mL of DMF was treated with 2.1 equiv of NaH (0.03 g, 1.1 mmol) to generate a bright orange solution. A batch of 0.138 g (0.53 mmol) of $RuCl_3 \bullet 3H_2O$ was then added to the solution of deprotonated ligand and the green mixture was heated to reflux temperature for 16 h. Next, it was cooled to room temperature and filtered to remove solid NaCl. The dark green filtrate was degassed and NO gas was bubbled through the solution at reflux temperature for 1 h. The resulting red/orange solution was cooled, and the solvent was removed in vacuo. The oily residue was triturated several times with MeCN to remove DMF. The solid was finally washed with portions of MeCN (2 × 5 mL) and THF (2 × 5 mL) to afford an orange-brown compound which was dried in vacuo. Yield: 0.205 g (72%). Selected IR bands (KBr disk, in cm^{-1}): 1845 (vs, ν_{NO}), 1631 (vs, $\nu_{C=O}$), 1596 (m), 1566 (w), 1497 (s), 1402 (m), 1368 (m), 1278 (w), 1254 (m), 1080 (w), 988 (w), 872 (w), 756 (w), 489 (w). UV/vis in DMF, λ in nm (ε in M^{-1} cm^{-}

^{1}): 319 (12 500), 420 (7 800). ^{1}H NMR in CDCl3, δ from TMS: 8.74 (d 2H), 8.49 (s 2H), 8.39 (d 2H), 8.24 (t 2H), 7.74 (t 2H), 3.98 (s 6H).

[((OMe)$_2$IQ1)Ru(NO)(Cl)]. A yellow solution of $H_2(OMe)_2IQ1$ (0.15 g, 0.31 mmol) in 20 mL of DMF was treated with 2.1 equiv of NaH (16 mg, 0.67 mmol) to generate a red solution and to it was added a batch of 0.082 g (0.31 mmol) of $RuCl_3 \bullet 3H_2O$. The dark brown mixture was then heated to reflux temperature for 20 h. Next. the green-brown solution was cooled to room temperature and filtered to remove NaCl. The filtrate was degassed and NO gas was bubbled through it at reflux temperature for 2 h. The resulting red/maroon solution was cooled, and the solvent was removed in vacuo. The oily residue was triturated several times with MeCN to afford a red-brown solid. This solid was then stirred in hot MeCN and filtered to remove impurities. The dark maroon solid was finally washed with Et_2O and dried in vacuo. Yield: 0.16 g (80%). Selected IR frequencies (KBr disk, in cm^{-1}): 2923 (w), 1832 (m ν_{NO}), 1614 (vs), 1585 (s), 1492 (s), 1253 (s), 1091 (s). ^{1}H NMR in $CDCl_3$, δ from TMS: 10.45 (d 2H), 8.72 (d 2H), 8.61 (s H), 8.06 (d 2H), 7.90 (d 2H), 7.93 (t 2H), 7.90 (t 2H), 4.05 (s 6H). UV/vis in DMF, λ in nm (ε in M^{-1} cm^{-1}): 290 (27 000), 320 sh (22 300), 475 (8 700).

[((OMe)$_2$bpb)Ru(NO)(Resf)]. A mixture of [((OMe)$_2$bpb)Ru(NO)(Cl)] (0.100 g, 0.18 mmol) and 1 equiv of $AgBF_4$ (36 mg, 0.18 mmol) in 30 mL of MeCN was heated to reflux for 15 min and then a batch of 43 mg (0.18 mmol) of Resorufin (sodium salt) was added. The resulting red solution was heated to reflux for an additional 16 h. The red/orange mixture thus obtained was filtered and concentrated

under vacuum and then stored at 4 ^{o}C for 12 h. The red precipitate thus obtained was filtered and washed with ether (2 x 5 mL). Yield: 36 mg (27%). Selected IR bands (KBr disk, in cm^{-1}): 1831 (s, ν_{NO}), 1630 (vs, $\nu_{C=O}$), 1592 (vs), 1485 (vs), 1403 (m), 1370 (m), 1322 (w), 1272 (s), 1205 (m), 1102 (m), 1082 (m), 863 (m), 758(w), 683 (w), 588 (w), 493 (m). UV/vis in MeCN, λ in nm (ε in M^{-1} cm^{-1}): 402 (14 600), 495 (29 000). ^{1}H NMR in $CDCl_3$, δ from TMS: 8.75 (d 2H), 8.52 (d 2H), 8.32 (s 2H), 8.13 (t 2H), 7.81 (t 2H), 7.56 (t 2H), 7.30 (d 1H), 7.12 (2 1H), 6.72 (d 1H), 6.11 (s 1H), 6.08 (d 1H), 5.67 (s 1H), 4.00 (s 6H).

[((OMe)$_2$IQ1)Ru(NO)(Resf)]. A solution of [((OMe)$_2$IQ1)Ru(NO)(Cl)] (0.130 g, 0.20 mmol) in 20 mL of MeCN was treated with $AgBF_4$ (0.040g, 0.20 mmol) and heated to reflux temperature for 3 h. Next, a batch of 0.048 g (0.20 mmol) of Resorufin dye (as Na salt) was added to the hot maroon solution and continued to reflux for 4 h. The resulting bright red solution was cooled to 4° C and the dark red precipitate was filtered. The dried precipitate was then re-dissolved in CH_2Cl_2 and filtered to remove AgCl and $NaBF_4$. The filtrate was concentrated and loaded on a silica gel column. A CH_2Cl_2/THF gradient was used to elute the final product. Yield: 0.075 g (45%). Selected IR frequencies (KBr disk, in cm^{-1}): 1827 (vs ν_{NO}), 1617 (s), 1580 (m), 1487 (s), 1323 (m), 1270 (s), 1266 (s), 1199 (m), 1095 (m), 849 (w), 491 (w) . ^{1}H NMR in $CDCl_3$, δ from TMS: 10.27 (d 2H), 8.78 (d 2H), 8.55 (s 2H), 8.14 (d 2H), 8.01 (d 2H), 7.92 (t 2H), 7.83 (t 2H), 7.24 (s 1H), 7.03 (d 1H), 6.72 (d 1H), 5.99 (s 1H), 5.97(d 1H), 5.36 (d 1H), 4.09 (s 6H). UV/vis in MeCN, λ in nm (ε in M^{-1} cm^{-1}): 330 (15 000), 495 (30 000).

[(Me_2bpb)Ru(NO)(FlEt)]. A solution 0.150 g of [(Me_2bpb)Ru(NO)(Cl)] (0.294 mmol) was prepared in 20 mL of MeCN and treated with $AgBF_4$ (0.057g, 0.294 mmol). A separate solution 0.106 g of FlEt (0.294 mmol) in 20 mL of MeCN was treated with NaH (0.007g, 0.294 mmol). Both solutions were then heated to reflux temperature and the FlEt solution was slowly added to the [(Me_2bpb)Ru(NO)(Cl)] solution with stirring. Heating of the mixture (with constant stirring) was continued at reflux temperature for 5 h. Next, the bright red solution was cooled to –20°C for 1 h to allow full precipitation of impurities which were filtered off using a Celite pad. The filtrate was condensed to half the original volume, 5 mL of Et_2O was added, and then stored at –20°C for 48 h. The red precipitate was filtered, washed several times with Et_2O, and dried in vacuo. It was finally recrystallized from $CHCl_3$. Yield: 0.100 g (41%). Selected IR frequencies (KBr disk, in cm^{-1}): 1846 (s), 1715 (m), 1635 (s), 1578 (vs), 1473 (s), 1379 (m), 1273 (s), 1206 (m), 1104 (m). ^{1}H NMR in $CDCl_3$, δ from TMS: 8.83 (d 2H), 8.39 (s 2H), 3.32 (d 1H), 8.28 (d 1H), 8.24 (t 1H), 8.21 (t 1H), 8.16 (d 1H), 7.79 (t 1H), 7.76 (t 1H), 7.64 (t 1H), 7.60 (t 1H), 7.17 (d 1H), 6.77 (d 1H), 6.49 (d 1H), 6.39 (d 1H), 6.30 (s 1H), 5.81 (d 1H), 5.74 (s 1H), 3.98 (q 1H), 3.89 (q 1H), 2.27 (s 6H), 0.84 (t 3H). ESI-MS: m/z 836 (M^+). UV-Vis in MeCN, λ_{max} in nm (ε in $M^{-1}cm^{-1}$): 270 (25 500), 375 (11 000), 450 sh (18 500), 475 (24 000), 510 sh (20 100).

[($(OMe)_2$IQ1)Ru(NO)(FlEt)]. A batch of [($(OMe)_2$IQ1)Ru(NO)(Cl)] (0.150 g, 0.233 mmol) was treated with $AgBF_4$ (0.045 g, 0.233 mmol) in 15 mL of MeCN and heated to reflux temperature. Meanwhile, a slurry of FlEt (0.084 g, 0.233 mmol)

was treated with 1 equiv of NaH (0.006 g, 0.233 mmol) in MeCN and also brought to reflux temperature. The hot FlEt solution was then added to the [((OMe)$_2$IQ1)Ru(NO)(Cl)] solution and the mixture was kept at reflux temperature for 8 h. Over the course of the reaction, a red orange precipitate separated out. The precipitate was collected by filtration and recrystallized from $CHCl_3$/pentane. Yield: 0.172 g (76%). Selected IR frequencies (KBr disk, in cm^{-1}): 1832 (m), 1712 (w), 1617 (vs), 1579 (vs), 1496 (s), 1332 (m), 1287 (s), 1213 (w), 1097 (s). ^{1}H NMR in $CDCl_3$, δ from TMS: 10.339 (d 1H), 10.193 (d 1H), 8.790 (dd 2H), 8.521 (s 1H), 8.482 (s 1H), 8.141 (m 3H), 7.996 (tt 3H), 7.891 (dt 2H), 7.809 (t 1H), 7.596 (dt 2H), 7.054 (d 1H), 6.703 (d 1H), 6.440 (d 1H), 6.293(d 1H), 6.057 (s 1H), 5.875 (d 1H), 5.363 (s 1H), 4.012 (s 3H), 3.994 (s 3H), 3.885 (q 1H), 3.796 (q 1H), 0.701 (t 3H). ESI-MS: m/z 968 (M+). UV-Vis in MeCN, λ_{max} in nm (ε in $M^{-1}cm^{-1}$): 280 (28 700), 320 sh (17 000), 365 sh (10 200), 450 sh (21 800), 475 (28 000), 510 sh (22 700).

[((OMe)$_2$IQ1)Ru(NO)(PyFlEt)](BF$_4$). A batch of [((OMe)$_2$IQ1)Ru(NO)(Cl)] (0.220 g, 0.342 mmol) was treated with $AgBF_4$ (0.067 g, 0.344 mmol) in 15 mL MeCN, and heated to reflux temperature for 2 hours. PyFlEt (0.154 g, 0.341 mmol) was added neat to the hot solution and kept at reflux temperature for an additional 2 hours. The solution was condensed to 10 mL and 5 mL of Et_2O was added. The resulting solution was cooled -20 ºC and filtered to remove solid impurities. The solvent was removed in vacuo and the residue was stirred in a 3:10 mixture of warm $CHCl_3$ and THF to dissolve any remaining imuprities. The orange produced was then isolated by filtration. Yield: 0.130 g (59%). Selected IR frequencies (KBr disk, in cm$^-$

[1]):1880 (w, ν_{NO}), 1626 (vs), 1593 (vs), 1497 (s) 1443 (m), 1323 (m), 1255 (s), 1205 (w), 1090 (s), 1034 (s). H NMR in chloroform, δ from TMS: 10.145 (d 1H), 10.130 (d 1H), 9.503 (d 2H), 8.630 (dd 2H), 8.511 (s 1H), 8.500(s 1H), 8.218 (dd 1H), 8.087 (dt 3H), 7.955 (tt 3H), 7.870 (t 3H), 7.69 (t 1H), 7.64 (t 1H), 7.41 (d 2H), 7.24 (d 1H), 6.82 (dd 1H), 6.72 (s 1H), 6.61 (dd 1H), 6.49 (dd 1H), 6.33 (s 1H), 4.93 (s 2H), 4.08(s 6H), 4.03 (q 1H), 3.99 (q 1H), 0.920 (t 3H). UV-Vis in MeCN, λ_{max} in nm (ε in $M^{-1}cm^{-1}$): 300 sh (32 000), 340 sh (21 250), 430 sh (23 650), 454 (28 000), 480 sh (22 150).

4.11. 2 Experimental Data: ^{1}H-NMR and IR Spectra

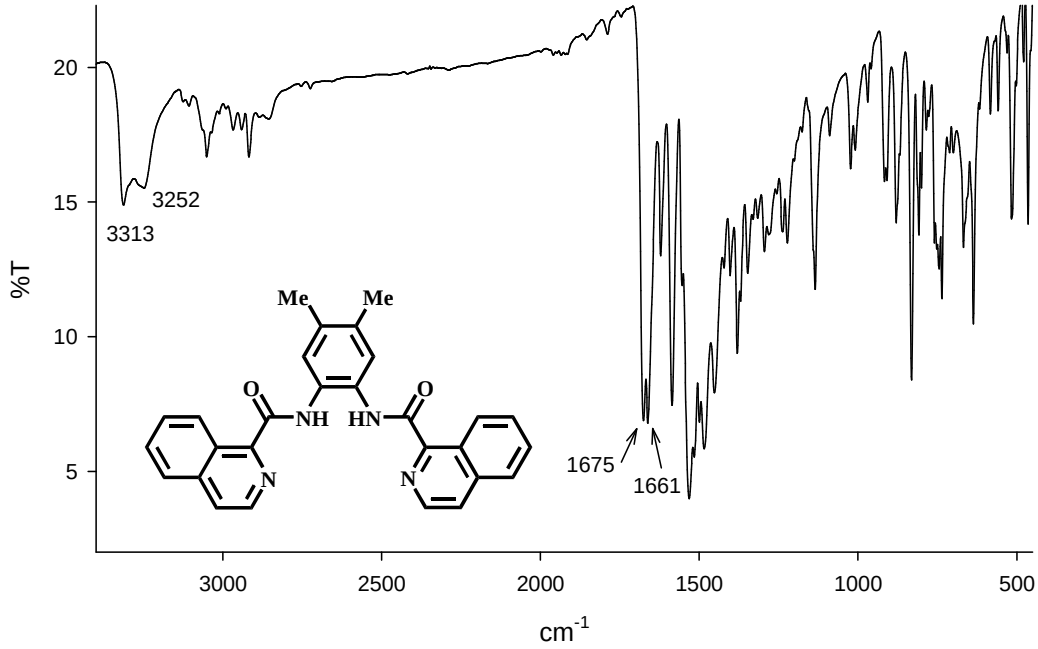

Figure 4.29. IR spectrum of $H_2(Me)_2IQ1$ in KBr pellet

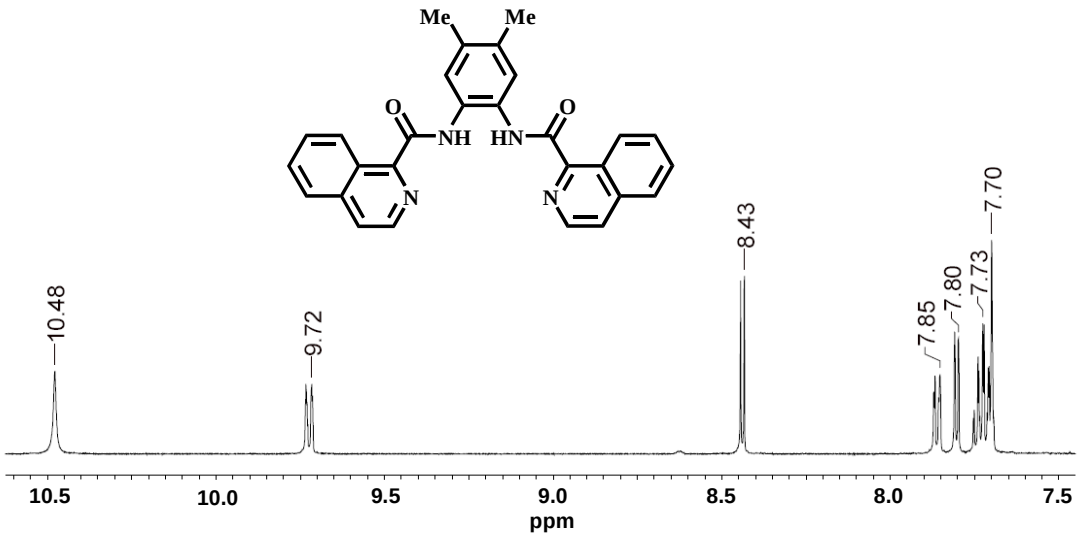

Figure 4.30. ^{1}H-NMR spectrum (7.5-10.6 ppm) of H_2Me_2IQ1 in $CDCl_3$ at 298 K

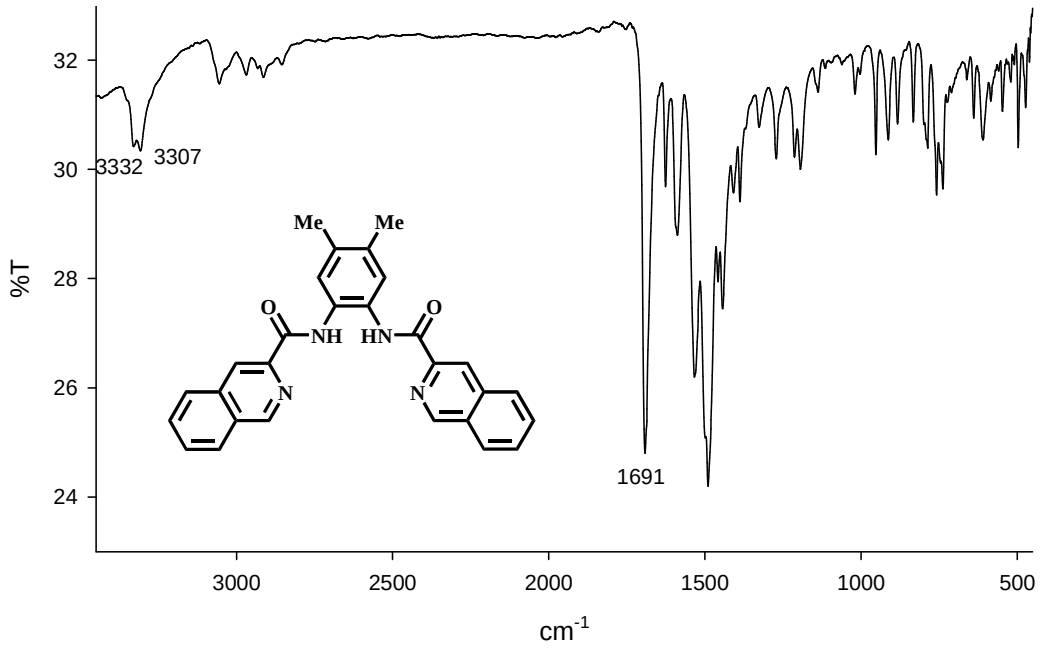

Figure 4.31. IR spectrum of $H_2(Me)_2IQ3$ in KBr pellet

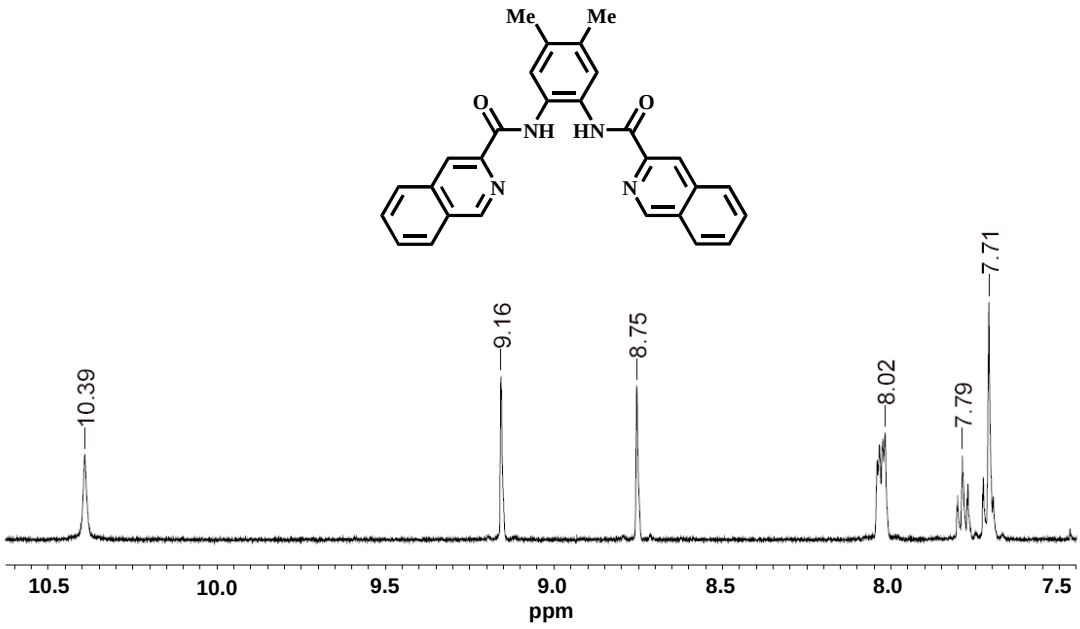

Figure 4.32. ^{1}H-NMR spectrum (7.5-10.6 ppm) of H_2Me_2IQ3 in $CDCl_3$ at 298 K

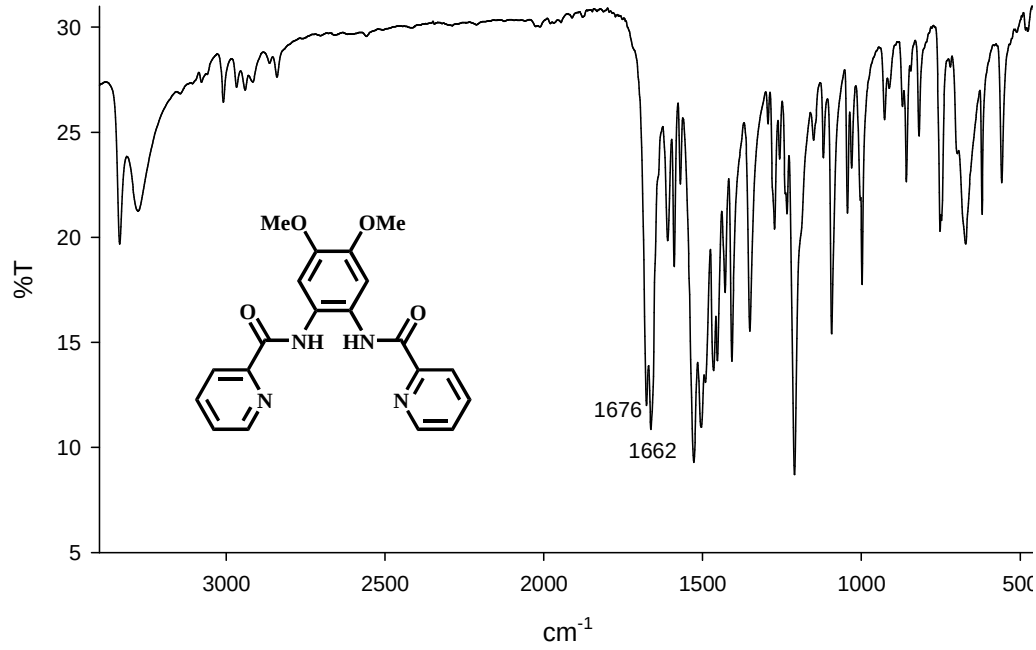

Figure 4.33. IR spectrum of $H_2(OMe)_2bpb$ in KBr pellet

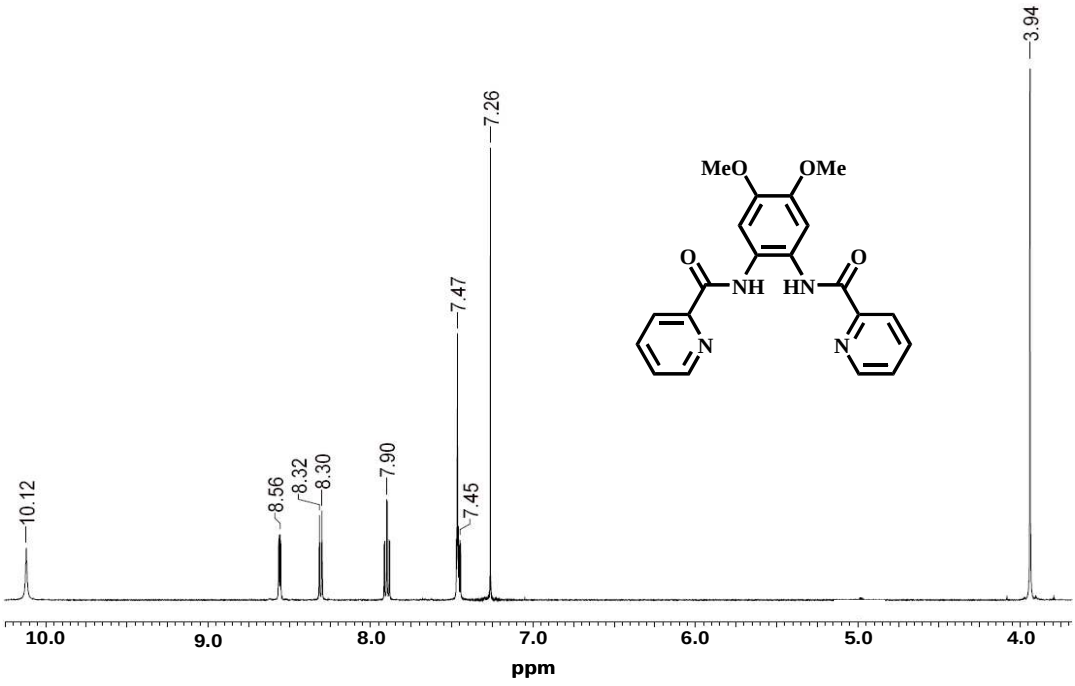

Figure 4.34. ^{1}H-NMR spectrum (3.8-10.2 ppm) of $H_2(OMe)_2bpb$ in $CDCl_3$ at 298 K

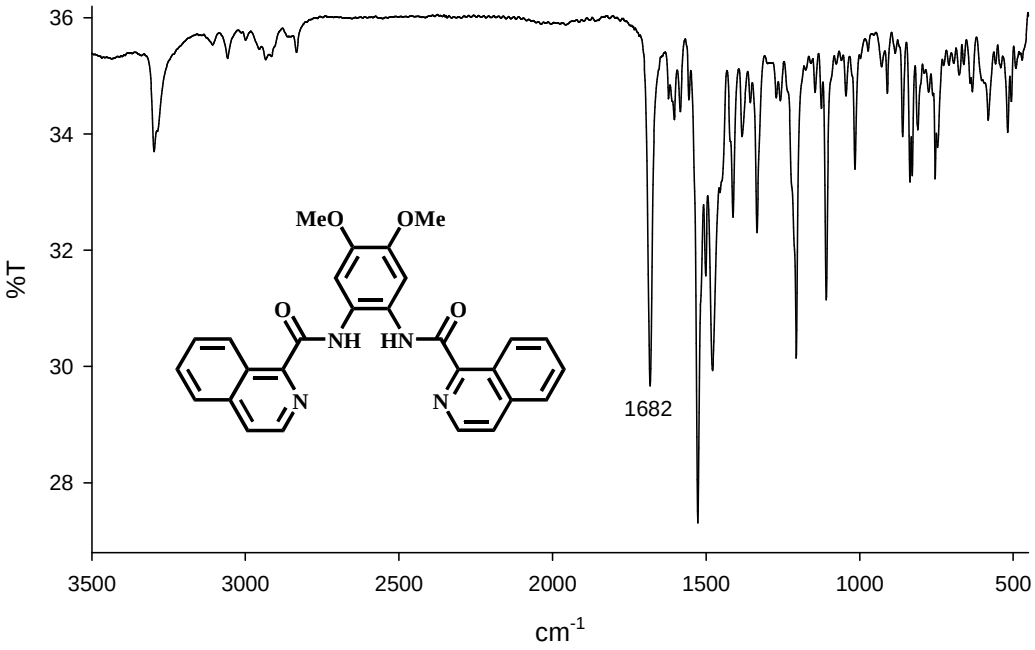

Figure 4.35. IR spectrum of $H_2(OMe)_2IQ1$ in KBr pellet

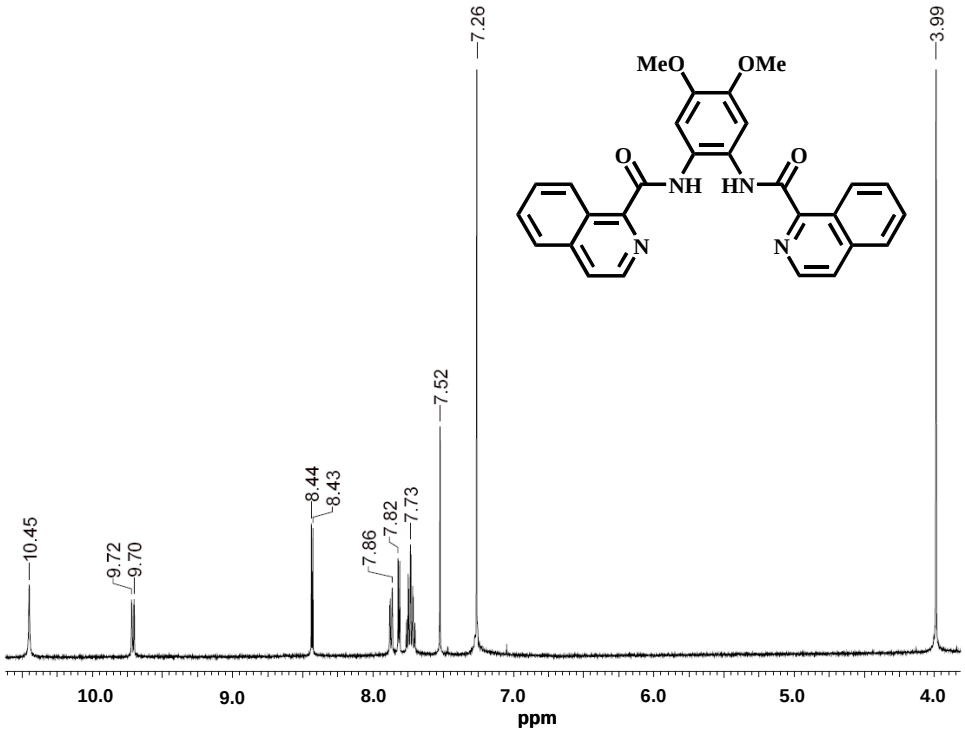

Figure 4.36. ^{1}H-NMR spectrum (3.8-10.5 ppm) of $H_2(OMe)_2IQ1$ in $CDCl_3$ at 298 K

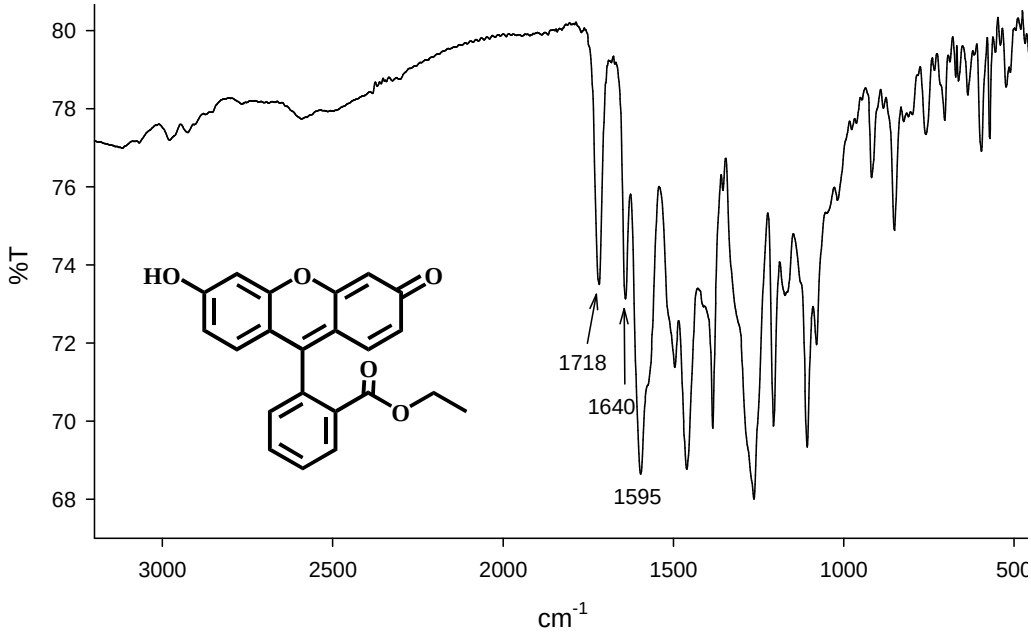

Figure 4.37. IR spectrum of FlEt in KBr pellet

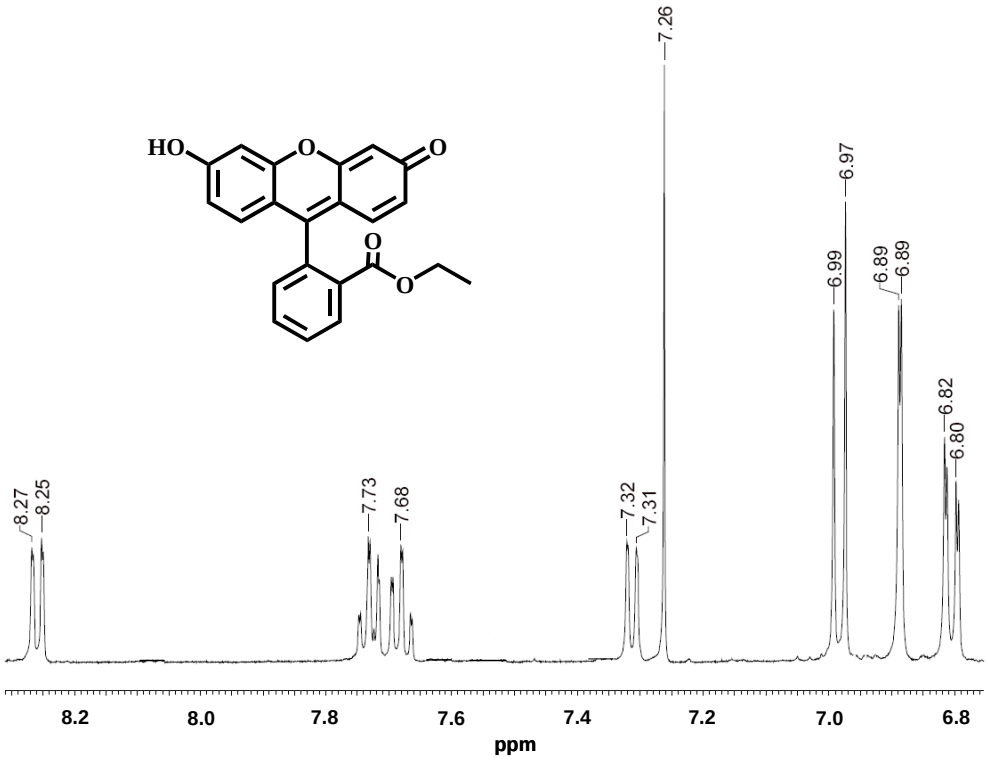

Figure 4.38. ^{1}H-NMR spectrum (6.8-8.3 ppm) of FlEt in $CDCl_3$ at 298 K.

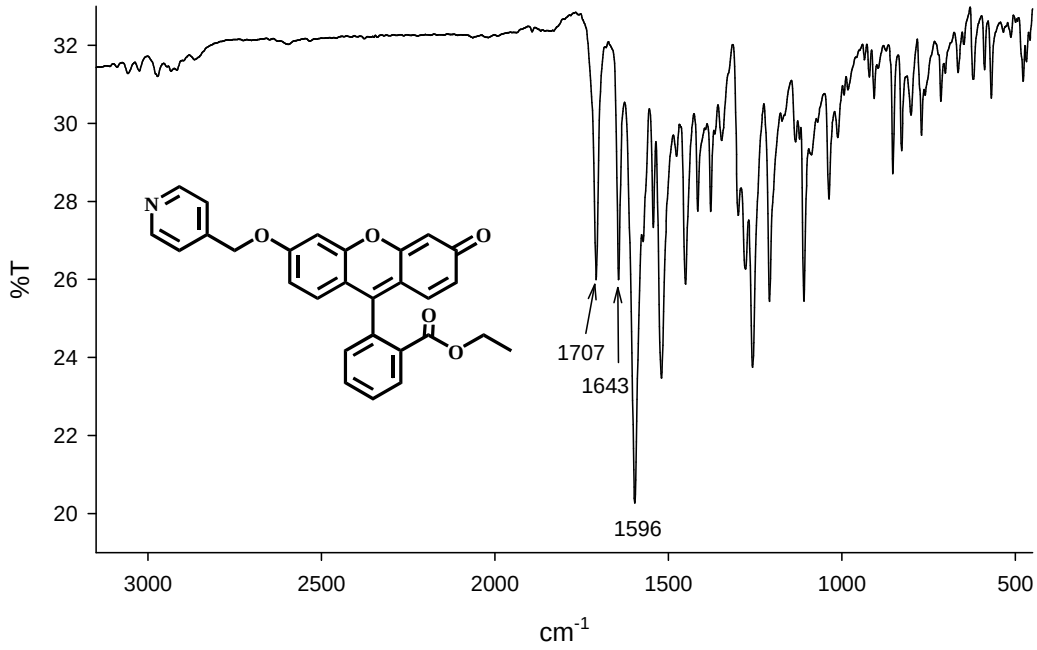

Figure 4.39. IR spectrum of PyFlEt in KBr pellet

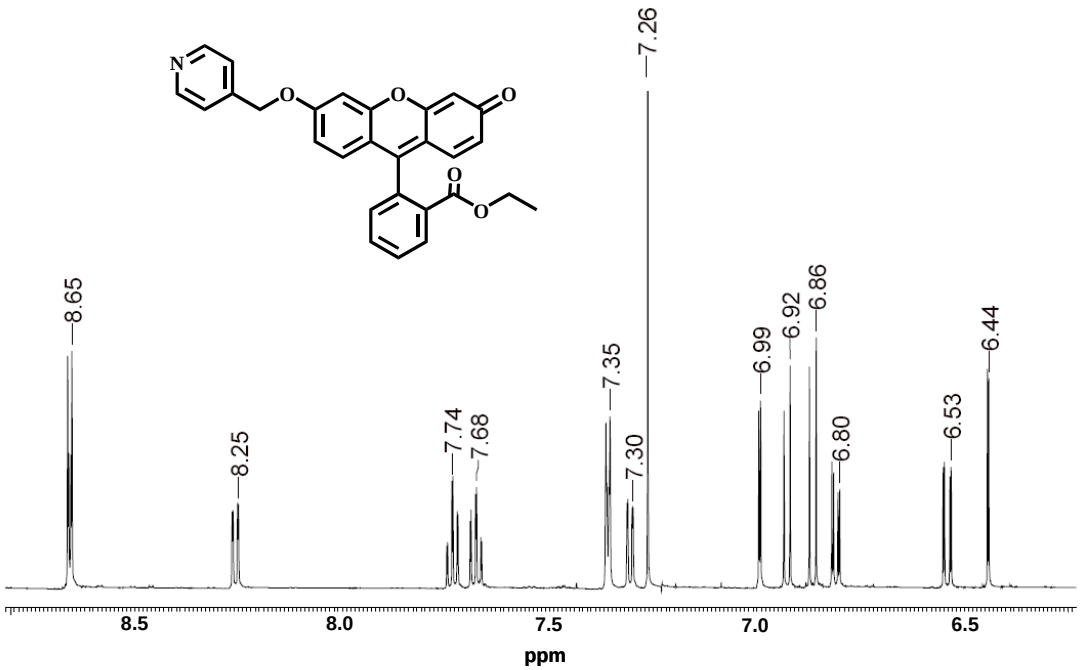

Figure 4.40. ^{1}H-NMR spectrum (6.2-8.8 ppm) of PyFlEt in $CDCl_3$ at 298 K

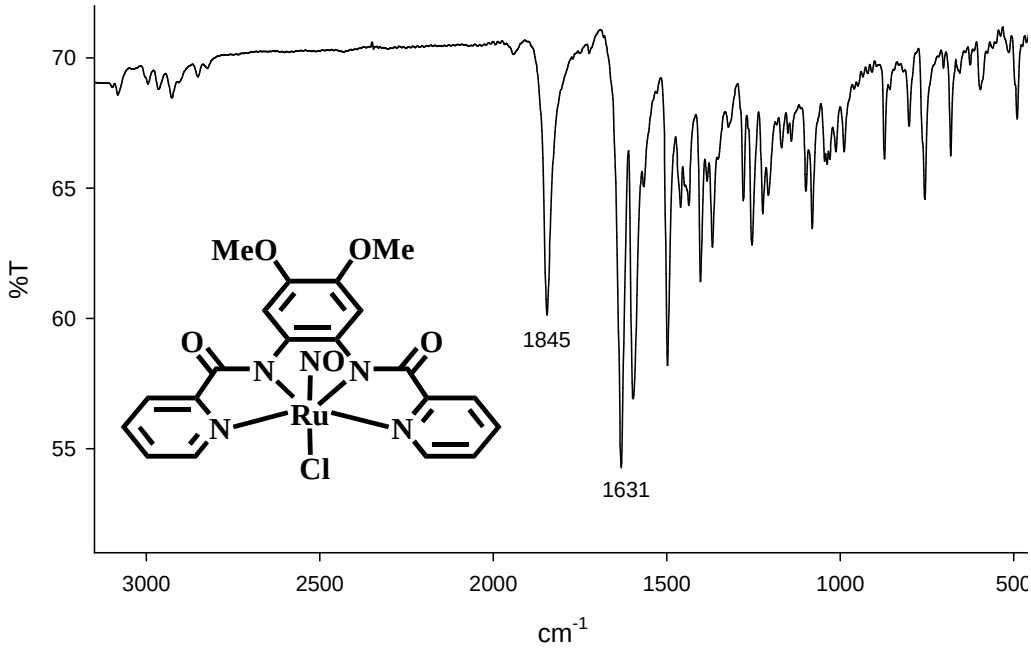

Figure 4.41. IR spectrum of [((OMe)$_2$bpb)Ru(NO)(Cl)] in KBr pellet

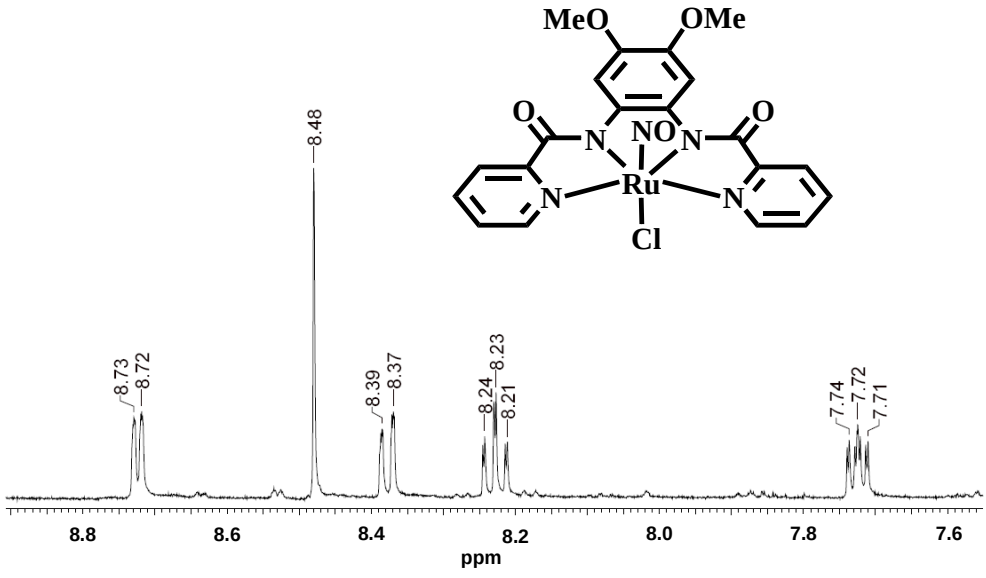

Figure 4.42. ^{1}H-NMR spectrum (7.5-8.9 ppm) of [((OMe)$_2$bpb)Ru(NO)(Cl)] in $CDCl_3$ at 298 K

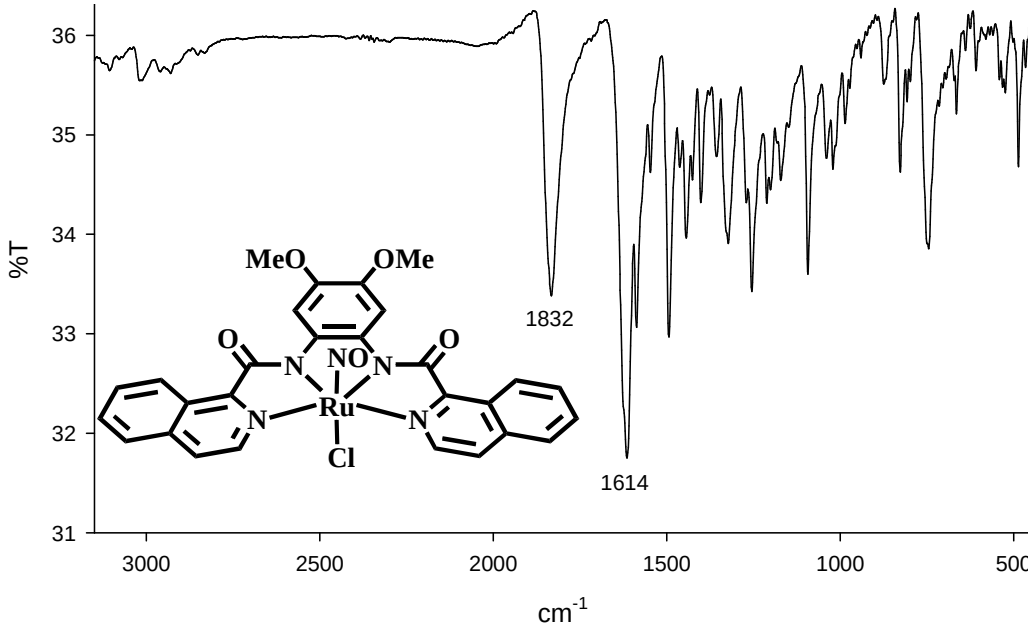

Figure 4.43. IR spectrum of [((OMe)$_2$IQ1)Ru(NO)(Cl)] in KBr pellet

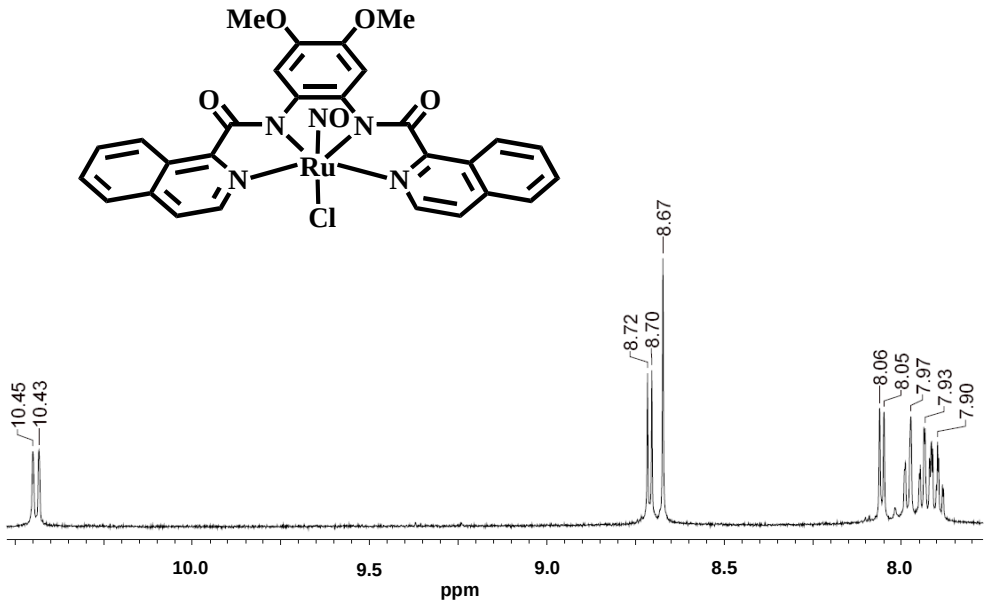

Figure 4.44. ^{1}H-NMR spectrum (7.7-11.0 ppm) of [((OMe)$_2$IQ1)Ru(NO)(Cl)] in $CDCl_3$ at 298 K

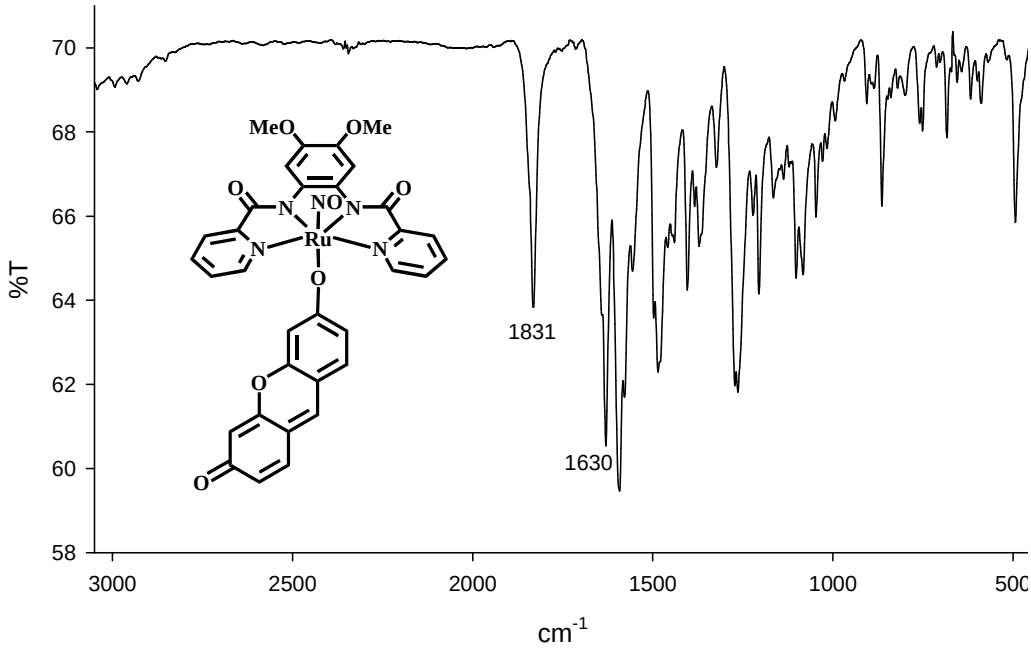

Figure 4.45. IR spectrum of [((OMe)$_2$bpb)Ru(NO)(Resf)] in KBr pellet

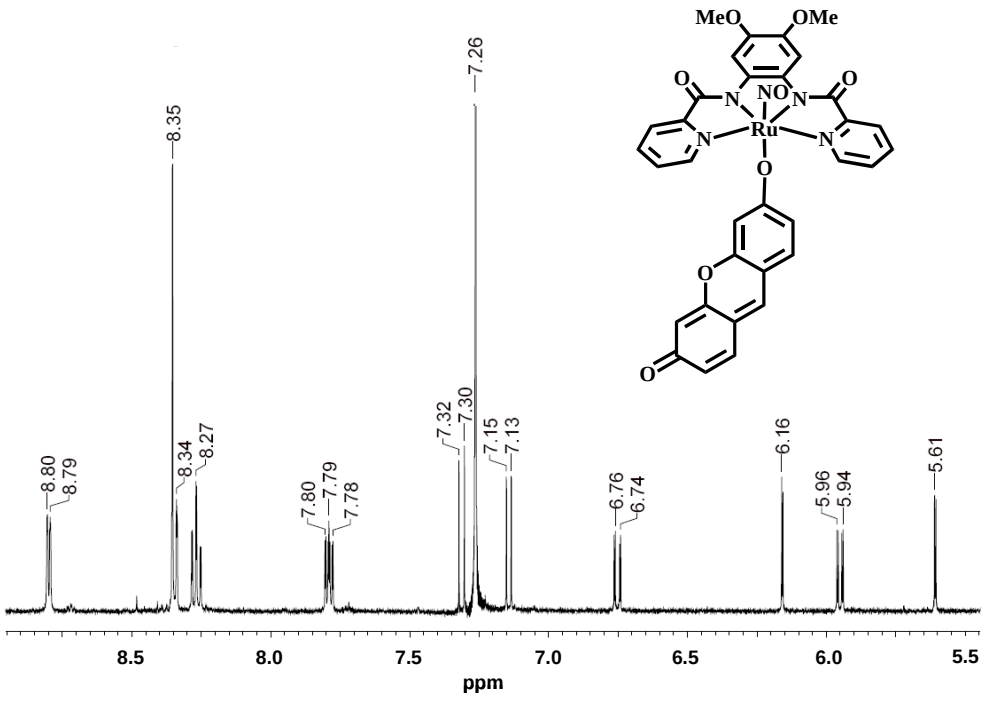

Figure 4.46. ^{1}H-NMR spectrum (5.5-9.0 ppm) of [((OMe)$_2$bpb)Ru(NO)(Resf)] in $CDCl_3$ at 298 K

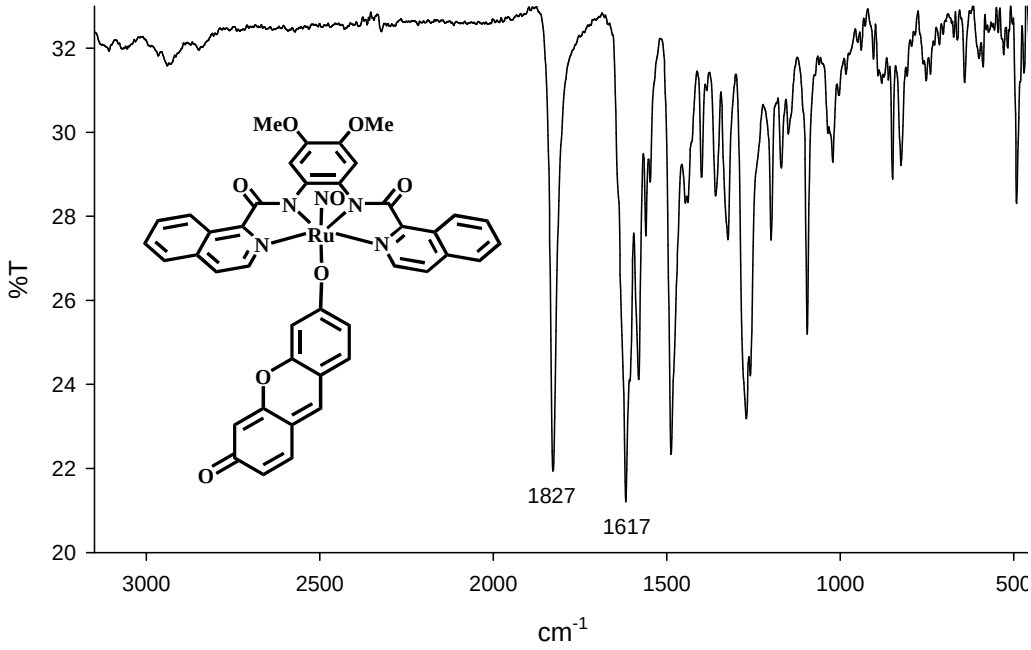

Figure 4.47. IR spectrum of [((OMe)$_2$IQ1)Ru(NO)(Resf)] in KBr pellet

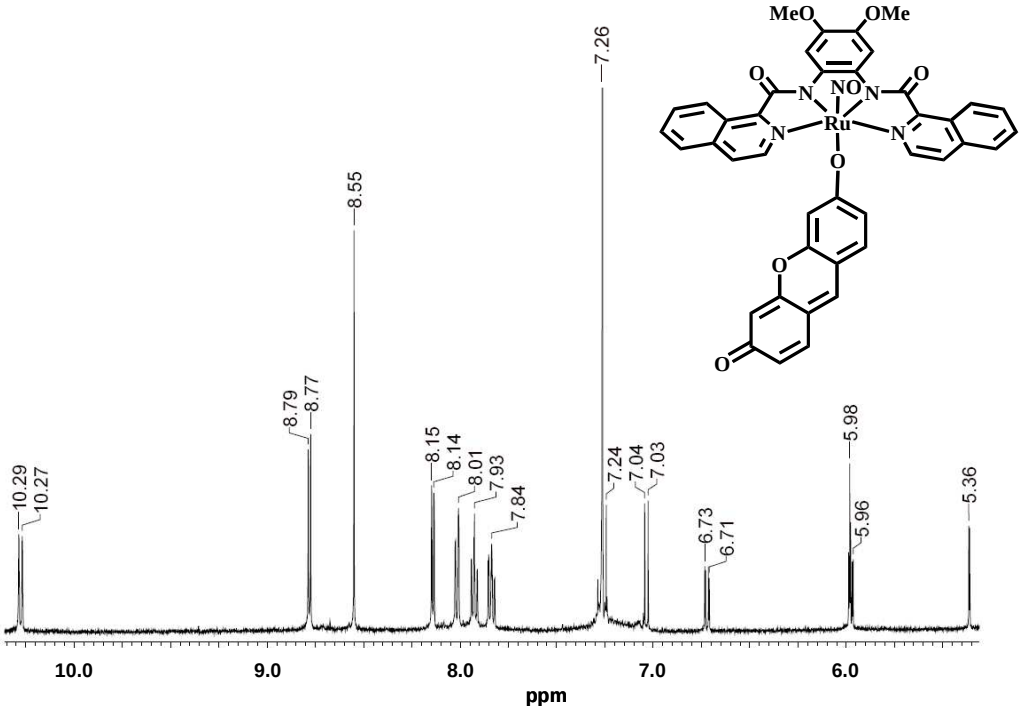

Figure 4.48. ^{1}H-NMR spectrum (5.1-10.4 ppm) of [((OMe)$_2$IQ1)Ru(NO)(Resf)] in $CDCl_3$ at 298 K

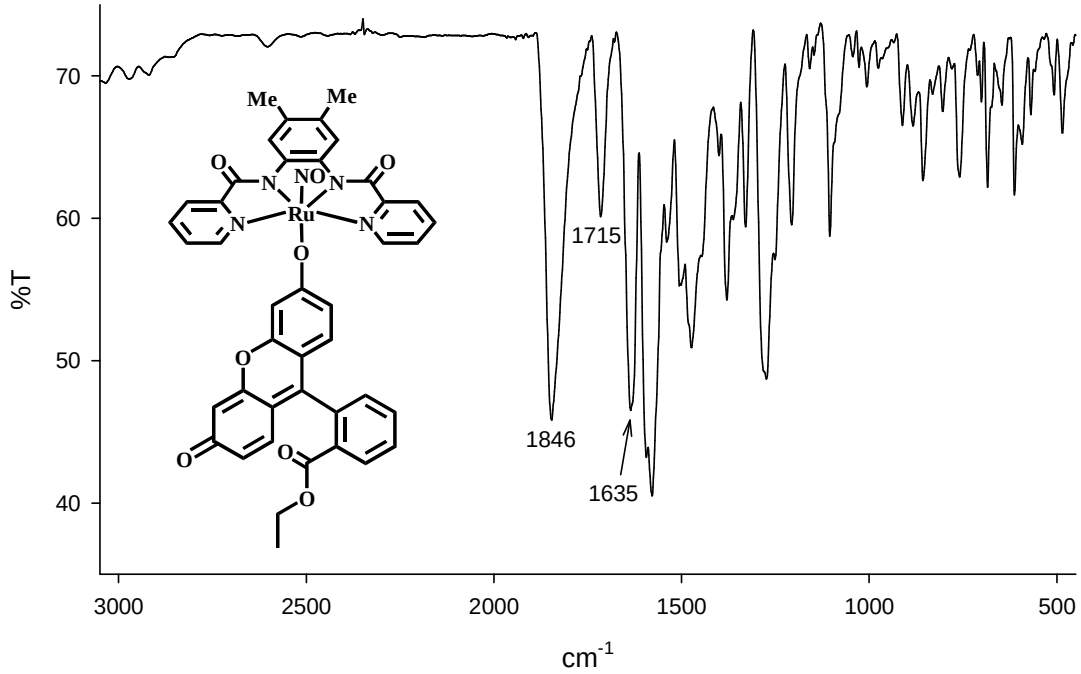

Figure 4.49. IR spectrum of [(Me_2bpb)Ru(NO)(FlEt)] in KBr pellet

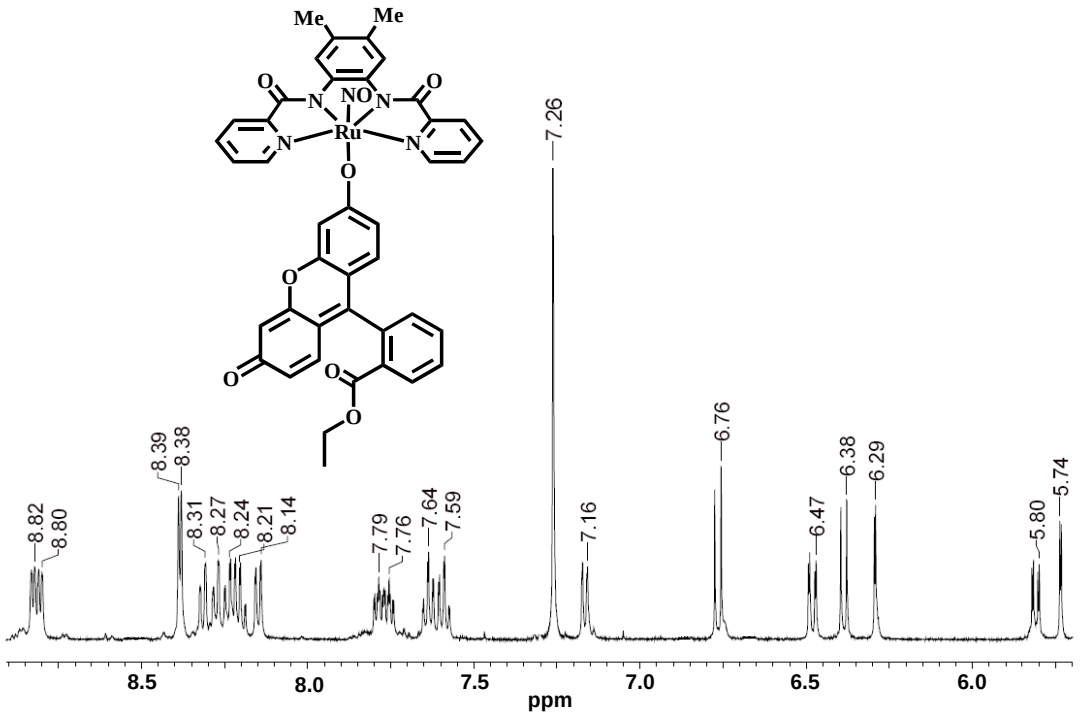

Figure 4.50. ^{1}H-NMR spectrum (5.7-9.0 ppm) of [(Me_2bpb)Ru(NO)(FlEt)] in $CDCl_3$ at 298 K

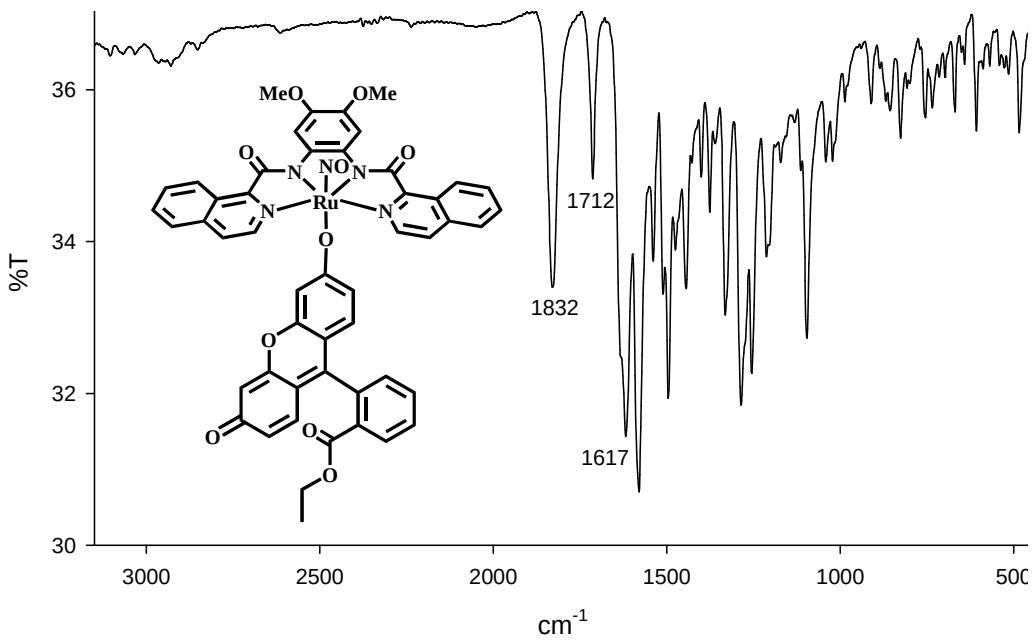

Figure 4.51. IR spectrum of [((OMe)$_2$IQ1)Ru(NO)(FlEt)] in KBr pellet

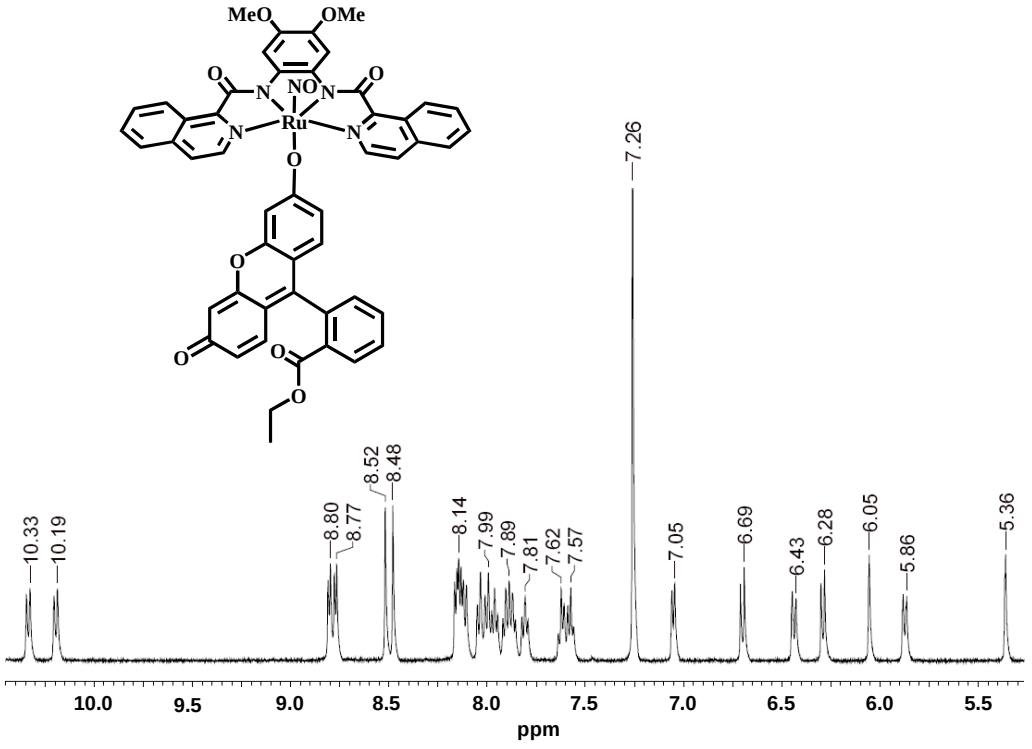

Figure 4.52. ^{1}H-NMR spectrum (5.3-10.5 ppm) of [((OMe)$_2$IQ1)Ru(NO)(FlEt)] in $CDCl_3$ at 298 K

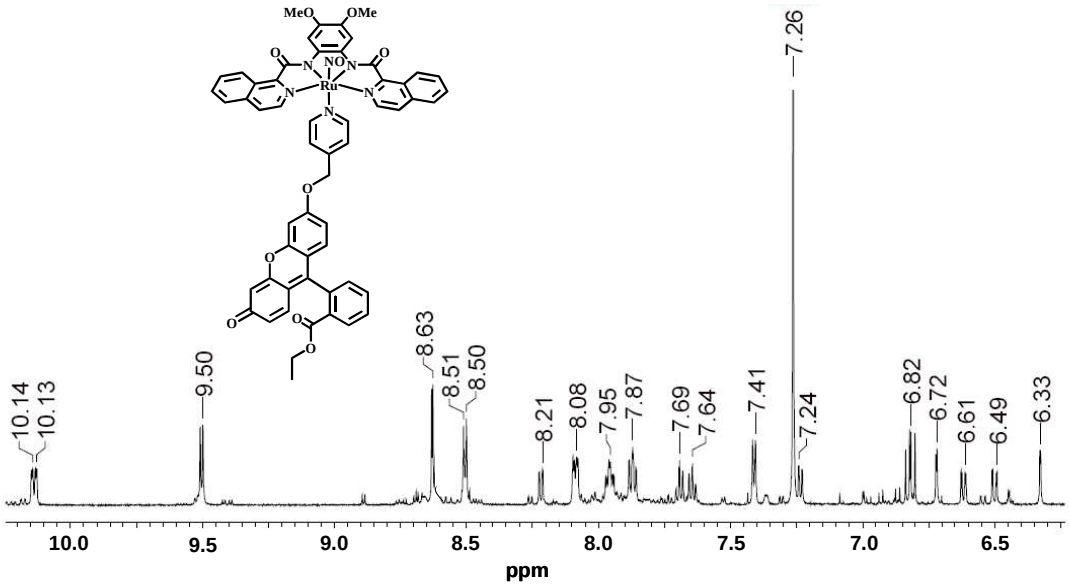

Figure 4.53. ^{1}H-NMR spectrum (6.3-10.2 ppm) of [((OMe)$_2$IQ1)Ru(NO)(PyFlEt)] in $CDCl_3$ at 298 K

4.10 References

1. Wecksler, S. R.; Hutchinson, J.; Ford, P. C. *Inorg. Chem.* **2006**, *45*, 1192.

2. Conrado, C. L.; Wecksler, S.; Egler, C.; Magde, D.; Ford, P. C. *Inorg. Chem*. **2004**, 43, 5543.

3. Rose, M. J.; Mascharak, P. K. *Inorg. Chem.* **2009**, *48*, 6904.

4. Rose, M. J.; Mascharak, P. K. *Curr. Opin. Chem. Biol*. **2008**, *12*, 238.

5. a) Rose, M. J.; Olmstead, M. M.; Mascharak, P. K. *J. Am. Chem. Soc.* **2007**, *129*, 5342; b) Rose, M. J.; Fry, N. L; Marlow, R.; Hinck, L.; Mascharak, P. K. *J. Am. Chem. Soc.* **2008**, *130*, 8834.

6. Smith, L. M.; Sanders, J. Z.; Kaiser, R. J.; Dodd, C.; Connell, C. R.; Heiner, C.; Kent, S. B. H.; Hood, L. E. *Nature* **1986**, *321*, 674.

7. Nolan, E. M.; Jaworski, J.; Okamoto, K.; Hayashi, Y.; Sheng, M.; Lippard, S. J. *J. Am. Chem. Soc.* **2005**, *127*, 16812.

8. Patra, A. K.; Rose, M. J.; Murphy, K. M.; Olmstead, M. M.; Mascharak, P. K. *Inorg. Chem.* **2004**, *43*, 4487.

9. Rosa, D. T.; Reynolds, R. A.; Malinak, S. M.; Coucouvanis, D. *Inorg. Synth.* **2002**, *35*, 112.

10. a) Bordini, J.; Hughes, D. L.; Da Motta Neto, J. D.; da Cunha, J. C. *Inorg. Chem.* **2002**, *41*, 5410; b) Sellmann, D.; Häuβinger, D.; Gottschalk-Gaudig, T.; Heinemann, F. W. Z. Naturforsch. **2000**, *55b*, 723.

11. Conrado, C.; Bourassa, J. L.; Egler, C.;Wecksler, S.; Ford, P. C. *Inorg. Chem.* **2003**, *42*, 2288.

12. a) McQuade L. E.; Lippard, S. J. *Curr. Opin. Chem. Biol*. **2010**, *14*, 43; b) Lim M. H.; Lippard, S. J. *Acc. Chem. Res.* **2007,** *40*, 41.

13. Lim, M. H.; Xu, D.; Lippard, S. J. *Nat. Chem. Biol*. **2006**, *2*, 375.

Appendix A

Additional Ruthenium Nitrosyl Syntheses

A.1 Syntheses and Structures

A.1.1 Characterization of [((OMe)$_2$IQ1)Ru(NO)(MIN)](BF$_4$)

We decided to synthesize a ruthenium nitrosyl with a methyl isonicotinate (MIN) ligand. This ligand was specifically chosen for its methyl ester functionality. Ester groups could potentially be used to attach various cell targeting moieties that would direct the nitrosyls to a specific cell type (such as cancerous cells) thus increasing its site specificity. The MIN ligand was attached by first removing the chloride ligand of [((OMe)$_2$IQ1)Ru(NO)(Cl)] via Cl-extraction with $AgBF_4$ in dry MeCN followed by addition of MIN to generate [((OMe)$_2$IQ1)Ru(NO)(MIN)](BF$_4$). Since the initial Cl-extraction reaction never goes to completion, there is always some Ag^+ still in solution once MIN is added. As a consequence of Ag^+ high affinity for pyridine-N donors, a Ag-MIN species is also formed during the reaction (as seen by ^{1}H-NMR in CD_3CN, δ from TMS: 8.75 (d 2H), 7.82 (d 2H), 3.91 (s 3H)). This species is very difficult to separate from the [((OMe)$_2$IQ1)Ru(NO)(MIN)](BF$_4$) product due to their similar 1+ charges.

The crystal structure of [((OMe)$_2$IQ1)Ru(NO)(MIN)](BF$_4$) reveals that the MIN ligand is bound through the pyridine-N trans to NO (Figure A.1). The neutral pyridine donor decreases the amount of π-backbonding compared to the charged Cl^- bound species. This causes a lengthening of the N-O bond in [((OMe)$_2$IQ1)Ru(NO)(MIN)](BF$_4$) as evidenced by its NO stretching frequency of 1854 cm^{-1} compared to that of [((OMe)$_2$IQ1)Ru(NO)(Cl)] at 1832 cm^{-1}. The IR

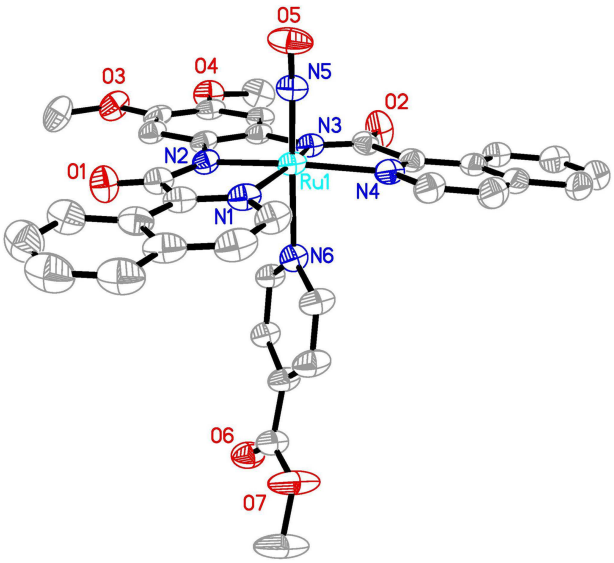

Figure A.1. Thermal ellipsoid (probability level 50%) plot of $[((OMe)_2IQ1)Ru(NO)(MIN)]^+$ with select atom-labeling. H atoms are omitted for the sake of clarity.

spectrum of $[((OMe)_2IQ1)Ru(NO)(MIN)](BF_4)$ also has a peak at 1740 cm^{-1} corresponding to the carbonyl stretching frequency of the methyl ester in the bound-MIN ligand.

A.1.2 Characterization of $[(Me_2bpb)Ru(NO)(Rd\text{-}B)](BF_4)$ and $[((OMe)_2IQ1)Ru(NO)(Rd\text{-}B)](BF_4)$

The bright pink dye, Rodamine-B (Rd-B), was attached via its carboxylate-O atom to the ruthenium center of the Me_2bpb- and $(OMe)_2$IQ1-containing $\{RuNO\}^6$ nitrosyls. Similar to the reaction describe above, the chloride bound species ($[(Me_2bpb)Ru(NO)(Cl)]$ and $[((OMe)_2IQ1)Ru(NO)(Cl)]$) were treated with $AgBF_4$ to remove the chloride ligand allowing binding of Rd-B to form both $[(Me_2bpb)Ru(NO)(Rd\text{-}B)](BF_4)$ and $[((OMe)_2IQ1)Ru(NO)(Rd\text{-}B)](BF_4)$ (Figure

A.2). In its bound form, Rd-B contains a positively charged imine-N center which increases the solubility of the Rd-B bound nitrosyls in aqueous media compared to the corresponding neutral resorufin (Resf)- and fluorescein ethyl ester (FlEt)-bound ruthenium nitrosyls.

Free Rd-B has a strong absorption band at 554 nm (ε = 106 000 $M^{-1}cm^{-1}$). Its strong visible light absorption is attributed to a π–π^* transition centered on the conjugated tricyclic ring system of the dye. Resf and FlEt contain similar tricyclic ring systems that also give rise to strong visible light absorption bands at 590 nm (ε = 105 000 $M^{-1}cm^{-1}$) and 504 nm (ε = 80 000) when these dyes are in their deprotonated forms.

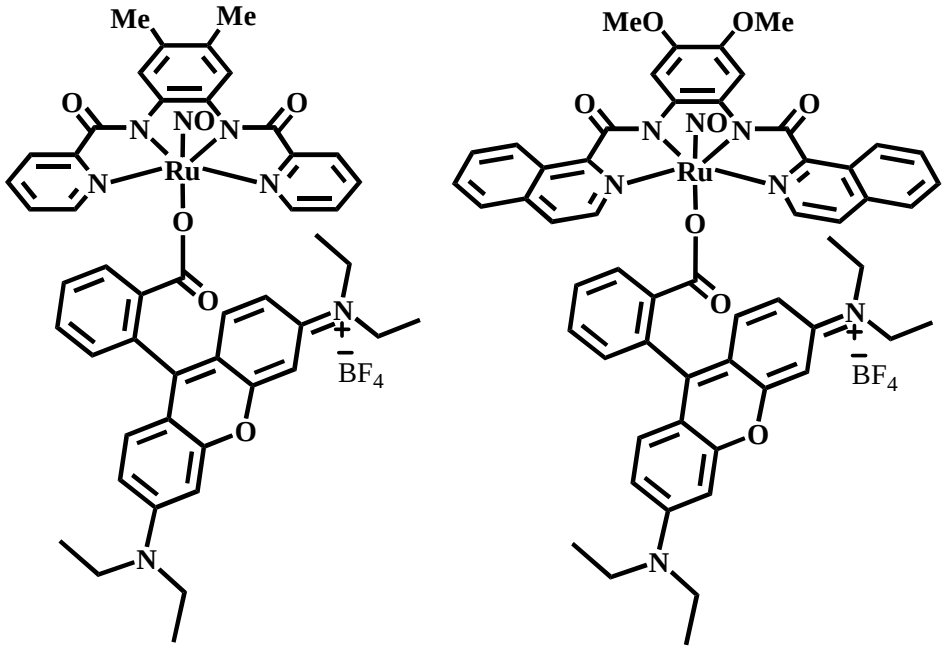

[(Me$_2$bpb)Ru(NO)(Rd-B)](BF$_4$) **[((OMe)$_2$IQ1)Ru(NO)(Rd-B)](BF$_4$)**

Figure A.2. Rodamine-B (Rd-B) Bound {RuNO}^{6} Nitorsyls

These transitions appear at low energy due to the extensive delocalization of electron density (on the amine-N of Rd-B or the phenolato-O moiety of Resf and FlEt) over the entire tricyclic ring system (Figure A.3). Resf and FlEt both bind the ruthenium center via their deprotonated phenolato-O moieties. This greatly perturbs the delocalized tricyclic ring system and causes a blue-shift of the dyes' absorption bands

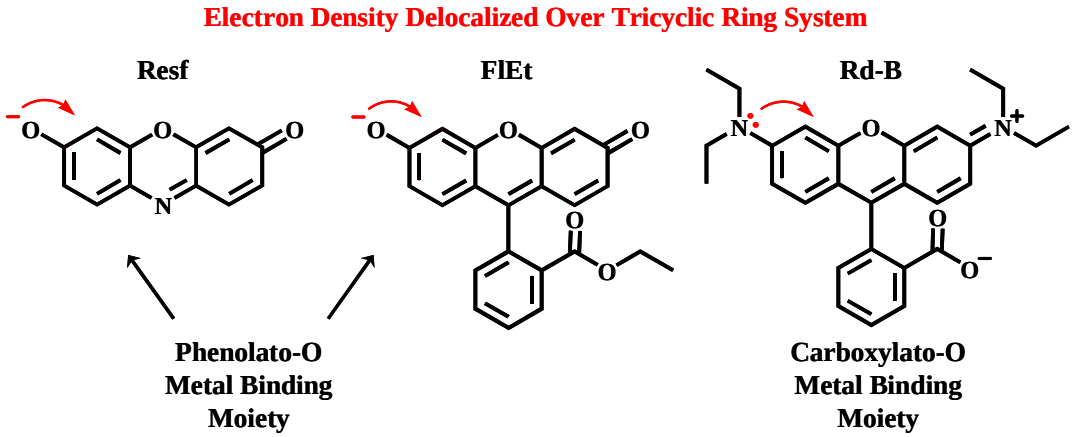

Figure A.3. Chemical structure of resorufin (Resf), fluorescein ethyl ester (FlEt), and rodamine-B (Rd-B) with their metal binding moieties and delocalized electron density emphasized.

in the electronic absorption spectra of [((OMe)$_2$IQ1)Ru(NO)(Resf)] and [((OMe)$_2$IQ1)Ru(NO)(FlEt)] (λ_{max} = 500 nm and 475 nm, respectively). However, since Rd-B binds the metal center through its carboxylato-O moiety, the delocalized system remains undisturbed and thus the absorption band of Rd-B is very slightly shifted in the case of [(Me$_2$bpb)Ru(NO)(Rd-B)](BF$_4$) and [((OMe)$_2$IQ1)Ru(NO)(Rd-B)](BF$_4$) (λ_{max} = 558 nm for both nitrosyls, Figure A.4). In addition, the intensity of absorption band of bound Rd-B in these nitroysls (ε = 67 000 $M^{-1}cm^{-1}$ and ε = 70 000

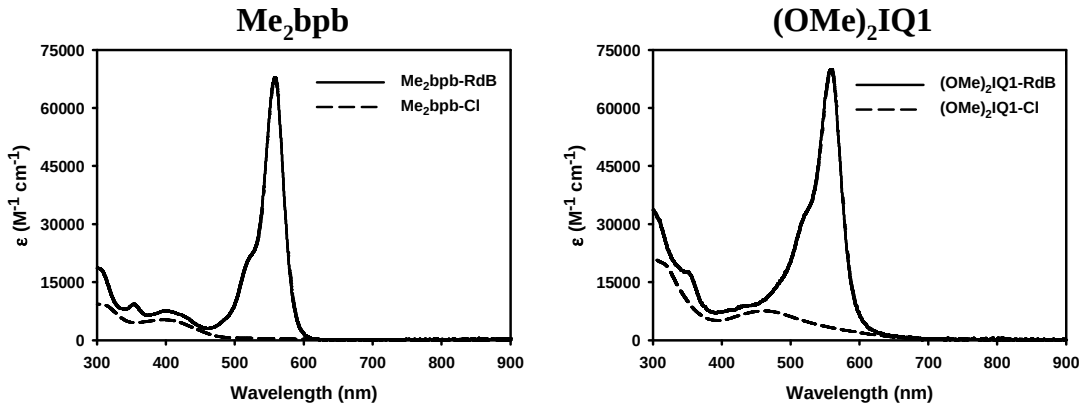

Figure A.4. Electronic absorption spectrum of chloride-bound [(Me_2bpb)Ru(NO)(Cl)] and [(($OMe)_2$IQ1)Ru(NO)(Cl)] compared to dye-bound [(Me_2bpb)Ru(NO)(Rd-B)](BF_4) and [(($OMe)_2$IQ1)Ru(NO)(Rd-B)](BF_4) in MeCN that seen for [(($OMe)_2$IQ1)Ru(NO)(Resf)] and [(($OMe)_2$IQ1)Ru-(NO)(FlEt)]

$M^{-1}cm^{-1}$, respectively) is decreased compared to that of free dye by a much lesser extent than seen for the Resf and FlEt bound $\{RuNO\}^6$ nitrosys (ε = 28 000 $M^{-1}cm^{-1}$ for both [(($OMe)_2$IQ1)Ru(NO)(Resf)] and [(($OMe)_2$IQ1)Ru(NO)(FlEt)]). This provides a dramatically increased amount of visible light absorption by the Rd-B bound nitrosyls compared to the related chloride-bound species (Figure A.4). Studies are currently in progress to see if this increased amount of visible light absorption in [(Me_2bpb)Ru(NO)(Rd-B)](BF_4) and [(($OMe)_2$IQ1)Ru(NO)(Rd-B)](BF_4) leads to increased quantum yield values for NO photorelease using visible light as was seen for the Resf- and FlEt-bound ruthenium nitrosyls. We hypothesize that since the tricyclic ring system of Rd-B is not directly conjugated to the ruthenium center, but instead through the carboxylate tail of the dye there will be less enhancement of the NO photolability in the visible region.

A.2 Experimental Section

A.2.1 Syntheses of Compounds

[((OMe)$_2$IQ1)Ru(NO)(MIN)](BF$_4$). A batch of [((OMe)$_2$IQ1)Ru(NO)(Cl)] (0.161 g, 0.250 mmol) was treated with $AgBF_4$ (0.049 g, 0.251 mmol) in 15 mL of MeCN and heated to reflux temperature. After 2 h, 3 equiv of methyl isonicotinate (MIN) (0.103 g, 0.752 mmol) was added to the hot solution which was then kept at reflux temperature for an additional 4 h. The solution was cooled to room temperature and condensed down to 5 mL. Roughly 2 mL of diethyl ether was added and the solution was stored at -20°C overnight. The resulting precipitant was removed by filtration using a celite pad. Vapor diffusion of ether into the filtrate afforded the crude product as a brown solid. X-ray quality crystals of [((OMe)$_2$IQ1)Ru(NO)(MIN)](BF$_4$) were obtained by vapor diffusion of pentane into a solution of the crude product in $CHCl_3$ at room temperature. Selected IR frequencies (KBr disk, in cm^{-1}): 1854 (m, $\mathbf{\nu}_{NO}$), 1740 (w), 1617 (vs), 1585 (m), 1496 (s), 1323 (m), 1253 (m), 1091 (s), 1050 (s). ^{1}H-NMR in CD_3CN, δ from TMS: 10.10 (d 2H), 9.17 (d 2H), 8.62 (s 2H), 8.43 (d 2H), 8.39 (d 2H), 8.17 (d 2H), 8.01 (t 2H), 7.92 (t 2H), 7.64 (d 2H), 3.96 (s 6H), 3.72 (s 3H).

[(Me$_2$bpb)Ru(NO)(Rd-B)](BF$_4$). A batch of [(Me$_2$bpb)Ru(NO)(Cl)] (0.10 g, 0.196 mmol) in 20 mL of MeCN was treated with $AgBF_4$ (0.038 g, 0.196 mmol) and stirred at reflux temperature for 12 h. Rhodamine-B (0.094 g, 0.196 mmol) was then dissolved in 5 mL of MeCN and deprotonated with NaH (0.005 g, 0.196 mmol). The resulting slurry was added to the hot solution and kept at reflux temperature for an

additional 5 h. The pink solution was cooled in a ice bath and then filtered through a celite pad to remove solid NaCl and AgCl. The filtrate was then condensed under vacuum until only 5 mL of the solution remained and then 2 mL of diethyl ether was added. The resulting solution was cooled to -20°C for several hours causing a dark red solid to form which was isolated by filtration. Yield: 0.080 g (41%). Selected IR frequencies (KBr disk, in cm^{-1}): 1846 (m ν_{NO}), 1636 (s), 1590 (vs), 1484 (m), 1413 (m), 1338 (s), 1180 (s), 1072 (m). ^{1}H-NMR in $CDCl_3$, δ from TMS: 9.07 (d 2H), 8.25 (s 2H), 8.06 (t 2H), 7.98 (d 2H), 7.71 (t 2H), 7.54 (d 1H), 7.35 (d 2H), 6.79 (dd 1H), 6.74 (s 1H), 6.72 (s 1H), 6.65 (d 2H), 6.58 (d 2H), 3.67 (m 8H), 2.33 (s 6H), 1.42 (t 12H).UV/vis in MeCN, λ in nm (ε in M^{-1} cm^{-1}): 558 (67 000).

[((OMe)$_2$IQ1)Ru(NO)(Rd-B)](BF$_4$). A solution of [((OMe)$_2$IQ1)Ru-(NO)(Cl)] (0.080 g, 0.124 mmol) in 15 mL of MeCN was treated with $AgBF_4$ (0.024 g, 0.124 mmol) and heated to reflux temperature for 2 h. Meanwhile, a batch of 0.089 g (0.187 mmol) of rhodamine-B dye (Rd-B, as Cl salt) was dissolved in 10 mL MeCN and NaH (0.005 g, 0.187 mmol) was added causing a light pink solid (deprotonate Rd-B as a zwitterion) to form. The resulting mixture was then added to the hot nitrosyl containing solution and continued to stir at reflux temperature overnight. The resulting bright red solution was filtered and concentrated to 5 mL under vacuum. Roughly 10 mL of diethyl ether were added to the concentrated solution until a dark red solid began to form which was then filtered. Yield: 0.065 g (46%). Selected IR frequencies (KBr disk, in cm^{-1}): 1836 (s ν_{NO}), 1633 (s), 1617 (s), 1590 (vs), 1495 (s), 1413 (m), 1325 (s), 1338 (s), 1254 (m), 1182 (s), 1092 (m), 1064

(m) . ^{1}H-NMR in $CDCl_3$, δ from TMS: 10.11 (d 2H), 9.08 (d 2H), 8.27 (s 2H), 8.10 (d 2H), 8.03 (d 2H), 7.92 (t 2H), 7.80 (t 2H), 7.58 (d 1H), 7.28 (d 2H), 6.68 (d 1H), 6.62 (d 2H), 6.58 (s 2H), 6.29 (d 2H), 4.03 (s 6H), 3.63 (m 8H), 1.34 (t 12H).UV/vis in MeCN, λ in nm (ε in M^{-1} cm^{-1}): 558 (70 000).

A.2.2 Experimental Data: ^{1}H-NMR and IR Spectra

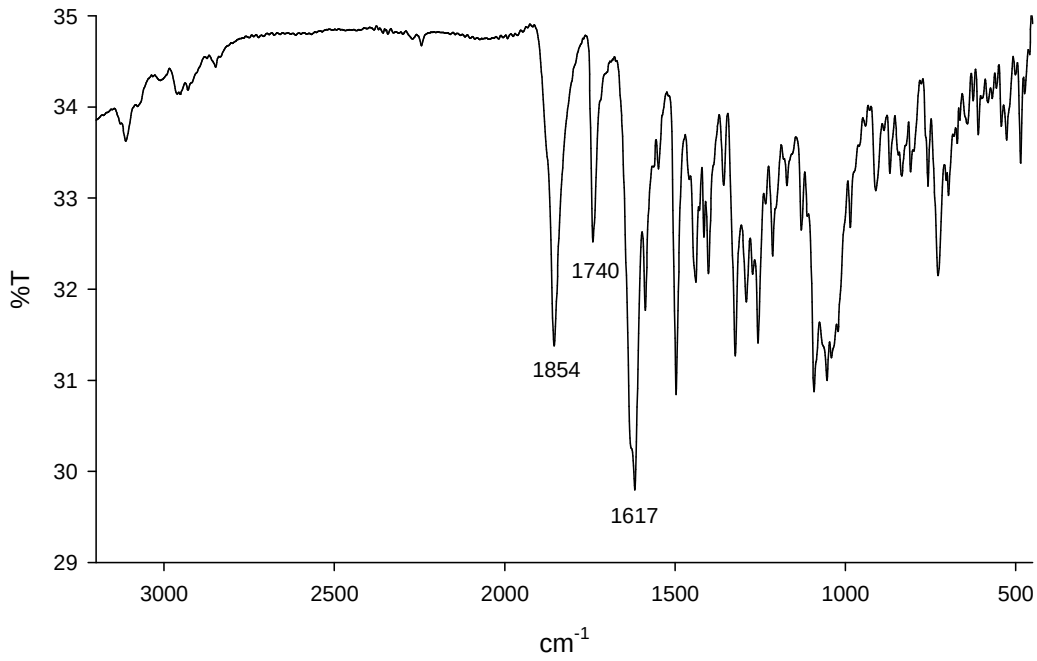

Figure A.5. IR spectrum of [((OMe)$_2$IQ1)Ru(NO)(MIN)](BF$_4$) in KBr pellet

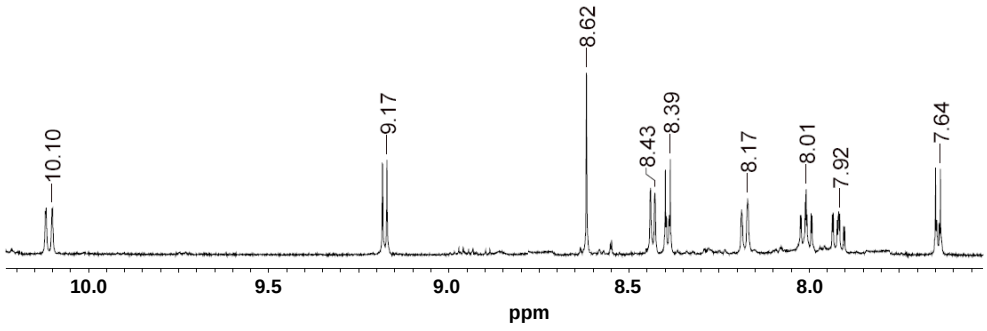

Figure A.6. ^{1}H-NMR spectrum (6.5-10.2 ppm) of ((OMe)$_2$IQ1)Ru(NO)(MIN)](BF$_4$) in CD_3CN at 298 K

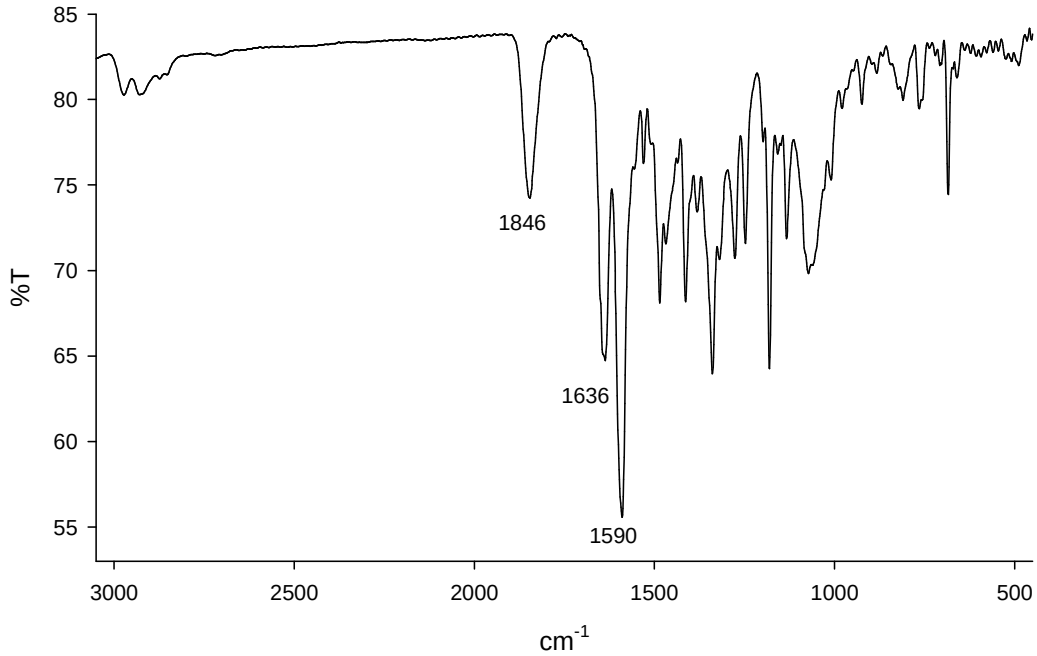

Figure A.7. IR spectrum of $[(Me_2bpb)Ru(NO)(Rd\text{-}B)](BF_4)$ in KBr pellet

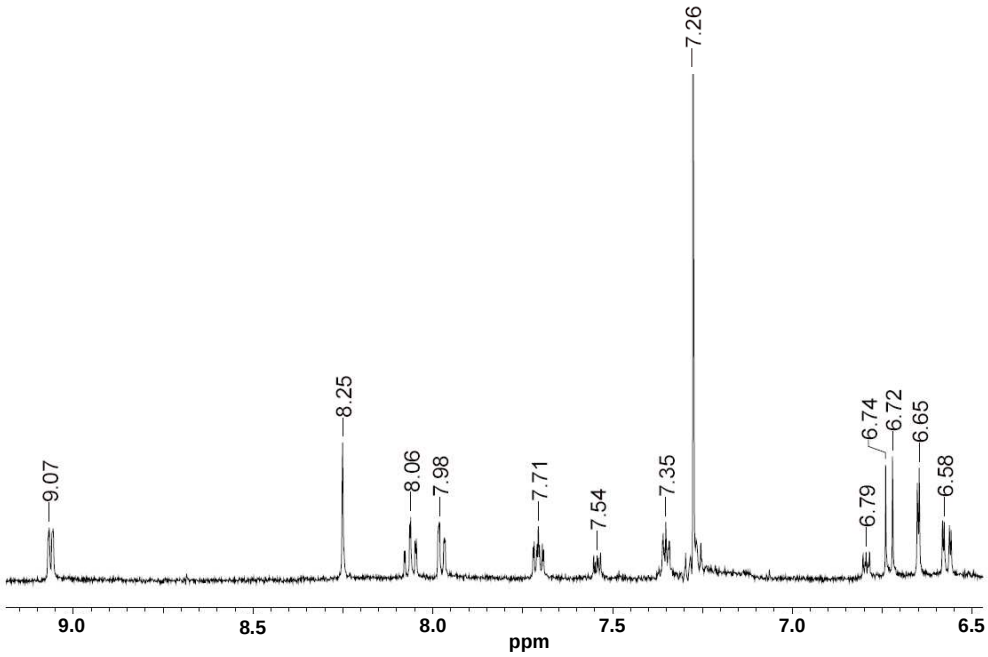

Figure A.8. ^{1}H-NMR spectrum (6.5-9.4 ppm) of $[(Me_2bpb)Ru(NO)(Rd\text{-}B)](BF_4)$ in $CDCl_3$ at 298 K

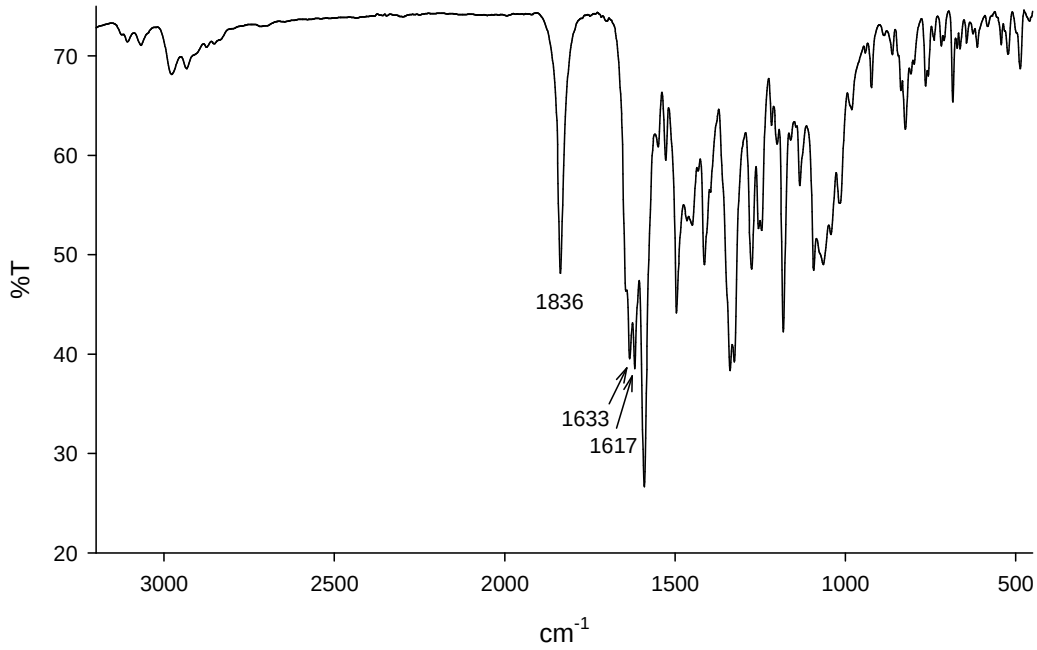

Figure A.9. IR spectrum of [((OMe)$_2$IQ1)Ru(NO)(Rd-B)](BF$_4$) in KBr pellet

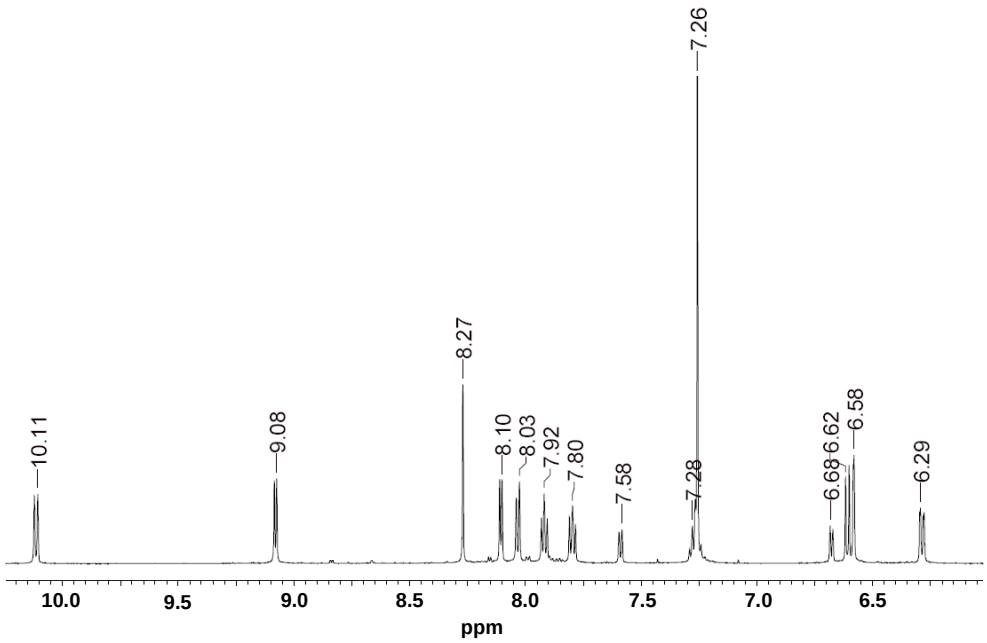

Figure A.10. ^{1}H-NMR spectrum (6.0-10.4 ppm) of [((OMe)$_2$IQ1)Ru(NO)(Rd-B)](BF$_4$) in CDCl$_3$ at 298 K